# FSBs with Stainless Steel Strands and GFRP Shear Reinforcement

Contract Number BED30-977-09
FSU Project 102114/102115

*Submitted to:*

Florida Department of Transportation
Research Center
605 Suwannee Street
Tallahassee, Florida 32399-0450

Vickie Young, P.E.
Project Manager
FDOT Structures Design Office

*Prepared by:*

Michelle Rambo-Roddenberry, Ph.D., P.E.
Principal Investigator

Omar Abdulsalam Abdulateef
Graduate Research Assistant

FAMU-FSU College of Engineering
Department of Civil and Environmental Engineering
2525 Pottsdamer Street
Tallahassee, FL 32310-6046

April 2026
Final Report

# FSBs with Stainless Steel Strands and GFRP Shear Reinforcement

Contract Number BED30-977-09
FSU Project 102114/102115

*Submitted to:*

Florida Department of Transportation
Research Center
605 Suwannee Street
Tallahassee, Florida 32399-0450

Vickie Young, P.E.
Project Manager
FDOT Structures Design Office

*Prepared by:*


Michelle Rambo-Roddenberry, Ph.D., P.E.
Principal Investigator

Omar Abdulsalam Abdulateef
Graduate Research Assistant

FAMU-FSU College of Engineering
Department of Civil and Environmental Engineering
2525 Pottsdamer Street
Tallahassee, FL 32310-6046


July 2026
Final Report

# Disclaimer

# Technical Report Documentation Page

| 1. Report No. | 2. Government Accession No. | 3. Recipient's Catalog No. |
|---|---|---|
| 4. Title and Subtitle<br>FSBs with Stainless Steel Strands and GFRP Shear Reinforcement | | 5. Report Date<br>July 2026 |
| | | 6. Performing Organization Code<br>FSU Project 102114/102115 |
| 7. Author(s)<br>Michelle Rambo-Roddenberry, Ph.D., P.E.<br>and Omar Abdulsalam Abdulateef | | 8. Performing Organization Report No. |
| 9. Performing Organization Name and Address<br>FAMU-FSU College of Engineering<br>Department of Civil and Environmental Engineering<br>2525 Pottsdamer St.<br>Tallahassee, FL 32310-6046 | | 10. Work Unit No. (TRAIS) |
| | | 11. Contract or Grant No.<br>BED30-977-09 |
| 12. Sponsoring Agency Name and Address<br>Florida Department of Transportation<br>605 Suwannee Street, MS 30<br>Tallahassee, FL 32399 | | 13. Type of Report and Period Covered<br>Final Report<br>April 2023 – July 2026 |
| | | 14. Sponsoring Agency Code |
| 15. Supplementary Notes | | |

16. Abstract

Prestressed concrete Florida slab beams (FSBs), often used for short-span and low-profile bridges, are susceptible to corrosion of their carbon steel prestressing strands and reinforcement due to chloride exposure. To extend service life and reduce long-term maintenance costs, the Florida Department of Transportation (FDOT) has moved toward requiring corrosion-resistant materials such as stainless steel prestressing strands and glass fiber-reinforced polymer (GFRP) transverse reinforcement for some bridges. This research evaluated the fabrication, structural behavior, ductility, and design efficiency of FSBs with these materials through full-scale testing and analytical modeling. Four (4) full-scale FSBs (12 in. × 48 in. × 34 ft) with cast-in-place toppings were fabricated and tested. Stainless steel prestressing strands were used in all beams, with varied strand quantities, and one beam used GFRP for all transverse and interface reinforcement. Analytical models, including incorporation of tension stiffening, for flexural response and ductility were developed and validated. A parametric study of nine (9) FSB sections and 254 prestressing strand configurations was conducted. FSBs required more stainless steel strands than those designed with carbon steel strands due to lower initial prestress. However, they demonstrated comparable flexural strength, deformation, and moment–curvature behavior. Performance of the FSB with GFRP reinforcement under the conditions tested was acceptable. This study provides FDOT and practicing engineers full-scale experimental evidence and validated analytical tools that support the use of these materials in FSBs.

| 17. Key Word | 18. Distribution Statement |
|---|---|
| Florida slab beam; Beams; Girders; Glass fiber reinforced plastics; Guidelines; Precast concrete; Prestressed concrete; Reinforcing bars; Slabs; Stainless steel | No restrictions. |

| 19. Security Classif. (of this report) | 20. Security Classif. (of this page) | 21. No. of Pages | 22. Price |
|---|---|---|---|
| Unclassified. | Unclassified. | 231 | |

**Form DOT F 1700.7** (8-72) Reproduction of completed page authorized

# Acknowledgements

The authors wish to express their gratitude and sincere appreciation to the Florida Department of Transportation (FDOT) for funding this project. The authors would like to thank Vickie Young for her technical input, reviews, and support (both managerial and moral) throughout the project. Thanks also to Steve Nolan and Yukai Yang for their help and technical reviews of the deliverables. Also, the work could not have been completed without the expertise and assistance of the amazing crew at the FDOT Structures Research Center in Tallahassee. This includes Steve Eudy, Christina Freeman, Miguel Ramirez, Justin Robertson, and Michael Waters. Collaborating on this project as well as on other projects with all the FDOT staff and working alongside them has been one of the greatest pleasures in our professional lives. The work was enjoyable and well executed due to their help and unwavering commitment. Thanks also go to Elizabeth Hazard for her help, attention to detail, and cheerful disposition. Lastly, we sincerely thank CDS Manufacturing Inc. for their willingness to embrace the challenge of fabricating a new concept, an effort that directly contributes to advancing the state of the art.

# Executive Summary


A significant portion of Florida's prestressed concrete slab bridges are aging, exposed to aggressive marine environments, and vulnerable to corrosion of carbon steel prestressing strands and reinforcement. Florida slab beams (FSBs), often used for short-span and low-profile bridges, are particularly susceptible due to their exposure to chlorides. To extend service life and reduce long-term maintenance costs, the Florida Department of Transportation (FDOT) has moved toward requiring corrosion-resistant materials such as stainless steel prestressing strands and glass fiber-reinforced polymer (GFRP) transverse reinforcement for some bridges. However, the fabrication, structural behavior, ductility, and design efficiency of FSBs with these materials has not yet been fully validated through full-scale testing and analytical modeling.

This research evaluated the flexural behavior of FSBs with stainless steel strands and the shear behavior of FSBs with GFRP bars that served as both transverse and interface shear reinforcement. Four (4) full-scale FSBs (12 in. × 48 in. × 34 ft) with cast-in-place toppings were fabricated and tested. Stainless steel prestressing strands were used in all beams, with varied strand quantities. One specimen used GFRP for all transverse and interface reinforcement and was compared to an otherwise similar specimen with carbon steel reinforcement. Strains in the prestressing strands were also measured during the fabrication detensioning process. All beams failed in a ductile manner governed by concrete crushing in compression, not brittle strand rupture (except one low-strand-count specimen after crushing). Performance of the FSB with GFRP reinforcement under the conditions tested was also acceptable. Transfer lengths measured using fiber optic sensors were consistent with prior research and within acceptable ranges.

Analytical models for flexural response and ductility were developed and validated. Conventional sectional analysis underestimated stiffness in post-cracking behavior. Due to the wide, shallow geometry of FSBs, incorporating tension stiffening in the analytical model resulted in better predictions of flexural stiffness and capacity.

A parametric study of nine (9) FSB sections and 254 prestressing strand configurations was conducted. FSBs required more stainless steel strands than those designed with carbon steel strands due to lower initial prestress. However, they demonstrated comparable flexural strength, deformation, and moment–curvature behavior.

This research demonstrated that stainless steel prestressing strands and GFRP shear reinforcement are structurally viable for FSBs, providing flexural strength, ductility, and deformation comparable to carbon steel strands. This study provides FDOT and practicing engineers full-scale experimental evidence and validated analytical tools that support the use of these materials in FSBs.

# Table of Contents

# List of Figures

# List of Tables

# CHAPTER 1 – INTRODUCTION

## 1.1 Project background

At the conception of this research project in 2022, according to the National Bridge Inventory, there were 6473 prestressed concrete bridges in Florida, 1622 (25%) of which had prestressed concrete slabs for their superstructure. About 34% of them were older than 50 years, another 24% were between 40 and 50 years old (see Figure 1-1), and 27% of them had a superstructure condition that was rated fair or below. Of the 1622 prestressed concrete slab bridges, 1401 had span lengths between 25 and 50 ft, and 1549 were over water. Prestressed concrete slab bridges over water are prone to deterioration because of corrosion of the carbon steel strands due to their exposure to chlorides, primarily from salt water, especially as they age. Those bridges require many resources for inspection, maintenance, rehabilitation, and replacement. To prolong bridge service life, corrosion-resistant or corrosion-free prestressing strands and reinforcing bars are worth consideration but need further testing to refine the design efficiency for flexural and shear strength limit states.

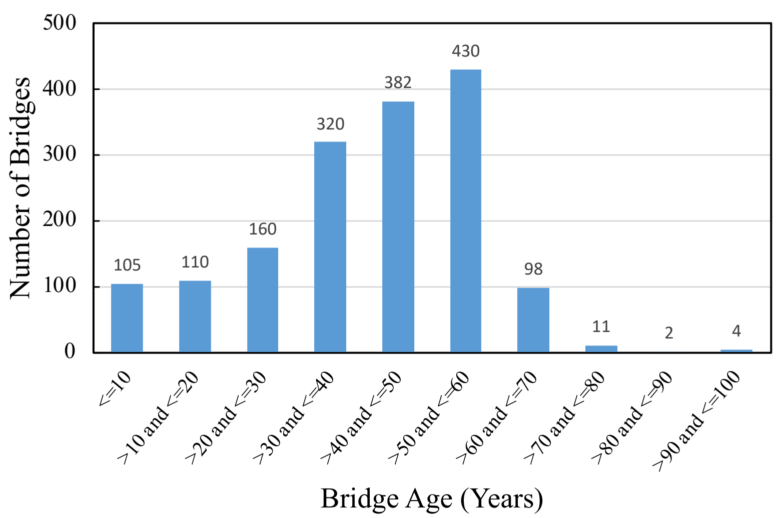


**Figure 1-1. Age of prestressed slab bridges in Florida (2022 National Bridge Inventory, https://infobridge.fhwa.dot.gov/Data)**

Currently, the Florida slab beam (FSB) is a popular choice for short bridges as well as low profile bridges in aggressive marine environments. The primary advantages of the FSB over other superstructure configurations include the elimination of deck forming, accelerated construction, reduced depth compared to girder bridges, and their efficiency to resist stream and wave loading due to the shallow profile, heavier weight, and high lateral stiffness. For Florida bridge piles in coastal waters, stainless steel strands and carbon fiber reinforced polymer (CFRP) strands are the required longitudinal prestressing reinforcement, and while this enhances the substructure durability, there is still a need to enhance the durability of the superstructure components. The 2022 FDOT Structures Manual – Volume 1, SDG 4.3.1.A, added the following requirement: "For pretensioned concrete beams located within the splash zone, use

CFRP or stainless steel prestressing strands." Although stainless steel strands are more expensive than carbon steel strands, they may be more economical in the long run because they are highly resistant to corrosion.

The mechanical properties and stress-strain relationship of stainless steel strands differ from those of carbon steel strands. Namely, stainless steel strands have a lower elastic modulus, ultimate stress, and ultimate strain. Lower elastic modulus slightly reduces the flexural stiffness of the member, which means the member exhibits more deformation under load. Lower ultimate stress influences the initial prestressing force, which should be maximized in designs controlled by Service III, which is the predominant governing limit state for shallow prestressed members. Lower ultimate strain limits the deformability and ductility of the member and the remaining capacity to carry load beyond the effective prestressing force.

For the transverse reinforcement in FSBs, one of the corrosion-resistant options is stainless steel rebar, which offers excellent durability, mechanical strength, ductility, and strain hardening capacity. However, a lower cost alternative is glass fiber-reinforced polymer (GFRP) rebar. Recently, there has been more widespread use of fiber-reinforced polymer (FRP) bars, as design codes and specifications have been developed such as ACI 440.1R-16 for FRP bars and ACI 440.11-22 for GFRP bars for the building industry and the AASHTO LRFD Bridge Design Guide Specifications for GFRP-reinforced concrete (AASHTO, 2018). In the FSB, transverse shear reinforcement also serves as interface shear reinforcement between the precast FSB and cast-in-place concrete topping.

Current design specifications conservatively limit the tensile strain in GFRP bars to 0.4% for transverse shear, and they reduce the tensile strength of the GFRP bar at the bend (typically less than 60% of the straight tensile strength after environmental reduction factors are applied). Before GFRP bars can be efficiently implemented as transverse reinforcement in FSBs for non-splash zone applications, additional testing needs to be conducted because GFRP bars have lower transverse shear strength than stainless and carbon steel bars, as well as lower elastic tensile modulus and ultimate strain.

Recently, NCHRP Project 12-121 established new guidelines and design specifications for auxiliary reinforcement in prestressed concrete girders. The project's scope included confinement, web splitting, transverse shear, and interface shear reinforcements, which are of interest to this research. While the project results are now available, the investigation did not specifically address the behavior of prestressed slab beams, such as the FSB. Complementing this work, NCHRP Project 12-120 developed AASHTO design and construction guidelines for stainless steel prestressed concrete girders. This project expanded on FDOT's initial research recommendations under BDV30-977-22 and the 2022 SDG 4.3.1 guidance. The final outcomes of this effort were published in 2025 as NCHRP Research Report 1161.

## 1.2 Project objectives

FDOT Structures Design Guidelines (SDG) (FDOT, 2026b) require the use of corrosion-resistant materials for bridges located in splash zones. High-strength stainless steel strands are identified as an alternative corrosion-resistant prestressing material for use in aggressive environments, and

Article 4.3.1.4 of the FDOT SDG provides design provisions for their application. However, these provisions were primarily developed based on testing of AASHTO Type II girders.

The primary objective of this research was to evaluate the use of high-strength stainless steel strands as longitudinal prestressing reinforcement in FSBs and to investigate the structural performance of GFRP reinforcing steel used as combined transverse and interface shear reinforcement. To achieve this objective, four full-scale FSB specimens with varying numbers of stainless steel strands were designed in accordance with FDOT SDG criteria and tested under monotonic loading to failure. The experimental program was intended to evaluate the influence of strand quantity on the flexural behavior of shallow prestressed members and to verify and validate the FDOT SDG criteria currently being implemented in active FDOT projects. In particular, the study evaluated whether FSBs prestressed with stainless steel strands can achieve adequate flexural strength and ductile behavior prior to failure

## 1.3 Report organization

This report is organized into chapters as follows. The design of the FSB test specimens is presented in Chapter 2; design calculations and design drawings are in Appendices 1 and 2, respectively, and drawings and details of the testing and instrumentation plans are in Appendix 3. Chapter 3 describes the fabrication of the FSBs, including the reinforcement placement, formwork, concrete casting, and cast-in-place topping. Instrumentation of the FSBs prior to fabrication and of the prestressing strands is also discussed. Appendix 4 provides data collected during fabrication, and Appendix 5 is documentation of the delivery of the fabricated girders. Chapter 4 provides information on mechanical properties and testing of the prestressing strands and concrete. In Chapter 5, data collected during detensioning of the prestressing strands is provided. Chapter 6 provides information about the flexural test setup, instrumentation, and experimental results. In Chapter 7, an analytical model for the flexural response is provided, along with validation by the test results. In Chapter 8, a modified analytical model is presented that includes the effect of tension stiffening. Chapter 9 provides methods for evaluating ductility, curvature, deflection, energy, and ductility; also, the flexural test results are analyzed and flexural resistance is calculated. In Chapter 10, the test setup and results for the FSBs with GFRP as shear reinforcement are presented.

# CHAPTER 2 – DESIGN OF FSBs

## 2.1 Dimensions and strand patterns of FSB test specimens

Standard Florida slab beams are available in three depths (see Table 2-1). For the experimental program in this study, a 12-in.-deep, 48-in.-wide FSB with a 6-in.-thick cast-in-place (C-I-P) topping was chosen. The span length was designed to be 34 ft. Calculations for the design of the FSB test specimens are provided in Appendix 1, and design drawings are in Appendix 2.

**Table 2-1. Available Florida slab beams and recommended maximum span lengths**

| C-I-P type: | 6” C-I-P topping with future wearing surface (short bridge) | 6” C-I-P topping with future wearing surface (short bridge) | 6 ½” C-I-P topping with ½” sacrificial thickness (long bridge) | 6 ½” C-I-P topping with ½” sacrificial thickness (long bridge) |
|---|---|---|---|---|
| **Beam type** | **4’-0” beam width** | **5’-0” beam width** | **4’-0” beam width** | **5’-0” beam width** |
| **12” FSB** | 40’-11” | 43’-11” | 41’-2” | 44’-5” |
| **15” FSB** | 52’-11” | 56’-3” | 53’-3” | 56’-9” |
| **18” FSB** | 62’-3” | 64’-4” | 62’-8” | 64’-10” |

Typically, FSBs can accommodate a maximum of 30 strands distributed in two layers. Three different strands patterns were used in this experimental study, as shown in Figure 2-1. The first pattern (Type 1) had 30 strands – the maximum number of strands that the FSB can accommodate. The second pattern (Type 2) was designed to have a total of 22 strands, which theoretically causes the condition of the strand’s maximum net tensile strain being reached. The third pattern (Type 3) had a total of 14 strands, which is the minimum number of strands that the section can accommodate. Four (4) FSBs were fabricated and tested: specimens FSB-1 and FSB-4 with Type 1 pattern; FSB-2 with Type 2 pattern; and FSB-3 with Type 3 pattern.

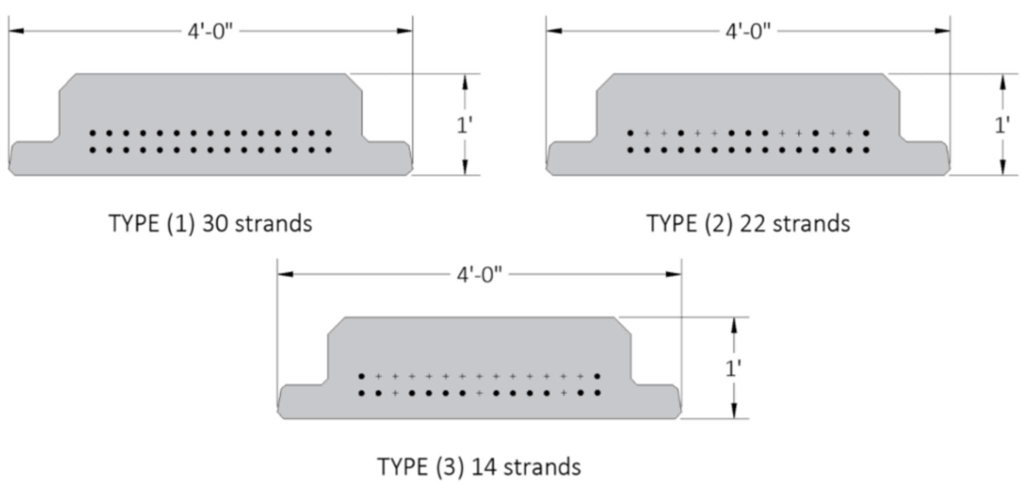


**Figure 2-1. Strand patterns in FSBs for experimental study**

## 2.2 Test matrix for experimental program

The test matrix for the experimental program is given in Table 2-2. FSB-1 served as the control specimen for FSB-4, where they both had the same number of stainless steel strands; however, the transverse reinforcement was carbon steel for FSB-1 and GFRP for FSB-4. For FSB-1, FSB-2, and FSB-3, the number of stainless steel strands was 30, 22, and 14, respectively.

**Table 2-2. Test matrix for experimental program**

| Girder Designation | No. of stainless-steel strands | Longitudinal stainless-steel strand pattern | Interface/shear reinforcement |
|---|---|---|---|
| **FSB-1** | 30 | 1 (maximum no,) | Carbon steel |
| **FSB-2** | 22 | 2 (maximum net tensile strain in strand) | Carbon steel |
| **FSB-3** | 14 | 3 (minimum no.) | Carbon steel |
| **FSB-4** | 30 | 1 (maximum no.) | GFRP |

## 2.3 Design methodology

The four beams were designed such that shear failure would not occur during the tests. The design process began by identifying the material properties used for the beam design, which includes concrete for the beam and topping, stainless steel for the strands, carbon steel and Glass Fiber Polymer (GFRP) for transverse reinforcement. Once the material properties were established, the geometry of the beam test setup was defined. This involved specifying the dimensions and configuration of the test setup.

Next, the section properties for the member at different stages were determined. This included calculating the gross section properties, transformed section properties, and composite section properties. Afterward, the applied loads on the beam were defined, considering the expected loading conditions. The prestressing force and the associated losses were then calculated for the beam.

Subsequently, a stress check was conducted at the top and bottom of the member. This check compared the calculated stresses with the limits specified in the Florida Department of Transportation Structures Design Guidelines (FDOT, 2026b). The goal was to ensure that the stresses would be within the allowable limits to maintain the structural integrity of the beam.

The flexural capacity of the beam with 30 strands was calculated. Additionally, a summary of the capacities for the other strand patterns was determined, along with stress checks for the beam at different stages of loading.

To assess the shear capacity of the beam, calculations were performed considering the shear interface capacity. This evaluated the beam's ability to resist shear forces and ensured that it met the required design criteria.

Finally, the design process included determining the transverse capacity of the GFRP reinforcement. This involved assessing the shear resistance provided by the GFRP rebars and considering their interaction with the surrounding concrete.

## 2.4 Test setup

The test setup for the four specimens, each with a length of 34 ft, was designed for four-point bending. Each FSB was supported at a distance of 1 ft from the specimen's ends, resulting in a 32-ft span. The load was applied at two points located 3 ft away from the center of the FSB. To distribute the load to the two loading points, a W16x100 steel beam was utilized. The load was increased incrementally until the member failed.

The spreader beam was supported at the specified points using neoprene pads. The loading was applied at the top center of the spreader beam as shown in Figure 2-2. This setup allowed for controlled and uniform loading, enabling accurate observation and measurement of their flexural behavior during the tests.

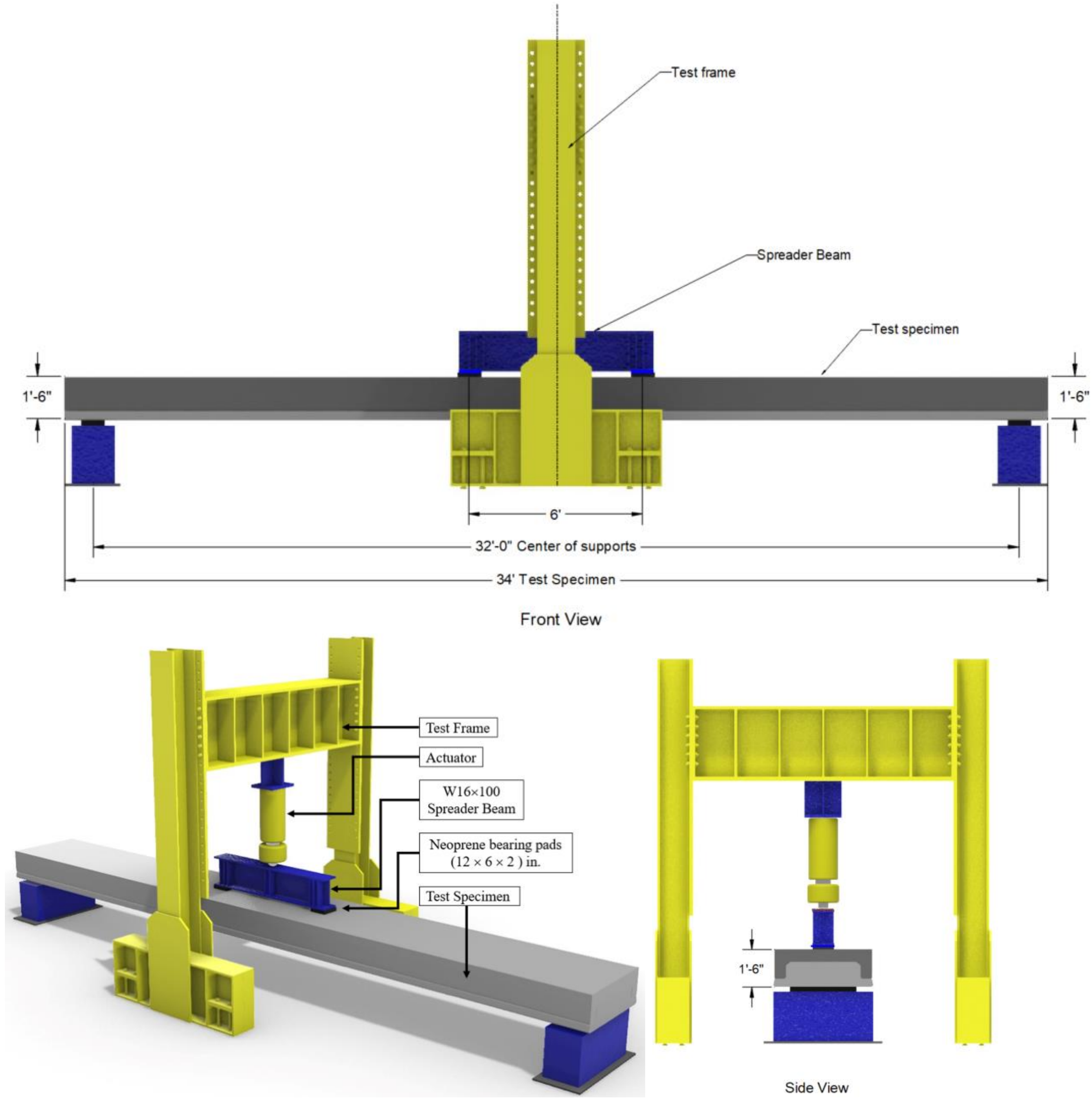


**Figure 2-2. Test setup**

# CHAPTER 3 – FABRICATION OF GIRDERS AND FIELD EVALUATION

## 3.1 Beam fabrication

Four (4) Florida slab beams (FSBs) were cast at CDS Manufacturing Inc. in Gretna, Florida. Each beam had a length of 34 ft and dimensions of 12 in. × 48 in. A single 154-ft-long casting bed was used to accommodate the four FSBs (Figure 3-1). Thirty (30) 0.6-in.-diameter low-relaxation stainless steel strands were pretensioned. In FSB-1 and FSB-4, all 30 strands were fully bonded; FSB-2 had 8 fully-debonded strands; and FSB-3 had 16 fully-debonded strands. Figure 3-2 shows the strand patterns. The FSBs were cast on the same day, and they were removed from the casting bed to construct the 4-in.-thick cast-in-place (C-I-P) concrete toppings.

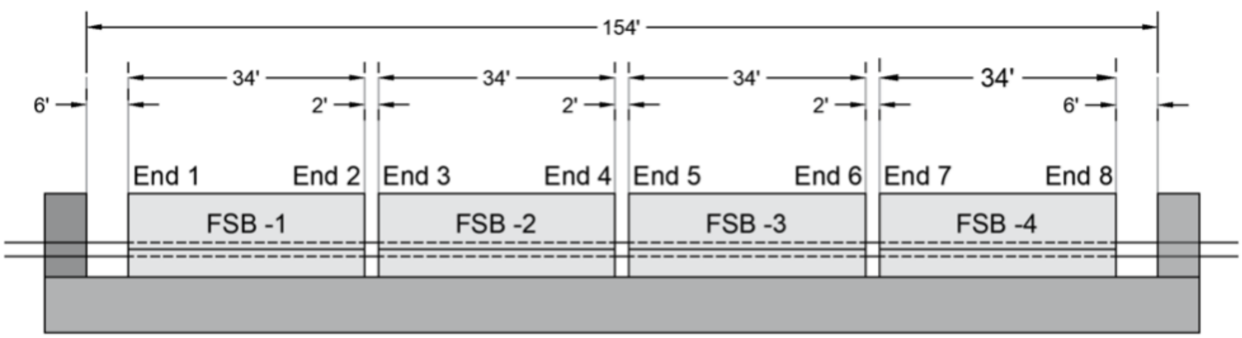


**Figure 3-1. FSB positions in casting bed**

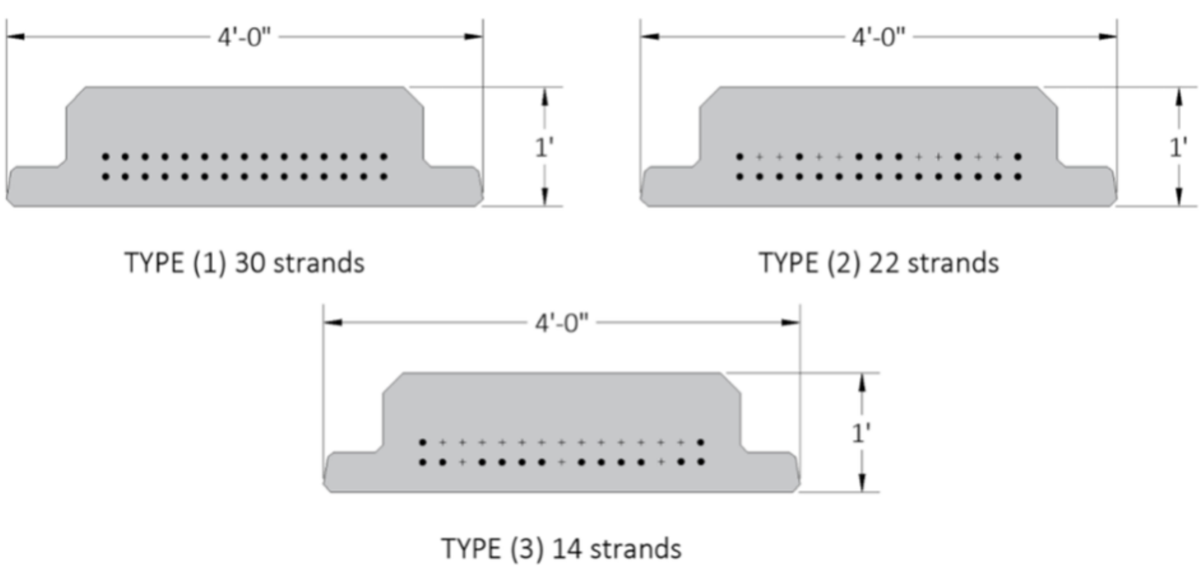


**Figure 3-2. Strand patterns in FSBs**

All the beams were constructed using FDOT Class VI concrete. The specified concrete strength for the beams at 28 days was 8.5 ksi with a release strength of 6.8 ksi. The specified concrete strength for C-I-P toppings at 28 days was 4.5 ksi.

Conventional carbon steel reinforcement was utilized for transverse and interface shear reinforcement on all beams except for FSB-4, which utilized Glass Fiber Reinforced Polymer (GFRP) bars. Table 3-1 provides the test matrix.

**Table 3-1. Test matrix**

| Girder designation | Number of strands | Longitudinal stainless steel strand pattern | Interface/shear reinforcement |
|---|---|---|---|
| **FSB-1** | 30 | Type (1) | Carbon steel |
| **FSB-2** | 22 | Type (2) | Carbon steel |
| **FSB-3** | 14 | Type (3) | Carbon steel |
| **FSB-4** | 30 | Type (1) | GFRP |

## 3.2 Fabrication and instrumentation activities

Drawings and details of the testing and instrumentation schemes are in Appendix 3. The timeline for the fabrication and instrumentation activities at CDS and the FDOT Structures Research Center (SRC) is given in Table 3-2. Details of tasks are discussed in following sections.

**Table 3-2. Fabrication and instrumentation activities**

| Task | Location | Start date | End date |
|---|---|---|---|
| Install strain gauges on transverse rebars and fiber optic sensors on rebars. | FDOT SRC | 08/1/2023 | 08/2/2023 |
| Install FSBs formwork, place reinforcement, tension strands and cast concrete in FSBs. | CDS casting yard | 08/9/2023 | 08/11/2023 |
| Remove formwork and detension strands. | CDS casting yard | 08/14/2023 | 08/14/2023 |
| Fabricate formwork for concrete toppings, place reinforcement and cast concrete. | CDS casting yard | 08/15/2023 | 08/16/2023 |
| Remove formwork. | CDS casting yard | 08/21/2023 | 08/21/2023 |
| Ship FSB-1 & FSB-4 specimens to the FDOT SRC. | FDOT SRC | 09/13/2023 | 09/13/2023 |
| Ship FSB-2 & FSB-3 specimens to the FDOT SRC. | FDOT SRC | 10/24/2023 | 10/24/2023 |

### 3.2.1 Lab instrumentation prior to fabrication

After the rebars from the manufacturers were delivered, the rebars were instrumented with foil strain gauges and fiber optic strain gauges. The foil type strain gauges were installed on 4K and 4D rebars at the locations shown in Figures 3-3 and 3-4.

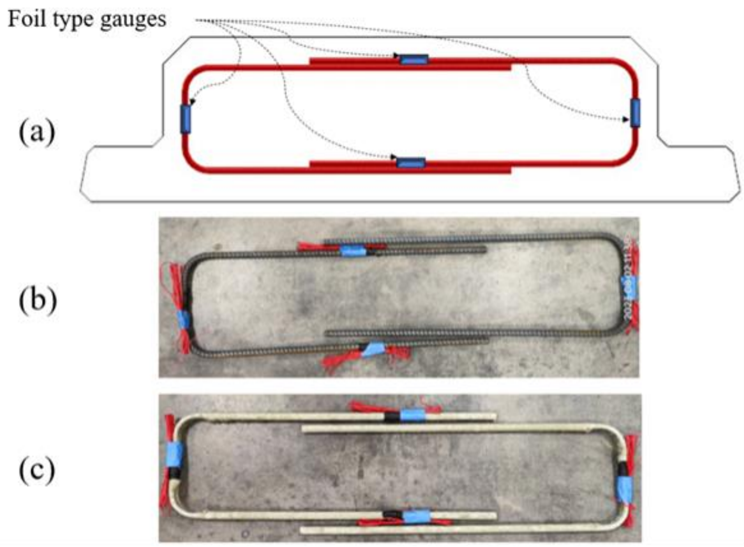


**Figure 3-3. Strain gauges installed on 4D rebar pairs: (a) Instrumentation plan, (b) Carbon steel, and (c) GFRP**

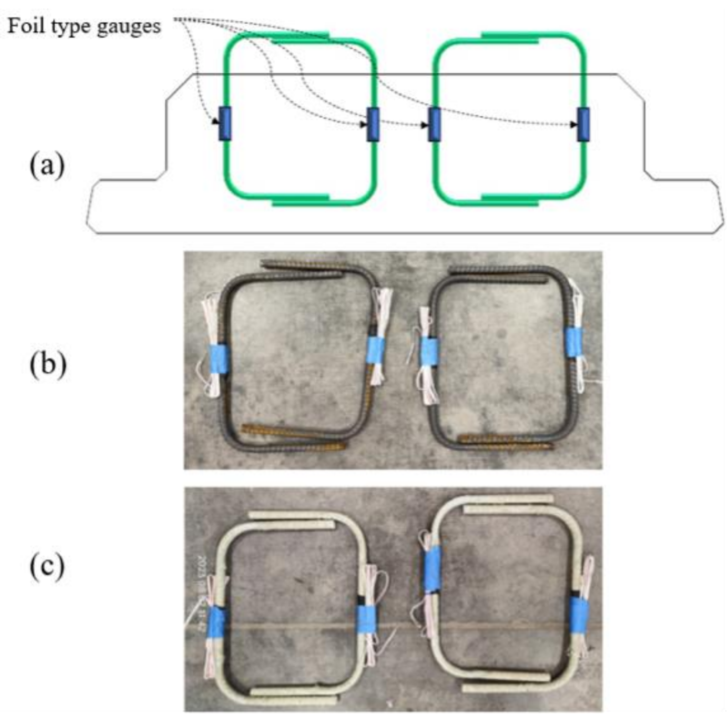


**Figure 3-4. Strain gauges installed on 4K rebar pairs: (a) Instrumentation plan, (b) Carbon steel, and (c) GFRP**

Subsequently, the strain gauges were installed on the rebars using an appropriate adhesive. Finally, two layers of different protection were added to safeguard the strain gauges against heat and physical damage (Figure 3-5).

**Figure 3-5. Gauge protection layers**

The lab instrumentation activities included preparing four (4) grooved #3 GFRP rebars, each with a length of 42 in.; the fiber optic sensors were placed inside the grooves to protect them from damage. These rebars were placed at the ends of FSB-1 and FSB-4.

### 3.2.2 Prestressing strands and initial tensioning

The casting bed underwent a thorough inspection to detect any defects, after which it was cleaned and sprayed with form release agent (Figure 3-6). Next, as shown in Figure 3-7, the stainless steel strands were arranged along the bed according to the specified patterns shown in Figure 3-2. To straighten and remove slack, the strands were initially tensioned to 10% of their ultimate tensile strength (3.86 kips per strand) (Figure 3-8).

The tensioning sequence is shown in Figure 3-9. The tensioning process involved using a hydraulic monostrand jack to tension the strands (Figure 3-10). Jacking was performed at End 1 (the live end). Each stainless steel strand was stressed to a force of 38.8 kips, which was 70% of the ultimate tensile force specified in ASTM A1114 (ASTM, 2020b). The strain in the strands was monitored with a load cell. Once the target force was reached, the strand was securely positioned within the chuck by wedges (Figure 3-11). The elongation was measured at the live end to verify the applied load.

**Figure 3-6. Casting bed preparation**

**Figure 3-7. Running the strands**

Figure 3-8. Seated strands in the chucks

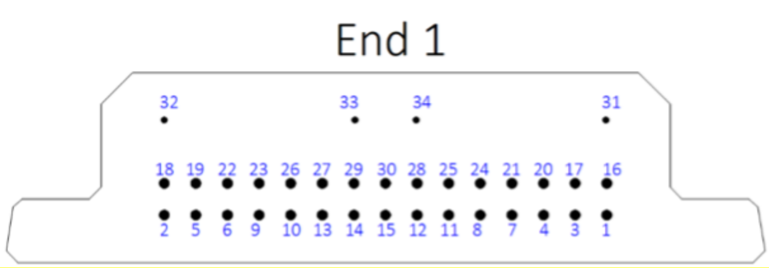


Figure 3-9. Tensioning sequence; looking upstation towards End 8

Figure 3-10. Tensioning the strands

**Figure 3-11. Strands are tensioned initially**

### 3.2.3 Instrumentation of prestressing strands

After applying the initial tension (10% of the full tension force), instrumentation was added to the strands at the midpoint of the free length (i.e., at mid distance between the abutment and the end of the beam) (Figure 3-12), at both ends of the casting bed. At each end, electrical resistance strain gauges (ERSGs) were adhered to three (3) strands in the bottom layer and nine (9) strands in the top layer. These gauges were to provide strain measurements during the strand detensioning process.

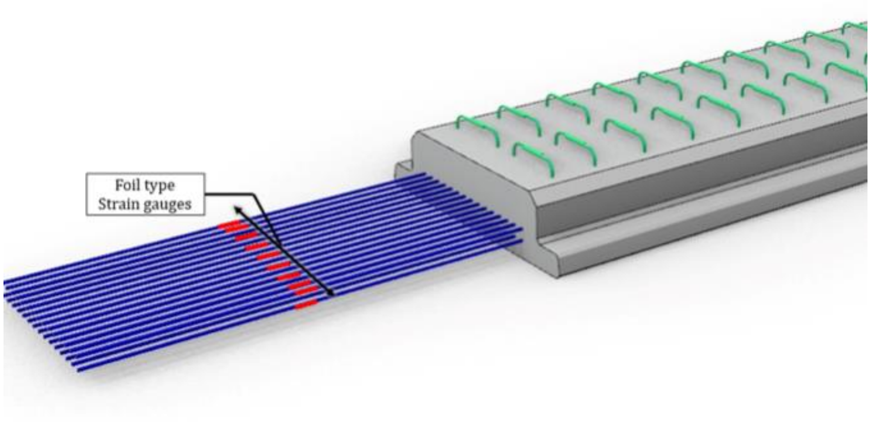


**Figure 3-12. Location of ERSGs in the free length**

The ERSGs were installed using a thin coat of adhesive (M-Bond 200). Then, a coating agent was applied to protect the gauges. The final step was labelling the wires and wrapping them with rubber mastic tape (Figure 3-13).

**Figure 3-13. ERSG installation**

Eight (8) vibrating wire strain gauges (VWSGs) were used. A pair of gauges was installed to the bottom layer of the strands at the mid length of each beam. Each VWSG was installed using two (2) short GFRP rebars tied to the adjacent strands (Figure 3-14).

**Figure 3-14. Installed VWSG**

## 3.2.4 Rebar cage assembly

First, each strand was tensioned to the full force of 38.8 kips. The locations for instrumented bars were marked on the fully-tensioned strands (Figure 3-15). Then, the stirrup pairs, type D and K bars, with instrumentation were carefully placed and tied to the strands for only FSB-1 and FSB-4 (Figure 3-16). Note that only FSB-1 and FSB-4 were instrumented with internal strain gauges attached to Type D and Type K rebars.

**Figure 3-15. Marking and placing the instrumented D-pairs at FSB-1**

**Figure 3-16. Instrumented GFRP K-pairs placed and tied in FSB-4**

Next, the rest of the K rebars were placed. Afterwards, the gauge wires were routed out of the forms to prevent them from being damaged during the concrete pour (Figure 3-17).

**Figure 3-17. Transverse reinforcement, placed and tied**

To measure the prestressing force transfer length during strand detensioning, the four grooved GFRP bars with fiber optic sensors were installed on both ends of FSB-1 and FSB-4. On each end, the fiber optic gauges were installed along a 42-in. length starting from the end of the beam and vertically mid distance between the two layers of strands. Figure 3-18 shows the installed fiber optic gauges in End 8 at FSB-4.

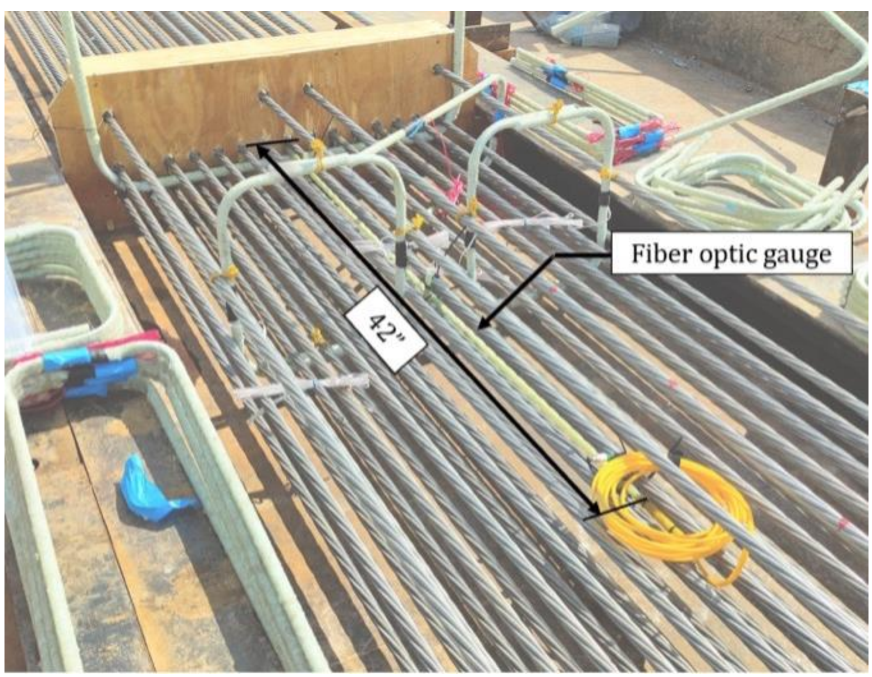


**Figure 3-18. Fiber optic installed on End 8 of FSB-4**

## 3.3 FSB formwork

Prior to the concrete casting, steel side forms were installed along the length of the four (4) FSBs (Figure 3-19). The forms were cleaned and checked as a final step before concrete casting (Figure 3-20).

**Figure 3-19. Side form installation**

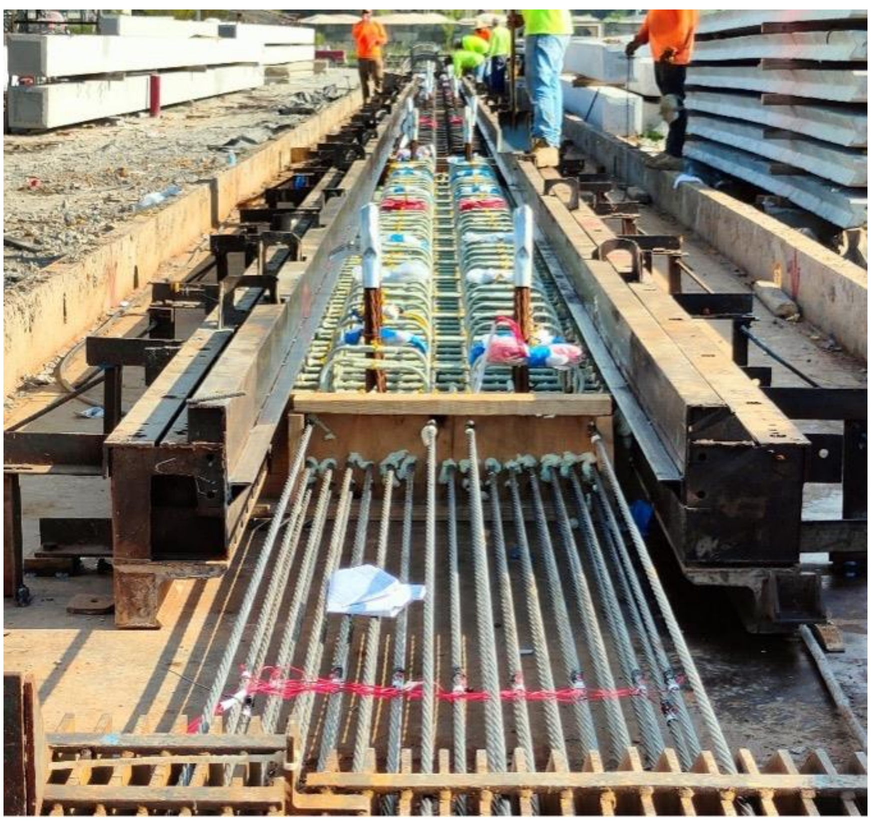

**Figure 3-20. FSB forms with reinforcement in place are ready for concrete casting**

## 3.4 Beam casting

As mentioned, the FSB concrete was Class VI with a specified strength at release and 28 days of 6.8 ksi and 8.5 ksi, respectively. The mix used was flowing concrete. FDOT Standard Specifications for Road and Bridge Construction (FDOT, 2025) Section 346 for Portland Cement Concrete specifies 7.5-in. to 10.5-in. slump for flowing concrete, and for all classes of concrete a range of 1% to 6% for air content. The ratio of water-to-cementitious material is limited to 0.37 for Class VI concrete (FDOT, 2025).

During casting, fresh concrete tests were performed, including slump and air content (Figure 3-21). The slump tests were conducted in accordance with AASHTO T119M/T119 (AASHTO, 2023) or ASTM C143 (ASTM, 2020a) procedure for two trucks, and the air content tests were in accordance with ASTM C231 (ASTM, 2022a) procedure. All test results met the standard limits, as shown in Table 3-3.

**Figure 3-21. Concrete mix tests**

**Table 3-3. Concrete test results (slump, air content and water-cement ratio)**

| Truck number | Slab beam | Slump (in.) | FDOT slump limit | Air content (%) | FDOT air content limit | W/C | FDOT W/C limit |
|---|---|---|---|---|---|---|---|
| **Truck 1** | FSB-4 | 10 | 7.5-10.5 | 1.8 | 1-6 % | 0.24 | ≤ 0.37 |
| **Truck 2** | FSB-4 | 10 | 7.5-10.5 | 1.8 | 1-6 % | 0.24 | ≤ 0.37 |
| **Truck 3** | FSB-3 | 10 | 7.5-10.5 | 1.1 | 1-6 % | 0.23 | ≤ 0.37 |
| **Truck 4** | FSB-1 | 10.5 | 7.5-10.5 | - | 1-6 % | 0.22 | ≤ 0.37 |
| **Truck 5** | FSB-2 | 10.5 | 7.5-10.5 | - | 1-6 % | 0.22 | ≤ 0.37 |

The surface of the concrete was levelled during placement (Figure 3-22) and then roughened to an amplitude of ¼ in. Afterwards, the concrete surface was sprayed with curing agent (Figure 3-23).

**Figure 3-22. Concrete casting**

**Figure 3-23. Concrete surface finish**

## 3.5 Detensioning

At release, the concrete compressive strength was an average of 8.43 ksi. Table 3-4 summarizes the concrete compressive strength four (4) days after casting the beams.

**Table 3-4. Concrete cylinder test results**

| No. | Date | Cylinder age | Target strength (psi) | Failure type | Break strength (psi) |
|---|---|---|---|---|---|
| **1** | 8/14/2023 | 4 days | 6,800 | Shear | 8,390 |
| **2** | 8/14/2023 | 4 days | 6,800 | Shear | 8,462 |

The side forms were removed. Prior to the strand release process, additional external gauges were installed. The gauges included two cameras pointed at Imetrum targets and two strandmeters, both of which were at End 1 and End 8. Two Imetrum targets installed at each end with a camera focused on them were set up to monitor the end's movement (Figure 3-24). The Imetrum targets were spaced 38 in. horizontally apart and located vertically at the same level of 4.5 in. from the top of the FSB (Figure 3-25).

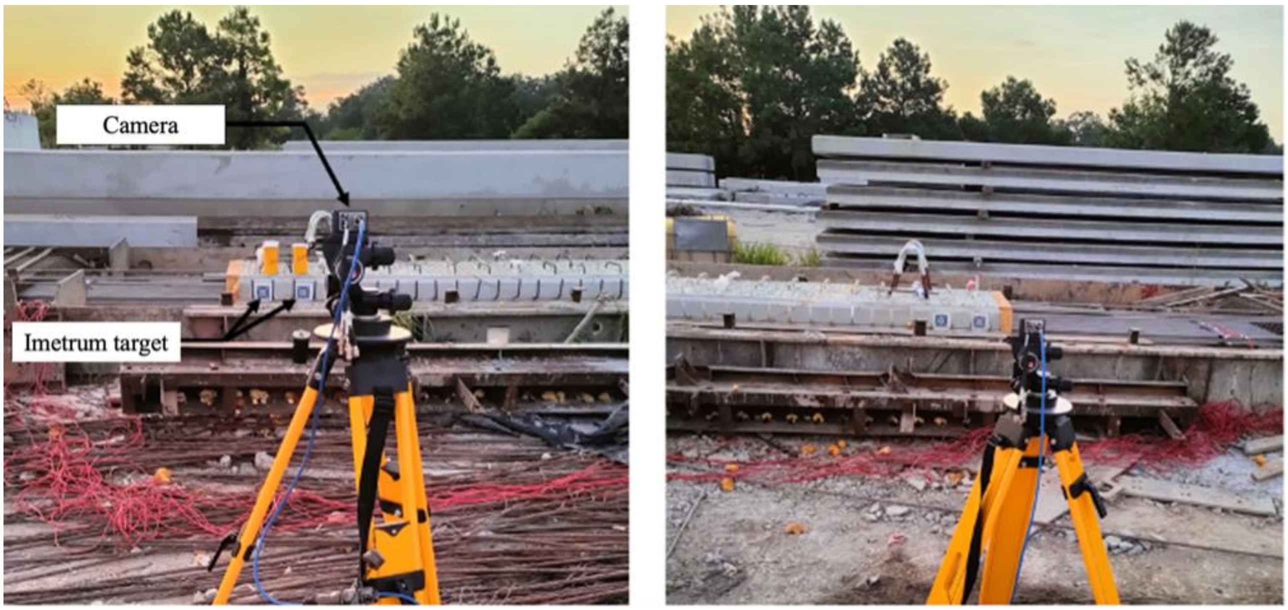


**Figure 3-24. Two cameras monitor targets' movements on End 1 and End 8**


**Figure 3-25. Two targets glued at End 8**

The strandmeters were installed on the free length of the strands at Ends 1 and 8 (Figure 3-26). Each strandmeter was mounted on top of the strand located at the middle of the top layer of strands. The strandmeter was used to monitor the strain in the strand during detensioning, and the measurements would be useful to validate the strain measurements collected from the installed ERSGs.

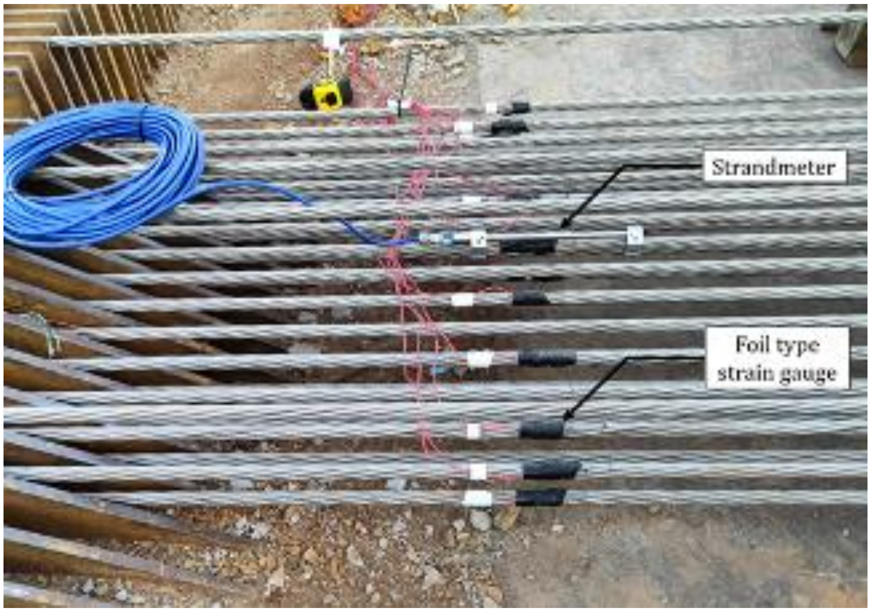


**Figure 3-26. Strandmeter and strain gauges installed at the free length**

All gauges were connected to the data acquisition system, and checks were run to ensure that gauges were functioning (Figure 3-27). All gauges were working except for one (1) VWSG installed in FSB-4 and two (2) ERSGs installed on 4D pairs in FSB-1. The strand release method used was flame cutting. Each strand was cut using gradual heating by a torch flame until the strand was completely cut. Two personnel simultaneously cut one strand at a time at each end (Figure 3-28).

**Figure 3-27. Acquisition system connected to the gauges to monitor the data**

**Figure 3-28. Strand cutting at End 1**

During cutting of the 27th strand, the remaining uncut seven (7) strands ruptured. All ruptured strands were located in the top layer. Figure 3-29 shows the proposed and actual strand release sequences for both ends, as well as the ruptured strands.

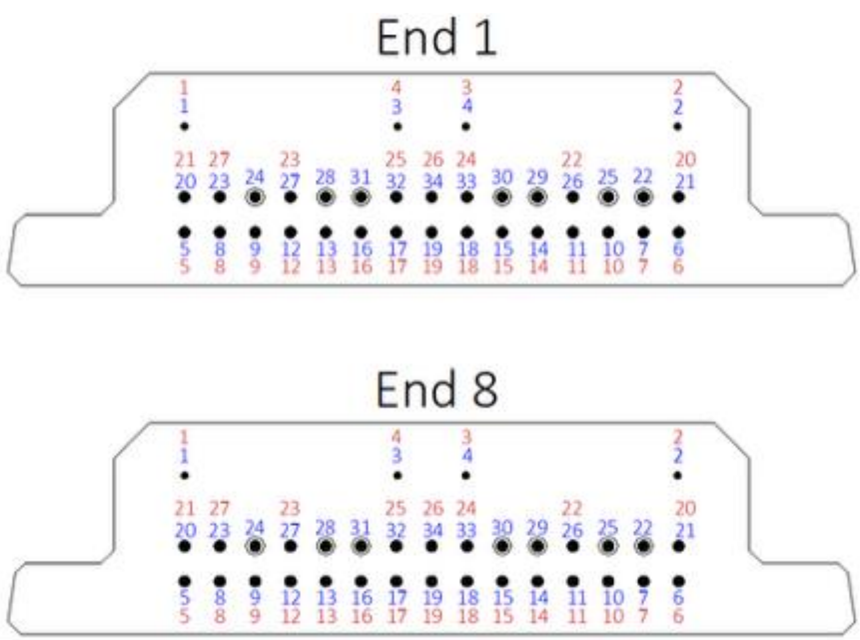


**Figure 3-29. Proposed detensioning sequence (blue), actual site detensioning (red) and ruptured strands (circled); looking upstation towards End 8**

Rupturing of the uncut strands initiated at End 8; see Figure 3-1 for the location of End 8. Figure 3-30 shows the end of the casting bed after the strands ruptured. The sudden impact pushed the FSBs in the direction of End 1 (see Figure 3-1 for the location of End 1), as shown in Figure 3-

31. End 8 pushed towards the center of the bed a distance of 24.5 in. away from its original location, while End 1 pulled out a distance 16 in.

**Figure 3-30. Location of the ruptured strands at End 8**

**Figure 3-31. End 8 after rupture**

Finally, the free strands were cut in the remaining locations (at Ends 2-7) and then the FSBs were removed from the casting bed to prepare them for topping fabrication.

## 3.6 Cast-in-place topping

Wooden formwork was used to fabricate the toppings of the FSBs (Figure 3-32).


**Figure 3-32. Topping formwork**

Prior to concrete casting, the gauges' wires were routed out of the formwork. The concrete was cast, and Table 3-5 summarizes the concrete mix test results.

**Table 3-5. C-I-P concrete topping test results (slump, air content, and water-cement ratio)**

| Truck number | Slump (in.) | FDOT slump limit | Air content (%) | FDOT air content limit | W/C | FDOT W/C limit |
|---|---|---|---|---|---|---|
| **Truck 1** | 10 | 7.5-10.5 | 1.0 | 1-6 % | 0.34 | ≤ 0.44 |
| **Truck 2** | - | 7.5-10.5 | - | 1-6 % | 0.34 | ≤ 0.44 |
| **Truck 3** | 10.5 | 7.5-10.5 | 1.9 | 1-6 % | 0.33 | ≤ 0.44 |

# CHAPTER 4 – MECHANICAL PROPERTIES

## 4.1 Introduction

In traditional prestressed concrete, mitigation of corrosion has generally involved techniques of either enhancing concrete properties or applying corrosion protection to strands (Podolny, 1992). Another solution is using corrosion-resistant reinforcing materials. In 1912, a corrosion-resistant iron alloy was introduced and called rustless steel. Later, this alloy was called stainless steel. The term “stainless steel” refers to iron alloys that contain a minimum of 10.5% chromium (Gardner, 2005). Stainless steel alloys were investigated as a reinforcement alternative in prestressed concrete structures (Moser et al., 2013). Currently, the term stainless steel refers to iron-based alloys containing at least 12% chromium. Stainless steel also contains elements such as nickel, molybdenum and nitrogen (ASTM, 2020b). Similar to carbon steel, stainless steel has various grades. These grades result from different chemical compositions and heat treatments. Two main types of stainless steel are used in reinforced concrete: ferritic and austenitic (Gardner, 2005). Duplex is a mix of both types. Duplex Grade 2205 was found to be the best choice for stainless steel strands (Moser, 2011). In 2017, the American Society for Testing and Materials (ASTM) issued a specification requiring that duplex alloy 2205 stainless steel (UNS S32205) be used for stainless steel strands in prestressed concrete (ASTM, 2017).

Design of prestressed concrete members requires knowledge of the elastic modulus, breaking strength, yield strength, and ultimate strain of the prestressing strands. Therefore, tensile tests are performed to determine these parameters and obtain the stress-strain curve for the strands. ASTM A1061/1061M describes the standard method to perform tensile tests on strands (ASTM, 2020c). The results of tensile tests performed on stainless steel strands must meet the criteria specified in ASTM A1114 (ASTM, 2020b). Besides mechanical properties, the strand diameter must be within a permissible tolerance.

This chapter examines the mechanical properties of 0.6-in.-diameter, ASTM A1114 stainless steel, low-relaxation, Grade 240 strands. Tensile tests were conducted on five (5) samples of 0.6-in.-diameter, high-strength stainless steel (HSSS) strands from one spool. The spool was manufactured by Sumiden Wire Products Corporation. Stress-strain equations for the strands were developed based on previous research by Al-Kaimakchi and Rambo-Roddenberry (2021a) as well as other equations suggested by literature; the equations were evaluated against experimental data obtained in this project.

## 4.2 Tensile tests

### 4.2.1 Specimen preparation

A single 0.6-in.-diameter HSSS strand spool was used in this research project. The spool was supplied by Sumiden Wire, and it was received by the Florida Department of Transportation (FDOT) Structures Research Center (SRC) in good condition without rust or visible defects. While stored at FDOT SRC, the spool was protected from potential damage such as oil, excessive bending, and physical harm. The length of the strand in the spool was 6,519 ft. The manufacturer provided a mill test certificate outlining the mechanical properties of the strand. Five (5) HSSS strand specimens were extracted from this single spool, and all specimens were taken from the beginning of the spool. During the sampling process, care was taken to ensure the specimens were free from severe bending, abrasion, or nicking, as these defects could negatively affect the tensile test results and cause premature failure. All specimens, each 50 in. long, were sent to the FDOT State Materials Office (SMO) for subsequent tensile testing. To address grip slippage and complications associated with gripping mediums, a coating of high modulus epoxy and 80 grit silicon carbide was applied to the ends of the strands, as shown in Figure 4-1. This provided friction for grip and prevented slippage during the tensile test.

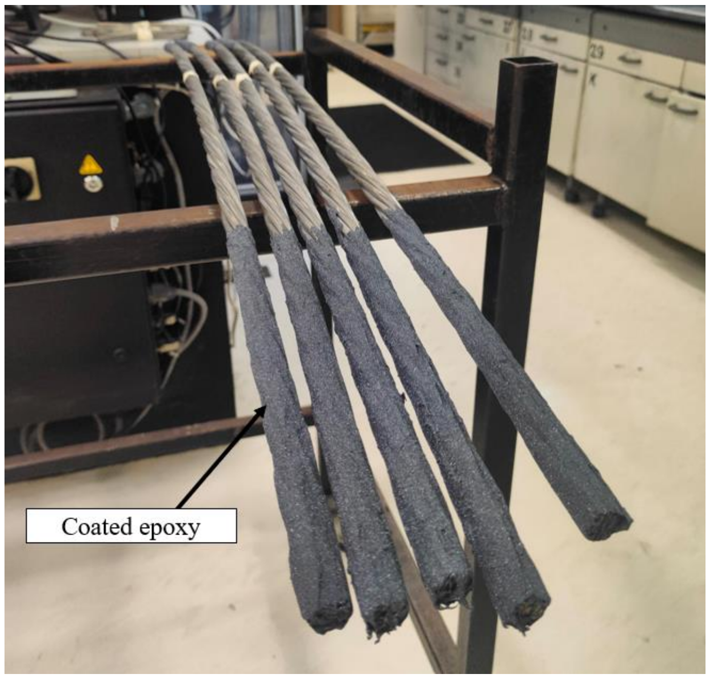


**Figure 4-1. Samples coated with epoxy**

The tensile tests were conducted using a Universal Testing Machine (UTM) conforming to ASTM A1061 test requirements (ASTM, 2020c). The UTM has a load frame supporting load cells and a movable cross head. The load cells collect readings during the tensile tests. The movable cross head has grips to hold the sample ends. To facilitate proper gripping, the samples were embedded a length of 8 in. (Figure 4-2a), which allows for a complete load transfer from the grips to the strand. A pre-load of approximately 10% of the breaking strength was applied to align the strand and secure the ends in the grips (Figure 4-2b). Following alignment, a 24-in. extensometer was mounted to the strand, maintaining a 5-in. clear distance between the jaws and the extensometer (Figure 4-2c). The extensometer accurately measured strain up to around 1% extension, with a precision of 0.01%. After reaching this limit, the extensometer was removed to prevent potential damage, considering the low ultimate strain of the strand material. Subsequently, the machine was reloaded, and data collection transitioned from the extensometer to the UTM, which calculates strain by measuring the displacement between the machine's crossheads.

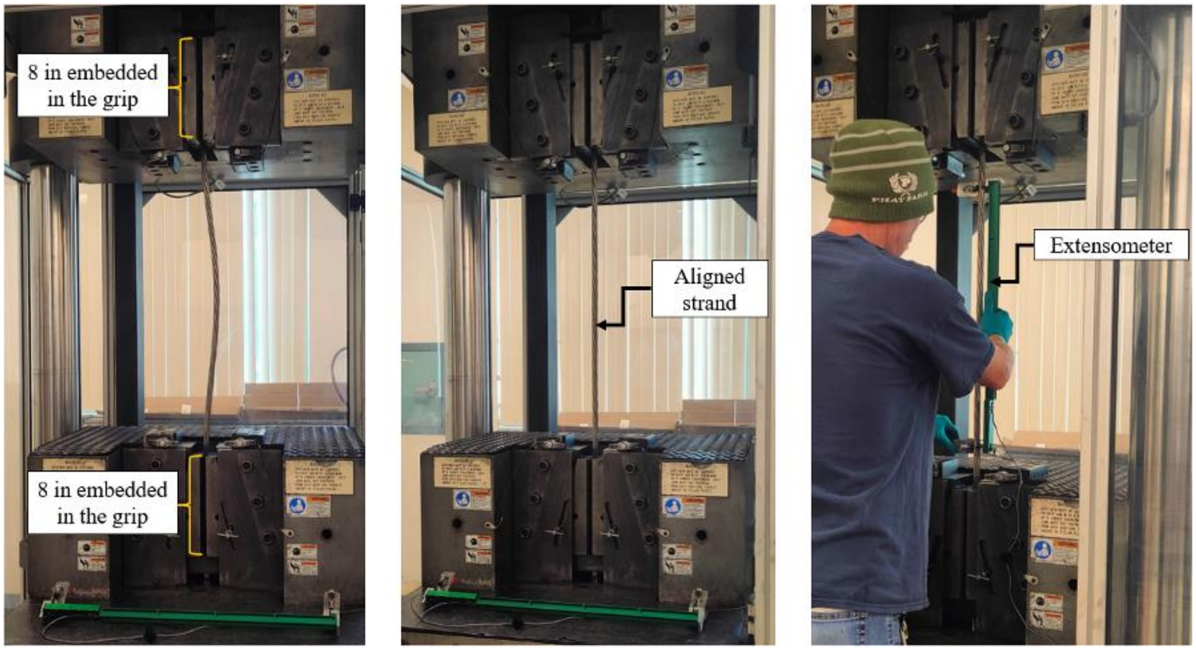


**Figure 4-2. Preparation of specimen: (a) Coated strand ends placed inside the grips, (b) Strand is aligned after 10% of fracture force is applied, and (c) Extensometer is mounted to the sample to take strain measurements**

### 4.2.2 Results

Tensile tests were conducted on the five (5) 0.6-in.-diameter HSSS strand specimens. All specimens failed by rupture near the grips, as shown Figure 4-3. Because the fracture was near the grip, ASTM A1061/A1061M deems the test as invalid unless the results meet the minimum criteria for yield strength, breaking strength, and total elongation (ASTM, 2020c).

#### 4.2.2.1 Tensile strength

During the tensile tests, strand elongations were recorded. The force-elongation curves were smooth and free from irregularities. To account for grip seating losses and normal elongation errors, the preload method and elastic modulus extrapolation method were used. In the preload method, the specimen was initially loaded with 10% of the required minimum breaking strength and held in the test frame. An extensometer, shown in Figure 4-2c, was then attached and adjusted to a 0.1% gauge length reading. Loading continued until the extensometer indicated a total extension of 1.0% of the gauge length. The recorded load at 1.0% extension represented the yield strength. To ensure accurate measurements, the extensometer remained attached until reaching at least 1.05% of the elastic unit limit, after which it was typically removed to prevent potential damage due to strand rupture. To calculate the elastic modulus, the cross-sectional area of the specimen was calculated on the acquisition system based on diameter readings taken from each specimen (Figure 4-4). Table 4-1 summarizes the measurements taken.

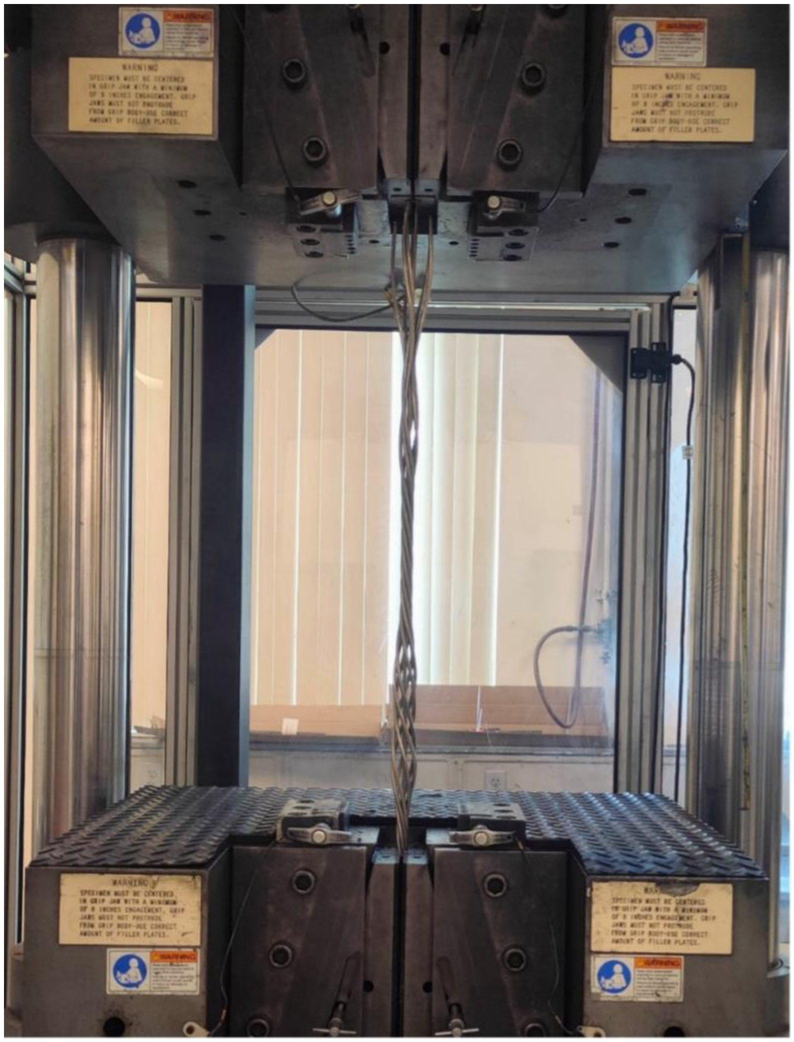

**Figure 4-3. Strand specimen failure near the top grip**


**Figure 4-4. Wires taken from each specimen to determine diameter measurements**

**Table 4-1. Strand wire measurements**

| Specimen | Outer diameter (in.) | Inner diameter (in.) | Strand diameter (in.) | Area ($in^2$) | Weight per thousand feet (lbs/1000 ft) |
|---|---|---|---|---|---|
| **Strand 1** | 0.2150 | 0.206 | 0.6270 | 0.2360 | 803.0 |
| **Strand 2** | 0.2160 | 0.206 | 0.6280 | 0.2370 | 804.0 |
| **Strand 3** | 0.2160 | 0.206 | 0.6280 | 0.2370 | 804.0 |
| **Strand 4** | 0.2160 | 0.206 | 0.6280 | 0.2370 | 804.0 |
| **Strand 5** | 0.2160 | 0.206 | 0.6280 | 0.2370 | 804.0 |
| **Average** | 0.2185 | 0.206 | 0.6278 | 0.2368 | 803.8 |

The yield strength criteria in ASTM A1114 requires the strength to be 90% of the specified breaking strength. In Table 4-2, the yield strength for each specimen is compared to ASTM A1114. The stress-strain curves obtained for the five (5) specimens are plotted in Figure 4-5.

**Table 4-2. Tensile test results compared to FDOT and ASTM standards**

| Item | Area ($in^2$) | Yield strength (kips) | Breaking strength (kips) | Ultimate stress (ksi) | Elongation (%) | Elastic modulus (psi $\times 10^6$) |
|---|---|---|---|---|---|---|
| **FDOT Standard** | 0.2310 | ≥ 49.86 | ≥ 55.40 | ≥ 240 | ≥ 1.4 | - |
| **ASTM Standard** | 0.2310 | ≥ 49.86 | ≥ 55.40 | ≥ 240 | ≥ 1.4 | - |
| **Manufacturer** | 0.2379 | 54.21 | 60.12 | 263.65 | 1.7 | 24.4 |
| **Specimen 1** | 0.2364 | 53.30 | 62.32 | 264.58 | 2.0 | 23.9 |
| **Specimen 2** | 0.2367 | 52.46 | 62.63 | 262.76 | 2.3 | 23.4 |
| **Specimen 3** | 0.2367 | 53.36 | 62.20 | 264.24 | 1.9 | 23.7 |
| **Specimen 4** | 0.2367 | 53.45 | 62.55 | 263.95 | 2.1 | 23.9 |
| **Specimen 5** | 0.2367 | 53.12 | 62.48 | 263.85 | 2.1 | 23.7 |
| **Average of Specimens 1-5** | 0.2366 | 53.14 | 62.44 | 263.88 | 2.1 | 23.7 |

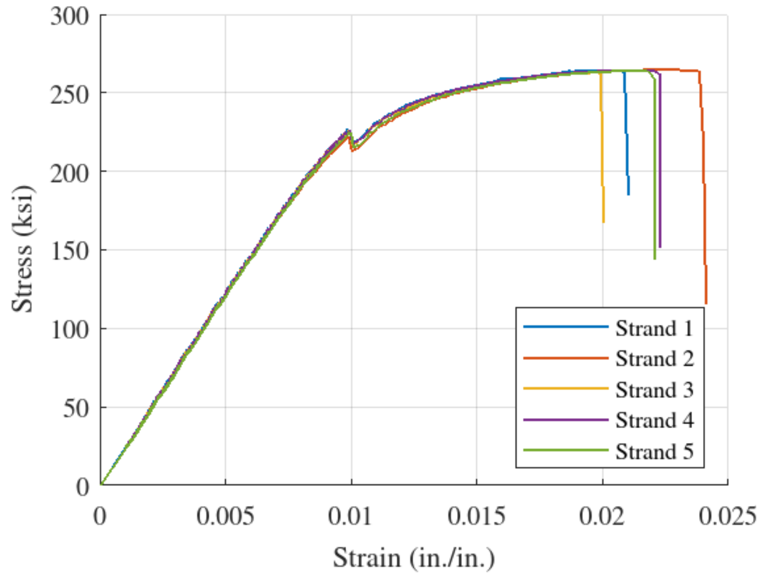


**Figure 4-5. Stress-strain curve for all specimens**

#### 4.2.2.2 Breaking strength

The breaking strength corresponds to the force at failure. Values are provided in Table 4-2. All strands failed by rupture near the grips, which is considered valid per ASTM 1061 (ASTM, 2020c). In carbon steel strands, the failure near the grip has a significant effect on the resulting elongation, whereas its effect on breaking strength can be negligible (Lequesne et al., 2020).

#### 4.2.2.3 Total elongation

The total elongation at maximum force was determined by measuring the movement between the gripping jaws. When the yield strength was reached, loading was halted, and the extensometer was removed. Then, the distance between the gripping jaws was measured. Loading was then resumed until failure, and the distance between the jaws was measured again. The total percent elongation was calculated by taking the percent change in the jaw-to-jaw distance and adding this value to the extension measured by the extensometer (Table 4-2).

#### 4.2.2.4 Modulus of elasticity

ASTM A1114 does not provide any requirements for the modulus of elasticity of stainless steel strands. However, it requires a cross-sectional area, which is used to calculate the modulus of elasticity. The strand area was calculated by measuring the diameters of the wires taken from each strand specimen. The FDOT Structures Design Guidelines (SDG) specify a design value of 24,000 ksi for the elastic modulus. The five (5) specimens had an elastic modulus ranging between 23,400 and 24,400 ksi, with an average of 23,700 ksi (Table 4-2).

## 4.3 Stress-strain curve model

The stainless steel stress-strain behavior is generally different from that of carbon steel. It has a rounded stress-strain curve with no sharp yield point (Gardner, 2005) and is nonlinear. For such a curve type, Ramberg and Osgood (1943) suggested a simple formula, involving three parameters, for aluminum and stainless steel alloys. Subsequently, Hill (1944) modified these parameters using the offset yield strength method. A similar power formula utilizing three parameters was proposed by Mattock (1979).

Recent research on Duplex Grade 2205 HSSS confirmed the applicability of the power formula (Al-Kaimakchi and Rambo-Roddenberry, 2021a). The power formula models the stress-strain curve as two lines connected by a curve. The first line represents the linear-elastic region while the second line represents the linear strain-hardening plastic region. The curved part represents the gradual nonlinear transition between these two lines. The power formula parameters can be defined using the procedure outlined in Collins and Mitchell (1991):

$$\sigma = \varepsilon E \left\{ A + \frac{1-A}{\left[1+(B\varepsilon)^C\right]^{1/C}} \right\} \qquad \text{(Eq. 4.1)}$$

where E is the modulus of elasticity, $\sigma$ is the stress, $\varepsilon$ is the strain, and A, B, and C are parameters used to fit the curve. Table 4-3 provides various formulas, from literature, to model the stress-strain curve, and Figure 4-6 shows plots of these curves. A calibration for the three parameters A, B, and C was performed to obtain a better fit that will be used in the analysis of results in subsequent chapters. The resulting calibrated power formula curve is shown in Table 4-3 as the suggested formula. This formula provided a good match with the tension tests and was used in the analytical model, for better comparisons with the experimental results; however, for the parametric study, the FDOT SDG (FDOT, 2026b) formula was used.

**Table 4-3. Stress-strain models**

| Reference | E (ksi) | Equation |
|---|---|---|
| **FDOT SDG (2026b)** | 24,000 | $\sigma = \varepsilon \times 24{,}000\left\{0.06 + \frac{1-0.06}{[1+(101\varepsilon)^{6.45}]^{1/6.45}}\right\}$ (Eq. 4.2) |
| **Collins and Mitchell (1991)** | 23,700 | $\sigma = \varepsilon \times 23{,}700\left\{0.025 + \frac{0.975}{[1+(118\varepsilon)^{10}]^{1/10}}\right\}$ (Eq. 4.3) |
| **Eurocode 1993-1-4 (CEN, 2006)** | 23,700 | $\varepsilon = \begin{cases} \frac{\sigma}{E} + 0.002\left(\frac{\sigma}{f_y}\right)^{\frac{\ln(20)}{\ln\left(\frac{224.2}{212.3}\right)}} & for\ \sigma \le f_y \\ 0.002 + \frac{f_y}{E} + \frac{\sigma - f_y}{E}\left(1 + 0.002\frac{E}{f_y}\right) + \varepsilon_u\left(\frac{\sigma - f_y}{f_u - f_y}\right)^{1+3.5\left(\frac{f_y}{f_u}\right)} & for\ f_u < \sigma \le f_y \end{cases}$ (Eq. 4.4) |
| **Suggested formula** | 24,400 | $\sigma = \varepsilon \times 24{,}400\left\{0.058 + \frac{1-0.058}{[1+(97.5\varepsilon)^{5.72}]^{1/5.72}}\right\}$ (Eq. 4.5) |

In Table 4-3, the FDOT SDG formula, which is suggested by Al-Kaimakchi and Rambo-Roddenberry (2021a), is based on the power formula with parameters calibrated to obtain a design curve. The FDOT SDG formula results in a stress-strain curve lower that the experimental curves from this study; this can be considered as a small measure of conservatism. However, the Eurocode 3 model (CEN, 2006) curve underestimates the experimental data and does not fit well in the plastic region.  Similarly, the Collins and Mitchell (1991) model is not a good fit, as this model was intended for carbon steel strands.

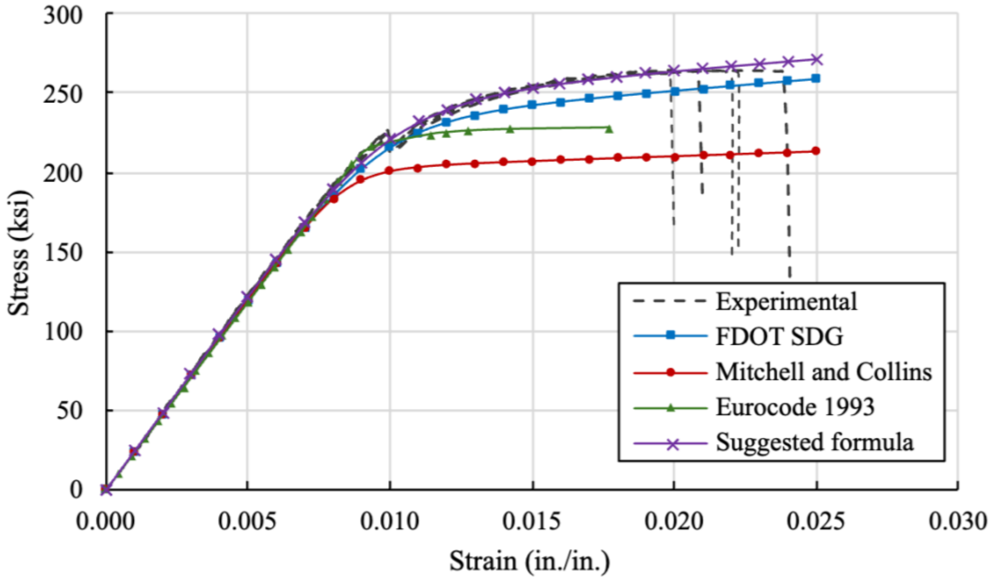


**Figure 4-6. Different models plotted vs. experimental data**

## 4.4 Concrete material properties

Understanding the concrete properties is necessary for assessing the flexural performance of the test specimens.  An important parameter to characterize is the concrete strength.  The specified 28-day concrete compressive strengths for the FSBs and cast-in-place topping were 8.5 and 4.5 ksi, respectively.  To measure the concrete strength, sample cylinders were taken from the batches during casting and stored near the specimens to experience similar curing conditions (Figure 4-7).  These cylinders were tested for compressive strength on the same day as the corresponding specimen's flexural test.  Table 4-4 summarizes the tested concrete properties.

**Figure 4-7. Concrete cylinders stored near the specimens**

**Table 4-4. Summary of tested concrete properties**

| Specimen ID | Age (days) | $f'_{c,design}$ (ksi) | $f'_{c,measured}$ (ksi) | $E_{c,design}$ (ksi) | $E_{c,measured}$ (ksi) |
|---|---|---|---|---|---|
| **FSB-1** | 63 | 8.5 | 10.810 | 5390 | 5987 |
| **FSB-2** | 78 | 8.5 | 11.734 | 5390 | 6227 |
| **FSB-3** | 91 | 8.5 | 11.644 | 5390 | 6204 |
| **FSB-4** | 61 | 8.5 | 11.912 | 5390 | 6272 |
| **FSB-1 topping** | 57 | 4.5 | 6.224 | 4171 | 4691 |
| **FSB-2 topping** | 72 | 4.5 | 6.358 | 4171 | 4733 |
| **FSB-3 topping** | 85 | 4.5 | 7.272 | 4171 | 5009 |
| **FSB-4 topping** | 55 | 4.5 | 7.112 | 4171 | 4962 |

## 4.5 Summary

The design of prestressed concrete members requires the use of the prestressing strand material properties such as elastic modulus, breaking strength, yield strength, and elongation. Tensile tests, following ASTM A1061/1061M standards (ASTM, 2020c), were conducted on five (5) 0.6-in.-diameter stainless steel strand specimens. The specimens, each 50 in. long, were obtained from a single spool supplied by Sumiden Wire.

The results of the tensile tests were presented, including the stress-strain curves for five (5) specimens. All specimens failed by rupture near the grips, meeting the ASTM 1061 criteria for test validity. The breaking strength, yield strength, total elongation, and modulus of elasticity were determined for each specimen and compared against ASTM and FDOT standards. The breaking strength was recorded as the force at failure, with all strands failing by rupture near the grips. The total elongation was measured at maximum force, and the modulus of elasticity ranged between 23,400 and 24,400 ksi, with an average of 23,700 ksi.

This chapter also provided stress-strain curves determined using different models. The most accurate model is the power formula with three parameters (A, B, and C). These parameters were calibrated for a better fit curve, resulting in a calibrated power formula curve that will be used in the verification of the experimental flexural tests.

At the end of the chapter, concrete compression test results were provided. All the concrete strengths were higher than the design values for the members and the toppings.

# CHAPTER 5 – DATA COLLECTED DURING DETENSIONING

## 5.1 Introduction

Pretensioning a prestressed concrete member involves transferring the prestressing force to the concrete member in the casting bed during the fabrication stage. This force is transferred through the bond between the concrete and the surface of the strands. This transfer process is achieved by releasing the strand's force after the concrete has reached adequate strength to resist the stresses induced by this release. This strand release process is also known as detensioning. There are different types of detensioning methods, the most common of which is the flame cutting method. This requires gradual heating of a strand until it is completely cut.

For more efficient production, several pretensioned members are cast in a single casting bed. Detensioning of the members is carried out by at least two trained technicians who simultaneously apply a torch flame to each strand, at both ends of the casting bed. Generally, the process lasts only a few seconds for each strand. Because the detensioning process causes abrupt changes in strains in short periods of time, it can cause cracks in the member. The abrupt strain changes due to strand cutting also affect the uncut strands by creating additional tension in them due to shortening of the member. In carbon steel strands, these strains are low compared to their ultimate strain. However, in the case of stainless steel strands, which have a different stress-strain behavior and lower ultimate strain than carbon steel strands, there is relatively more potential for sudden rupture to occur during the cutting process. Unexpected rupture of the last stainless steel strand during the detensioning process occurred in a previous FDOT project BDV30-977-22, Stainless Steel Strands and Lightweight Concrete for Pretensioned Concrete Girders (FDOT, 2022). That rupture resulted in interest in monitoring strains during the detensioning process in this project. During fabrication of the FSBs, strain gauges were installed on some of the free strands located between the bulkheads and the first and last FSBs in the casting bed. Additionally, the movement and rotation of the ends, adjacent to the bulkheads, were monitored.

In this chapter, a literature review for the topic of detensioning is presented. Following that, the experimental data are presented. At the end of the chapter, transfer length of the members is analyzed and compared to experimental data obtained during the detensioning process.

## 5.2 Literature review

The mechanical characteristics of stainless steel strands are different than those of carbon steel strands. Previous research has shown that all examined stainless steel strands, irrespective of their variety, exhibited rounded stress-strain curves beyond the linear-elastic region. The extent of this roundedness, along with ultimate stress, ultimate strain, and corrosion resistance, differed across the types of strands (Al-Kaimakchi and Rambo-Roddenberry, 2021d).

Mirza and Tawfik (1978), investigated cracks that occurred during the detensioning process. The study proposed that when strands are released, the member undergoes deformation that is restrained by unreleased strands. These restraining strands induce tensile stresses that cause cracks near the end region of the member. Moreover, the study developed a mathematical model to calculate the increase in tensile force in the remaining uncut strands during detensioning. The model considers the axial force in the sequentially cut strands acting on the uncut strands by modelling the strands as bilinear springs. This approach allows one to determine the increase in force in each strand as detensioning progresses. The accuracy of the model was validated by experimental measurements of strand strains and end deformations on full-scale experimental members during detensioning. The model showed good correlation. However, the model did not account for the nonlinearity of the stress-strain curve; it assumed an elastic-perfectly plastic model, it did not account for friction between the bed and the members, and it did not account for the effect of end rotation due to the eccentric prestressing force. Despite these simplifications, the study provided valuable conclusions. The model explains that a shorter free strand is subjected to more strain than a longer one under the same level of elastic shortening. Consequently, the restraining force exerted by the shorter strand is higher. Thus, structures with shorter free strands are subjected to greater restraining forces, increasing the risk of crack development. The model also shows that simultaneous release of all strands will cause equal restraining force in all free lengths. However, non-simultaneous release of free strands (when a certain free span is cut prior to the other free spans) will cause higher stresses at the location of the cut compared to the other free spans. In summary, the study demonstrated the effect of the strand release sequence on the distribution of forces among the restraining strands.

A further study by Kannel et al. (1997) investigated end region crack causes and prevention during detensioning. The study involved numerical and experimental investigation. Numerical solution was obtained from 3D finite element models to account for the three-dimensional effect of stresses in the end region of a beam. Different detensioning patterns were implemented by the effect of debonding some of the strands. The study confirmed the conclusions of Mirza and Tawfik (1978) that the reduction of free strands in the casting bed will reduce end region cracks, and cutting longer free strands is recommended to avoid higher tensile stresses in uncut strands during detensioning. Furthermore, the study recommended cutting some of the bottom straight strands before cutting draped strands to produce compression stresses that help reduce cracks. The study also recommended cutting strands in alternating columns from the interior of the member going to outside.

A previous study conducted by Moon et al. (2010) on seven-wire carbon steel strands showed the effect of different detensioning methods: namely, flame cutting and hydraulic jacking. The study implemented embedded strain gauges placed at different locations along the member, to measure strain changes at the strands. However, no data were reported about the strain change in the strands outside the member. The study also employed the hardening plastic theory to convert strain gauge measurements to forces using a method called elastic strain recovery. This method gave good results since carbon steel strands behave mostly elastic and the inelastic strains are negligible.

## 5.3 Experimental data

In previous chapters, instrumentation of the test specimens was discussed. In this section, data collected during detensioning is further discussed. This data includes strain measurements in the strands at their free length (Ends 1 and 8; see Figure 5-1), movements, rotations, strains measurements inside the concrete at the transfer length, and strains in the concrete measured with vibrating wire strain gauges (VWSGs).

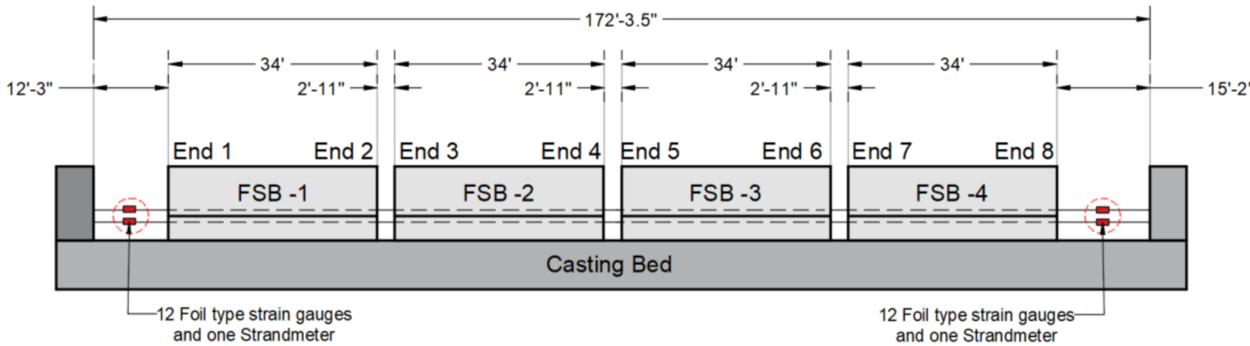


**Figure 5-1. Casting bed layout of beam specimens**

### 5.3.1 Strains at free length using foil type strain gauges

Strains in the strands at their free length were measured by two means: foil strain gauges and strandmeters. The foil gauges were instrumented at the casting yard (Figure 5-1). Figure 5-2 shows the locations of the gauges at Ends 1 and 8. The data acquisition system measured the strain every 0.1 seconds while cutting the strands, providing data to capture the strains in the instrumented strands as each strand was cut.

Figures 5-3 and 5-4 show the strain measurement as each strand was cut until rupture occurred during cutting of the $27^{th}$ strand. The strain gauges were installed after initially prestressing the strands; accordingly, the initial strain of 0.00688 (in./in.) was added to the strain measurements. In both curves, the strain reached approximately 0.011 (in./in.), which is less than the ultimate strain of 0.021 (in./in.) obtained from tensile tests presented in Chapter 4. In Chapter 7, these measured strains will be compared to an analytical mathematical model that was obtained from literature and that was further improved in Chapter 8.

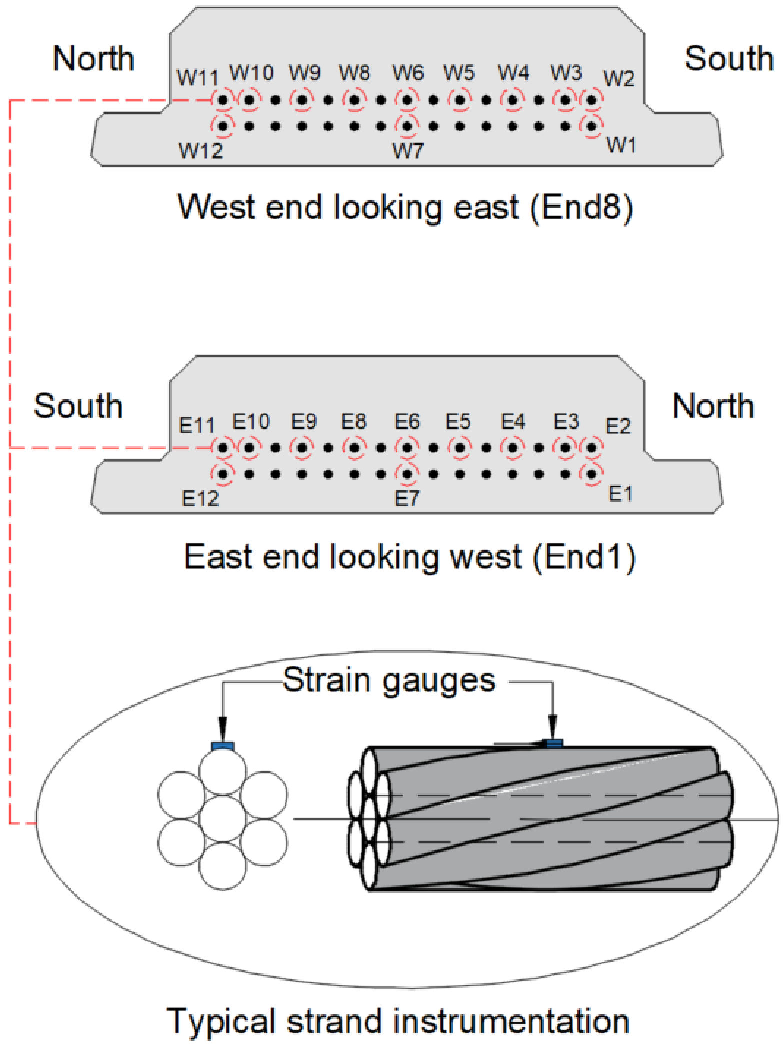


**Figure 5-2. Foil type strain gauge locations**

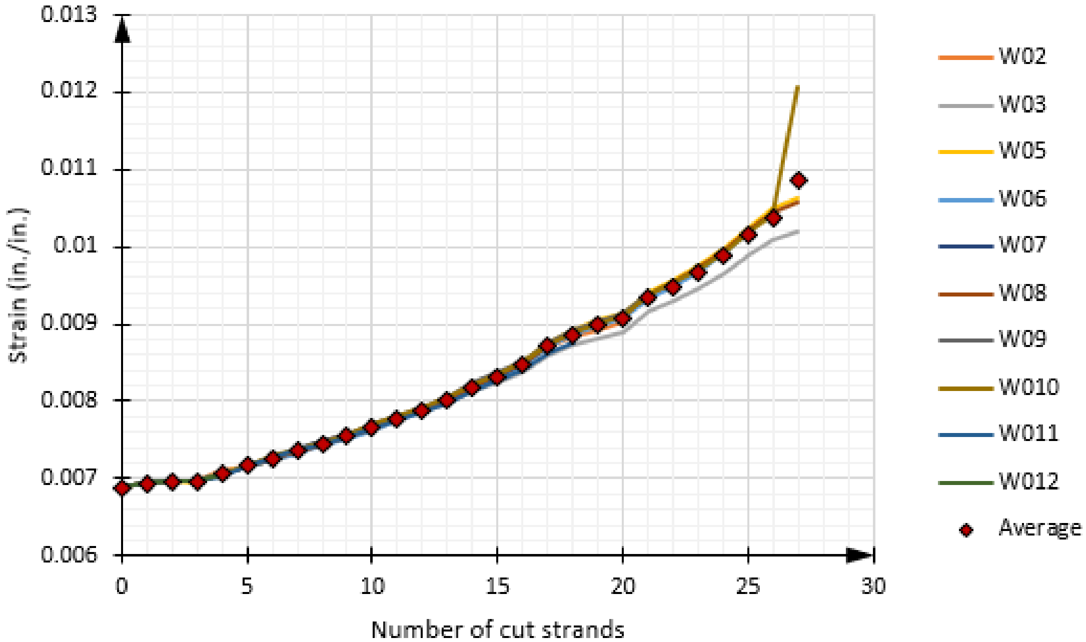


**Figure 5-3. Strain measurement for gauges near End 8**

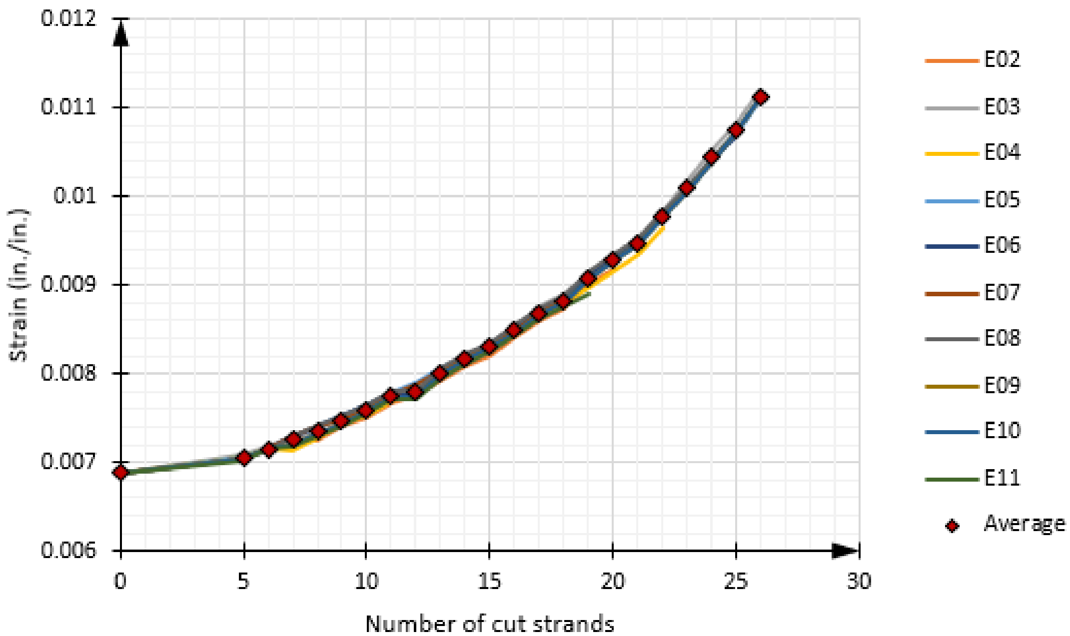


**Figure 5-4. Strain measurements for gauges near End 1**

## 5.3.2 Strains at free length using strandmeter strain gauges

The strandmeter measurements were used to verify the foil strain gauge measurements. Two (2) strandmeters were installed, at End 1 and End 8, and mounted on top of the middle strand in the top layer (Figure 5-5). As was done for the foil gauges, the initial strain measurement was added to the strandmeter readings, because the strandmeters were also installed after initial stressing. Figures 5-6 and 5-7 compare strandmeter measurements to foil gauge measurements; strandmeters did not fully capture the behavior of the strands because they measured strains only every 30 seconds.

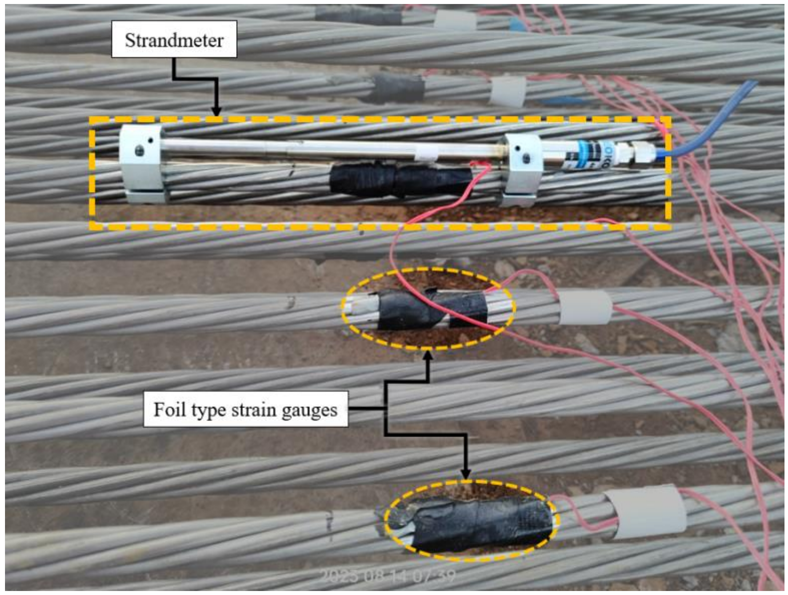


**Figure 5-5. Strandmeter mounted on the middle top strand**

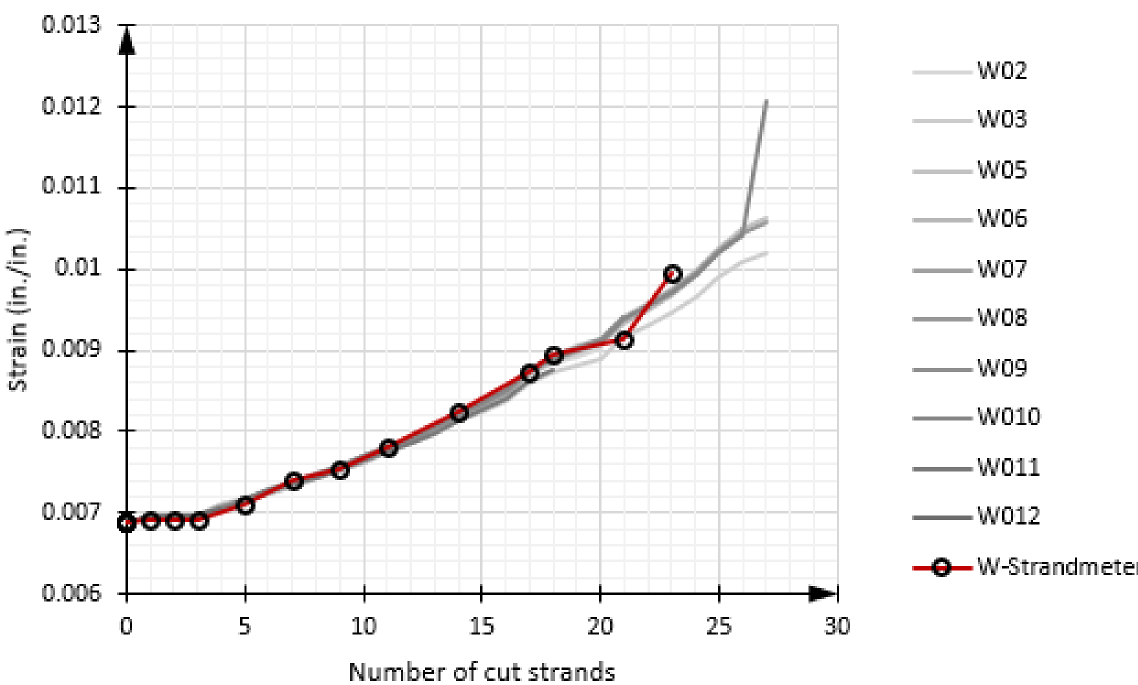


**Figure 5-6. End 8 strain measurements, strandmeter compared to foil type strain gauges installed at the same end**

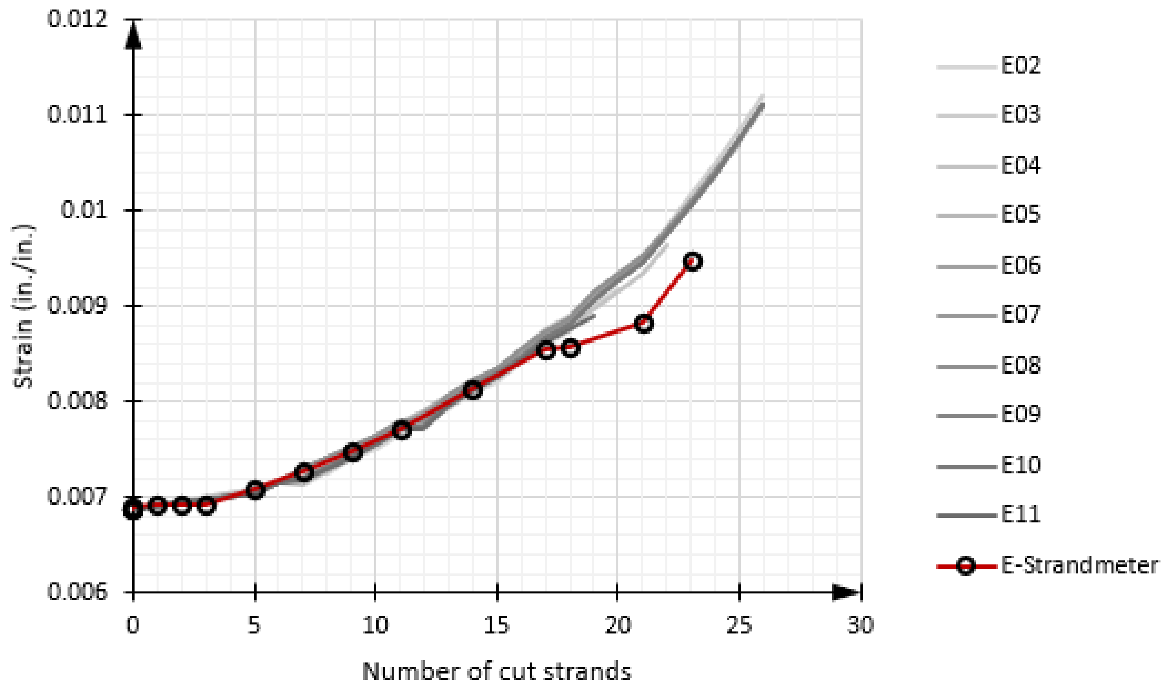


**Figure 5-7. End 1 strain measurements, strandmeter compared to foil type strain gauges installed at the same end**

### 5.3.3 End movements and rotations

The prestress force is transferred to the concrete during the detensioning process. The eccentric force applies compression stress and a moment that cause the member to shorten and rotate near the member ends. This rotation and shortening affect the strain in the strands. To monitor them, two targets and one camera were installed at the member ends where the strands were released first. When releasing the 27$^{th}$ strand, End 1 in FSB-1 had a horizontal displacement of about 0.5 in. and a rotation of 0.14 degrees. Figures 5-8 and 5-9, respectively, show the displacement and rotation vs. the number of cut strands.

This end displacement causes elongation in the uncut strands. If this elongation is divided by the length of free strand near End 1, which is about 147 in. (Figure 5-1), the result is the strain in the strands. To obtain the total strain in the strands at the free length, the initial strain must be added. Figure 5-10 shows strain values obtained from end movement measurements and compares them to strain measurements obtained from the strain gauges installed on the strands near End 1.

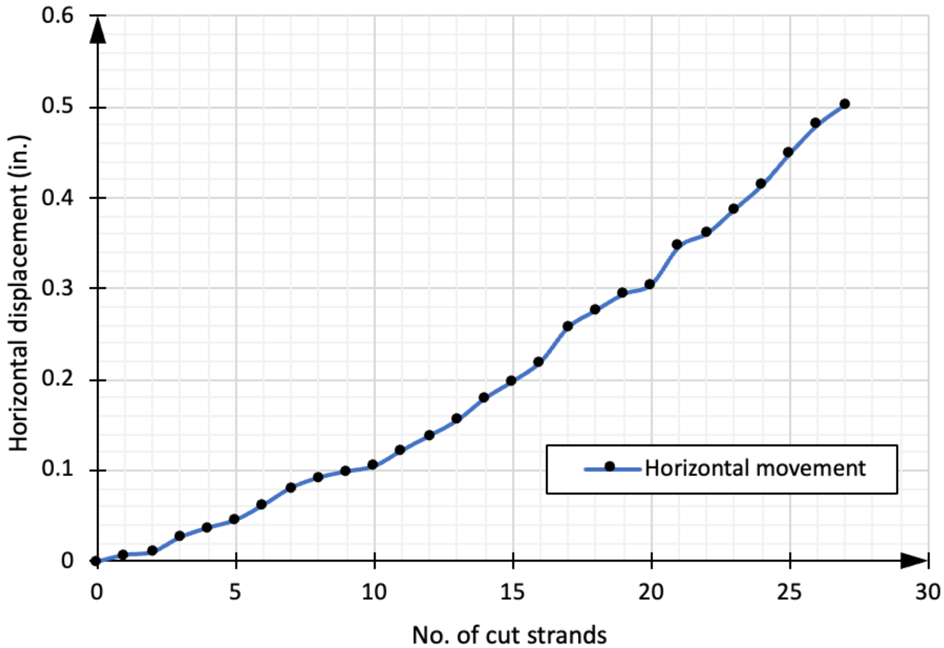


Figure 5-8. End 1 horizontal movement vs. number of cut strands

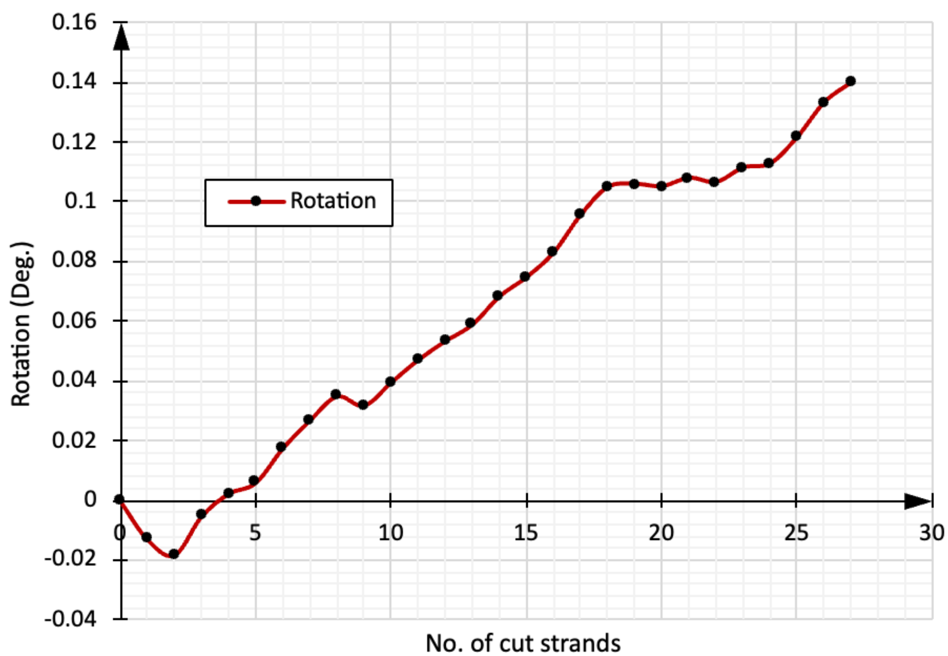


Figure 5-9. End 1 rotation vs. number of cut strands

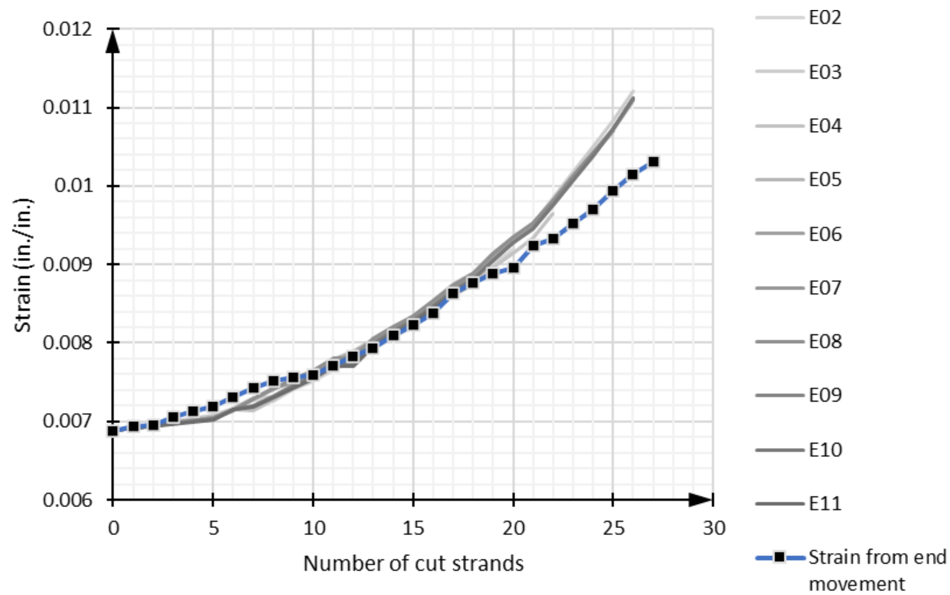


**Figure 5-10. Strain obtained from End 1 displacement compared to strain gauges installed on strands**

At End 8, the deformations were higher. During release of the 27th strand, the horizontal displacement reached 0.95 in., and the rotation was 0.2 degrees. Figures 5-11 and 5-12, respectively, show the displacement and rotation vs. the number of cut strands. The strain obtained from the displacement of End 8 is shown in Figure 5-13.

Comparing Figure 5-8 with Figure 5-11, the horizontal movement in End 8 was higher, possibly due to the rate of cutting at that end being higher or friction along the form.

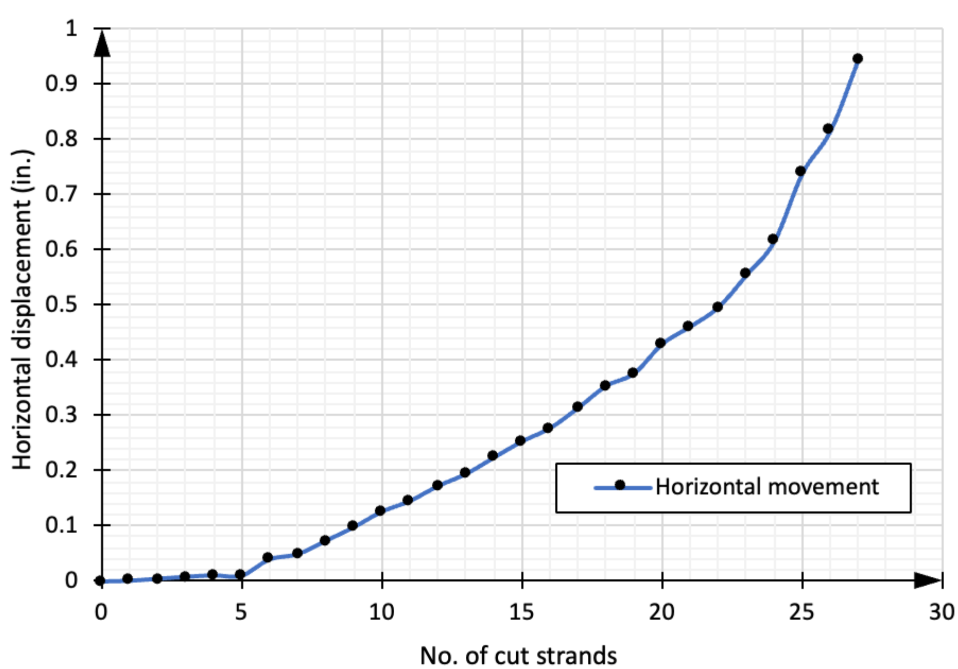


**Figure 5-11. End 8 horizontal movement vs. number of cut strands**

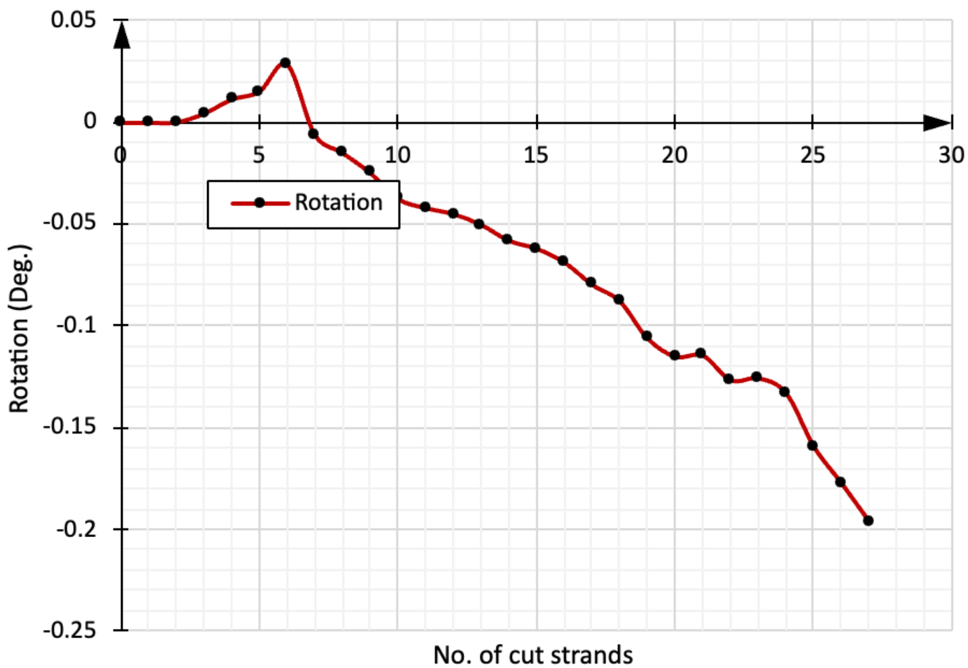


**Figure 5-12. End 8 rotation vs. number of cut strands**

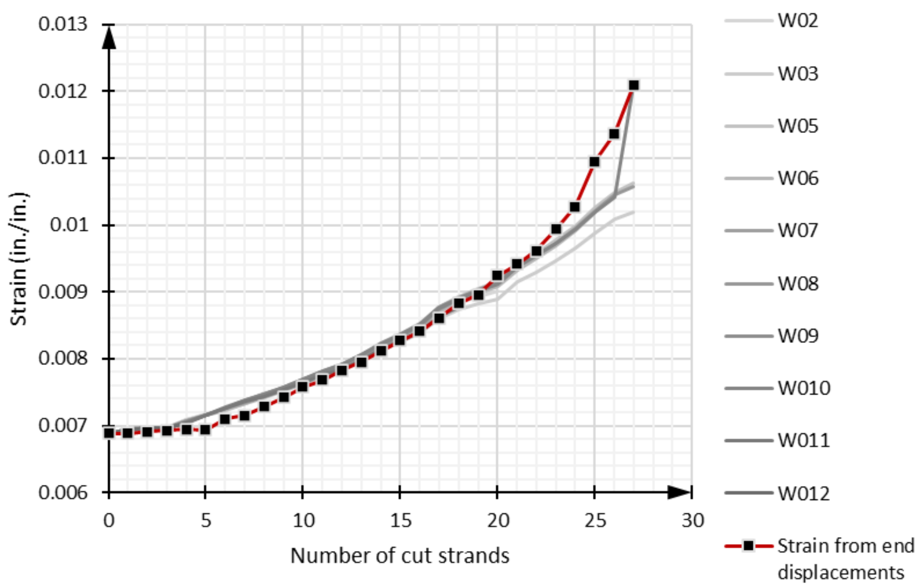


**Figure 5-13. Strain obtained from End 8 displacement compared to strain gauges installed on strands**

## 5.4 Transfer length

During construction of a prestressed concrete member, the strands are tensioned. During detensioning, the tensile force is transferred to the concrete through bond, which causes internal stresses in the concrete. Full transfer of the strand force into the concrete occurs in the member's end region over a distance referred to as the transfer length. Strain measurements in the concrete have proven to be an efficient way to measure the transfer length (Russell and Burns, 1996). Previous research on transfer length of HSSS strands was conducted by Paul et al. (2017a). They measured the transfer length using external strain measurements using detachable mechanical (DEMEC) strain gauges installed in piles reinforced with HSSS strands. Al-Kaimakchi and Rambo-Roddenberry (2021b) measured transfer length in pretensioned bridge concrete members. They used external DEMEC and ERSGs to measure the strain at the concrete surface. In other research, external and internal Fiber Optic Sensors (FOS) were installed to measure transfer length of HSSS strands (Al-Kaimakchi and Rambo-Roddenberry, 2021c). In this project, four (4) internal FOS were installed in both ends of two (2) specimens, FSB-1 and FSB-4, at the live end and dead end, respectively (Figures 5-14 and 5-15), to investigate transfer length in two (2) specimens that have the same parameters except for the confinement transverse reinforcement. FSB-1 contained carbon steel rebar for shear, shear interface, and anchorage zone reinforcement, while FSB-4 contained Glass Fiber Reinforced Polymer (GFRP) rebar instead.

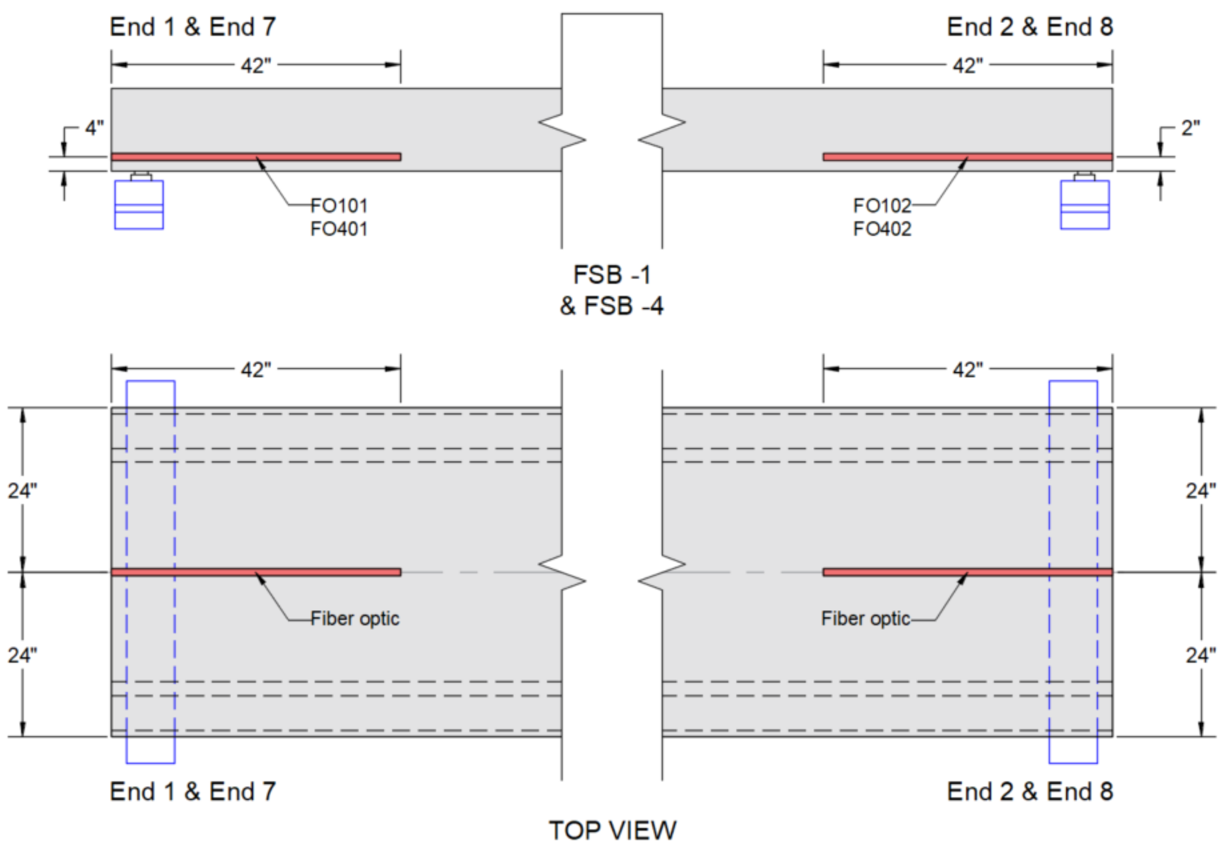


**Figure 5-14. Locations of fiber optic strain sensors**

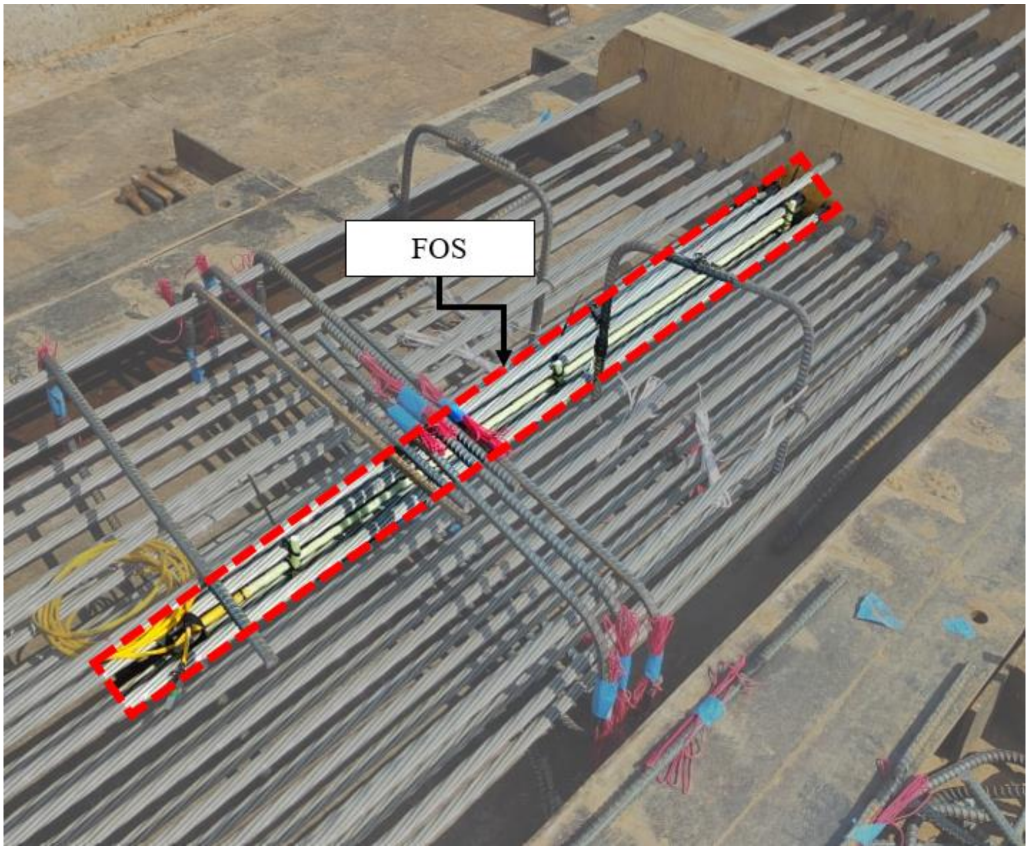


**Figure 5-15. Fiber optic sensors installed during construction of specimens**

In Figure 5-16, the FOS strain measurements are plotted along the length of the specimens. The typical strain distribution near the end increased linearly until it reached a peak. The data analysis was performed after filtering out anomalies. Then, the 95 percent average maximum strain was found. The intersection of the linear portion of the plot with the 95 percent average maximum strain represents the end of the transfer length.

From the results, the live and dead ends (Ends 1 and 8, respectively) had longer transfer lengths compared to the other ends (Ends 2 and 7). Also, End 8 had a slightly longer transfer length than End 1. Table 5-1 summarizes the transfer lengths obtained from Figure 5-16 and compares them to a previous FDOT project.

A previous FDOT project (BDV30-977-22) (FDOT, 2022) investigated the transfer length of stainless steel strands in prestressed concrete members. In that study, five AASHTO Type II girders were fabricated on a single casting bed. The concrete compressive strength was reported as 6.32 ksi at one day and 10.02 ksi at six days. Assuming linear strength gain, the estimated concrete strength at release after two days was approximately 7.06 ksi. The first and last girders in the casting bed were prestressed with thirteen 0.6-in.-diameter stainless steel strands stressed to approximately 62.2 percent of the strand's ultimate strength, corresponding to a prestressing stress of 159.8 ksi.

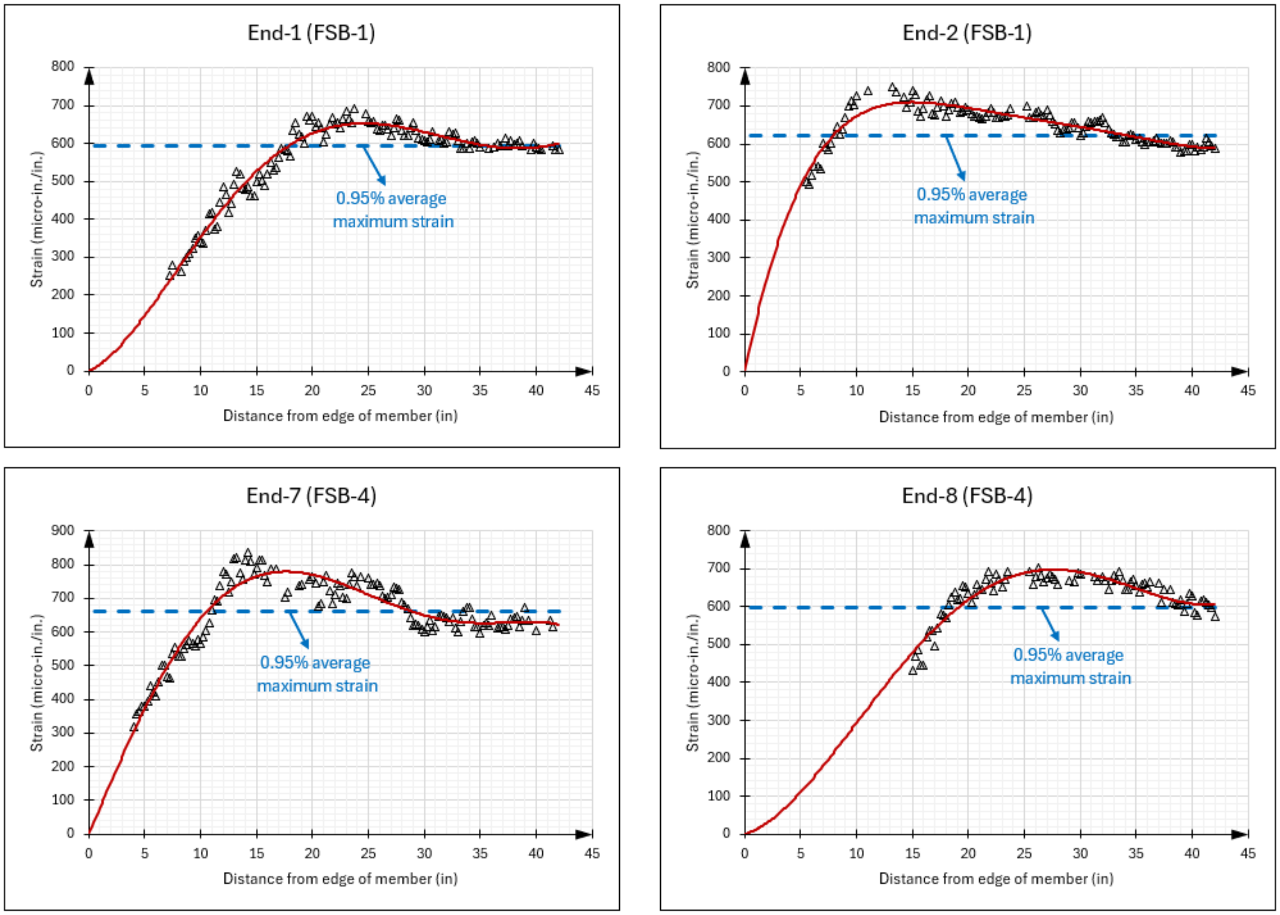


**Figure 5-16. FOS strain measurements along length near the edges of members, and the transfer length located using 95 percent maximum strain method**

**Table 5-1. Comparison of transfer lengths measured in current and previous FDOT projects**

| **Current project Specimen ID (transverse reinforcement)** | **Current project End ID** | **Current project Transfer length (in.)** | **Previous FDOT project Specimen ID (transverse reinforcement)** | **Previous FDOT project End ID** | **Previous FDOT project Transfer length (in.)** |
|---|---|---|---|---|---|
| **FSB-1 (carbon steel)** | End 1 (1st cut)<br>&<br>End 2 (2nd cut) | 18.0 (FOS)<br>&<br>8.0 (FOS) | C1 (carbon steel) | End 1 (1st cut)<br>&<br>End 2 (2nd cut) | 21.0 (ERSG)<br>20.5 (DEMEC)<br>&<br>16.8 (ERSG)<br>18.2 (DEMEC) |
| **FSB-4 (GFRP)** | End 7 (2nd cut)<br>&<br>End 8 (1st cut) | 11.0 (FOS)<br>&<br>19.0 (FOS) | C3 (stainless steel) | End 6 (2nd cut)<br>&<br>End 5 (1st cut) | 16.0 (ERSG)<br>15.7 (DEMEC)<br>&<br>19.7 (ERSG)<br>20.2 (DEMEC) |

Compared to the previous study, the current project utilized a higher prestressing level and significantly larger total prestressing force. The release stress in the current study was approximately 168 ksi, corresponding to about 70 percent of the strand's ultimate strength, while the concrete release strength in the previous study was approximately 16 percent lower than that of the current project.

Despite these differences, the experimentally measured transfer lengths obtained using fiber optic sensors (FOS) in the current study were generally comparable to those reported in the previous research.

## 5.5 Summary

The chapter reviewed literature on detensioning, noting that stainless steel strands exhibit a different stress-strain behavior than carbon steel. Previous studies investigated the detensioning of carbon steel strands to find the causes and preventions of end region cracks during detensioning, proposing models and recommendations to minimize cracking. However, lower ultimate strain of HSSS strands compared to carbon steel suggests that further study needed to be done.

Experimental data obtained during fabrication of specimens for this project was presented. Strains during detensioning were monitored using foil type strain gauges and strandmeters. The data showed the strain change in strands as each strand was cut. End movements and rotations during detensioning were analyzed, such that strains in the strands were obtained. It was observed that the end movement at End 8 was higher than at End 1, possibly due to a higher rate of cutting at End 8 or friction along the form. This is significant to precasters: assuming that the beams would shrink equally at each end of the precasting bed would result in unconservative calculations of strain in the strands during detensioning.

Finally, the transfer length, which is the length required to fully transfer the prestressing force from the strands to the concrete, was analyzed. Using measurements from FOS, transfer lengths were determined for the specimens. The measured transfer length was shorter than in the previous FDOT project, even though the prestressing force was higher. The second cut of the strands, however, resulted in a significantly lower transfer length compared to the previous research.

# CHAPTER 6 – FLEXURAL TESTS

## 6.1 Introduction

This chapter discusses the flexural test setup for the four (4) FSB specimens. First, the test setup is described, followed by details on the instrumentation used to collect data during the flexural tests. Then, the failure modes and observed crack patterns are described. At the end of the chapter, data collected during the flexural tests are presented, along with a conclusion and summary.

## 6.2 Test setup

The four (4) specimens were tested using a four-point bending test setup (Figure 6-1). Each specimen was supported at the bottom near the ends and had a span length of 32 ft. A constant-moment region was created by applying the load at two (2) points, each 3 ft from midspan. For this purpose, a 7-ft-long W16×100 steel spreader beam was used. Neoprene pads with dimensions of 12 in. × 6 in. × 2 in. were placed between the spreader beam and specimen to transfer the load efficiently and prevent localized damage. The load was applied by an actuator (Enerpac with an 800-kip capacity) at a rate of 0.25 kips/sec and was measured using a load cell. The displacements were measured at the top surface of the specimen at various points along its length, using laser displacement transducers (LDTs) spaced on both sides of the spreader beam and along the midline.

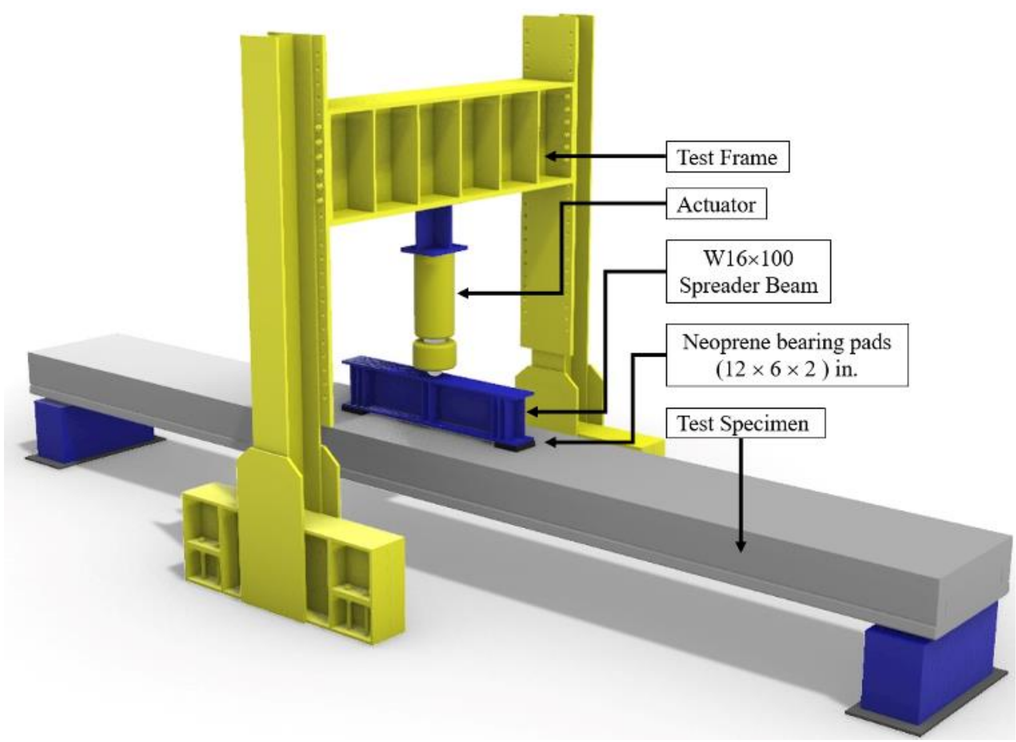


**Figure 6-1. Test setup**

## 6.3 Test instrumentation

Each specimen was instrumented with gauges to measure the strain, deflection, and strand slippage. Nine (9) foil type strain gauges were installed on the top surface of the concrete in the constant-moment region between the spreader beam bearing pads. One gauge was located at the top surface center of the specimen, and the remaining gauges were spaced at 2 ft in the longitudinal direction and 1 ft in the lateral direction (Figure 6-2). During the flexural test, additional strain gauges were installed on the bottom of the specimen at locations where the first cracks appeared.

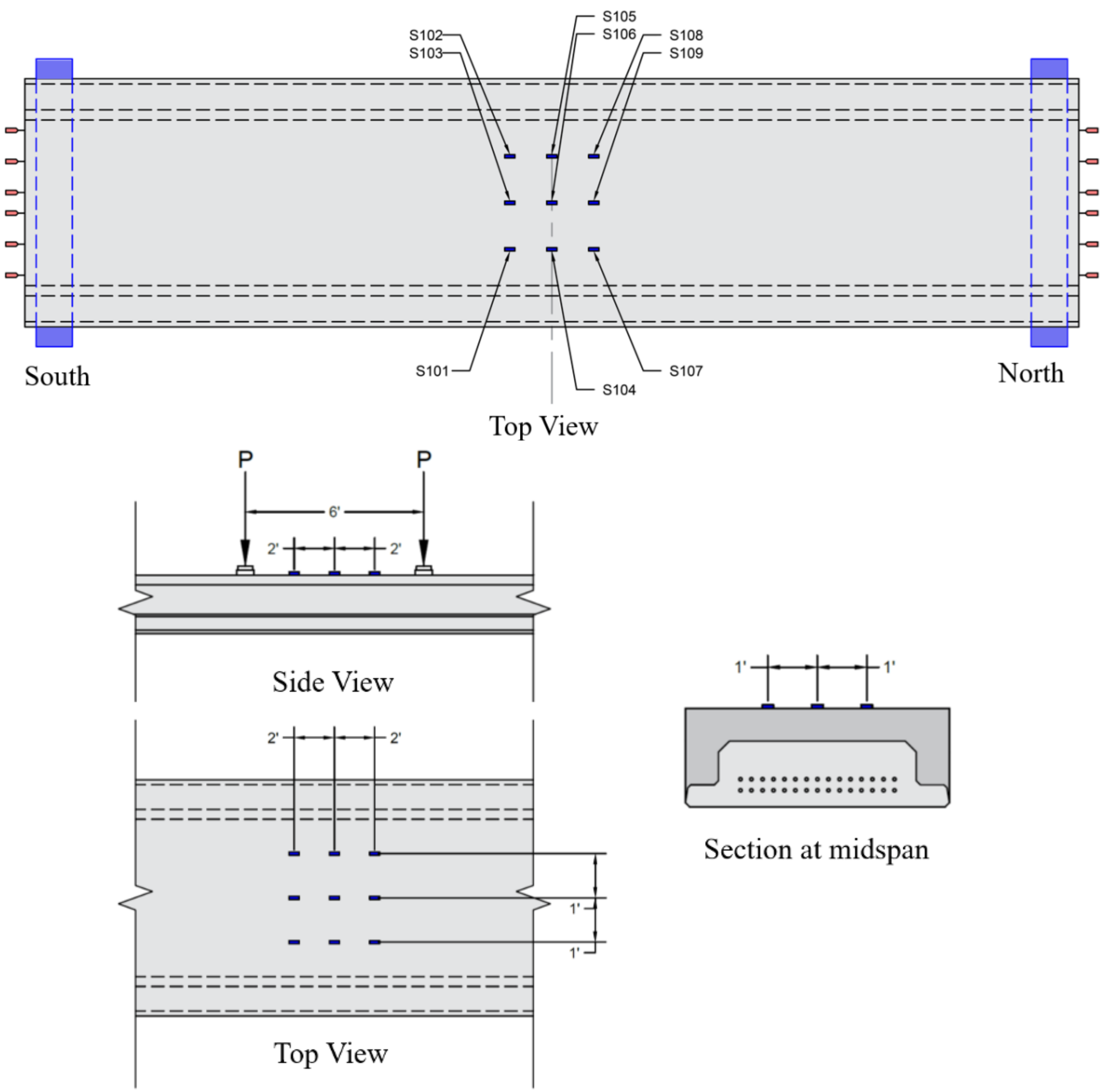


**Figure 6-2. Concrete strain gauge locations**

Deflections along the specimen were measured using 12 LDTs (Figure 6-3). As shown in Figure 6-4, two (2) of them were located at the supports. Between the supports and the spreader beam, the gauges were spaced at 4 ft 4 in. In the zone between the spreader beam bearing pads, they were spaced at 3 ft and in pairs.


**Figure 6-3. LDT sensor**

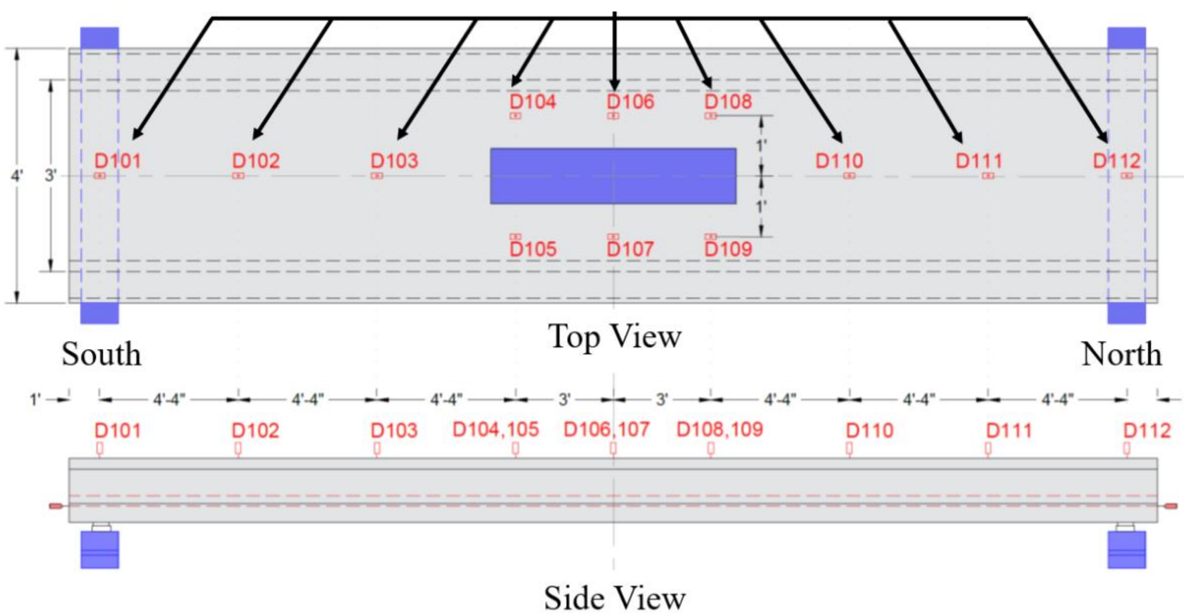


**Figure 6-4. LDT sensor locations**

Slip gauges were installed on the protruding strand ends (Figure 6-5). Six (6) slip gauges were installed on six (6) strands in the bottom layer and on each end of the specimen.

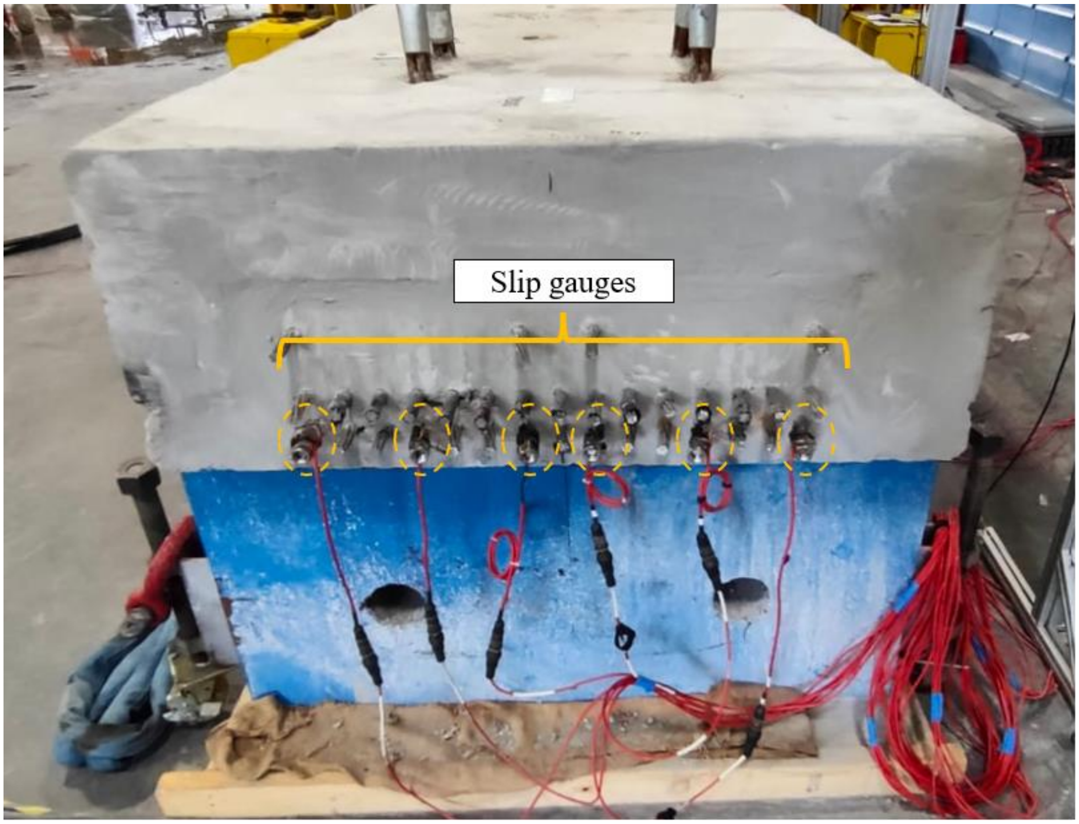


**Figure 6-5. Slip gauges installed on a specimen end**

## 6.4 Prestress losses

In this section, we evaluate the prestress losses in HSSS strands using three different methods: AASHTO (2024) formulas in Section 3.4.1; VWSG measurements (Section 3.4.2); and the decompression method using measurements from strain gauges installed at the locations of the first cracks that occurred during testing (Section 3.4.3).

### 6.4.1 AASHTO LRFD

AASHTO LRFD Bridge Design Specifications (AASHTO, 2024) specifies two types of losses: instantaneous losses (for pretensioned members, this is elastic shortening); and long-term losses, including relaxation, creep, and shrinkage. In the following section, losses are calculated per the AASHTO LRFD refined method.

#### 6.4.1.1 Elastic shortening

The elastic shortening of the member can be calculated in accordance with AASHTO (2024) Section 5.9.3.2.3a. It is an iterative method. First, elastic instantaneous losses must be assumed, and then the calculated losses must match the assumption. If no match is found, then another trial is needed. The following is a sample calculation for FSB-1 and FSB-4, followed by Table 6-1 which summarizes the elastic shortening losses calculated for all four (4) specimens:

$$f_{cgp} = \frac{P_i}{A} + \frac{P_i e^2}{I} - \frac{M_{sd} e}{I} = \frac{1233.0-13.07}{473.76} + \frac{(1233-13.07)*1.6^2}{5772} - \frac{875.67*1.6}{5772} = 2.858\ ksi \quad \text{(Eq. 6.1)}$$

$$\Delta f_{pES} = \frac{E_p}{E_{ct}} f_{cgp} = \frac{24{,}400}{5334} * 2.858 = 13.07\ ksi \quad \text{(Eq. 6.2)}$$

**Table 6-1. AASHTO elastic shortening losses**

| Specimen | Prestress loss (ksi) | Prestress loss (%) |
|---|---|---|
| **FSB-1** | 13.07 | 7.8% |
| **FSB-2** | 9.42 | 5.6% |
| **FSB-3** | 5.77 | 3.4% |
| **FSB-4** | 13.07 | 7.8% |

### 6.4.1.2 Shrinkage before deck placement

The shrinkage losses before deck placement can be calculated using AASHTO (2024) Section 5.9.3.4.2a:

$$\Delta f_{pSR} = \varepsilon_{bid} E_p K_{id} \quad \text{(Eq. 6.3)}$$

The variable $K_{id}$ is calculated using the gross section properties for the FSB without any topping (deck). The concrete age at the time of deck placement for all specimens was 2 days. A sample calculation for the shrinkage loss for FSB-1 is provided below, followed by Table 6-2 which summarizes the shrinkage loss before deck placement for all four (4) specimens.

$$K_{id} = \frac{1}{1+\frac{E_p A_{ps}}{E_{ci} A_g}\left(1+\frac{A_g e_{pg}^2}{I_g}\right)[1+0.7\psi_b(t_d,t_i)]} = \frac{1}{1+\frac{24{,}400}{5334.1}*\frac{30*0.2367}{473.76}\left(1+473.76*\frac{2.4^2}{5772}\right)(1+0.7*0.3)} = 0.89 \quad \text{(Eq. 6.4)}$$

$$\varepsilon_{bid} = k_s k_{hs} k_f k_{td} 0.48 \times 10^{-3} = 1.0(1.99)(0.5)(0.18)(0.48)(10^{-3}) = 0.00009 \quad \text{(Eq. 6.5)}$$

$$\Delta f_{pSR} = \varepsilon_{bid} E_p K_{id} = 0.00009(24{,}400)(0.89) = 1.948\ ksi \quad \text{(Eq. 6.6)}$$

**Table 6-2. AASHTO shrinkage losses before deck placement**

| Specimen | Prestress loss (ksi) | Prestress loss (%) |
|---|---|---|
| **FSB-1** | 1.9 | 1.2% |
| **FSB-2** | 2.0 | 1.2% |
| **FSB-3** | 2.1 | 1.2% |
| **FSB-4** | 1.9 | 1.2% |

### 6.4.1.3 Creep before deck placement

The creep losses before deck placement can be calculated using AASHTO (2024) Section 5.9.3.4.2b. A sample calculation for FSB-1 is shown below, followed by Table 6-3 which summarizes the creep losses for all four (4) specimens:

$$\Delta f_{pCR} = \frac{E_p}{E_{ci}} f_{cgp} \psi_b(t_d, t_i) K_{id} = \left(\frac{24{,}400}{5334.1}\right)(2.9)(0.3)(0.89) = 3.508\ ksi \qquad \text{(Eq. 6.7)}$$

**Table 6-3. AASHTO creep losses before deck placement**

| Specimen | Prestress loss (ksi) | Prestress loss (%) |
|---|---|---|
| **FSB-1** | 3.5 | 2.1% |
| **FSB-2** | 2.6 | 1.6% |
| **FSB-3** | 1.7 | 1.0% |
| **FSB-4** | 3.5 | 2.1% |

### 6.4.1.4 Relaxation of prestressing strands

The relaxation of prestressing strands from transfer to deck placement was determined in accordance with AASHTO LRFD Section 5.9.3.4.2c. The $K_L$ factor was taken to be 30 because the strands are low-relaxation type. The yield strength, $f_{py}$, was calculated based on experimental tensile test results (Chapter 4). A sample calculation for FSB-1 is shown below, followed by Table 6-4 which summarizes relaxation losses for all four (4) specimens:

$$\Delta f_{pR1} = \frac{f_{pt}}{K_L}\left(\frac{f_{pt}}{f_{py}} - 0.55\right) = \left(\frac{168-15.2}{30}\right)\left(\frac{168-15.2}{225.1} - 0.55\right) = 0.66\ ksi \qquad \text{(Eq. 6.8)}$$

**Table 6-4. AASHTO relaxation losses before deck placement**

| Specimen | Prestress loss (ksi) | Prestress loss (%) |
|---|---|---|
| **FSB-1** | 0.66 | 0.40 |
| **FSB-2** | 0.75 | 0.44 |
| **FSB-3** | 0.86 | 0.51 |
| **FSB-4** | 0.63 | 0.38 |

### 6.4.1.5 Shrinkage after deck placement to test day

The shrinkage losses for all specimens were calculated in accordance with AASHTO LRFD Section 5.9.3.4.3a. A sample calculation for FSB-1 is summarized as follows:

$$\psi_b(t_f, t_i) = 1.9 k_s k_{hc} k_f k_{td} t_i^{-0.118} = 1.9(1.0)(1.99)(0.5)(0.68)(4^{-0.118}) = 1.16 \qquad \text{(Eq. 6.9)}$$

$$K_{df} = \frac{1}{1 + \frac{E_p}{E_c}\frac{A_{ps}}{A_c}\left(1 + \frac{A_c e_{pc}^2}{I_c}\right)[1 + 0.7\psi_b(t_f, t_i)]}$$

$$= \frac{1}{1 + \frac{24{,}400}{5987}\left(\frac{30(0.2367)}{694.9}\right)\left(1 + \frac{694.9(3.6)^2}{17{,}557}\right)[1 + 0.7(1.16)]} = 0.898 \quad \text{(Eq. 6.10)}$$

$$\varepsilon_{bdf} = k_s k_{hs} k_f k_{td} 0.48 \times 10^{-3} = (1.0)(1.99)(0.5)(0.68)(0.48)(10^{-3}) = 0.00035 \quad \text{(Eq. 6.11)}$$

$$\Delta f_{pSR} = \varepsilon_{bid} E_p K_{id} = 0.00035 * 24{,}400 * 0.898 = 7.559\ ksi \quad \text{(Eq. 6.12)}$$

Because the test day is different for each specimen, the age of concrete is different. Table 6-5 provides the test date, age of concrete on test day, and calculated shrinkage losses for all four (4) specimens.

**Table 6-5. AASHTO shrinkage losses after deck placement**

| Specimen | Date of test | Age of concrete (days) | Shrinkage losses |
|---|---|---|---|
| **FSB-1** | 10/12/2023 | 63 | 7.6 ksi (4.5%) |
| **FSB-2** | 10/27/2023 | 78 | 8.3 ksi (4.9%) |
| **FSB-3** | 11/09/2023 | 91 | 8.9 ksi (5.3%) |
| **FSB-4** | 10/10/2023 | 61 | 7.5 ksi (4.5%) |

#### 6.4.1.6 Creep after deck placement to test day

The creep loss calculation is in accordance with AASHTO LRFD Section 5.9.3.4.3b. Sample calculations for FSB-1 are provided as follows:

$$\psi_b(t_d, t_i) = 1.9 k_s k_{hc} k_f k_{td} t_i^{-0.118} = (1.9)(1.0)(1.99)(0.5)(0.07)(4^{-0.118}) = 0.11 \quad \text{(Eq. 6.13)}$$

$$\psi_b(t_f, t_d) = 1.9 k_s k_{hc} k_f k_{td} t_i^{-0.118} = 1.9 * 1.0 * 1.99 * 0.5 * 0.72 * 2^{-0.118} = 1.34 \quad \text{(Eq. 6.14)}$$

$$K_{df} = \frac{1}{1 + \frac{E_p}{E_c}\frac{A_{ps}}{A_c}\left(1 + \frac{A_c e_{pc}^2}{I_c}\right)[1 + 0.7\psi_b(t_f, t_i)]}$$

$$= \frac{1}{1 + \frac{24{,}400}{6273} * \frac{30 * 0.2367}{694.9}\left(1 + \frac{694.9(3.6)^2}{17{,}887}\right)[1 + 0.7(1.16)]} = 0.898 \quad \text{(Eq. 6.15)}$$

$$\Delta f_{cd} = \left(\Delta f_{pSR} + \Delta f_{pSR} + \Delta f_{pR1}\right) * \frac{A_{ps} * No_{strands}}{A_G} - \frac{0.41 * 34^2}{8} * 12 * \frac{2.4}{5772} = -0.5 \quad \text{(Eq. 6.16)}$$

$$\Delta f_{pCD} = \frac{E_p}{E_{ci}} f_{cgp}\left[\psi_b(t_f, t_i) - \psi_b(t_d, t_i)\right] K_{df} + \frac{E_p}{E_c} \Delta f_{cd} \psi_b(t_f, t_d) K_{df} = 9.9\ ksi \quad \text{(Eq. 6.17)}$$

Because the test day is different for each specimen, the age of concrete is different. Table 6-6 provides the test date, age of concrete on test day, and calculated creep losses for all four (4) specimens.

**Table 6-6. AASHTO creep losses after deck placement to test day**

| Specimen | Date of test | Age of concrete (days) | Shrinkage losses |
|---|---|---|---|
| **FSB-1** | 10/12/2023 | 63 | 9.9 ksi (5.9%) |
| **FSB-2** | 10/27/2023 | 78 | 7.1 ksi (4.2%) |
| **FSB-3** | 11/09/2023 | 91 | 3.4 ksi (2.0%) |
| **FSB-4** | 10/10/2023 | 61 | 9.9 ksi (5.9%) |

## 6.4.2 VWSG

VWSGs were installed on two (2) strands in the bottom strand layer of each FSB. These gauges measure concrete strain at their locations. After release, the change in VWSG readings provides the elastic shortening loss. However, these readings do not include strand relaxation. Figure 6-6 provides elastic shortening losses taken from the VWSGs.

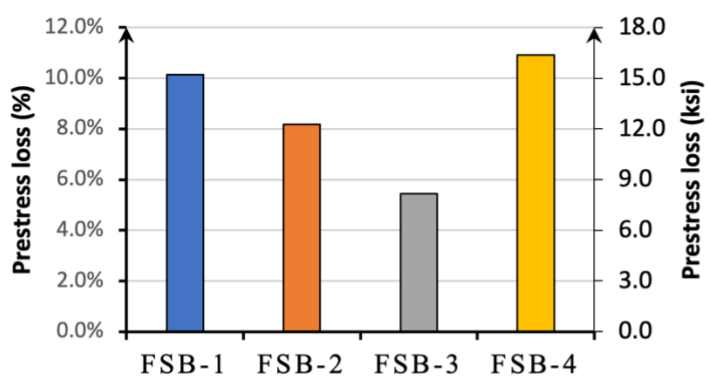


**Figure 6-6. Site readings for elastic shortening losses**

Prior to flexural tests, VWSG measurements provided final losses excluding relaxation in the strands. Subtracting these losses from the jacking force and adding relaxation provides the effective jacking stress. Table 6-7 provides details of these losses and effective stress for each specimen.

Table 6-7 Prestress losses of stainless steel strands using VWSGs

| Specimen ID | VWSG ID | Age (days) | Jacking stress (ksi) | VWSG (ksi) | Relaxation loss (ksi) | Total losses (ksi) | Effective stress (ksi) | Effective/ Jacking stress |
|---|---|---|---|---|---|---|---|---|
| **FSB-1** | VW101 | 63 | 168.0 | 23.39 | 2.4 | 25.79 | 142.21 | 84.65% |
| **FSB-1** | VW102 | 63 | 168.0 | 22.85 | 2.4 | 25.25 | 142.75 | 84.97% |
| **FSB-2** | VW201 | 78 | 168.0 | 19.19 | 2.4 | 21.59 | 146.41 | 87.15% |
| **FSB-2** | VW202 | 78 | 168.0 | 19.35 | 2.4 | 21.75 | 146.25 | 87.05% |
| **FSB-3** | VW301 | 91 | 168.0 | 12.66 | 2.4 | 15.06 | 152.94 | 91.04% |
| **FSB-3** | VW302 | 91 | 168.0 | 13.38 | 2.4 | 15.78 | 152.22 | 90.61% |
| **FSB-4** | VW401 | 61 | 168.0 | 24.52 | 2.4 | 26.92 | 141.08 | 83.98% |

### 6.4.3 Decompression method

To verify the VWSG measurements, the decompression method was used to calculate effective stress. The decompression method was used by Pessiki et al. (1996) to evaluate losses using strain measurements of foil strain gauges placed near the cracks. For that reason, all specimens were loaded gradually until 0.75% of the predicted cracking load was reached. After that, the loading was halted at 10-kip increments so that cracks could be visually inspected. When cracks were identified, 10 kips of load was further applied to allow more cracks to appear. The specimen was then fully unloaded, and strain gauges were placed on the bottom surface near the cracks (Figure 6-7). These strain gauges were to measure the decompression strain and allow prediction of prestress losses. Figure 6-8 summarizes the strain data obtained vs. the applied load. A bilinear response can be identified; the intersection of these lines corresponds to the decompression load.

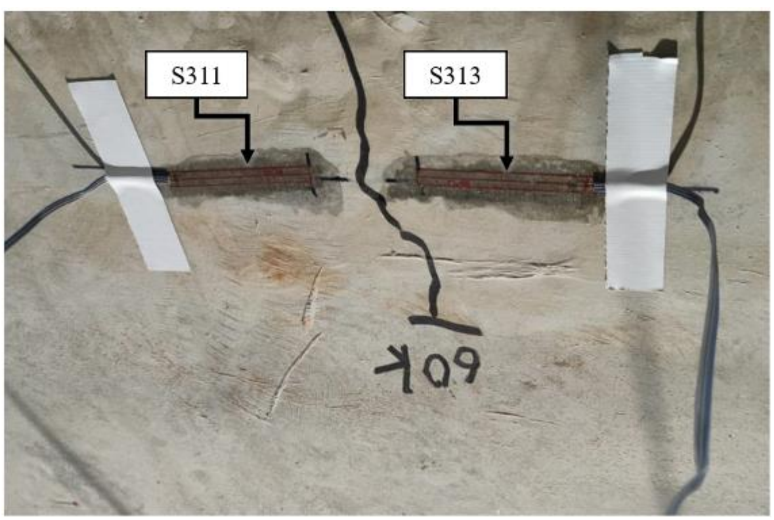


**Figure 6-7. Strain gauges installed near cracks**

Table 6-8 provides prestress losses and effective prestress based on the decompression method. For FSB-4, some strain gauges did not give good data, possibly because of damage, installation, or wiring issues, and as a result it was excluded from the table. Other gauges with bad strain measurements were also excluded. The decompression method resulted in average losses similar to the VWSG measurements (Figure 6-9). Table 6-9 compares experimental losses to AASHTO LRFD calculated losses.

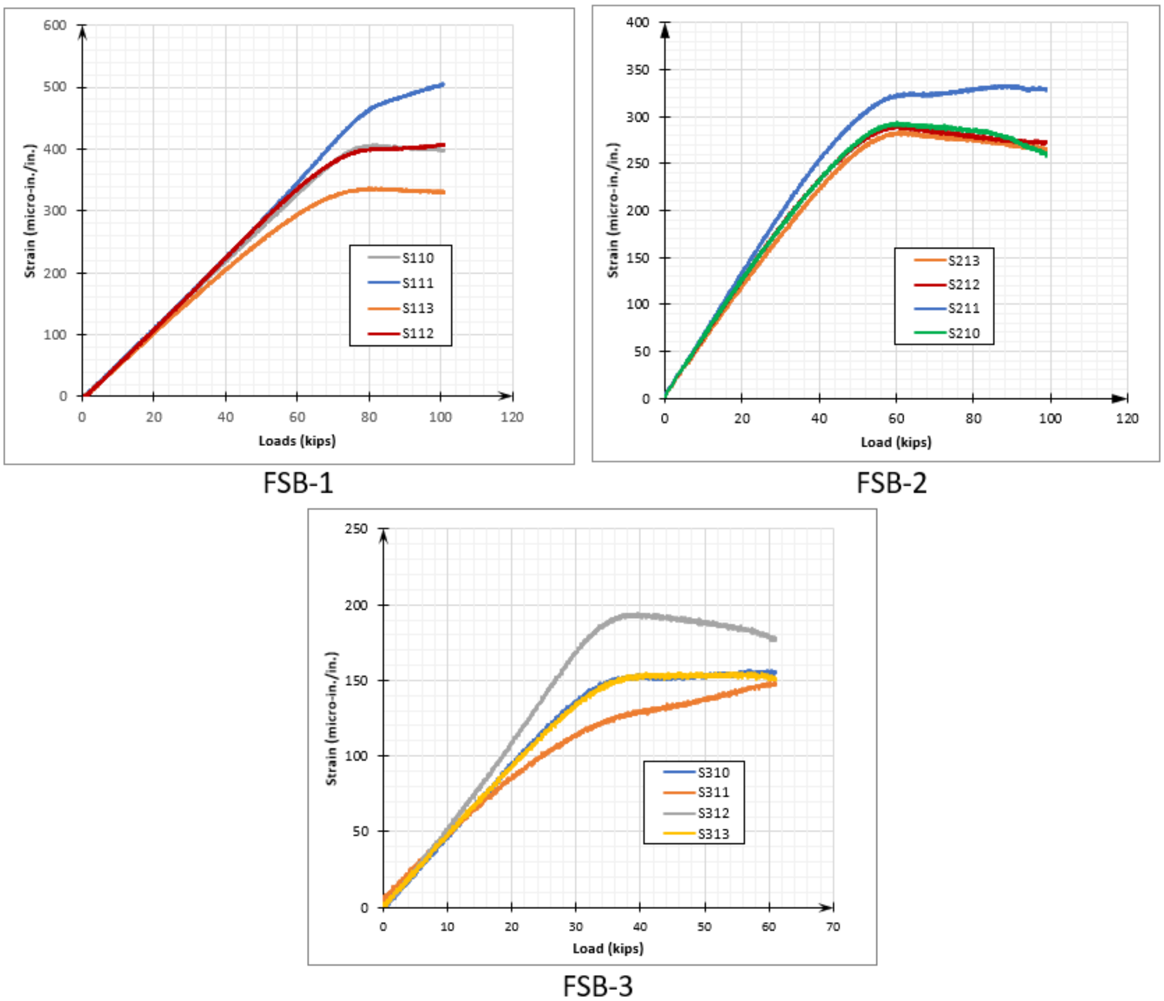


**Figure 6-8. Strain gauge measurements near cracks**

**Table 6-8. Summary for calculation of losses using decompression method**

| Specimen | Jacking stress (ksi) | Strain gauge ID | Decompression load (kips) | Total losses (ksi) | Effective prestress (ksi) | Effective / Jacking stresses |
|---|---|---|---|---|---|---|
| **FSB-1** | 168.0 | S110 | 74.0 | 24.8 | 143.2 | 85.2% |
| **FSB-1** | 168.0 | S111 | 79.0 | 29.8 | 138.2 | 82.3% |
| **FSB-2** | 168.0 | S210 | 55.0 | 19.8 | 148.2 | 88.2% |
| **FSB-2** | 168.0 | S212 | 60.0 | 19.4 | 148.6 | 88.4% |
| **FSB-2** | 168.0 | S213 | 55.0 | 24.8 | 143.2 | 85.3% |
| **FSB-3** | 168.0 | S310 | 31.0 | 23.2 | 144.8 | 86.2% |
| **FSB-3** | 168.0 | S312 | 32.0 | 18.9 | 149.1 | 88.7% |
| **FSB-3** | 168.0 | S313 | 32.0 | 13.6 | 154.4 | 91.9% |

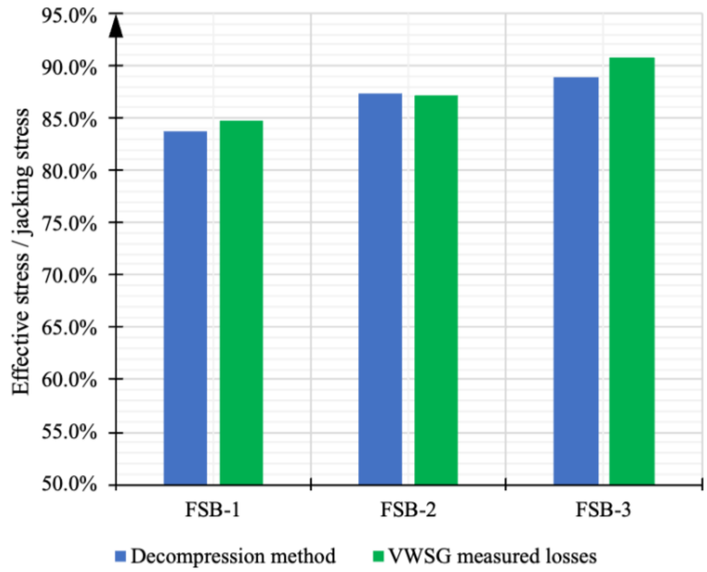


**Figure 6-9. Effective stress as a percentage of jacking stress from the decompression method compared to VWSG measurements**

**Table 6-9. Comparison of experimental losses and AASHTO LRFD calculated losses**

| Specimen | AASHTO losses (ksi) | Decompression losses (ksi) | Experimental losses (ksi) |
|---|---|---|---|
| **FSB-1** | 37.34 | 27.3 | 25.50 |
| **FSB-2** | 30.87 | 21.3 | 18.32 |
| **FSB-3** | 23.46 | 18.6 | 15.42 |
| **FSB-4** | 37.21 | - | 26.92 |

## 6.5 Experimental results

All four (4) specimens were tested in flexure until failure. Each specimen was loaded in two (2) stages. The first stage was loading until initiation of the first crack. Then, the specimen was unloaded, the locations of the cracks were marked, and two (2) foil type strain gauges were installed near the cracks. Following that, for the second stage, loading was continued until failure. The data collected during the flexural tests included applied load, deflection, surface concrete strain, slippage, and strain in the concrete at the level of the strands.

### 6.5.1 Load-deflection relationship

The LDT gauges measured the deflections for each load increment. The average of the readings from the central pair of LDTs was plotted against the loads; the load-deflection curves for all specimens are shown in Figure 6-10.

All specimens behaved linearly in the pre-cracking region, followed by nonlinear behavior beyond the crack until failure. The failure mode was crushing of concrete at the top fiber for all specimens. A summary of the main test results is given in Table 6-10. Discussion and comparison of the results are summarized in the following sections.

The reserved capacity is the amount of strength beyond the first crack. The ultimate load divided by the cracking load, as well as the reserve capacity, is plotted against the number of strands in Figure 6-11.

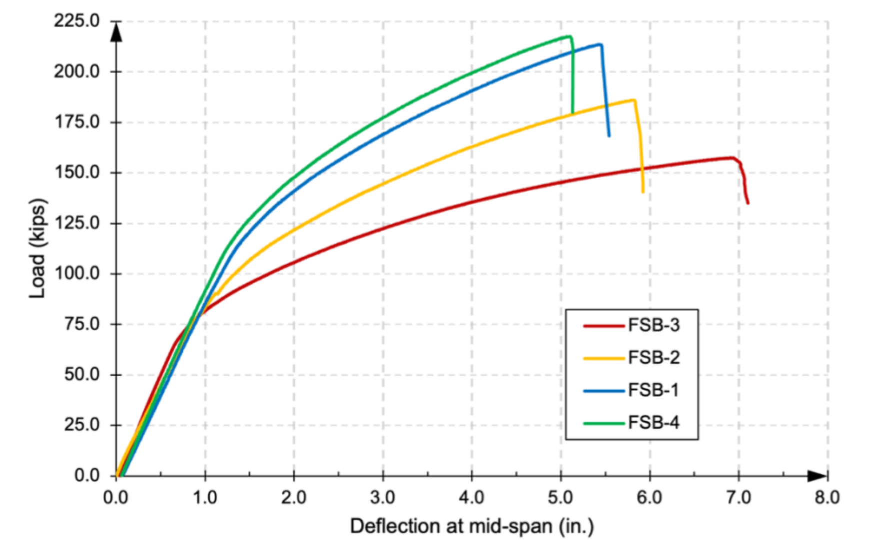


**Figure 6-10. Load-deflection relationships**

**Table 6-10. Flexural test load-deflection results**

| Specimen | Cracking load (kips) | Crack deflection (in.) | Ultimate load (kips) | Ultimate deflection (in.) | Failure mode |
|---|---|---|---|---|---|
| **FSB-1** | 100.0 | 1.103 | 213.6 | 5.444 | Concrete crushing |
| **FSB-2** | 80.3 | 0.932 | 186.1 | 5.817 | Concrete crushing |
| **FSB-3** | 60.3 | 0.580 | 157.5 | 6.900 | Concrete crushing |
| **FSB-4** | 100.3 | 1.045 | 217.7 | 5.097 | Concrete crushing |

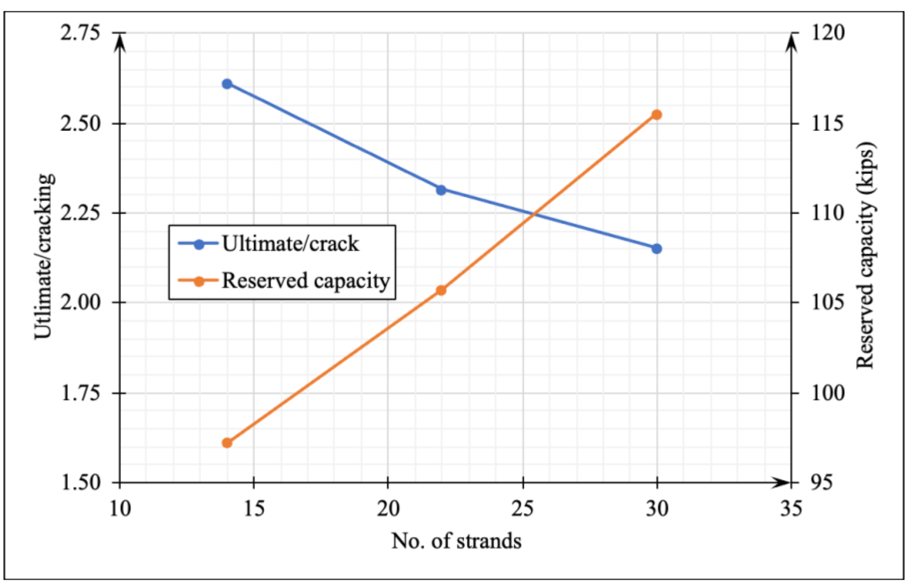


**Figure 6-11. Ultimate/cracking load and reserve capacity vs. the number of strands**

## 6.5.2 Strain at top of concrete topping

Foil type strain gauges were installed on the top surface of the concrete at mid span. These gauges provided concrete strain measurements to help adjust the analytical models to predict the flexural behavior of the member. Strain vs. load data for the specimens is provided in Figures 6-12 through 6-15. All FSBs had strain measurements on the top surfaces that exceeded 3000 microstrain, on the gauges located 2 ft south of the midsection of the member, except for FSB-4 on which strain measurements exceeded 3000 microstrain at 2 ft north of midsection. Figure 6-16 illustrates the failure of the specimens due to crushing of concrete.

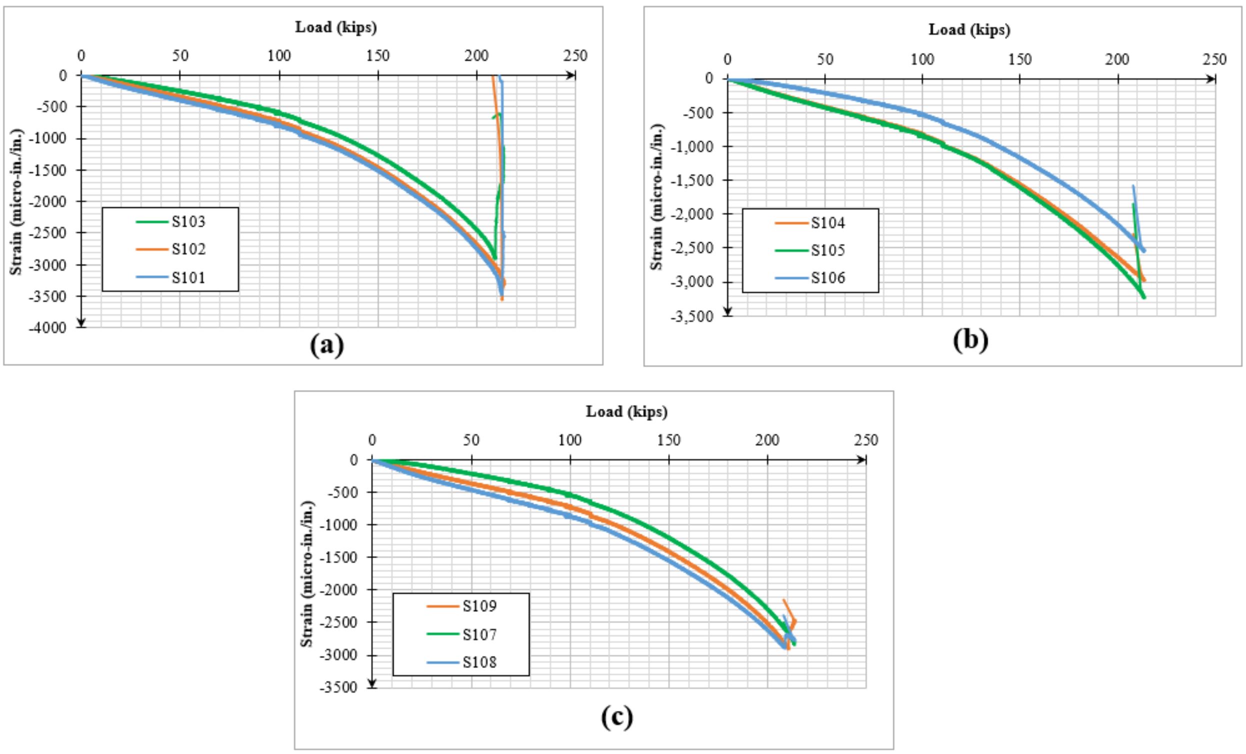


**Figure 6-12. Top surface concrete strain in FSB-1**

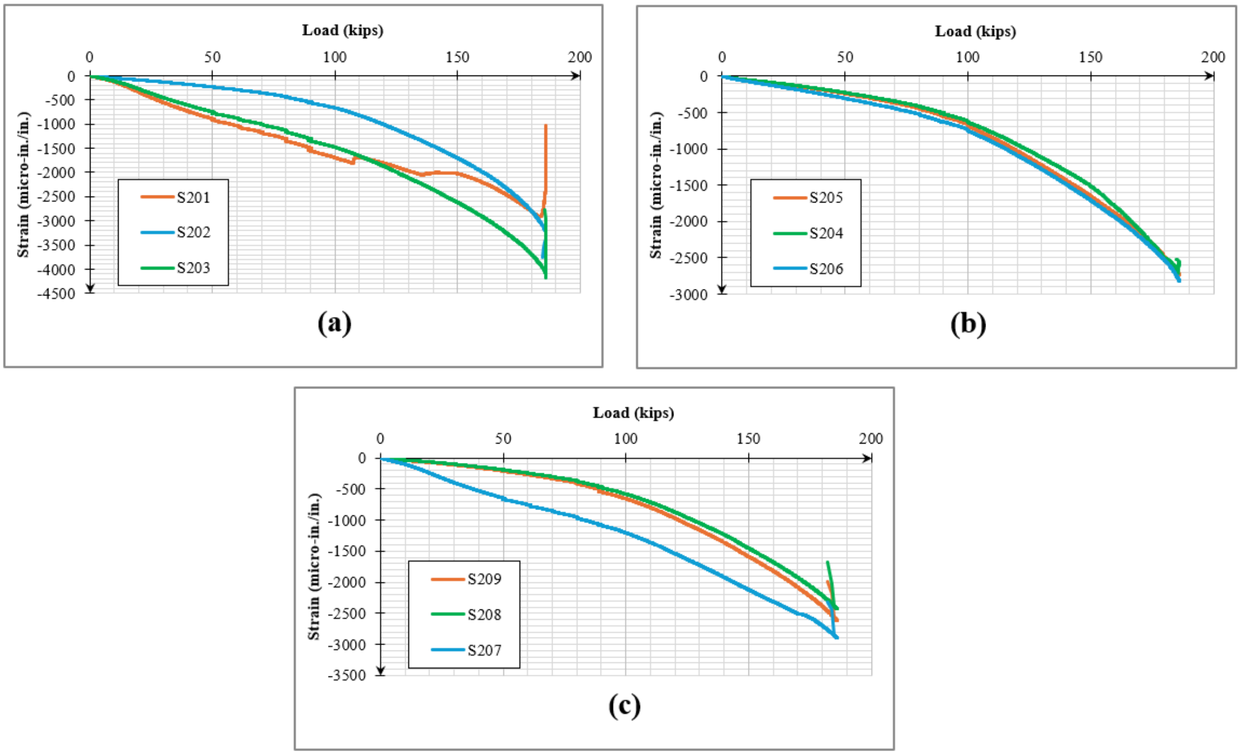


**Figure 6-13. Top surface concrete strain in FSB-2**

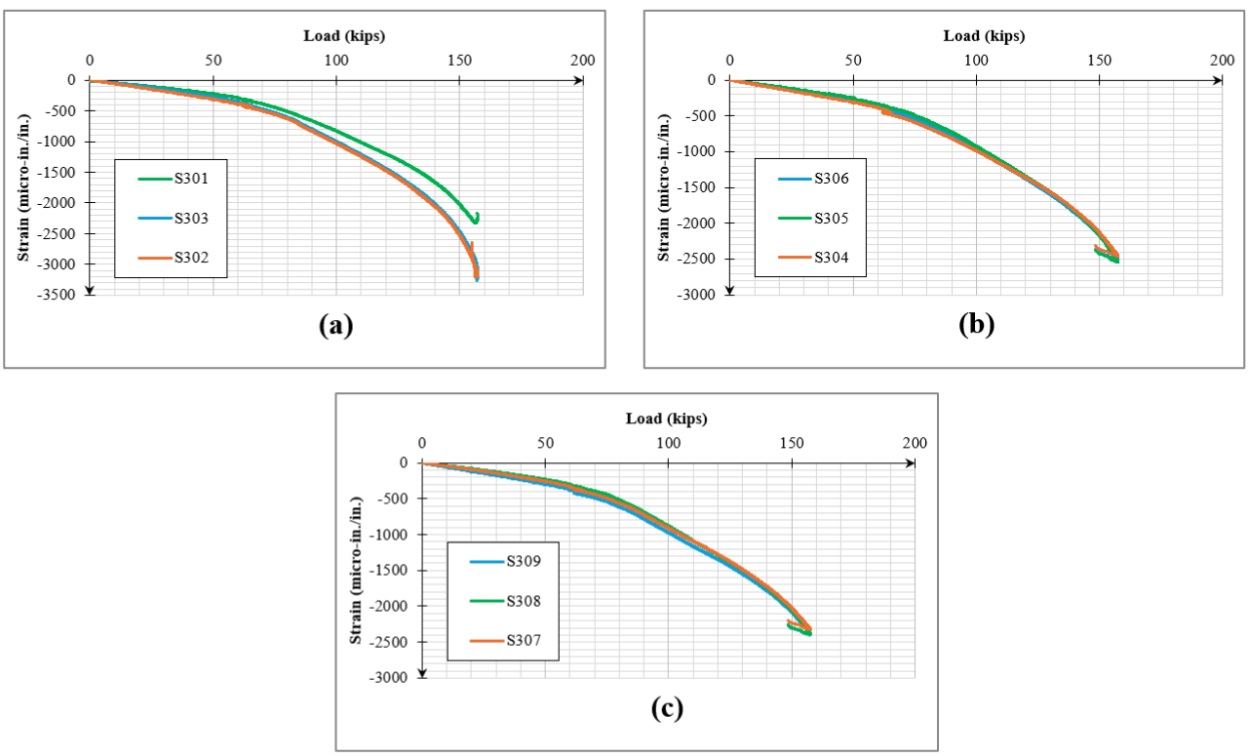


**Figure 6-14. Top surface concrete strain in FSB-3**

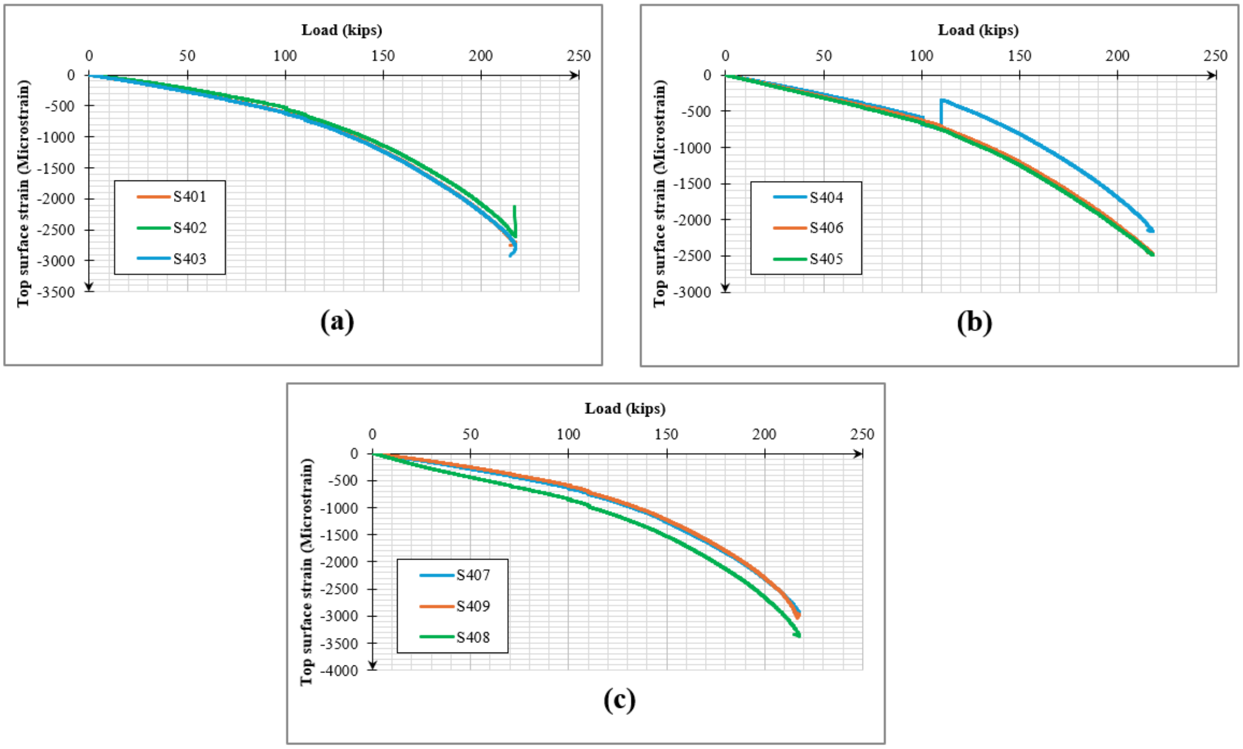


**Figure 6-15. Top surface concrete strain in FSB-4**

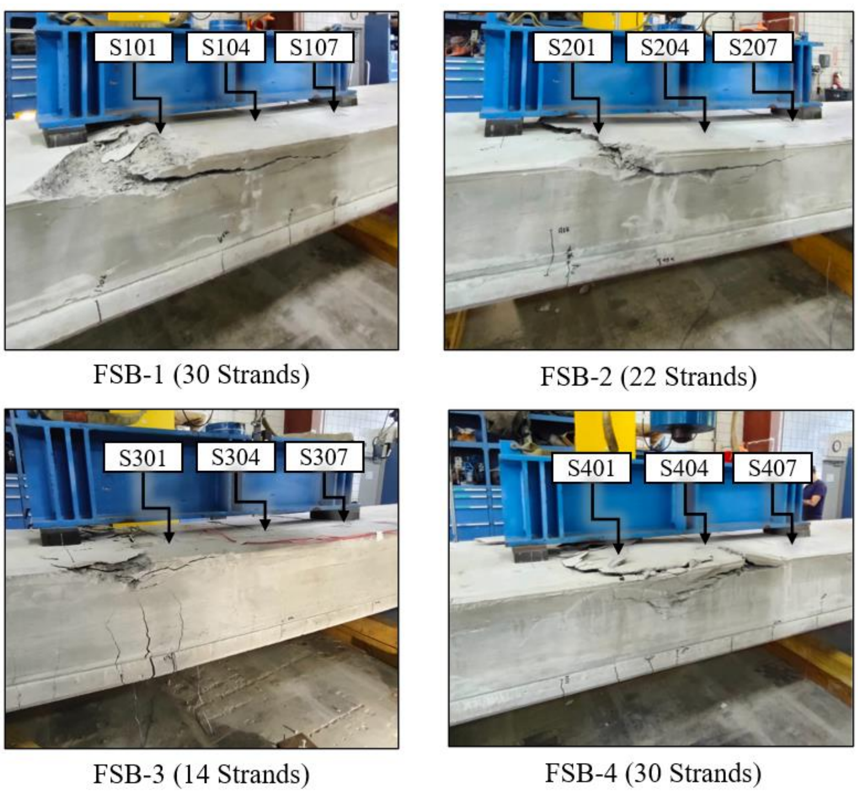


**Figure 6-16. Failure type and foil type strain gauges on top surface**

### 6.5.3 Deflection

Deflection is a parameter of the serviceability of a bridge. Deflection beyond the crack limits is a measure of a member's ductility. As described previously, 12 LDT gauges (Figure 6-4) were used to measure deflection during the entire test. At cracking and ultimate loads, the deflection measurements along the length are provided in Figures 6-17 to 6-20 for all specimens.

Compared to the other specimens, FSB-3 had the least number of strands and failed with the largest deflection, 6.9 in. However, it had the smallest deflection at cracking load. FSB-1 and FSB-4, which had the largest number of strands, failed at the lowest deflection (5.444 in. and 5.097 in., respectively). FSB-2 failed at an average deflection of 5.817 in.

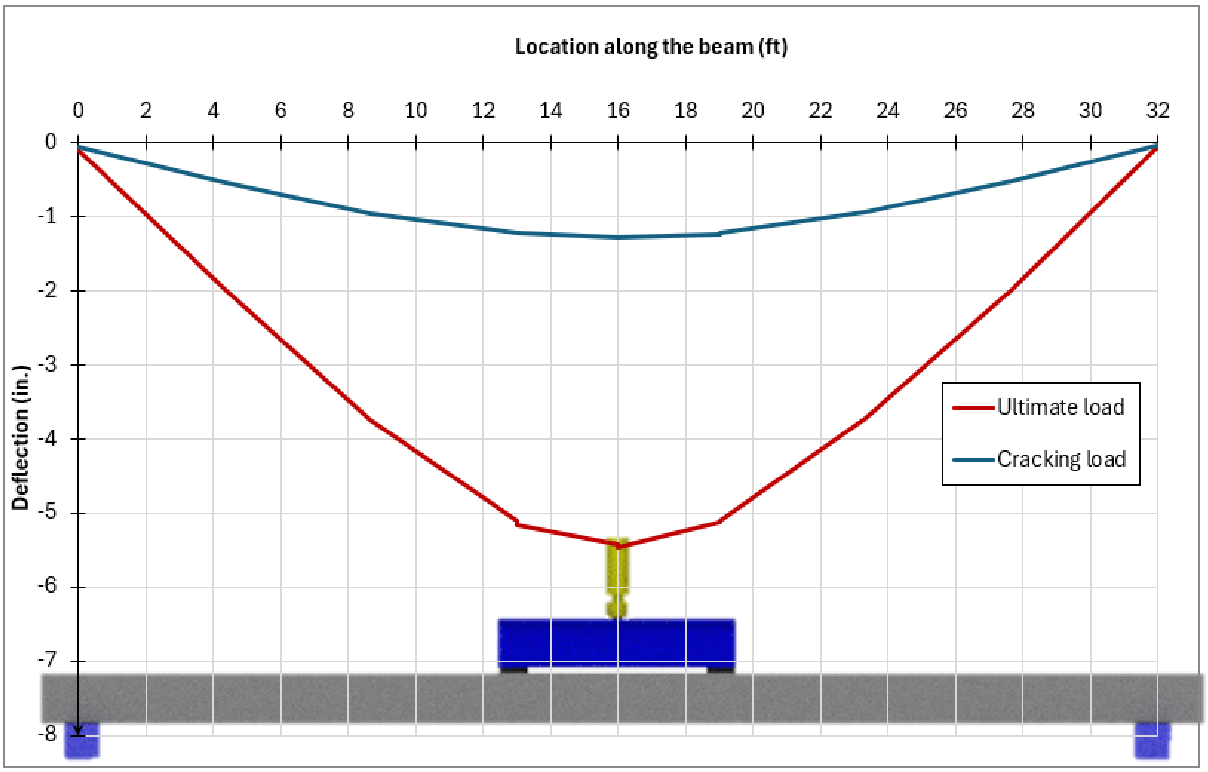


**Figure 6-17. Deflection of FSB-1**

### 6.5.4 Slippage

During the flexural tests, slip gauge measurements were recorded. The data showed that there was negligible slippage in all gauges during all tests, as shown in Figure 6-21.

### 6.5.5 Failure mode

The members were tested in two (2) loading cycles. The first cycle was until observation of the first cracks, and then the specimens were fully unloaded. The second cycle commenced after strain gauges were installed next to the cracks; loading continued until failure. All specimens failed by crushing of concrete at the top surface; Figure 6-16 and Table 6-9 summarized the loads and deflections at cracking and ultimate.

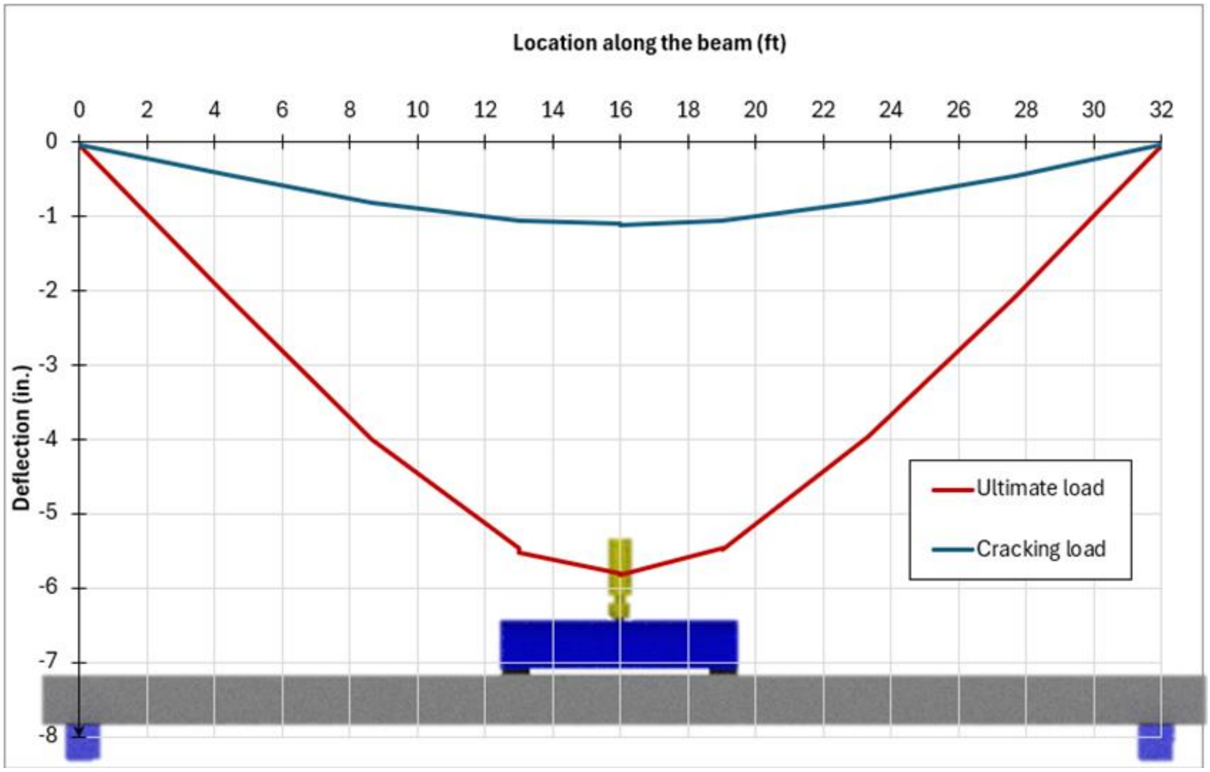

**Figure 6-18. Deflection of FSB-2**

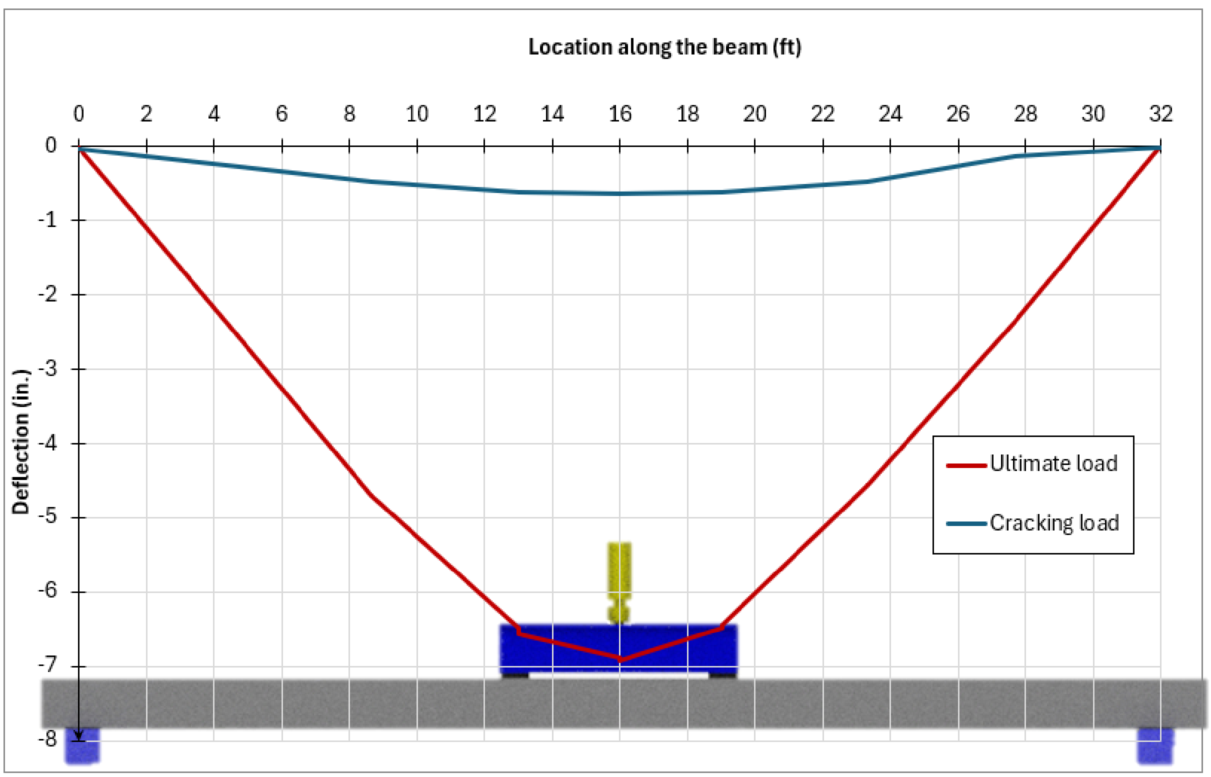

**Figure 6-19. Deflection of FSB-3**

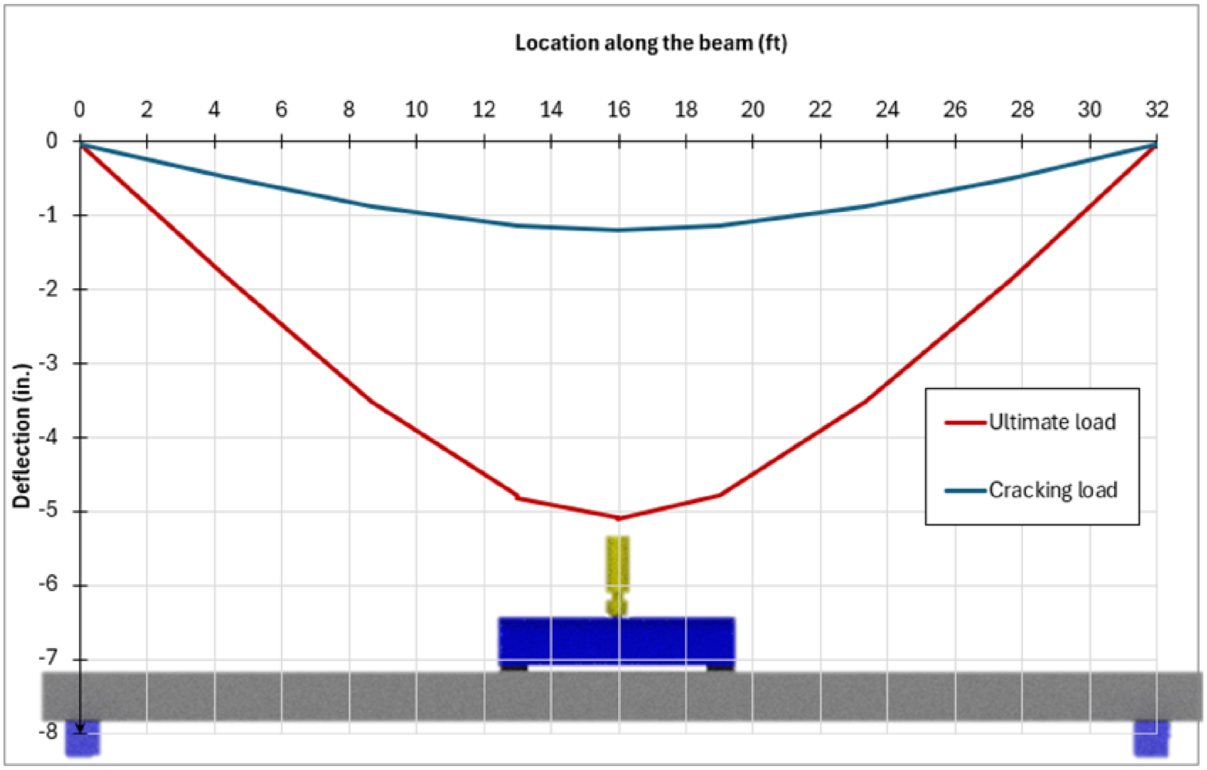


Figure 6-20. Deflection of FSB-4

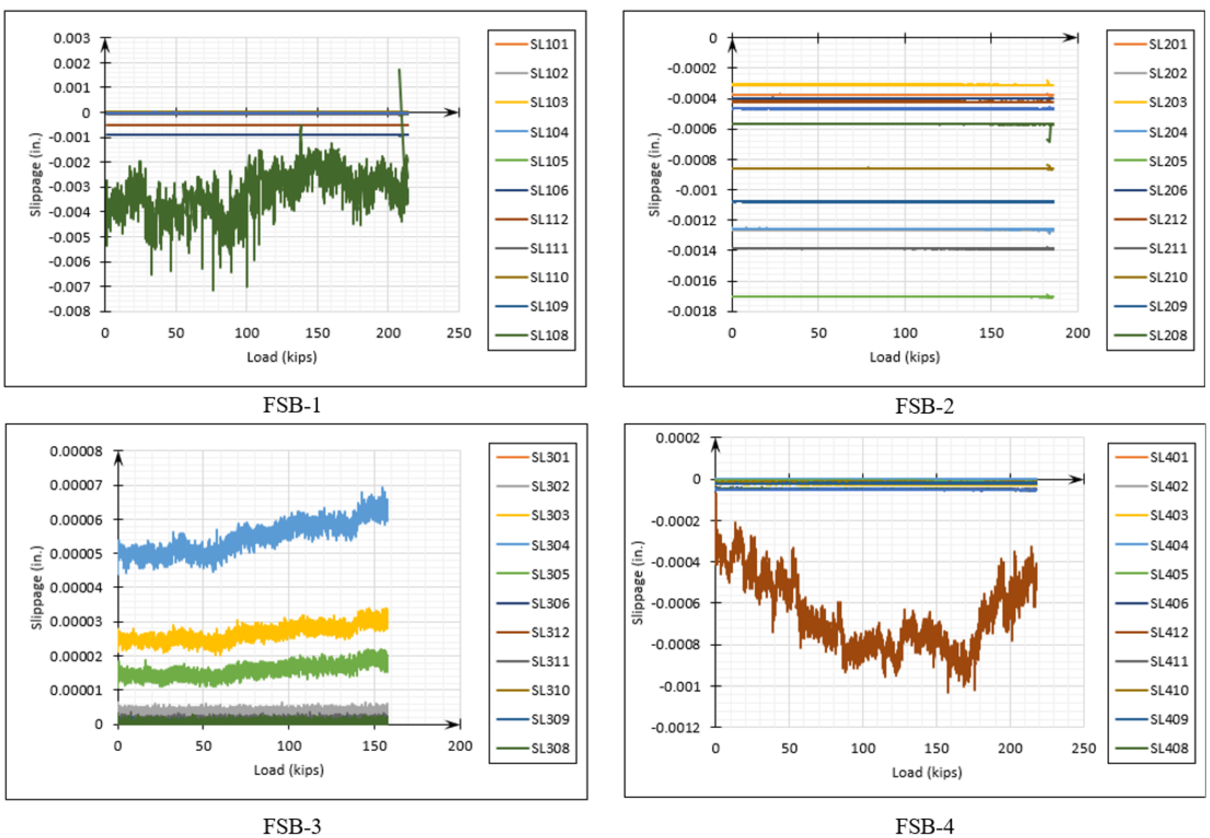


FSB-1

FSB-2

FSB-3

FSB-4

Figure 6-21. Slippage vs. the applied load

After the flexural tests, the crushed regions on the tops of the specimens were investigated. For FSB-1, FSB-2, and FSB-4, the concrete crushing at the top propagated down to the topping reinforcement (Figure 6-22). However, for FSB-3, there was one large crack that propagated to the strands (Figures 6-22 and 6-23), and all HSSS strands except the debonded strands had ruptured. The rupture apparently occurred immediately after the top concrete crushed.

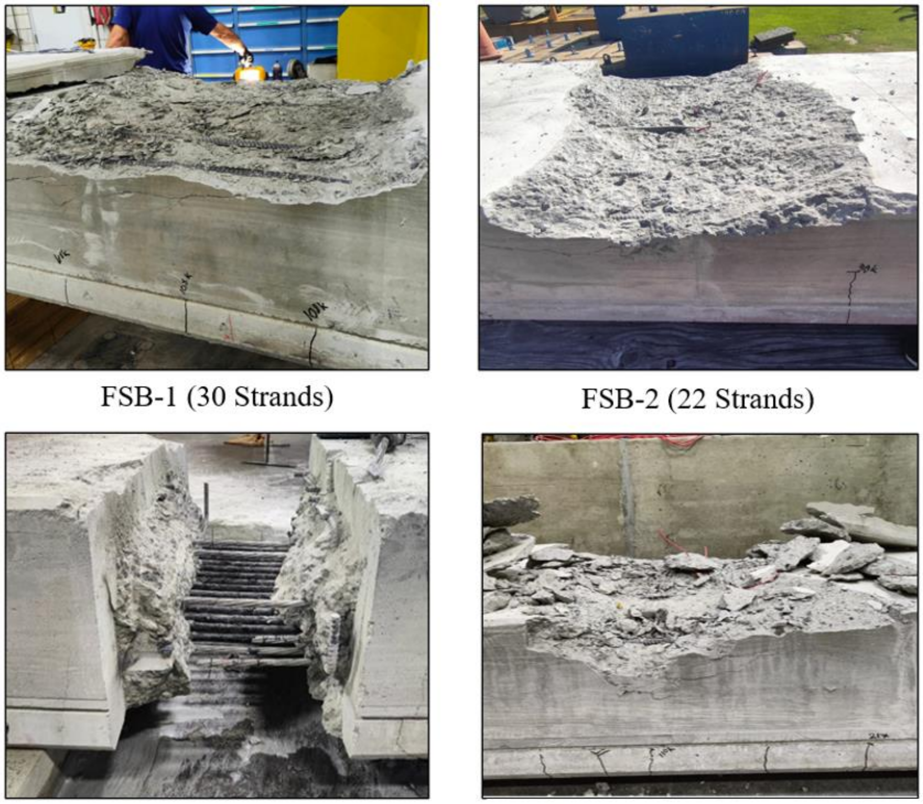

FSB-1 (30 Strands) FSB-2 (22 Strands)

FSB-3 (14 Strands) FSB-4 (30 Strands)

**Figure 6-22. Investigation of FSBs after the flexural tests**


**Figure 6-23. Failure sequence of FSB-3**

## 6.6 Summary

This chapter presented details of the flexural test setup and results for four (4) FSB specimen tests. The flexural tests were conducted using a four-point bending setup, ensuring a constant-moment region where theoretical strand stress could be determined. Instrumentation provided included strain gauges, LDT sensors, and slip gauges to measure various parameters such as strain, deflection, and strand slippage.

The prestress losses in high-strength stainless steel strands were analyzed using AASHTO LRFD Bridge Design Specifications and VWSG measurements. Instantaneous and long-term losses, including elastic shortening, shrinkage, creep, and relaxation, were calculated and compared. The decompression method using strain gauge measurements near cracks was utilized to further validate the VWSG measurements. Both methods measured similar losses.

During the flexural tests, all specimens were loaded to failure. The failure modes primarily involved crushing of concrete at the top fiber. FSB-3, which had the smallest number of strands, uniquely failed with a rupture of strands following concrete crushing at the top. Load-deflection relationships revealed that specimens with more strands exhibited lower ultimate deflections, whereas FSB-3 showed the largest deflection at ultimate load despite its lowest deflection at cracking load.

Strain measurements at the top surface indicated that all specimens reached significant strain levels, leading to concrete crushing near the specimen's midsection. Detailed data on deflection, strain, and slippage were documented, highlighting the specimens' behavior under load.

This chapter concluded with a summary of the key findings from the flexural tests, including the load-deflection characteristics, failure modes, and the effectiveness of the prestress loss measurements. Figures and tables provided throughout the chapter illustrate the test setups, instrumentation, and results, offering a comprehensive overview of the experimental procedures and results.

# CHAPTER 7 – ANALYTICAL MODELS

## 7.1 Introduction

This chapter documents the analytical models that were used to validate the experimental data. It starts with a flexural response model, followed by a detensioning model.

## 7.2 Flexural response model

To predict flexural response, the analytical model must incorporate geometry, material, and equilibrium conditions. These conditions are discussed, and the model is further explained in the following sections.

### 7.2.1 Compatibility conditions

The fundamental assumption for strain compatibility is that plane sections remain plane; this is based on the classical Euler-Bernoulli beam theory. Accordingly, the strain distribution along the section's depth is linear and can be predicted using only two parameters: for example, strain at a certain location and the neutral axis depth. An additional assumption for compatibility is perfect bond between the concrete and reinforcing strands, such that the strands are assumed to strain the same amount as the immediately surrounding concrete in response to load.

### 7.2.2 Equilibrium condition

The equilibrium conditions require that the sum of internal forces within a section must balance the externally applied forces. In mathematical terms, this means that the integration of the internal stress distributions must result in stress resultants (axial force, shear force, and bending moment) that are equal and opposite to the external loads. This principle ensures that the section is in a state of equilibrium, allowing prediction of axial, shear, and normal stresses under various loading conditions.

### 7.2.3 Material

The prediction of material behavior is based on its stress-strain relationship. This study considers two primary materials: concrete and stainless steel strands. Each material's behavior is characterized by specific models that account for their unique stress-strain relationships and other mechanical properties.

#### 7.2.3.1 Concrete

Concrete behaves differently under compression than tension. The concrete model for both is based on the work of Collins and Mitchell (1991). The Collins and Mitchell model characterizes the nonlinear stress-strain behavior of concrete under compression. Key parameters in this model include the initial modulus of elasticity, peak stress, and the strain at peak stress. The model can be expressed with the following equation:

$$\frac{f_c}{f_c'} = \frac{n\left(\frac{\epsilon_{cf}}{\epsilon_c'}\right)}{n-1+\left(\frac{\epsilon_{cf}}{\epsilon_c'}\right)^{nk}} \qquad \text{(Eq. 7.1)}$$

The variable $f_c'$ is the compressive strength of the concrete, $\epsilon_c'$ is strain at the compressive strength of the concrete, $\epsilon_{cf}$ is the strain at a point on the curve, and $n$ is a curve-fitting factor related to the concrete strength that is calculated using the following expression:

$$n = 0.8 + \frac{f_c'}{2500} \qquad \text{(Eq. 7.2)}$$

and where $k$ is the decay factor that is obtained as follows:

$$k = \begin{cases} 1 & if\ \epsilon_{cf} < \epsilon_c' \\ 0.67 + \frac{f_c'}{9000} & if\ \epsilon_{cf} \geq \epsilon_c' \end{cases} \qquad \text{(Eq. 7.3)}$$

The strain at peak compressive strength, $\epsilon_c'$, and the stiffness of concrete, Ec, are found with the following equations:

$$E_c = 40{,}000\sqrt{f_c'(psi)} + 1{,}000{,}000 \qquad \text{(Eq. 7.4)}$$

$$\epsilon_c' = \frac{f_c'}{E_c}\frac{n}{n-1} \qquad \text{(Eq. 7.5)}$$

#### 7.2.3.2 Stainless steel strands

A model for the stress-strain relationship for stainless steel strands was previously discussed in Chapter 4. The equation and calibrated parameters are as follows:

$$\sigma = \varepsilon \times 24{,}400\left\{0.058 + \frac{1-0.058}{[1+(97.5\varepsilon)^{5.72}]^{1/5.72}}\right\} \qquad \text{(Eq. 7.6)}$$

### 7.2.4 Analytical model

The analytical model predicted the flexural response by employing the compatibility and equilibrium conditions with the material model to find strain and stress distributions on the section. Then, the load-deflection relationship was found using the classical moment-area method. It was then compared to the experimental data. This process involved the following steps:

1. The cross section is discretized to strips with depth of 0.2 in. and a width equal to that of the section.
2. A value of strain is set. For each strain being analyzed, a neutral axis depth is assumed.
3. Strain distribution is found based on the strain compatibility conditions.
4. The strains are converted to stresses using material models.

5. The stresses are converted to forces and checked for equilibrium.
6. If no equilibrium is found, the model will return to step 2, and another iteration is conducted for a revised neutral axis assumption until equilibrium is found.
7. When equilibrium is found, the moment for each strip is calculated, and the sum of the moments is calculated. This becomes the moment corresponding to the strain set in step 2.
8. The curvature is found by dividing the neutral axis depth by the strain.
9. Moment vs. curvature is plotted. The moment-area method is used to create load-deflection curves. The curves are compared to experimental data.

### 7.2.5 Validation of flexural response

The data validation was performed by comparing the experimental data with the model predictions. Figures 7-1 to 7-4 show validation for the flexural response of each specimen.

The model predicts the cracking load and deflection with accuracy of 97% and 90%, respectively (Figure 7-5). However, the model underestimates the members' stiffness beyond the crack limit, and as a result the ultimate load is underestimated (Figure 7-6). Deflection is mostly overestimated as illustrated in Table 7-1, which compares results obtained from the prediction model with the experimental data. Table 7-2 shows the accuracy of the model. Further improvements on the model will be incorporated in Chapter 8.

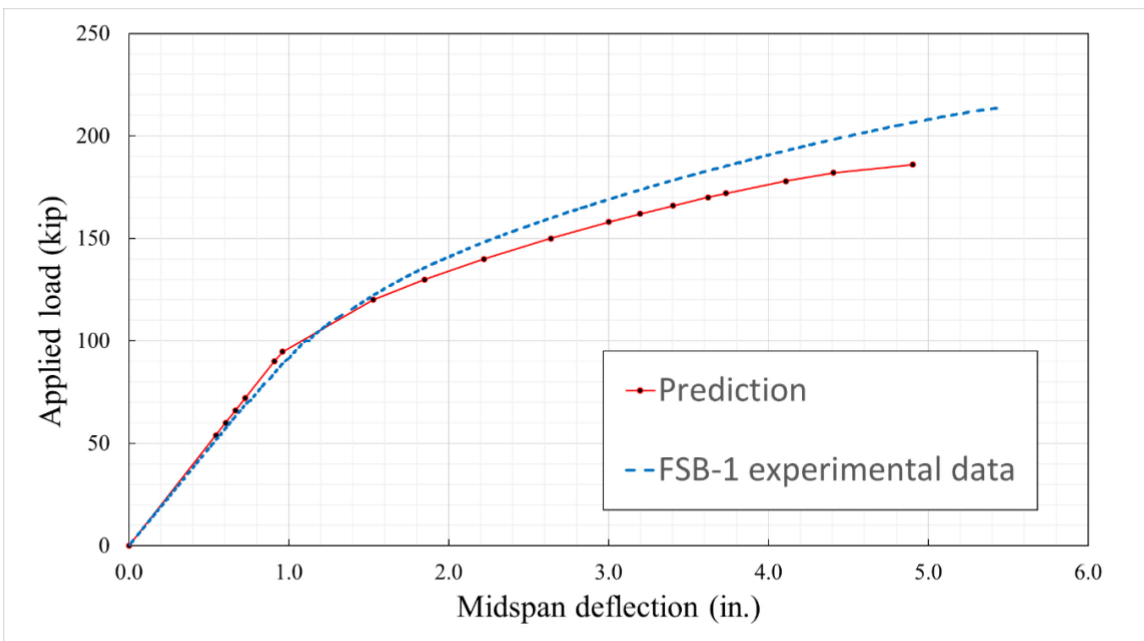


**Figure 7-1. Load-deflection curve, experimental vs. prediction for FSB-1**

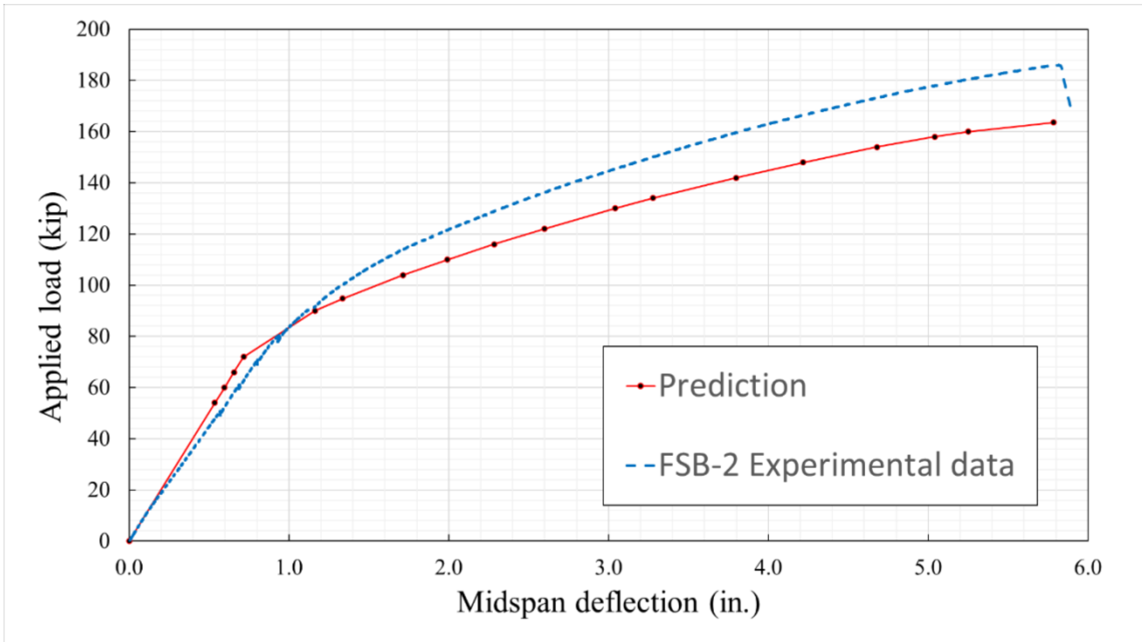


**Figure 7-2. Load-deflection curve, experimental vs. prediction for FSB-2**

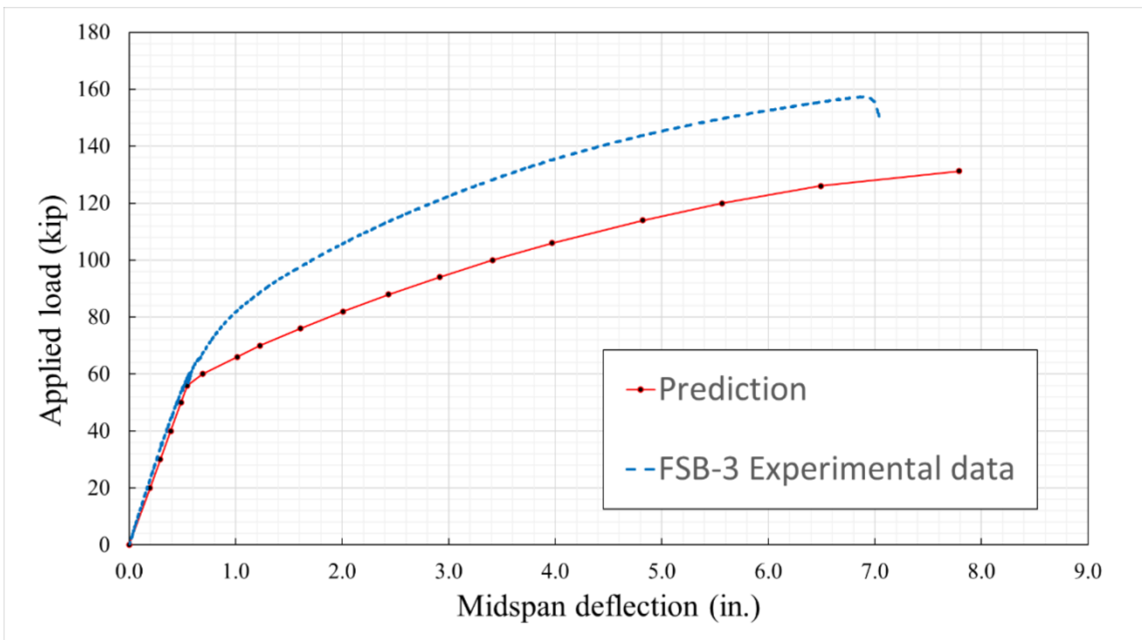


**Figure 7-3. Load-deflection curve, experimental vs. prediction for FSB-3**

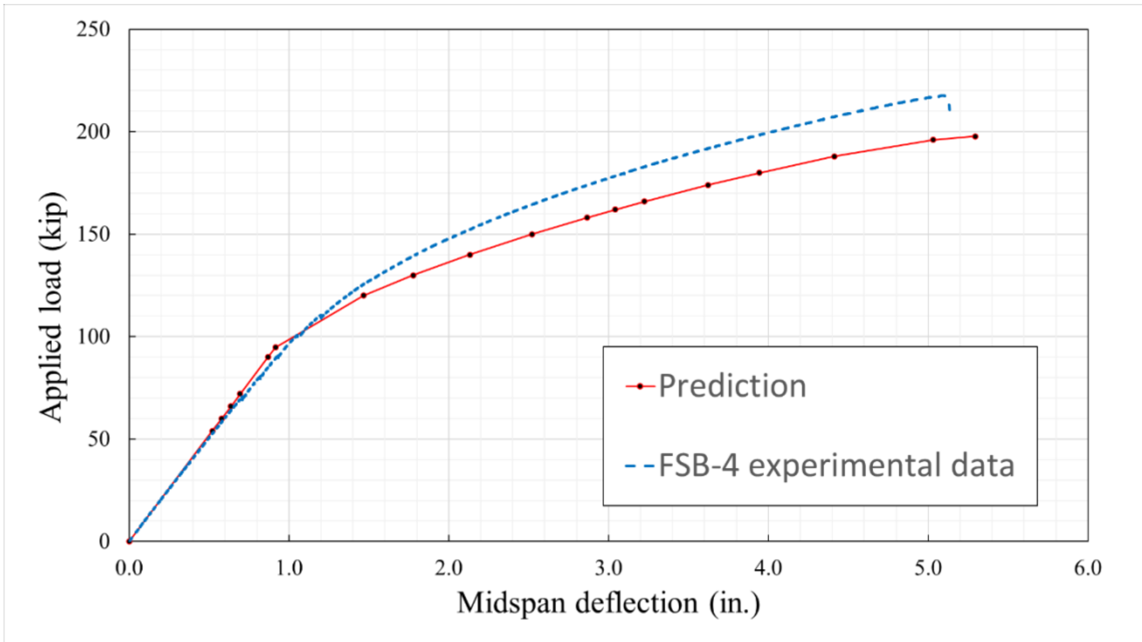

**Figure 7-4. Load-deflection curve, experimental vs. prediction for FSB-4**

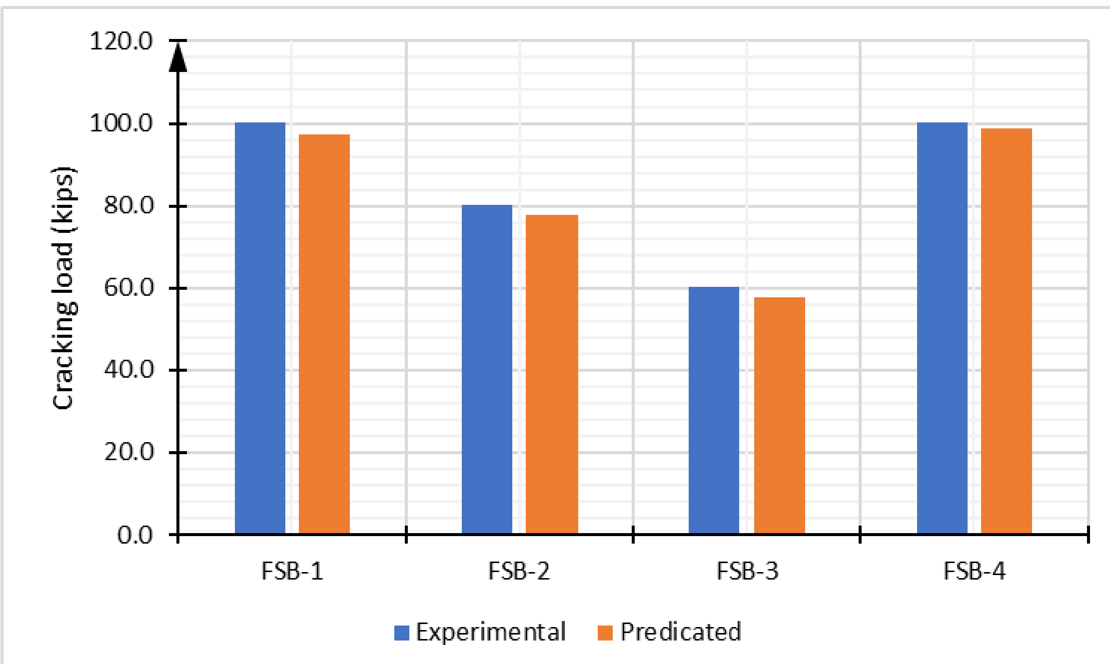

**Figure 7-5. Cracking load, experimental compared to predicted**

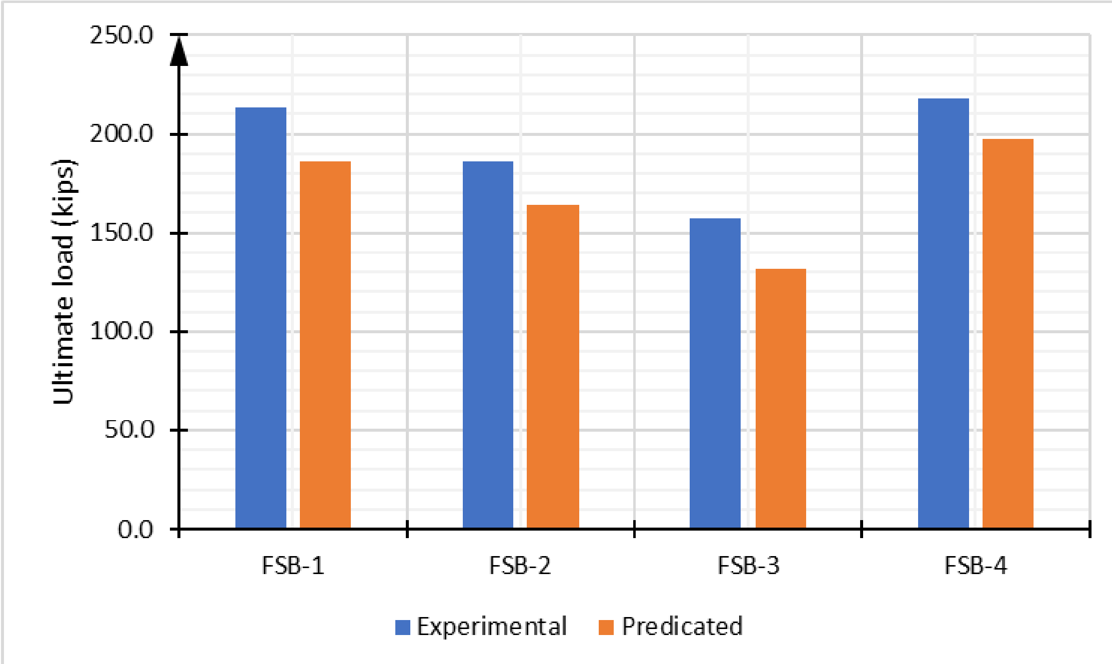


**Figure 7-6. Ultimate load, experimental compared to predicted**

**Table 7-1. Comparison of measured vs. predicted flexural response results**

| Specimen | Measured cracking load (kips) | Predicted cracking load (kips) | Measured crack deflection (in.) | Predicted crack deflection (in.) | Measured ultimate load (kips) | Predicted ultimate load (kips) | Measured ultimate deflection (in.) | Predicted ultimate deflection (in.) |
|---|---|---|---|---|---|---|---|---|
| **FSB-1** | 100.0 | 97.3 | 1.103 | 0.989 | 213.6 | 186.0 | 5.444 | 4.902 |
| **FSB-2** | 80.3 | 77.7 | 0.932 | 0.774 | 186.1 | 163.8 | 5.817 | 5.831 |
| **FSB-3** | 60.3 | 57.6 | 0.580 | 0.561 | 157.5 | 131.4 | 6.900 | 7.839 |
| **FSB-4** | 100.3 | 98.7 | 1.045 | 0.953 | 217.7 | 197.8 | 5.097 | 5.294 |

**Table 7-2. Accuracy of prediction model**

| Specimen ID | Cracking load | Crack deflection | Ultimate load | Ultimate deflection |
|---|---|---|---|---|
| **FSB-1** | 97.3% | 89.6% | 87.1% | 90.0% |
| **FSB-2** | 96.7% | 83.1% | 88.0% | 100.2% |
| **FSB-3*** | 95.5% | 96.8% | 83.4% | 113.6% |
| **FSB-4** | 98.4% | 91.2% | 90.8% | 103.9% |
| **Average** | 97.0% | 90.2% | 87.3% | 101.9% |

* These values were obtained using the intended number of strands for FSB-3 (14 strands). Refer to section 8.3 for further discussion.

## 7.3 Mathematical detensioning model

The mathematical detensioning model will be based on Mirza and Tawfik (1978). The model assumes linear-elastic behavior for the strands during the detensioning process. However, the strands behave linearly until the elastic limit, and then they start behaving nonlinearly. In this chapter, the model is similar to Mirza and Tawfik's linear-elastic model, and it also assumes symmetry on the mid-length of the casting bed. In Chapter 8, the model is extended to include nonlinearity of the stainless steel strands and without the assumption of symmetry.

Mirza and Tawfik (1978) models the members and the free strands along the casting bed as linear springs (Figure 7-7). The linear springs have an axial stiffness equal to the stiffness of the members and strands. When a strand is cut at an end, a force will be applied at that end equivalent to the force in the strand. The system will have a horizontal displacement due to this force. These displacements are converted to strains, then stress, and forces that add to existing strains, stresses, and forces in the uncut strands. Consequently, the next strand cut will cause a higher force in the uncut strands. The stiffness matrix that was used in the analysis is illustrated in Figure 7-8.

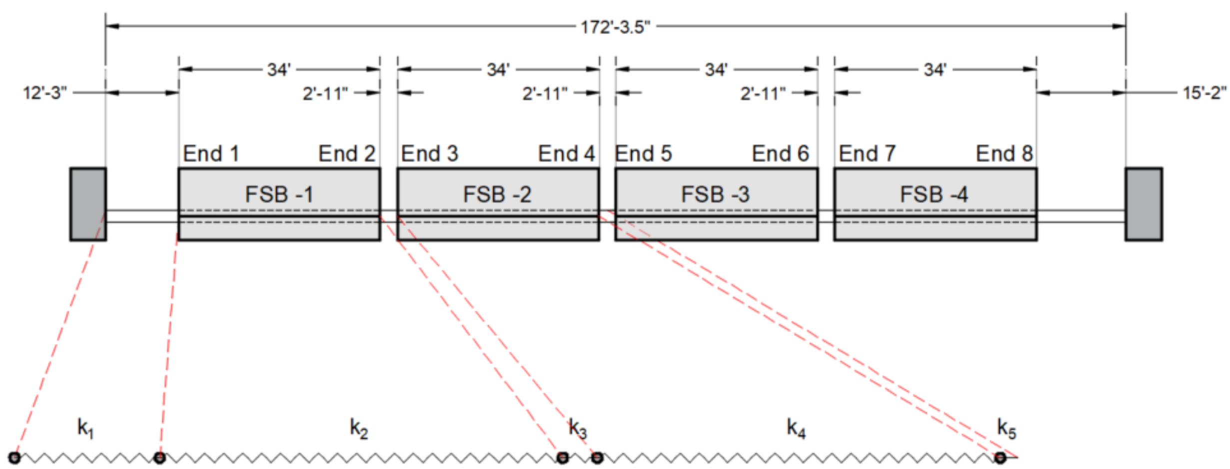


**Figure 7-7. Analytical model for detensioning near End 1**

$$
[\mathrm{K}] = \begin{bmatrix} k_1 + k_2 & -k_2 & 0 & 0 & 0 & 0 \\ -k_2 & k_2 + k_3 & -k_2 & 0 & 0 & 0 \\ 0 & -k_2 & k_3 + k_4 & -k_2 & 0 & 0 \\ 0 & 0 & -k_2 & k_4 + k_5 & -k_2 & 0 \\ 0 & 0 & 0 & -k_2 & k_5 + k_6 & -k_2 \\ 0 & 0 & 0 & 0 & -k_2 & k_6 \end{bmatrix}
$$

$$
[\mathrm{F}] = \begin{bmatrix} f_1 \\ f_2 \\ f_3 \\ f_4 \\ f_5 \\ f_6 \end{bmatrix} \qquad [\mathrm{u}] = \begin{bmatrix} u_1 \\ u_2 \\ u_3 \\ u_4 \\ u_5 \\ u_6 \end{bmatrix} = [\mathrm{K}]^{-1}[\mathrm{F}]
$$

**Figure 7-8. Mathematical model used for analysis**

The analytical model was validated with experimental data as shown in Figures 7-9 and 7-10. The model correlates well with End 1 and End 8 results at the beginning of the curves. However, as more strands are cut, the model starts to underestimate the strains because it only accounts for elastic strains. Improving the model to account for plastic strains is reported in Chapter 8.

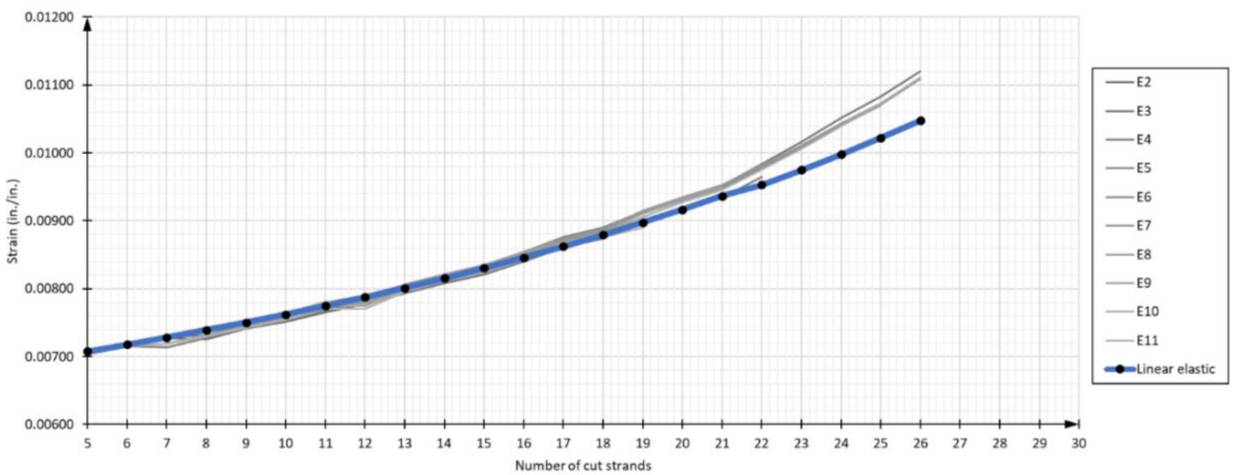


**Figure 7-9. Model results compared to experimental data at End 1**

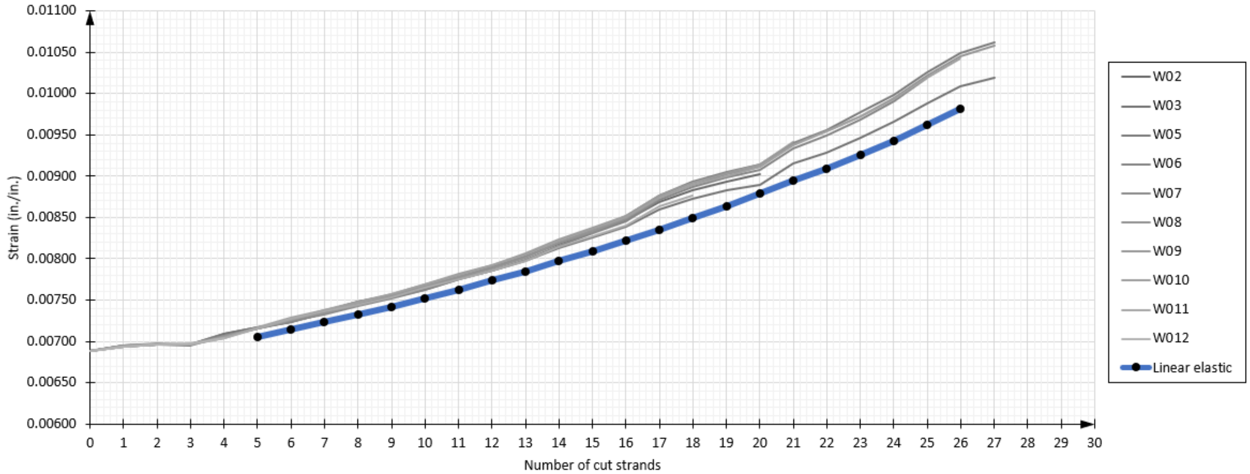


**Figure 7-10. Model results compared to experimental data at End 8**

# CHAPTER 8 – FLEXURAL RESPONSE

## 8.1 Introduction

Structural members are designed to resist the applied loads determined by structural analysis. The analysis must incorporate the member's geometry, material properties, and sectional characteristics. Sectional analysis involves determining the forces, strains, and stresses at critical cross-sections and using these values to characterize the member's performance. A fundamental assumption in this process is that plane sections remain plane during deformation, which is a reasonable assumption if the member is not considered a deep beam or the section is not in an area of discontinuity. This helps simplify the calculations while predicting the behavior fairly accurately. Sectional analysis primarily involves two steps for reinforced concrete and prestressed concrete members. The first step assumes the structural member behaves linearly and elastically and is uncracked. The second step addresses the member's behavior once cracked, characterized by non-linear plastic behavior.

For a beam, the linearly-elastic section means the strains vary linearly along the depth. At this stage, a further assumption of a perfect bond between concrete and reinforcement is made. This assumption results in equal strains in the concrete and reinforcement at a given depth. In simply-supported beams subjected to positive bending moment, the fibers above the neutral axis initially experience linear-elastic stresses. However, after the strain in the outermost top fiber exceeds the concrete's elastic limit, the stress distribution becomes non-linear until the top fiber reaches the ultimate strain of concrete, which is approximately 0.003, at which point the beam fails due to concrete crushing.

Cracking begins when the outermost bottom fiber reaches the concrete's tensile strength, causing cracks to initiate and propagate along the section. At the location of the cracks, the concrete is unable to transfer stress across cracks, and the reinforcement completely transfers the forces. However, the concrete can still transfer tensile stress in the regions between the cracks. This phenomenon of transferring tensile stresses in the uncracked concrete between the cracks is called tension stiffening. This phenomenon is usually ignored, but tension stiffening might considerably affect the flexural stiffness and deflection of shallow beams with wide webs.

The sectional analysis was the basis for the flexural evaluation in Chapter 7. Sectional analysis is done by incrementing strain, starting with zero moment and repeating until the cracking moment is reached, and then repeating until the ultimate moment is reached. The moment-curvature relationship, obtained from the sectional analysis, is vital for flexural response evaluation and determination of the load-deflection relationship. The moment-area analysis method may be used to generate the load-deflection relationship.

This chapter will start with a literature review about tension stiffening. Then, the model in Chapter 7 will be modified to account for this phenomenon, and it will be validated against the experimental data again.

## 8.2 Tension stiffening

The main parameter that affects tension stiffening is the bond between the reinforcement and the concrete that is due to chemical bonds, friction, and mechanical interlock (Polak and Blackwell, 1998). A parameter to estimate tension stiffening is the modulus of rupture of the concrete, $f_r$, which is typically a function of the concrete compressive strength, $f_c{}'$, and can be estimated using the AASHTO LRFD equation (AASHTO, 2024):

$$f_r = 0.24\sqrt{f_c'} \qquad \text{(Eq. 8.1)}$$

However, the equation overestimates the cracking strength for high-strength concrete; a better relationship is suggested by Bentz (2000):

$$f_r = 0.45\,(f_c')^{0.4} \qquad \text{(Eq. 8.2)}$$

Early tension stiffening studies were on the behavior of steel reinforcement embedded in concrete and tested against the bare bar (Collins and Mitchell, 1991). During the investigation of reinforced concrete panels, Vecchio and Collins (1986) found that concrete between cracks can resist tensile stresses and suggested the following formula:

$$f_{ct} = \frac{f_r}{1+\sqrt{200\,\varepsilon_{ct}}} \qquad \text{(Eq. 8.3)}$$

where
$f_{ct}$ = tensile stress in the cracked concrete zone, and
$\varepsilon_{ct}$ = tensile strain in the cracked concrete zone.

A similar model was suggested by Collins and Mitchell (1991) as follows:

$$f_{ct} = \frac{f_r}{1+\sqrt{500\,\varepsilon_{ct}}} \qquad \text{(Eq. 8.4)}$$

This relationship is adjusted with factors that account for variations in reinforcement bonding. In a similar manner, Bentz (2000) suggested a tension stiffening model that accounts for the effect of different parameters, such as the area of effectively bonded concrete to the bars and the diameter of the bars. The suggested expression is:

$$f_{ct} = \frac{f_r}{1+\sqrt{3.6\,m\,\varepsilon_{ct}}} \qquad \text{(Eq. 8.5)}$$

$$m = \frac{A_{ct}}{\sum d_p \pi} \qquad \text{(Eq. 8.6)}$$

where $A_{ct}$ is area of concrete under tension effectively bonded to the strands, and $d_p$ is the diameter of the strands.

However, a study by Gar et al. (2012) based on a closed-form solution for moment-curvature relationship demonstrated that the tension stiffening effect has negligible influence in fully prestressed concrete members. Furthermore, the authors found that increasing the effective prestressing force reduces the impact of tension stiffening on the section's moment capacity. The outcome of the study was also verified with another study conducted by Lee (2022), which used a different approach called reverse engineering. Despite these findings, the study focused primarily on members with significant depth, leaving a gap in understanding how tension stiffening affects shallow beams where the width exceeds the depth. This suggests a need for further investigation into the behavior of shallow members, which may exhibit different performance.

## 8.3 Modified analytical model

The previous model, presented in Chapter 7, for the FSBs did not accurately predict the load-deformation behavior, particularly in the post-cracking region, where it underestimated the member's stiffness as shown in Figure 8-1. The authors suggest that this difference is due to tension stiffening. Although previous research investigations suggest a negligible effect on fully prestressed members, for the FSB sections, the amount of tension force provided by the uncracked concrete between cracks is larger due to the width of the FSBs being greater compared to the beam flange width of typical prestressed concrete members.

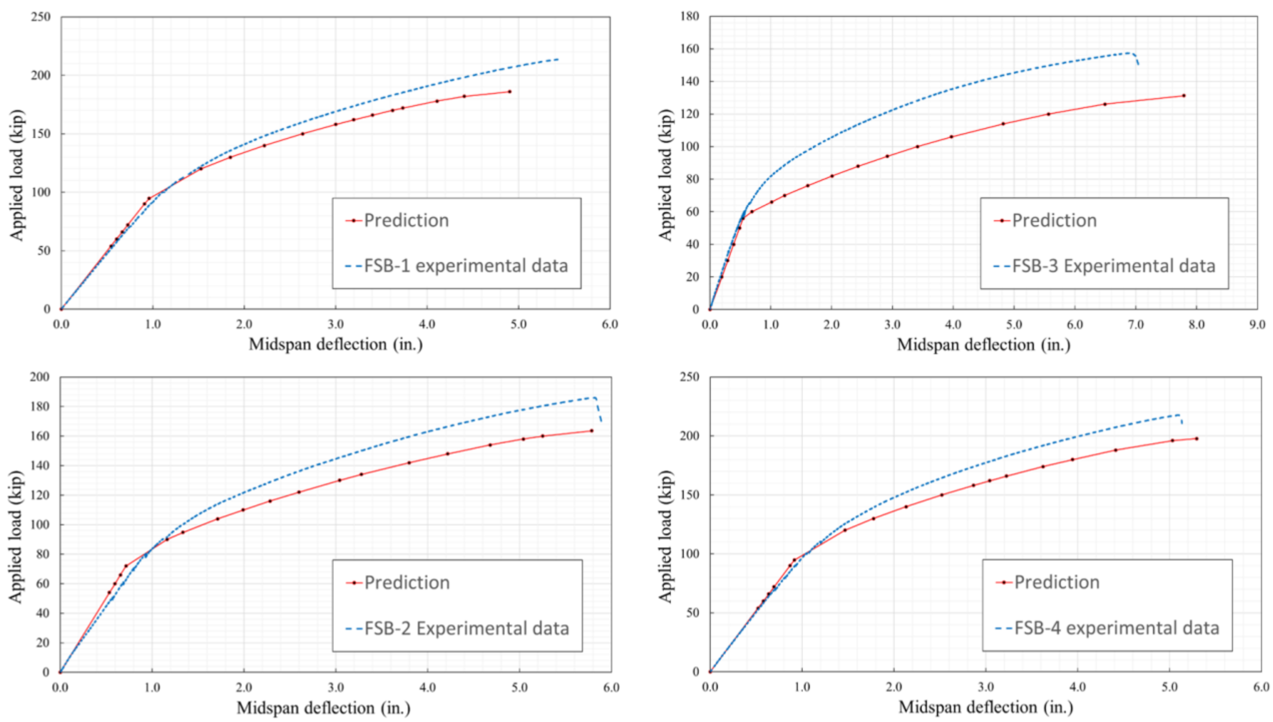


**Figure 8-1. Experimental vs. prediction without considering tension stiffening**

The prediction model was modified to account for tension stiffening. Several models were tested, and the Bentz (2000) model gave the best accuracy and therefore was chosen. The model changes with the number of strands and the cross section. The effective area of cracked concrete under tension was calculated following Collins and Mitchell (1991). The model more accurately predicted the cracking load, cracking deflection, ultimate load, ultimate deflection and load-deflection behavior, as shown in Table 8-1, Table 8-2, and Figure 8-2.

**Table 8-1. Comparison of the modified model vs. experimental data**

| Specimen | Measured cracking load (kips) | Predicted cracking load (kips) | Measured crack deflection (in.) | Predicted crack deflection (in.) | Measured ultimate load (kips) | Predicted ultimate load (kips) | Measured ultimate deflection (in.) | Predicted ultimate deflection (in.) |
|---|---|---|---|---|---|---|---|---|
| **FSB-1** | 100.0 | 99.9 | 1.103 | 1.036 | 213.6 | 193.2 | 5.444 | 4.687 |
| **FSB-2** | 80.3 | 82.7 | 0.932 | 0.844 | 186.1 | 174.0 | 5.817 | 5.389 |
| **FSB-3** | 60.3 | 62.1 | 0.580 | 0.622 | 157.5 | 138.9 | 6.900 | 7.111 |
| **FSB-4** | 100.3 | 100.9 | 1.045 | 1.001 | 217.7 | 206.3 | 5.097 | 5.080 |

**Table 8-2. Improved accuracy of the model**

| Specimen ID | Cracking load | Crack deflection | Ultimate load | Ultimate deflection |
|---|---|---|---|---|
| **FSB-1** | 99.9% | 94.0% | 90.4% | 86.1% |
| **FSB-2** | 103.0% | 90.6% | 93.5% | 92.6% |
| **FSB-3** | 103.0% * | 107.3% * | 88.2% * | 103.1% * |
| **FSB-4** | 100.7% | 95.8% | 94.8% | 99.7% |
| **Average** | 101.6% | 96.9% | 91.7% | 95.4% |

* These values were obtained using the intended number of strands for FSB-3 (14 strands). Refer to section 8.3 for further discussion.

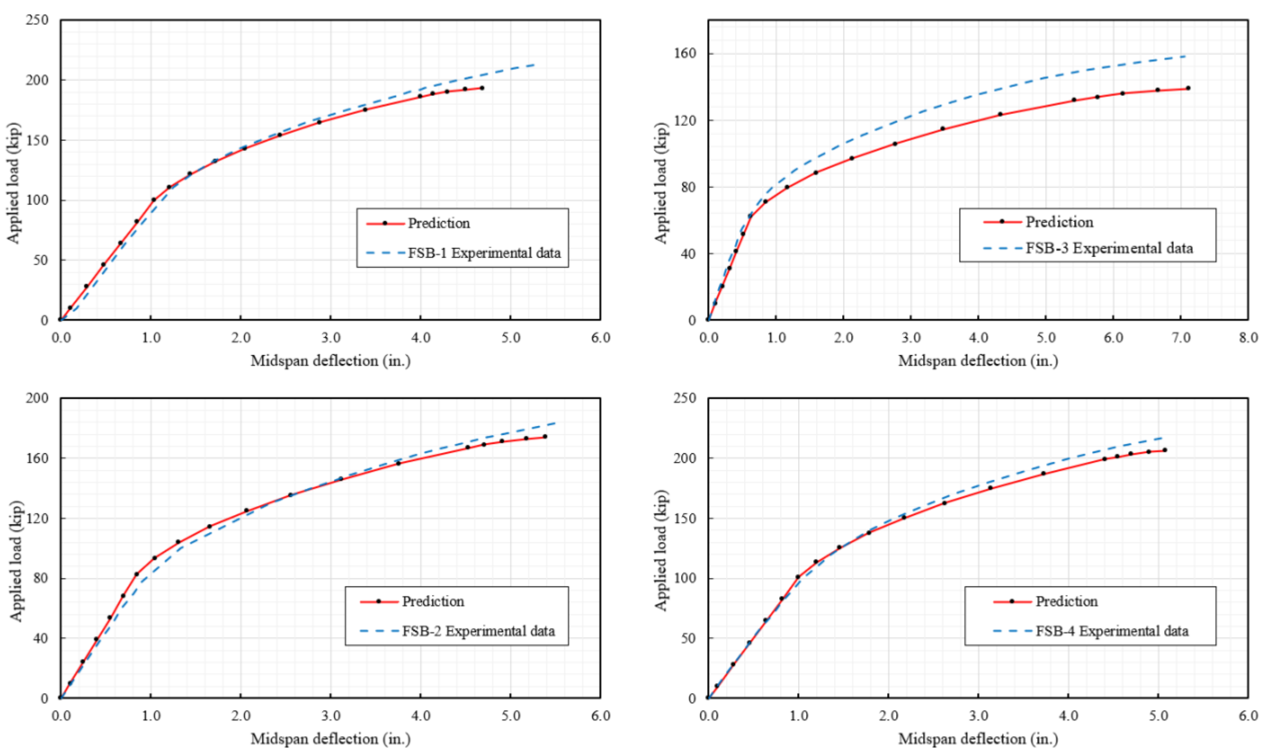


**Figure 8-2. Load vs. deflection (experimental and prediction) including tension stiffening**

In the case of FSB-3, the prediction model underestimates the member's behavior. The source of the additional strength may be due to unintentional bonding of some unbonded strands. FSB-3 had 14 fully bonded and 16 fully debonded strands, the highest number of debonded strands among the four specimens. When the number of bonded strands was modified from 14 to 16 in the model, and the behavior matched the experimental results well, as shown in Figure 8-3.

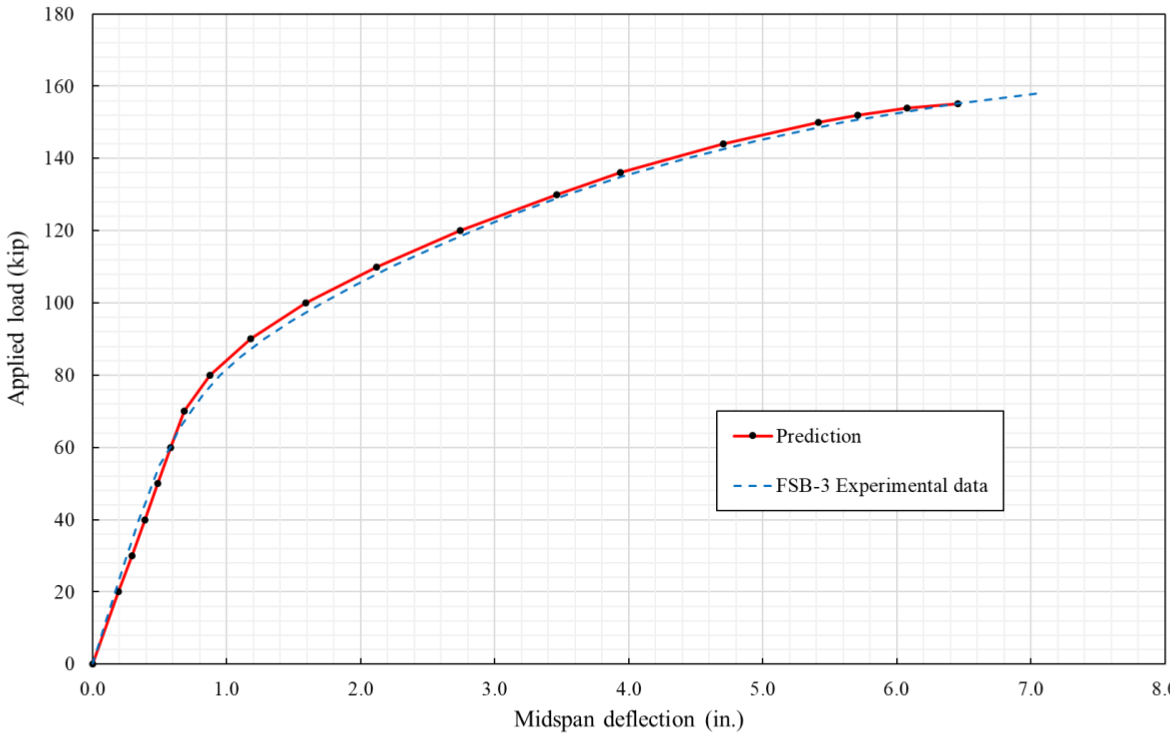


**Figure 8-3. FSB-3 prediction model better matches experimental data with 16 bonded strands assumed instead of 14**

## 8.4 Conclusion

Previous research with various approaches to predict load-deformation response has found that tension stiffening has negligible effects on flexural response. That is true in cases where beams have a small web thickness compared to the depth. However, in the case of an FSB, where width is significant compared to depth, the amount of tension stress due to tension stiffening seems to have a noticeable effect on the behavior. Different tension stiffening models were analyzed, and the most suitable one produces a more accurate flexural model to predict the load-deformation response of the FSBs. In the following chapter, this improved model is used in parametric studies to evaluate the flexural behavior of FSBs.

# CHAPTER 9 – FLEXURAL BEHAVIOR OF FLORIDA SLAB BEAMS

## 9.1 Introduction

This chapter investigates the flexural behavior of FSBs prestressed with stainless steel strands. The experimental program was used to validate an analytical model that can generate load-deflection and moment-curvature relationships, which are tools to assess a member's ductility. Several approaches from previous studies were used to evaluate ductility. The ductility evaluation is based on material type. For example, in the case of carbon steel reinforcement that has a distinct yield point, ductility was evaluated as the ratio of ultimate to yield deflection, rotation, or curvature. For FRP reinforcement, which behaves linear-elastically without any distinct yield point, ductility has been evaluated with deformability indices. The deformability indices were defined mostly in energy terms or as the ratio of the ultimate moment to the cracking moment (Zou, 2003). Similarly, Mast (1992) suggests only evaluation of ductility as ultimate curvature to curvature at service moment.

The ductility evaluation presented in this chapter was conducted by a parametric study that included nine (9) sections using 254 different strand configurations. This chapter also compares the performance of FSBs designed with stainless steel strands vs. those designed with carbon steel strands to establish the design recommendations. The focus was on the main design requirements that control the designs for both cases. Nine (9) different standard FSB design sections were used for nine (9) different design cases that were repeated for both stainless steel strands and carbon steel strands. To fully capture the behavior for each design case, the number of strands considered ranged from the maximum number to the minimum required for the controlling design requirements.

## 9.2 Literature review

Ductility is a critical design requirement in both reinforced and prestressed concrete. According to AASHTO LRFD, it is described as the ability of the member to exhibit noticeable inelastic deformation and cracking prior to failure (AASHTO, 2024). Ductile members are desired because they provide warning of imminent failure before collapsing. Therefore, they provide time to either rehabilitate the member or take it out of service. AASHTO LRFD addresses ductile behavior of members by a requirement for a minimum net tensile strain. If this minimum is not met, the capacity must be reduced by use of a lower resistance factor. These requirements were established based on previous research on reinforced and prestressed concrete members (Thompson and Park, 1980; Park and Falconer, 1983; Naaman et al., 1986; and Cohn and Riva, 1991). The research started with studying the parameters affecting ductility (Thompson and Park, 1980), studying the effect of each parameter (Naaman et al., 1986), establishing unified requirements for ductility (Skogman et al., 1988; Cohn and Riva, 1991), and establishing the basis for current AASHTO and ACI requirements for ductility (Mast, 1992).

Thompson and Park (1980) studied key parameters that influence the ductility of prestressed concrete members. They investigated the percentage and distribution of longitudinal reinforcement, transverse reinforcement, and concrete cover. They measured the ductility based on moment-curvature relationships driven from idealized stress-strain relationships for concrete and steel reinforcement. The outcome of this study was that the ratio of the depth of the concrete compression block to the total depth of the section should be limited to a value equal to or less than 0.2. However, the paper only studied rectangular sections and aimed to provide requirements for seismic design.

Following that, Naaman et al. (1986) evaluated ductility in prestressed concrete members and suggested modifications to the previous ductility investigations (Thompson and Park, 1980). The moment-curvature relationships were used as a basis to measure ductility. The study used the definition of curvature ductility as the ratio of ultimate curvature to yield curvature. The ultimate curvature was defined as the curvature at the maximum moment, while the yield curvature was defined as the intersection of the first linear part of the moment curvature with the final part of the moment curvature that was approximated as linear. With this approach, the effects of different variables were examined, including the effective prestress force, the ratio of partial prestressing, confinement, high-strength concrete, and the neutral-axis depth. Besides that, the experimental program included different section shapes, including rectangular, I-section, T-section, and box section. The ductility for all these parameters was analyzed using an independent variable called the reinforcing index, as follows:

$$\omega = \frac{A_p f_p + A_s f_s - A_s' f_s'}{b\ d\ f_c'} \qquad \text{(Eq. 9.1)}$$

where
$A_p$ = total area of prestressing (in$^2$),
$f_p$ = stress level in prestressing strands (ksi),
$A_s$ = total area of mild tension reinforcement (in$^2$),
$f_s$ = stress level in mild tension reinforcement (ksi),
$A_s'$ = total area of mild compression reinforcement (in$^2$),
$f_s'$ = stress level in mild-compression reinforcement (ksi),
$b$ = width of the flange or width of the rectangular section (in.),
$d$ = total depth from top compression fiber to centroid of tensile force (in.), and
$f_c'$ = the compressive strength of concrete member (ksi).

Naaman et al. (1986) concluded that the reinforcing index provided strong correlation to the ratio $c/d$ where $c$ is the depth from the top fiber to the neutral axis, and $d$ is the depth from the compression fiber to the centroid of the tensile force. Furthermore, the study suggests three equations to predict section ductility and plastic rotation that can be used for different design cases. However, this study did not suggest any limiting value for ductility.

Skogman et al. (1988) investigated changing the ductility requirements that were in effect at that time, which were based on limiting the amount of flexural reinforcement to a maximum value. The researchers suggested that the limiting curvature value must be defined to provide a ductile member design. To suggest such a limit, which is preferably a unitless value, a relationship to find the rotation in the plastic hinge formed at the critical section is used. The expression found three important parameters that affect ductility: the depth of the neutral axis, the total depth of the section, and the ultimate strain of the concrete at the top. A limiting rotation value is found when assuming a 0.003 ultimate concrete strain and decompression steel strain level of 0.00585. This limiting value can be established to a maximum limiting value to provide ductile members which was:

$$\frac{c}{h} \geq 0.36 \qquad \text{(Eq. 9.2)}$$

where
$h$ = the total depth of the member (in.).

The study provided simple and rational criteria for ductility requirements in both reinforced and prestressed concrete (Naaman et al., 1986).

Cohn and Riva (1991) conducted a comprehensive study on ductility and the factors affecting it. This study is similar to the study by Naaman et al. (1986); it used realistic models for materials to define the moment-curvature relationship. This study also evaluated ductility using curvature ductility, which is the ratio of the ultimate curvature to the yield curvature. The difference was the yield curvature was identified using a strain increment of 0.2 in prestressing strands from its effective strain. The research concluded that prestressing improves curvature ductility, and the reinforced concrete ductility factors can be used as a conservative estimate of the ductility of prestressed members.

Mast (1992) provided a modification to the ACI code provision to provide a limiting value that helps control ductility. The definition of the tension-controlled section was introduced for ductile members and the compression-controlled section for less ductile members. The limits for tension-controlled and compression-controlled were based on net tensile strain. However, these limits were evaluated based on the mechanical properties of carbon steel strands and rebar. For example, the yield strain for Grade 60 rebar is ($\varepsilon_y = \frac{f_y}{E} = \frac{60}{29{,}000} = 0.0021$). The author suggested a slightly higher limit to account for a wide range of different reinforcement types, including strands. While the tension limit suggests a limit of 0.005, which is beyond the yield strain for Grade 60 rebar, and in the case of the prestressed member, this value would add up to the prestress strain and reach beyond the yield limit of 0.01. Furthermore, it was stated that the strain change at service until ultimate is a better reflection of the amount of deflection and cracking, i.e., a better indication of failure.

The introduction of new reinforcement materials in prestressed concrete required new ductility measurements. Grace and Sayed (1998) evaluated the ductility of members prestressed with CFRP strands. Because CFRP strands have a predominantly linear-elastic behavior, the ratio of ultimate deflection to yield cannot be used to evaluate ductility. The investigation suggests that the ratio of absorbed energy to total energy be used as an alternative measurement to ductility. This measurement is also applicable to other materials. It also provided a design philosophy of members prestressed with CFRP strands based on inelastic deformation in concrete before failure. This means letting the concrete form cracks that absorb the energy. Based on this study, non-conventional reinforcing materials might need special consideration regarding ductility.

Another more recent study by Mast et al. (2008) investigated the design methodology for high-strength steel and suggested special strain limits. The tension-controlled limit was 0.009, and 0.004 for compression-controlled. It also shows that the ductility index is not the only measure for desirable behavior; members with high deformability that do not have a low ductility index can still produce desirable behavior before failure. For that, it suggests a ratio of nominal strength behavior to service load behavior, which is called the deformability ratio.

Furthermore, Abdelrahman et al. (1995) suggested evaluating the ductility for FRP with the ratio of equivalent uncracked deflection or curvature to the ultimate deflection or curvature. More recent research by Mufti et al. (1996) proposed that deformability be calculated as the product of the ratio of ultimate moment to moment at 0.001 strain and the ratio of ultimate curvature to the curvature corresponding to 0.001 strain ratio. Zou (2003) suggests another expression to evaluate the deformability of FRP beams. The expression is the product of the ratio of deflection at the ultimate-to-cracking by moment at the ultimate-to-cracking ratio.

Different approaches evaluated member ductility or deformability based on the material type. The stainless steel strands have different mechanical properties compared to carbon steel strands (Al-Kaimakchi and Rambo-Roddenberry, 2021a) and therefore need special considerations for ductility and deformability.

# 9.3 Ductility evaluation

## 9.3.1 Curvature ductility

Using the moment-curvature relationship based on the flexural model established in the previous chapter, curvature ductility for each type of section is calculated based on the curvature ductility index as follows:

$$\mu_\phi = \frac{\phi_u}{\phi_y} \qquad \text{(Eq. 9.3)}$$

where

$\mu_\phi$ = curvature ductility,

$\phi_u$ = ultimate curvature, and

$\phi_y$ = yield curvature.

The ultimate curvature is calculated as the curvature corresponding to the maximum moment similar to what was implemented in previous studies (Naaman et al., 1986; Cohn and Riva, 1991). Various methods were presented in the literature to find yield curvature; some of those methods define yield curvature as the curvature corresponding to yield strain (e.g., Cohn and Riva, 1991), while other methods defined it as curvature corresponding to 75% of the nominal moment capacity (e.g., Park and Falconer, 1983). For this study, the yield curvature is defined, from the moment-curvature relationship, as the intersection of the linear-elastic part of the curve with the line fit for the final plastic part of the curve – a method used by Naaman et al. (1986) as shown in Figure 9-1.

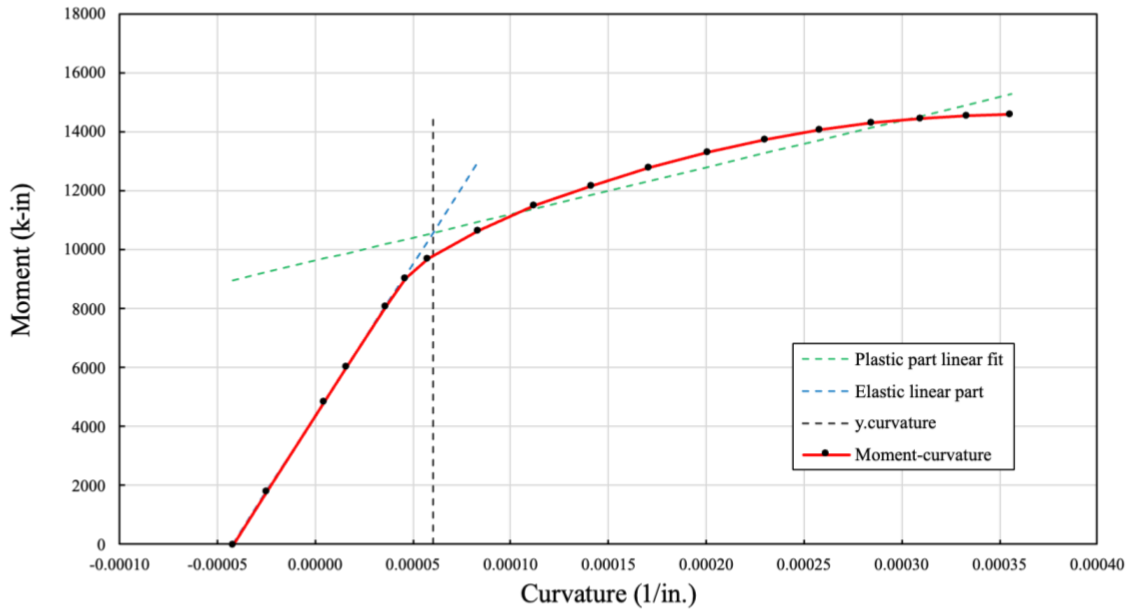


**Figure 9-1. Yield curvature determination**

## 9.3.2 Deflection ductility

The deflection ductility index is defined as the ratio of ultimate deflection to yield deflection (Naaman et al., 1986). These parameters are found from the load-deflection relationship. The ultimate deflection is the deflection at the ultimate load. The yield deflection is found similarly to the case of yield curvature, which is the intersection of the first linear part of the load-deflection curve and the assumed linear final part of the curve, as shown in Figure 9-2.

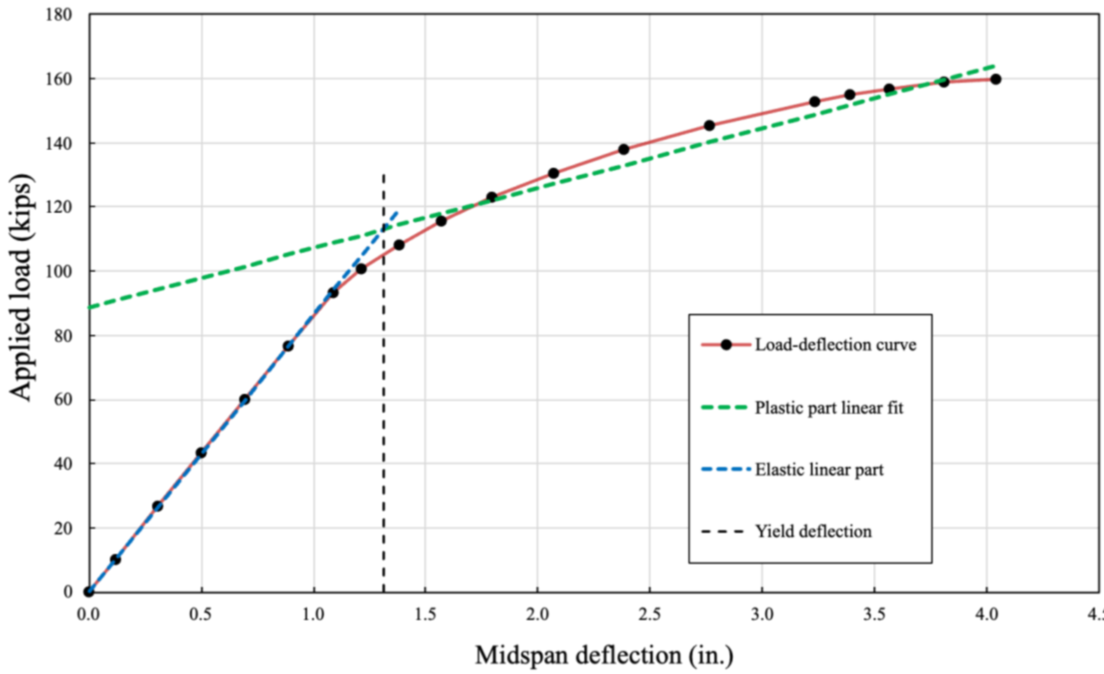


**Figure 9-2. Yield deflection determination**

### 9.3.3 Energy ductility

Ductility can be determined in terms of energy (Naaman and Jeong, 1995), using the following relationship:

$$\mu = \frac{1}{2}\left(\frac{E_{tot}}{E_{el}} + 1\right) \qquad \text{(Eq. 9.4)}$$

where
$E_{tot}$ = total energy represented by the total area under load-deflection curve (ksi), and
$E_{el}$ = the elastic energy (ksi).

The total energy and elastic energy are further illustrated in Figure 9-3.

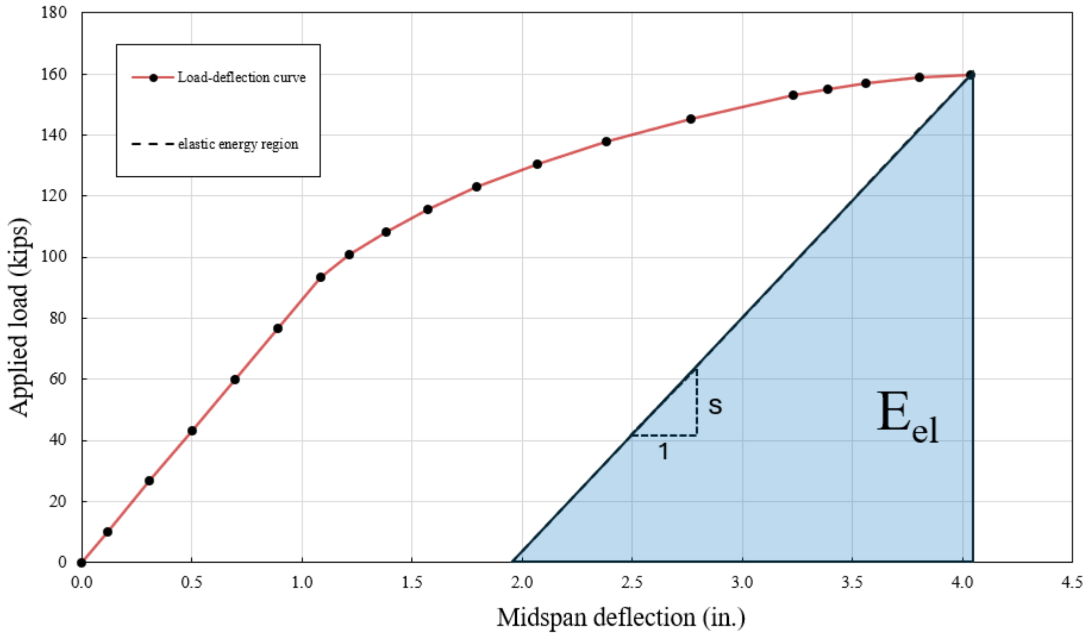


**Figure 9-3. Determination of elastic energy**

## 9.3.4 Deformability index

Deformability indices are mainly used for FRP material where no unique yield point can be observed. Three deformability indices are used in this study.

### 9.3.4.1 Mufti et al. model

The model suggested evaluating the deformability using the following expression (Mufti et al., 1996):

$$\mu_{mufti} = \frac{M_u}{M_{0.001}} \cdot \frac{\varphi_u}{\varphi_{0.001}} \qquad \text{(Eq. 9.5)}$$

where
$M_u$ = ultimate moment (kip-ft),
$M_{0.001}$ = moment at strain level 0.001 (kip-ft),
$\varphi_u$ = ultimate curvature, and
$\varphi_{0.001}$ = curvature at strain level 0.001.

### 9.3.4.2 Zou model

The model by Zou (2003) suggested evaluating the deformability using the following expression:

$$\mu_{zou} = \frac{M_u}{M_{cr}} \cdot \frac{\Delta_u}{\Delta_{cr}} \qquad \text{(Eq. 9.6)}$$

where
$M_{cr}$ = the cracking moment (kip-ft),
$\Delta_u$ = deflection at ultimate (in.), and
$\Delta_{cr}$ = cracking deflection (in.).

### 9.3.4.3 Mast model

The model by Mast et al. (2008) suggests calculating the deformability as the ratio of ultimate curvature to service curvature:

$$\mu_{mast} = \frac{\varphi_u}{\varphi_s} \quad \text{(Eq. 9.7)}$$

where $\varphi_s$ is the curvature at service moment.

### 9.3.4.4 Reserved capacity index

For this report, the authors suggest that ductility be calculated as:

$$\mu_{capacity} = \frac{\varphi_u}{\varphi_{cr}} \quad \text{(Eq. 9.8)}$$

where $\varphi_{cr}$ is the curvature at cracking moment.

## 9.4 Parameters affecting ductility

The parametric study conducted herein included various FSB sections with depths of 12 in., 15 in., and 18 in. Three widths for each section were evaluated: 48 in., 60 in., and the average value of 54 in. The span lengths vary depending on the section capacity. The specified compressive strength of concrete for the beams was 8.5 ksi unless stated otherwise. The topping strength was 4.5 ksi except when studying the effect of its change as a parameter. The pattern of the strands in the section aimed to maximize the depth of the strands' centroid to correspond to the maximum moment capacity and better ductility behavior.

### 9.4.1 Member concrete strength

Generally, during member construction, the contractor guarantees that concrete compressive strength requirements will be met by making mix designs that aim for higher strength. Accordingly, the specimens in this project had higher values of concrete strength than specified. An investigation for the effect of the higher strength was performed. The investigation was done for the FSB12x48 section with two parameters: the FSB concrete compressive strength and the number of strands. FSB concrete compressive strengths of 8.5 ksi, 10 ksi, and 11.5 ksi did not show any noticeable effect on ductility indices as shown in Figure 9-4.

However, if the C-I-P topping concrete strength is higher, the ductility of the member increases noticeably, as shown in Figure 9-5. There is no concern if the specified concrete strength is exceeded; the member would behave more ductile than the design. The increased ductility is the result of the compression force being closer to the top of the section, which increases curvature or, in other words, ductility.

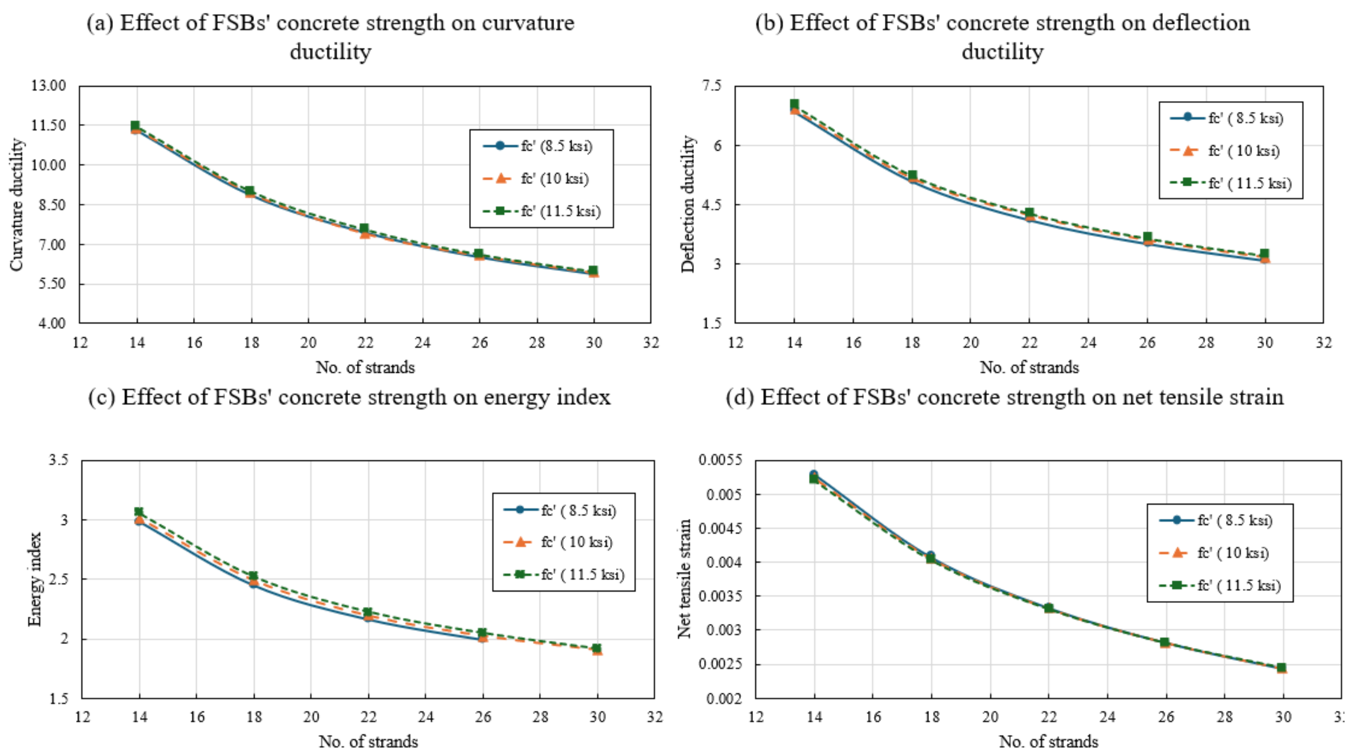


**Figure 9-4. Effect of concrete strength on ductility indices**

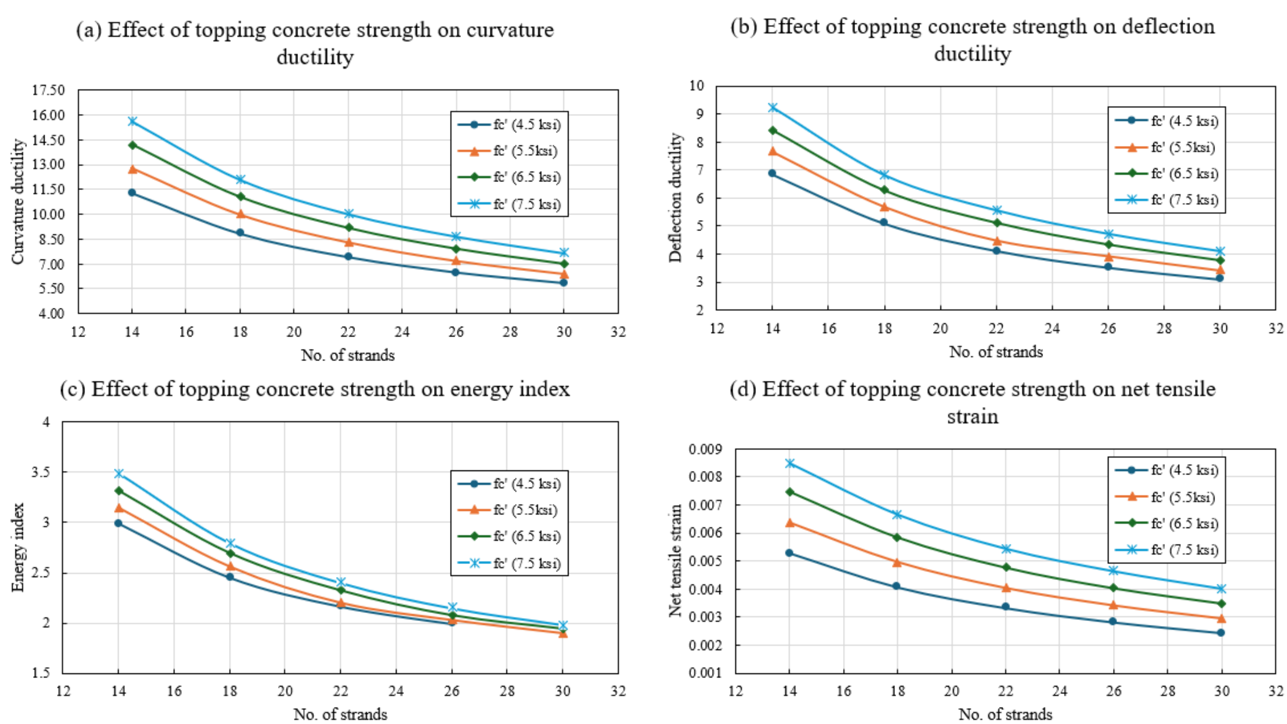


**Figure 9-5. Effect of C-I-P topping strength on ductility indices**

## 9.4.2 Effect of span length

The span length can affect the deflection and cracking. Increasing the span will increase the deflection. However, indices that are derived in terms of curvature are not affected by changes in span length, as shown in Figure 9-6. If the indices are derived in terms of a load-deflection relationship, they will be affected by changes in span length (Figure 9-7).

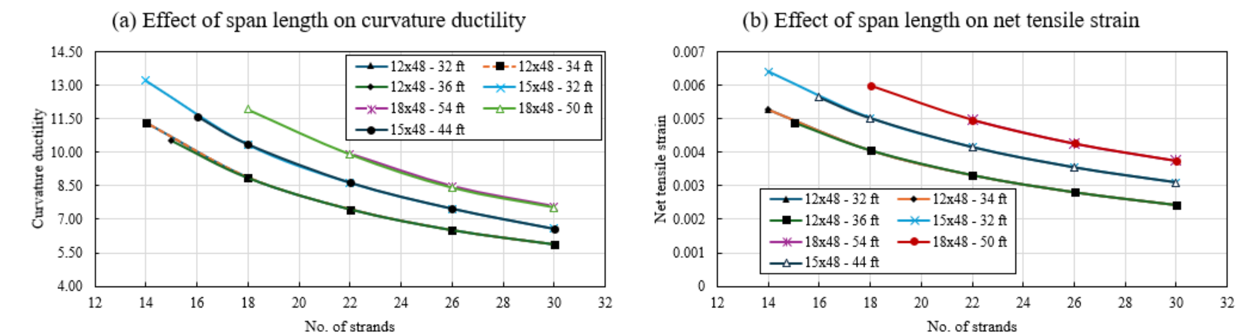


**Figure 9-6. Span length effect on ductility indices derived from moment-curvature relationship**

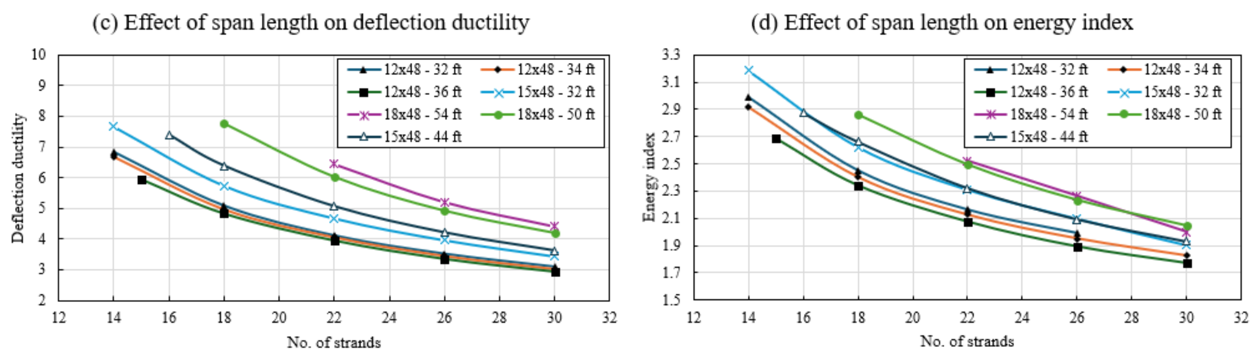


**Figure 9-7. Span length effect on ductility indices derived from load-deflection relationship**

## 9.4.3 Effect of the member width

For a given number of strands, increasing the member's width while maintaining other parameters increases the section's capability to sustain more deflection and cracking before failure, as shown in Figures 9-8, 9-9, and 9-10.

## 9.4.4 Effect of topping thickness

Increasing the topping thickness increases the member's self-weight and capacity. The capacity increases as a result of increased moment arm between the compressive and tensile resultant forces. When all design parameters of the section are constant, and the only variable is the topping thickness, the ductility slightly increases with the increase of topping, as shown in Figure 9-11.

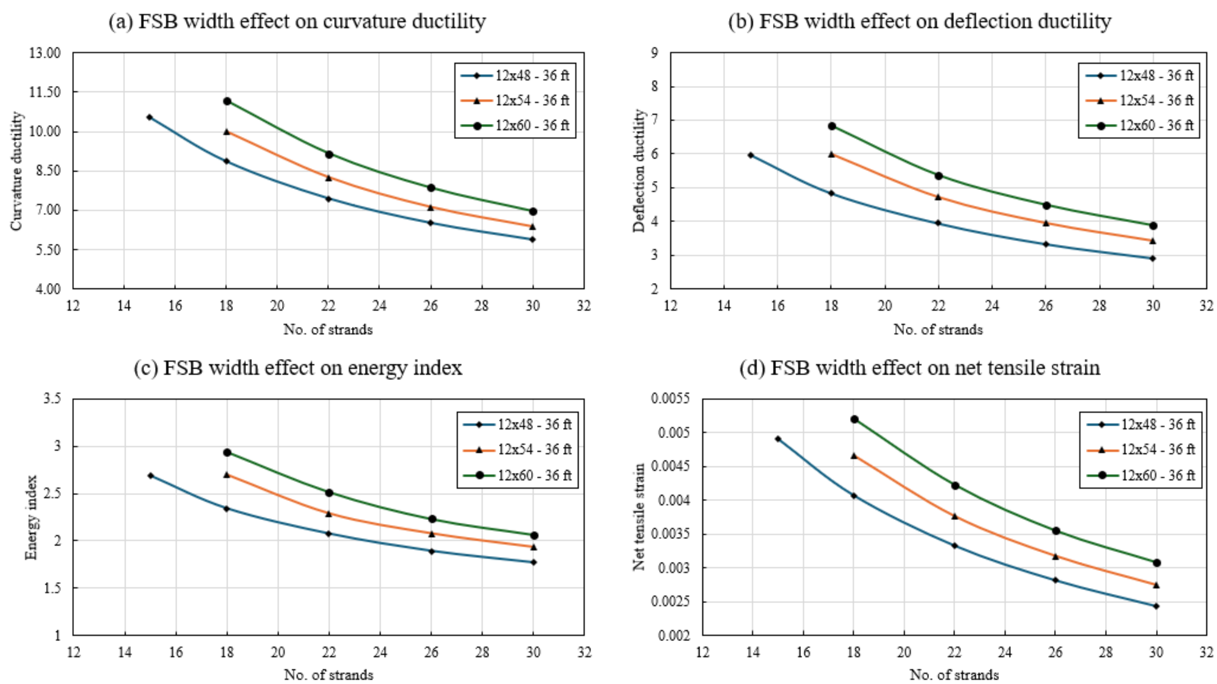


**Figure 9-8. Effect of width for section FSB-12" with a span of 36 ft**

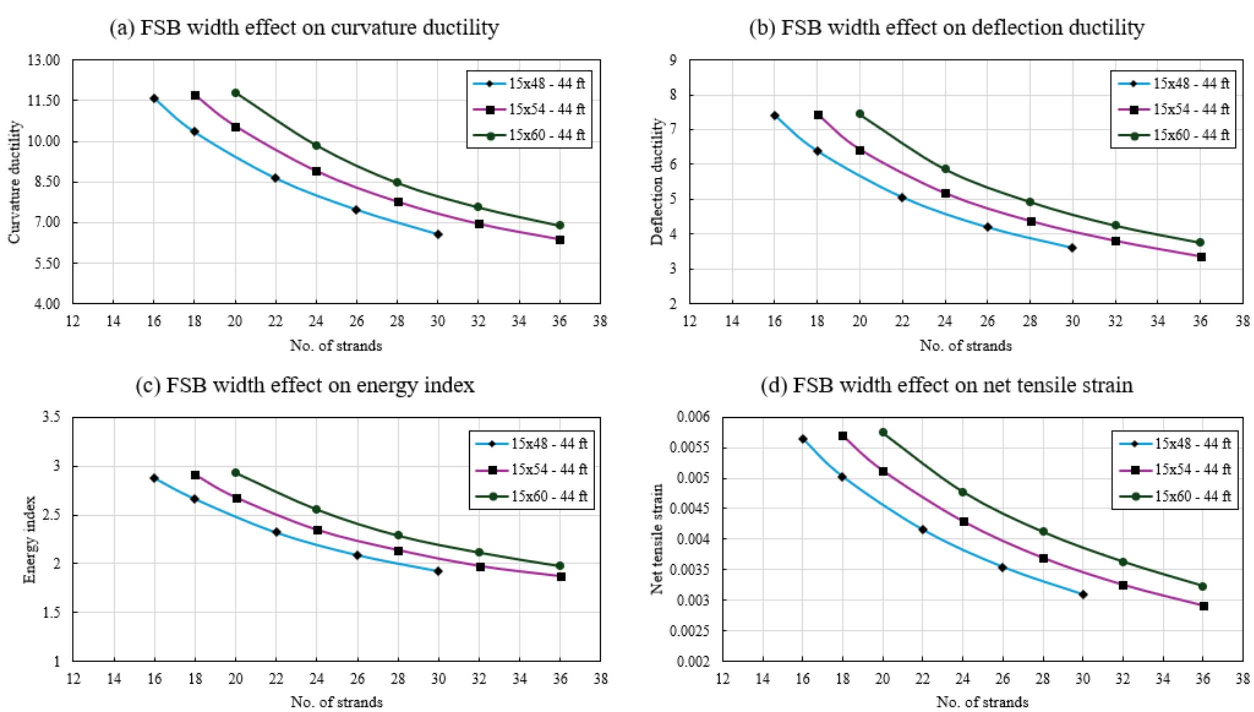


**Figure 9-9. Effect of width for section FSB-15" with span of 44 ft**

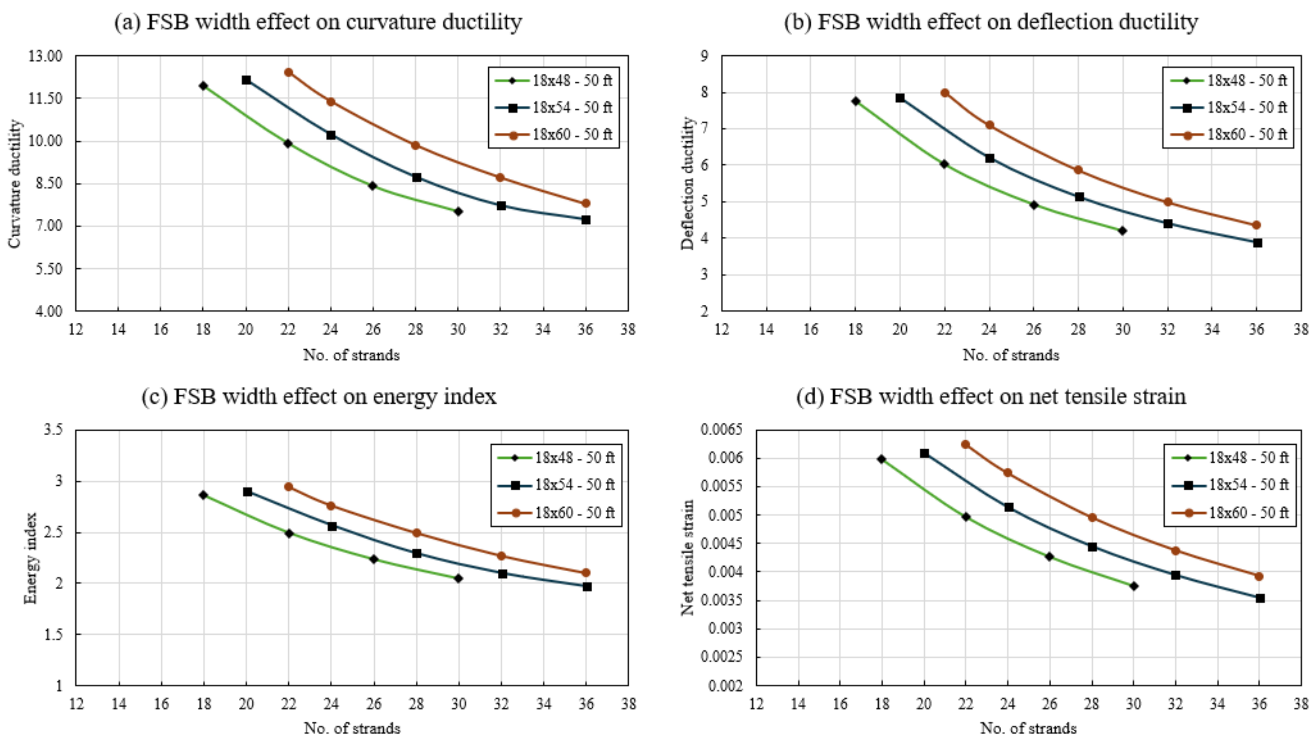


**Figure 9-10. Effect of width for section FSB-18" with a span of 50 ft**

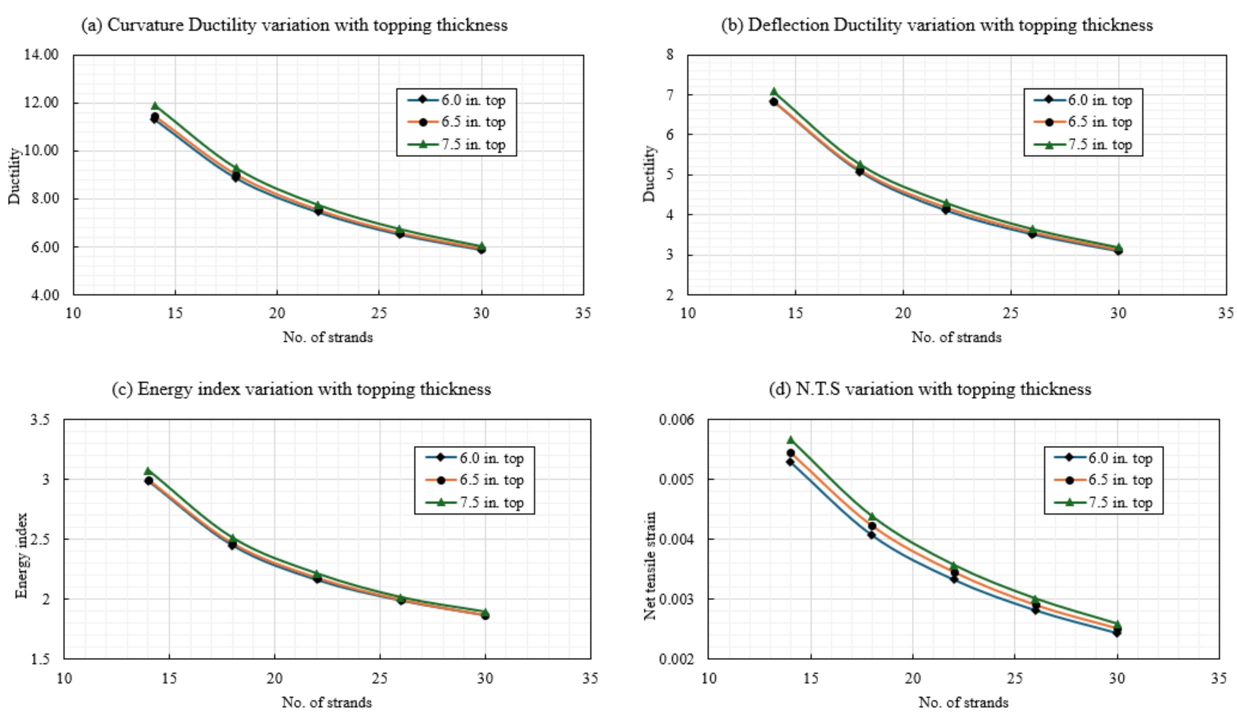


**Figure 9-11. Effect of topping thickness on ductility**

## 9.4.5 Effect of jacking force

The four specimens were constructed using a jacking force of about 70% of the ultimate stress of the strands. Increasing the jacking force causes a decrease in the ductility of the member, as shown in Figure 9-12.

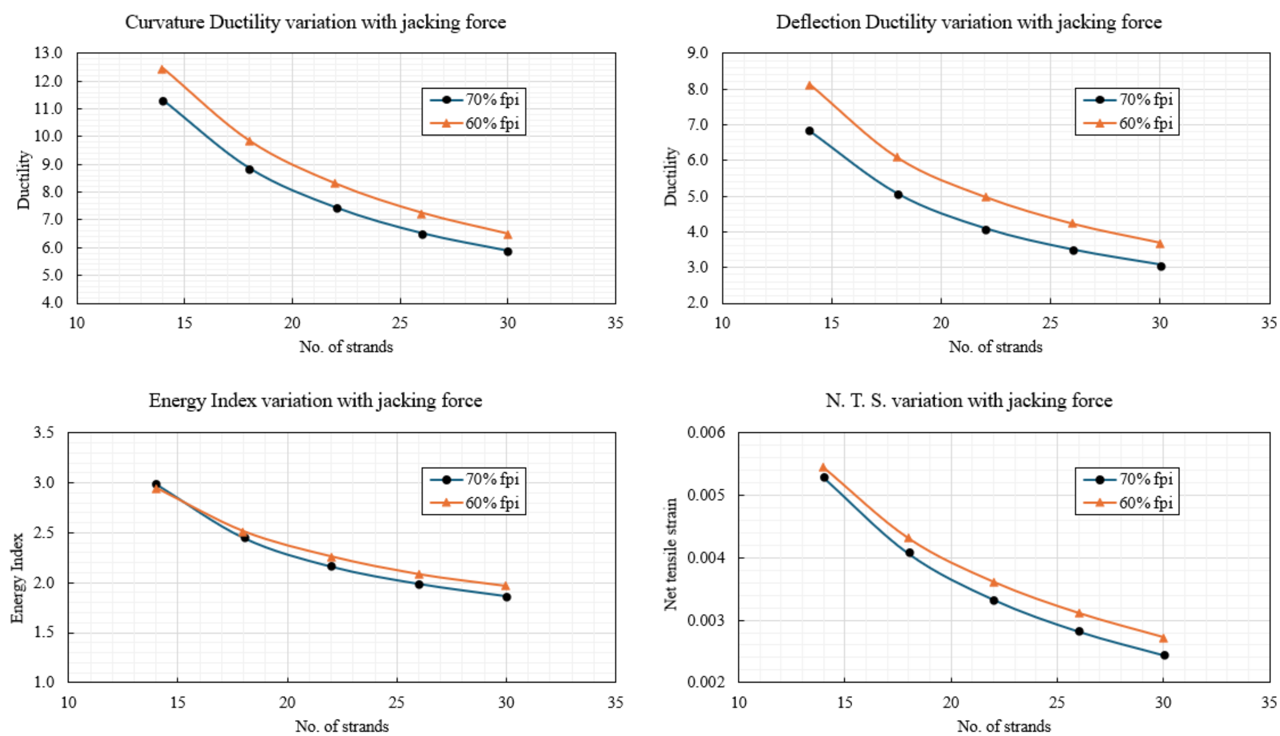


**Figure 9-12. Effect of jacking force on ductility**

# 9.5 Ductility vs. deformability

The concept of ductility in literature is mostly defined as the ratio of ultimate deformation to yield deformation – whether this deformation is curvature, rotation, or deflection. When it is not possible to identify the yielding of the reinforcement – for example in FRP reinforcement – this definition is no longer a good measurement of a section's ductility. Therefore, researchers suggest the concept of deformability, where several models are based on the ratio of ultimate to service parameters.

To compare different FSB sections that have different sizes, number of strands, and concrete strength, use of a prestressing index parameter is suggested by the authors as follows:

$$Prestressing\ index = \frac{n\,A_p\,f_{ps}}{t\,w\,f_c'(top)} \qquad \text{(Eq. 9.9)}$$

where
$n$ = number of strands,
$A_p$ = area of strands (in$^2$),

$f_{ps}$ = prestress level in outermost strands (ksi),
$t$ = the thickness of the topping (in.),
$w$ = the width of the topping (in.), and
$f_c'(top)$ = the compressive strength of the topping (ksi).

Using this unitless parameter, ductility and deformability indices can be evaluated to find a suitable approach to evaluate flexural behavior. The parameter correlates with the ratio of the depth of the neutral axis to the depth of the prestress force, $c/d$, and the tensile strain. The depth $d$ is defined as the depth from the extreme compression fiber to the outermost of tensile reinforcement, and $c$ is defined as the distance from the extreme compression fiber to the neutral axis. Figure 9-13 shows how the $c/d$ ratio correlates with the prestressing index of the different FSB sections with different design parameters. Figure 9-14 shows the variation of net tensile strain vs. prestressing index.

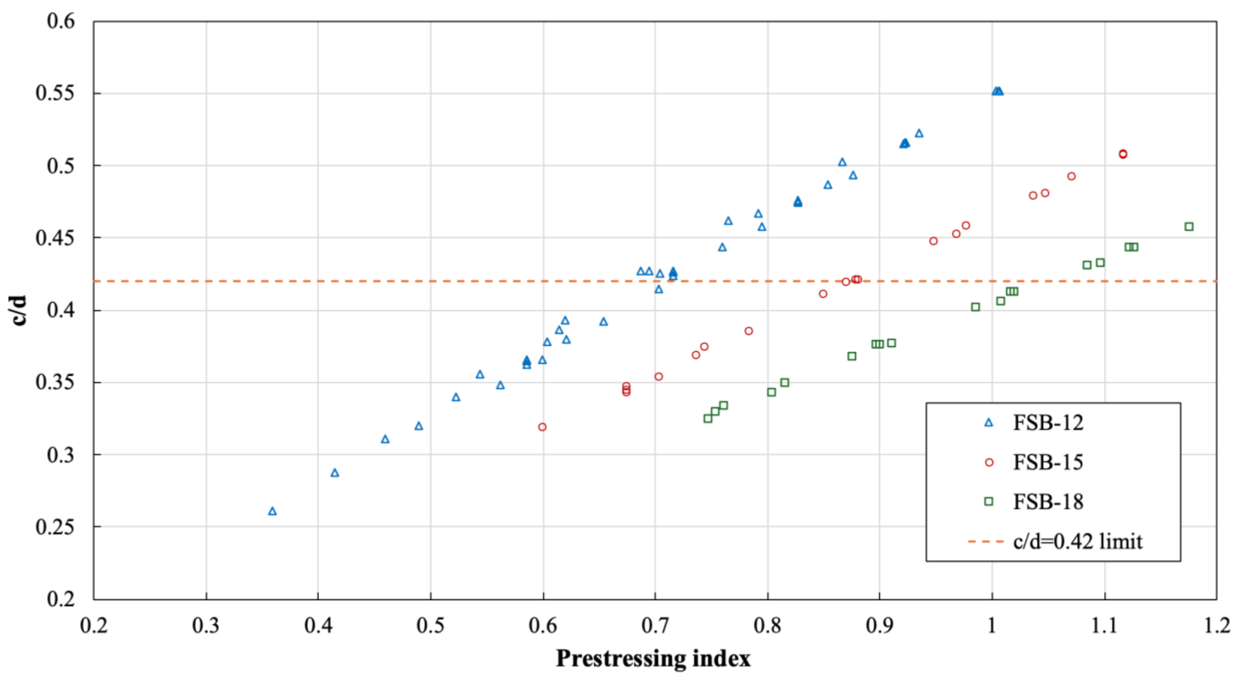


**Figure 9-13. Variation of prestressing index vs. $c/d$ ratio**

The curvature ductility and deflection ductility showed variability with distinct behavior for each FSB section type as shown in Figures 9-15 and 9-16, while the energy index shows similar behavior but less scattered (Figure 9-17).

In the case of deformability indices, Mufti's deformability did not show good variability in ductility, as most values were between 5.5 and 6 as shown in Figure 9-18. This deformability is only sensitive to topping strength variability represented by the three sets of points having deformability larger than 6 as shown in Figure 9-18. Mast deformability showed very scattered values due to service curvature in the denominator. When the service moment is very low, the corresponding curvature is either negative or very small and results in the negative or very high values of deformability shown in Figure 9-19. Zou deformability showed a good, scattered variability with changing section parameters, and it also showed distinct behavior for each FSB section type (Figure 9-20).

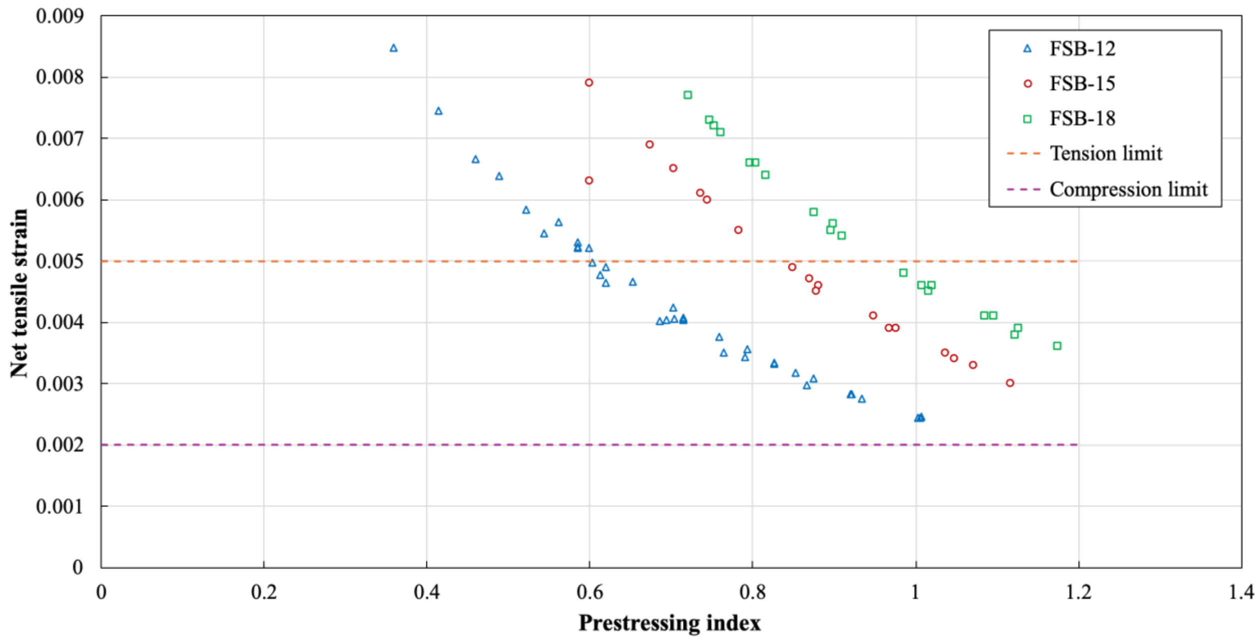


**Figure 9-14. Variation of the prestressing index with net tensile strain**

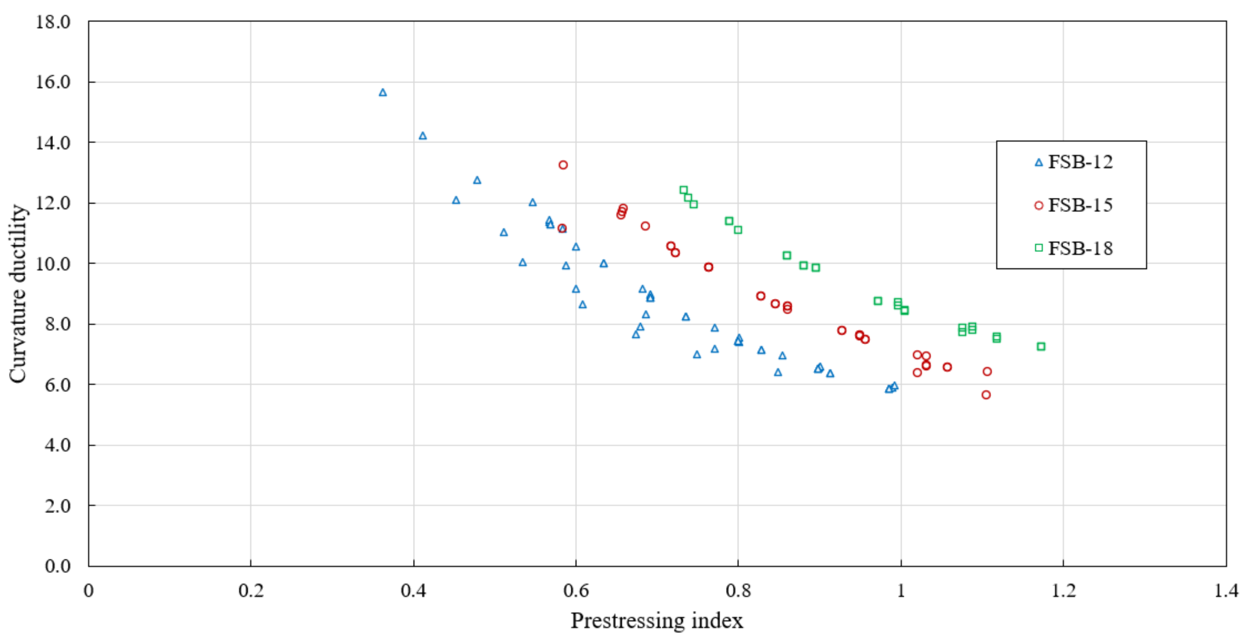


**Figure 9-15. Curvature-ductility variation with prestressing index**

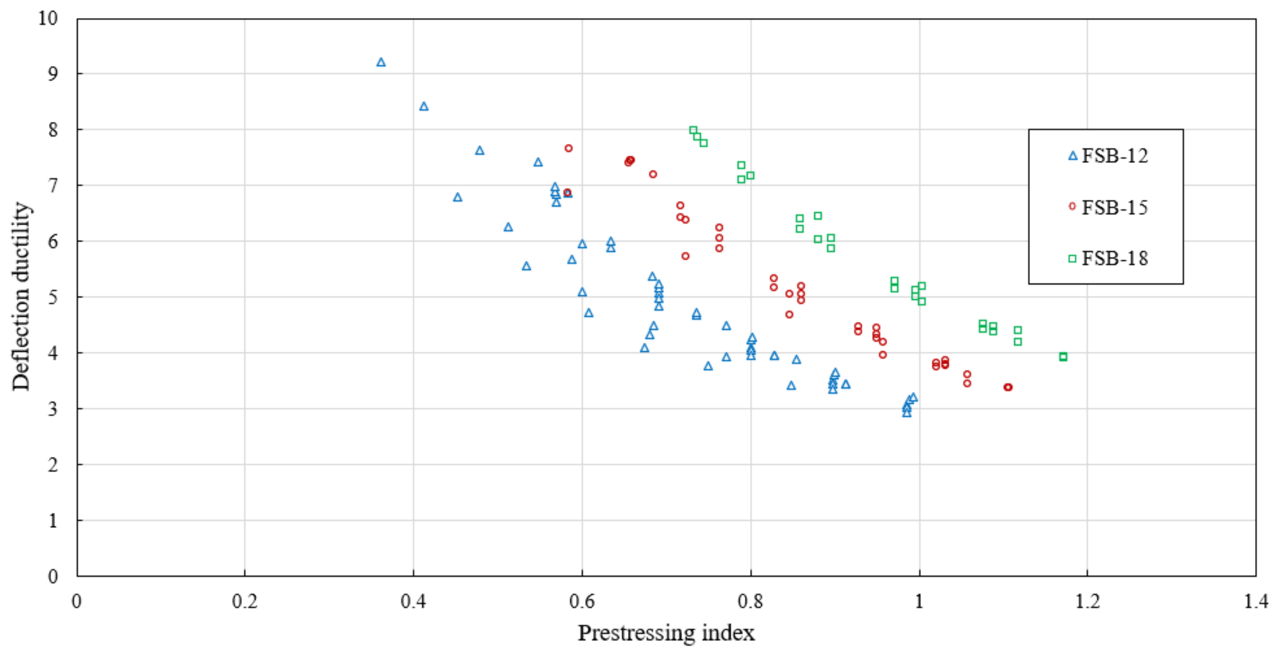


**Figure 9-16. Deflection-ductility variation with prestressing index**

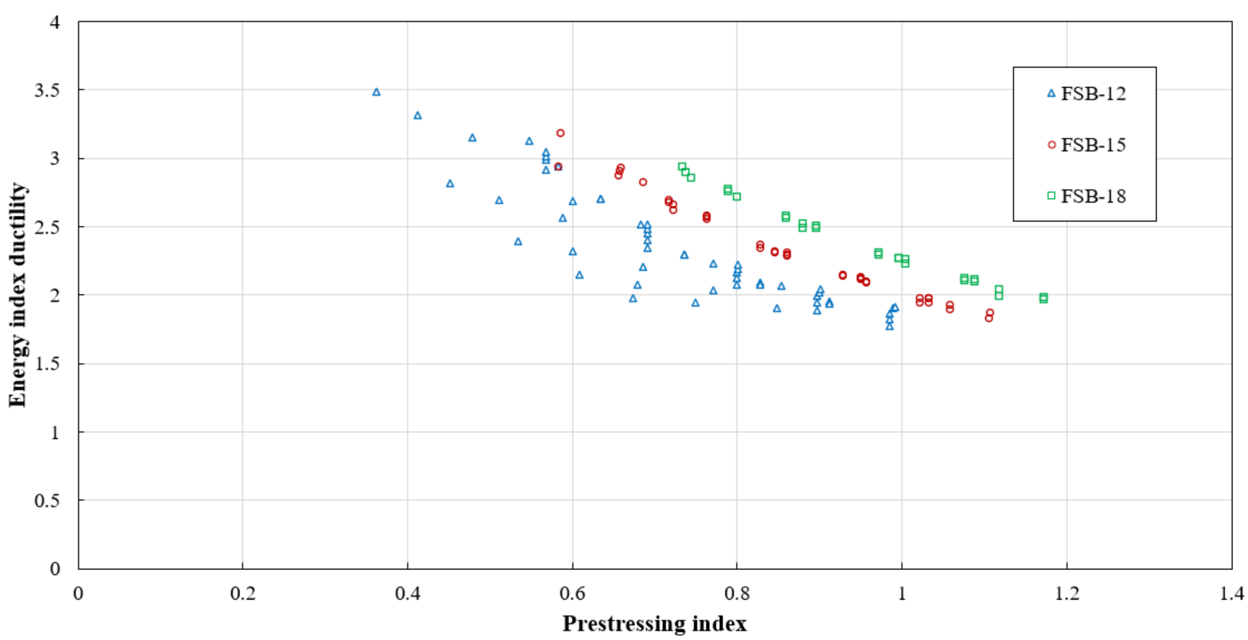


**Figure 9-17. Energy index variation with prestressing index**

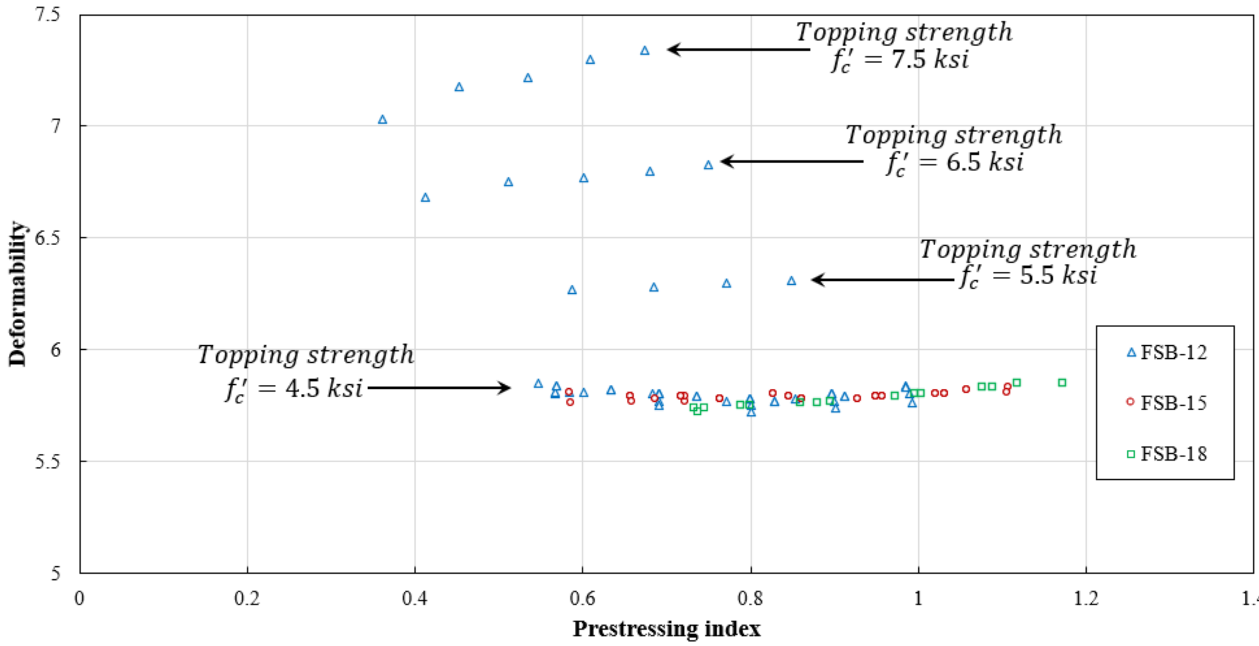


**Figure 9-18. Mufti deformability vs. prestressing index**

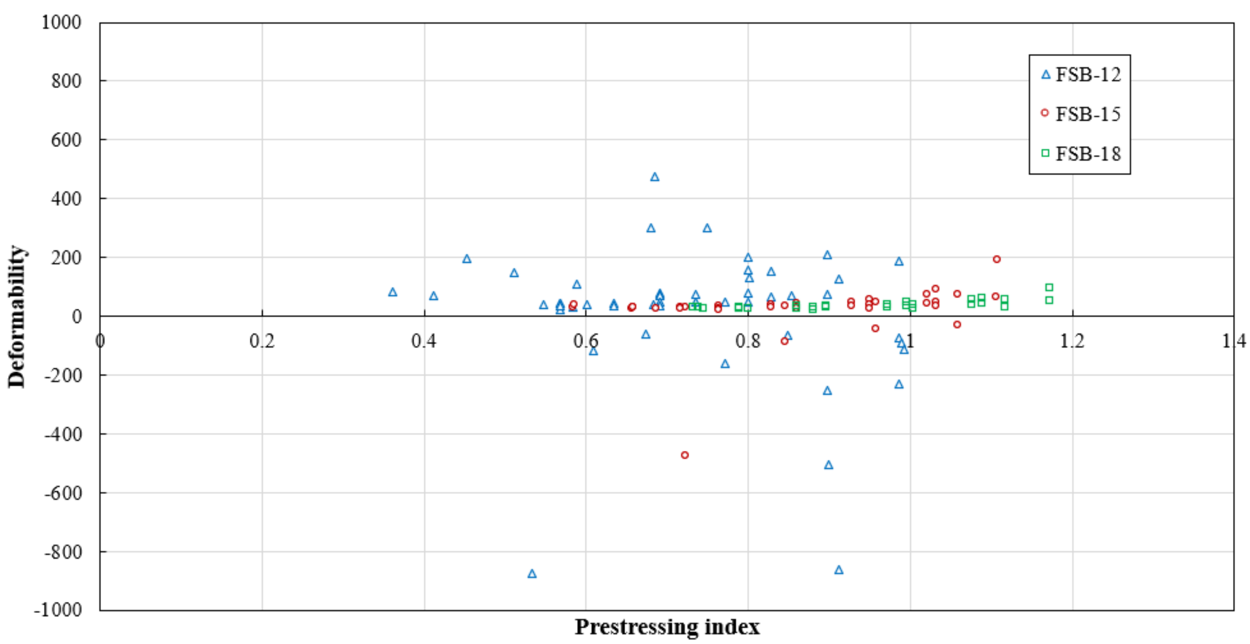


**Figure 9-19. Variation of Mast deformability vs. prestressing index**

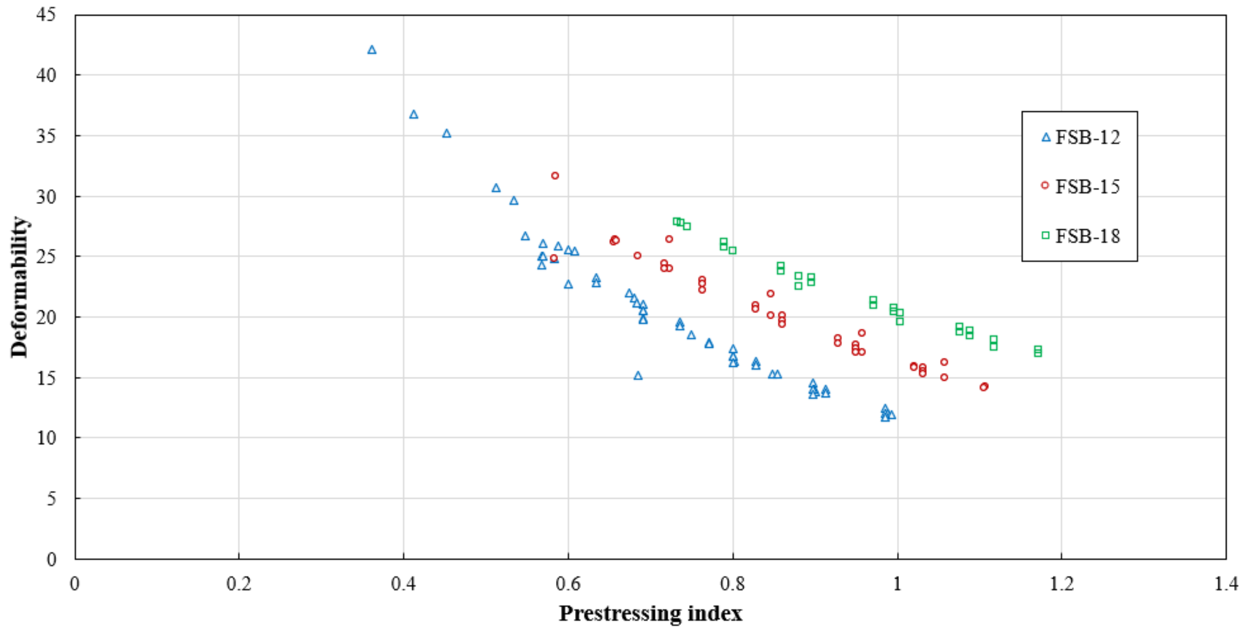


**Figure 9-20. Zou deformability vs. prestressing index**

The suggested reserved capacity index is plotted vs. the prestressing index for the different FSB sections and design parameters in Figure 9-21. The relationship shows distinct variability compared to other types of ductility, where all FSB sections have similar ductility for a given prestressing index.

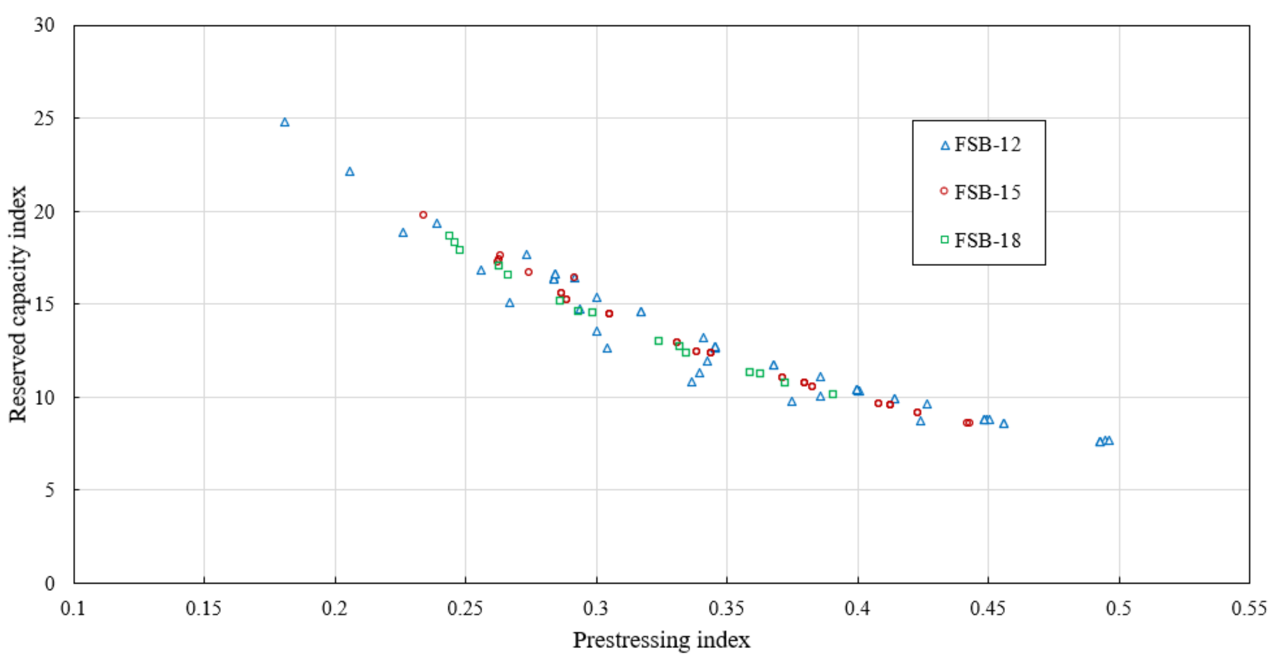


**Figure 9-21. Reserved capacity index vs. prestressing index**

## 9.6 Design of Florida slab beams

Flexural members prestressed with stainless steel strands fail in one of three modes: (1) concrete crushing at the top fiber, (2) strand rupture, or (3) balanced failure when both concrete crushing and strand rupture occur simultaneously (Figure 9-22). For FSBs, the second failure mode is desirable for efficiency, while the members show cracking and deflection before failure. The balanced failure is the most favorable because it allows a member to reach its highest curvature. In the balanced failure mode, the concrete reaches the highest strain of approximately 0.003, and the strands reach the highest strain where they rupture. However, this failure mode is least possible due to the variability of concrete and strand properties and other factors.

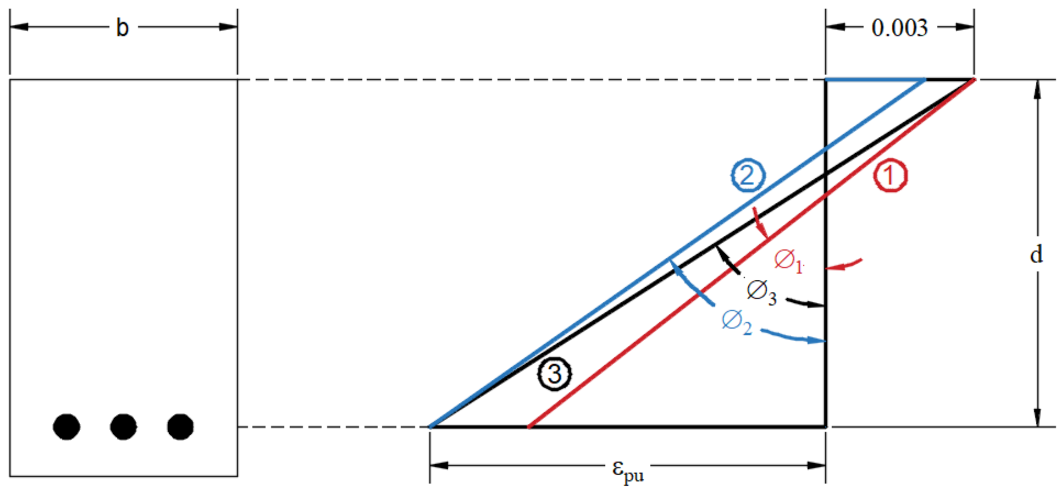


**Figure 9-22 Strain level for reinforced concrete failure modes: (1) Concrete crushing at top, (2) strand rupture, and (3) balanced failure**

For shallow depth members such as FSBs, serviceability limits predominantly govern the design, resulting in a large number of strands compared to other controlling limit states. Increasing the number of strands decreases the strain in the strands, making the strand rupture failure mode less possible and concrete crushing the most probable failure mode. When designing FSBs with carbon steel strands, members are mainly governed by the Service III tension limit or by camber. However, the members can still exhibit ductile behavior and reach a net tensile strain of 0.005. In members with stainless steel strands, due to the lower jacking force that is used compared to carbon steel strands, the members' designs are governed by camber. The question is whether these members can still exhibit ductile behavior similar to those with carbon steel strands. To answer this question, the design of a 32-ft-long bridge was used for the analysis. According to FDOT Standard Plans Instruction index 20450 for the FSB section (FDOT, 2026a), a 12 in. x 48 in. FSB would be recommended for a 32-ft span, for both stainless steel and carbon steel strands, as shown in Figure 9-23.

| Table of Recommended Maximum Span Lengths (CL Bearing to CL Bearing) ASTM A416, Grade 270, Low Relaxation, Carbon Steel Strands | | | | |
|---|---|---|---|---|
| Beam Type | 6" C-I-P Topping w/ Future Wearing Surface (Short Bridge) | | 6½" C-I-P Topping w/ ½" Sacrificial Thickness (Long Bridge) | |
| | Beam Width | | Beam Width | |
| | 4'-0" | 5'-0" | 4'-0" | 5'-0" |
| 12" FSB | 40'-11" | 43'-11" | 41'-2" | 44'-5" |
| 15" FSB | 52'-11" | 56'-3" | 53'-3" | 56'-9" |
| 18" FSB | 62'-3" | 64'-4" | 62'-8" | 64'-10" |

| Table of Recommended Maximum Span Lengths (CL Bearing to CL Bearing) ASTM A1114, Grade 240, Low Relaxation, Stainless Steel Strands | | |
|---|---|---|
| Beam Type | Short and Long Bridge<br>Note: Maximum lengths are applicable to both 6" C-I-P Topping with Future Wearing Surface and 6 ½" C-I-P Topping with ½" Sacrificial Thickness | |
| | Beam Width | |
| | 4'-0" | 5'-0" |
| 12" FSB | 36'-11" | 39'-9" |
| 15" FSB | 48'-5" | 51'-8" |
| 18" FSB | 57'-11" | 57'-11" |

**Figure 9-23. Recommended maximum span length per FDOT Standard Instruction index 20450**

The design process was started by varying the number of strands and checking if they meet the service and strength requirements for both stainless steel and carbon steel strands. The process was repeated for different span lengths and different sections to determine the most critical requirements that might govern the design. After the design was completed, the previously verified flexural model was used to compare the moment-curvature relationships of FSBs prestressed with stainless steel to those with carbon steel strands.

Considering a 32-ft-long bridge in a harsh marine environment, the bridge was first designed with stainless steel strands and then with carbon steel strands. The required concrete strength based on FDOT (2026b) is 8.5 ksi for the FSBs and 5.5 ksi for the topping, since the member is in extreme environment exposure. Figure 9-23 for recommended maximum spans shows that a 12in. x 48in. FSB is a suitable section for such a bridge span. The design process began with a high number of strands, for example, 30 strands, and the number of strands was decreased until the minimum number that is satisfactory for all the design requirements was found. Then, the number of strands was decreased further to determine the minimum number that meets critical design requirements. The three most critical requirements are: camber, Service III and flexural resistance; each is discussed in the following sections.

## 9.6.1 Camber

Camber refers to the upward deflection of a prestressed concrete member. This deflection occurs due to the eccentric prestressing force. It is a function of the cross-section shape, prestressing force, strand eccentricity, and member length. Because the FSB depth is shallower than other prestressed concrete members, the eccentricity of the prestressing force is relatively low. This means that camber often controls the design of FSBs. If stainless steel strands that typically have lower jacking force and ultimate stress are used in an FSB, the prestressing force would be lower in each layer of strands compared to the same FSB prestressed with carbon steel strands. Therefore, camber needs extra attention in FSBs with stainless steel strands. One way to increase camber is to use a higher jacking force for the strands. For example, stainless steel strands are currently allowed by FDOT to be initially stressed up to 65% of their ultimate stress; an increase to 70% would increase the camber and reduce the number of required strands. Another way to increase camber is by removing the dormant strands usually placed at the member's top. Dormant strands are typically provided to aid in the placement reinforcement during fabrication, and they also help reduce the stresses at the release and final stages. For an FSB section with a specific span length, increasing the number of strands increases the camber, as shown in Figure 9-24.

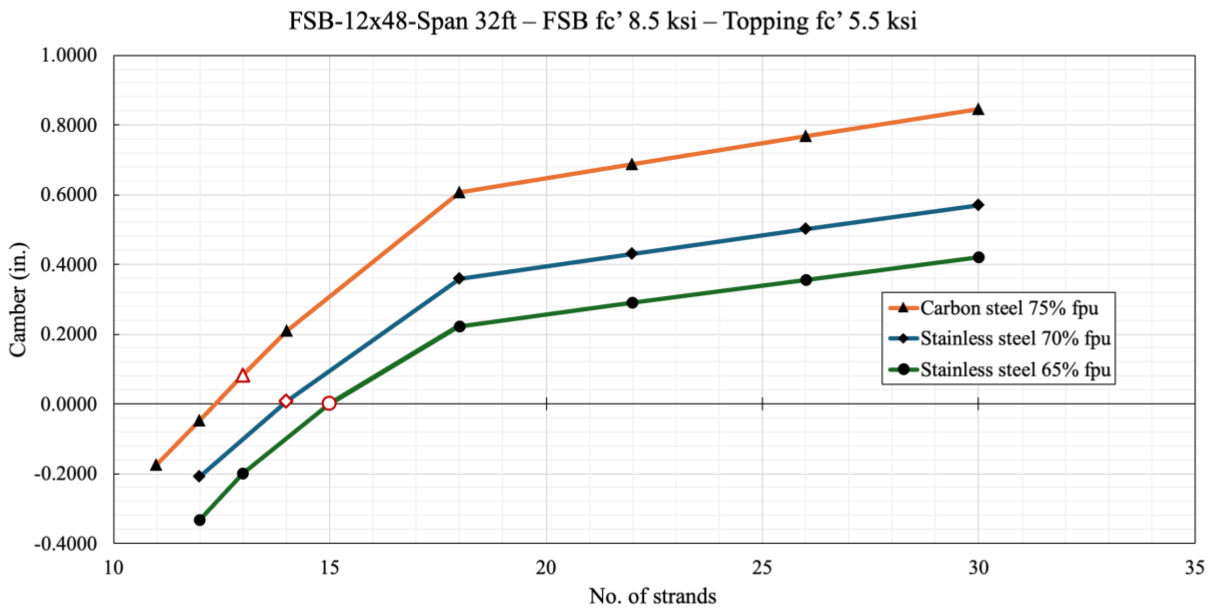


**Figure 9-24. Camber vs. number of strands for FSB-12x48 with a span of 32 ft and concrete strength for FSB and topping of 8.5 ksi and 5.5 ksi, respectively**

## 9.6.2 Service III

Service III requirement includes a stress check that helps limit cracks in the member, thereby increasing durability and protecting the internal reinforcement from corrosion. Service III requires stress levels at the bottom fiber of the member to be within the tensile stress limit, which depends on the environmental exposure and the specified concrete strength. The tensile limits are $0.19\sqrt{f_c'}$ and $0.0948\sqrt{f_c'}$ for slightly aggressive environmental exposure and aggressive environmental exposure, respectively (see Figure 9-25). The stress level depends on the section size, span length, prestressing force, and strand eccentricity, among other parameters. This requirement controls the design of FSBs with carbon steel strands due to their shallow depth compared to deeper members such as girders. Using stainless steel strands provides less prestressing force in each strand layer, causing lower prestressing moments and, consequently, higher tensile stress at the bottom fiber (Figure 9-25). However, stainless steel strands are corrosion resistant and need less protection against corrosion, meaning that the tensile stress limits could potentially be increased. With either carbon steel or stainless steel strands, the tensile stress at the bottom fiber decreases (or the compressive stress increases) with an increased number of strands, as shown in Figure 9-25.

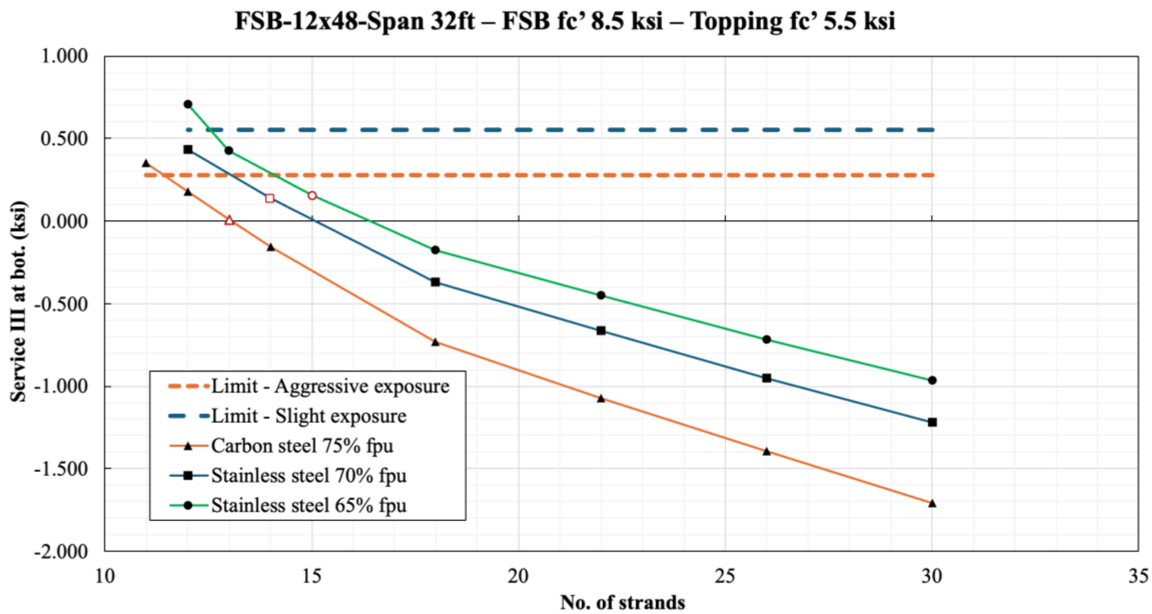


**Figure 9-25. Bottom fiber stress variation with number of strands**

## 9.6.3 Flexural resistance

The prestressed concrete member design needs to have a satisfactory factored flexural resistance, $\phi M_n$, that exceeds the factored moment (demand), $M_u$, per AASHTO LRFD strength limit state requirements (AASHTO, 2024). In these requirements, load combinations utilize load factors applied to load effects. To reduce the probability of brittle failure in non-compression-controlled flexural members, AASHTO LRFD specification has a minimum reinforcement provision that requires the factored flexural resistance, $\phi M_n$, to exceed the lesser of two values: the factored moment, $M_u$, multiplied by 1.33, and the cracking moment, $M_{cr}$. The first value depends on the loads and span length, while the cracking moment varies with the number of strands. The cracking moment can be obtained from the following expression:

$$M_{cr} = \left(1.6\, f_r + 1.1 f_{cpe}\right) S_c - M_{dnc}\left(\frac{S_c}{S_{nc}} - 1\right) \qquad \text{(Eq. 9.10)}$$

where
$f_r$ = modulus of rupture for concrete (ksi),
$f_{cpe}$ = compressive stress in concrete due to effective prestress (ksi),
$S_c$ = section modulus of composite section at the extreme fiber where the applied force causes tensile stresses ($\text{in}^3$),
$M_{dnc}$ = moment due to total unfactored dead load acting on non-composite section (kip-in.), and
$S_{nc}$ = section modulus for non-composite section at the extreme fiber where the applied force causes tensile stresses ($\text{in}^3$).

In some FSB designs, the required minimum reinforcement sometimes controls the required flexural resistance. Table 9-1 lists the cracking moment and factored moment for each design in the parametric study, as well as for cases with a higher and a lower number of strands than the design. The table also lists the required flexural resistance, $M_{req}$, which is governed by either the factored moment, $M_u$, or the minimum reinforcement provision (the lesser of $M_{cr}$ or $1.33M_u$); the column specifies which of the three values controls. These values were obtained using the FDOT LRFD Prestressed Beam Program Mathcad sheet, based on FDOT's current design Standard Plans and Specifications. From Table 9-1, it is evident that the required moment does not control the design, even for the cases with the lower number of strands. Therefore, it can be concluded that the resistance factor value is insignificant in FSB design.

**Table 9-1. Required flexural resistance and factored flexural resistance**

| Section type | Prestressing type | No. of strands | Span (ft) | $M_{cr}$ (k-ft) | $M_u$ (k-ft) | $M_{req}$ (k-ft) (Governing moment) | $\phi M_n$ (k-ft) | $M_{req}$ / $\phi M_n$ |
|---|---|---|---|---|---|---|---|---|
| **12x48** | SS | 18 | 32 | 666.4 | 496.1 | 659.8 ($1.33M_u$) | 737.4 | 89.5% |
| **12x48** | SS | 14* | 32 | 546.1 | 496.1 | 546.1 ($M_{cr}$) | 621.7 | 87.8% |
| **12x48** | SS | 12 | 32 | 476.6 | 496.1 | 496.1 ($M_u$) | 550.4 | 90.1% |
| **12x48** | CS | 14 | 32 | 615.9 | 496.1 | 615.9 ($M_{cr}$) | 804.0 | 76.6% |
| **12x48** | CS | 13* | 32 | 576.2 | 496.1 | 576.2 ($M_{cr}$) | 754.4 | 76.4% |
| **12x48** | CS | 12 | 32 | 536.2 | 496.1 | 536.2 ($M_{cr}$) | 703.6 | 76.2% |
| **12x54** | SS | 22 | 36 | 767.5 | 646.1 | 767.5 ($M_{cr}$) | 878.3 | 87.4% |
| **12x54** | SS | 19* | 36 | 682.9 | 646.1 | 682.9 ($M_{cr}$) | 804.1 | 84.9% |
| **12x54** | SS | 16 | 36 | 581.3 | 646.1 | 646.1 ($M_u$) | 709.6 | 91.1% |
| **12x54** | CS | 22 | 36 | 875.4 | 646.1 | 859.3 ($1.33M_u$) | 1180.1 | 72.8% |
| **12x54** | CS | 17* | 36 | 700.5 | 646.1 | 700.5 ($M_{cr}$) | 966.9 | 72.4% |
| **12x54** | CS | 16 | 36 | 661.3 | 646.1 | 661.3 ($M_{cr}$) | 918.8 | 72.0% |
| **12x60** | SS | 22 | 36 | 794.4 | 705.7 | 794.4 ($M_{cr}$) | 920.4 | 86.3% |
| **12x60** | SS | 20* | 36 | 727.4 | 705.7 | 727.4 ($M_{cr}$) | 861.6 | 84.4% |

**Table 9-1 (cont'd). Required flexural resistance and factored flexural resistance**

| Section type | Prestressing type | No. of strands | Span (ft) | $M_{cr}$ (k-ft) | $M_u$ (k-ft) | $M_{req}$ (k-ft) (Governing moment) | $\phi M_n$ (k-ft) | $M_{req}$ / $\phi M_n$ |
|---|---|---|---|---|---|---|---|---|
| **12x60** | SS | 17 | 36 | 625.3 | 705.7 | 705.7 ($M_u$) | 764.3 | 92.3% |
| **12x60** | CS | 22 | 36 | 904.7 | 705.7 | 904.7 ($M_{cr}$) | 1219.0 | 74.2% |
| **12x60** | CS | 18* | 36 | 749.9 | 705.7 | 749.9 ($M_{cr}$) | 1033.5 | 72.6% |
| **12x60** | CS | 17 | 36 | 710.6 | 705.7 | 710.6 ($M_{cr}$) | 984.5 | 72.2% |
| **15x48** | SS | 22 | 44 | 921.3 | 881.4 | 921.3 ($M_{cr}$) | 1048.4 | 87.9% |
| **15x48** | SS | 19* | 44 | 835.6 | 881.4 | 881.4 ($M_u$) | 967.7 | 91.1% |
| **15x48** | SS | 17 | 44 | 777.3 | 881.4 | 881.4 ($M_u$) | 905.9 | 97.3% |
| **15x48** | CS | 22 | 44 | 1051.4 | 881.4 | 1051.4 ($M_{cr}$) | 1402.7 | 75.0% |
| **15x48** | CS | 17* | 44 | 885.9 | 881.4 | 885.9 ($M_{cr}$) | 1174.0 | 75.5% |
| **15x48** | CS | 16 | 44 | 836.4 | 881.4 | 881.4 ($M_u$) | 1115.2 | 79.0% |
| **15x54** | SS | 26 | 46 | 1073.8 | 1045.2 | 1073.8 ($M_{cr}$) | 1225.3 | 87.6% |
| **15x54** | SS | 22* | 46 | 960.6 | 1045.2 | 1045.2 ($M_u$) | 1122.8 | 93.1% |
| **15x54** | SS | 21 | 46 | 931.8 | 1045.2 | 1045.2 ($M_u$) | 1093.7 | 95.6% |
| **15x54** | CS | 22 | 46 | 1098.4 | 1045.2 | 1098.4 ($M_{cr}$) | 1476.7 | 74.4% |
| **15x54** | CS | 20* | 46 | 1001.4 | 1045.2 | 1045.2 ($M_u$) | 1364.7 | 76.6% |
| **15x54** | CS | 19 | 46 | 967.9 | 1045.2 | 1045.2 ($M_u$) | 1315.9 | 79.4% |
| **15x60** | SS | 30 | 48 | 1192.6 | 1223.2 | 1223.2 ($M_u$) | 1386.2 | 88.2% |
| **15x60** | SS | 27* | 48 | 1108.6 | 1223.2 | 1223.2 ($M_u$) | 1315.7 | 93.0% |
| **15x60** | SS | 25 | 48 | 1051.8 | 1223.2 | 1223.2 ($M_u$) | 1262.6 | 96.9% |
| **15x60** | CS | 26 | 48 | 1239.1 | 1223.2 | 1239.1 ($M_{cr}$) | 1709.9 | 72.5% |
| **15x60** | CS | 24* | 48 | 1173.5 | 1223.2 | 1223.2 ($M_u$) | 1619.5 | 75.5% |

Table 9-1 (cont'd). Required flexural resistance and factored flexural resistance

| Section type | Prestressing type | No. of strands | Span (ft) | $M_{cr}$ (k-ft) | $M_u$ (k-ft) | $M_{req}$ (k-ft) (Governing moment) | $\phi M_n$ (k-ft) | $M_{req}$ / $\phi M_n$ |
|---|---|---|---|---|---|---|---|---|
| **15x60** | CS | 22 | 48 | 1092.0 | 1223.2 | 1223.2 ($M_u$) | 1515.8 | 80.7% |
| **18x48** | SS | 22 | 50 | 1157.3 | 1142.5 | 1157.3 ($M_{cr}$) | 1297.9 | 89.2% |
| **18x48** | SS | 20* | 50 | 1080.4 | 1142.5 | 1142.5 ($M_u$) | 1223.4 | 93.4% |
| **18x48** | SS | 19 | 50 | 1041.6 | 1142.5 | 1142.5 ($M_u$) | 1183.6 | 96.5% |
| **18x48** | CS | 22 | 50 | 1317.2 | 1142.5 | 1317.2 ($M_{cr}$) | 1703.3 | 77.3% |
| **18x48** | CS | 18* | 50 | 1139.5 | 1142.5 | 1142.5 ($M_u$) | 1468.8 | 77.8% |
| **18x48** | CS | 17 | 50 | 1094.4 | 1142.5 | 1142.5 ($M_u$) | 1407.3 | 81.2% |
| **18x54** | SS | 26 | 50 | 1346.4 | 1344.3 | 1346.4 ($M_{cr}$) | 1519.6 | 88.6% |
| **18x54** | SS | 24* | 50 | 1270.5 | 1344.3 | 1344.3 ($M_u$) | 1449.4 | 92.7% |
| **18x54** | SS | 22 | 50 | 1193.8 | 1344.3 | 1344.3 ($M_u$) | 1372.9 | 97.9% |
| **18x54** | CS | 22 | 50 | 1360.4 | 1344.3 | 1360.4 ($M_{cr}$) | 1777.1 | 76.6% |
| **18x54** | CS | 21* | 50 | 1316.1 | 1344.3 | 1344.3 ($M_u$) | 1717.4 | 78.3% |
| **18x54** | CS | 20 | 50 | 1257.4 | 1344.3 | 1344.3 ($M_u$) | 1647.6 | 81.6% |
| **18x60** | SS | 28 | 52 | 1462.5 | 1470.8 | 1470.8 ($M_u$) | 1657.9 | 88.7% |
| **18x60** | SS | 26* | 52 | 1386.7 | 1470.8 | 1470.8 ($M_u$) | 1585.2 | 92.8% |
| **18x60** | SS | 24 | 52 | 1310.2 | 1470.8 | 1470.8 ($M_u$) | 1507.1 | 97.6% |
| **18x60** | CS | 23 | 52 | 1447.1 | 1470.8 | 1470.8 ($M_u$) | 1887.2 | 77.9% |
| **18x60** | CS | 22* | 52 | 1388.6 | 1470.8 | 1470.8 ($M_u$) | 1817.1 | 80.9% |
| **18x60** | CS | 18 | 52 | 1152.2 | 1470.8 | 1470.8 ($M_u$) | 1527.5 | 96.3% |

*Design section

Therefore, increasing the number of strands increases cracking moment and, therefore, increases the required flexural resistance. The factored flexural resistance is much higher than the required moment for FSBs prestressed with carbon steel strands compared to FSBs prestressed with stainless steel strands jacked to 70% $f_{pu}$ and 65% $f_{pu}$. This is due to the resistance factor of 0.75 used for FSBs with stainless steel strands vs. 1.0 or less for FSBs with carbon steel strands as shown in Figures 9-26, 9-27, and 9-28. However, if the nominal flexural resistance is compared, the FSBs have relatively the same resistance for the three strand cases, as shown in Figure 9-29.

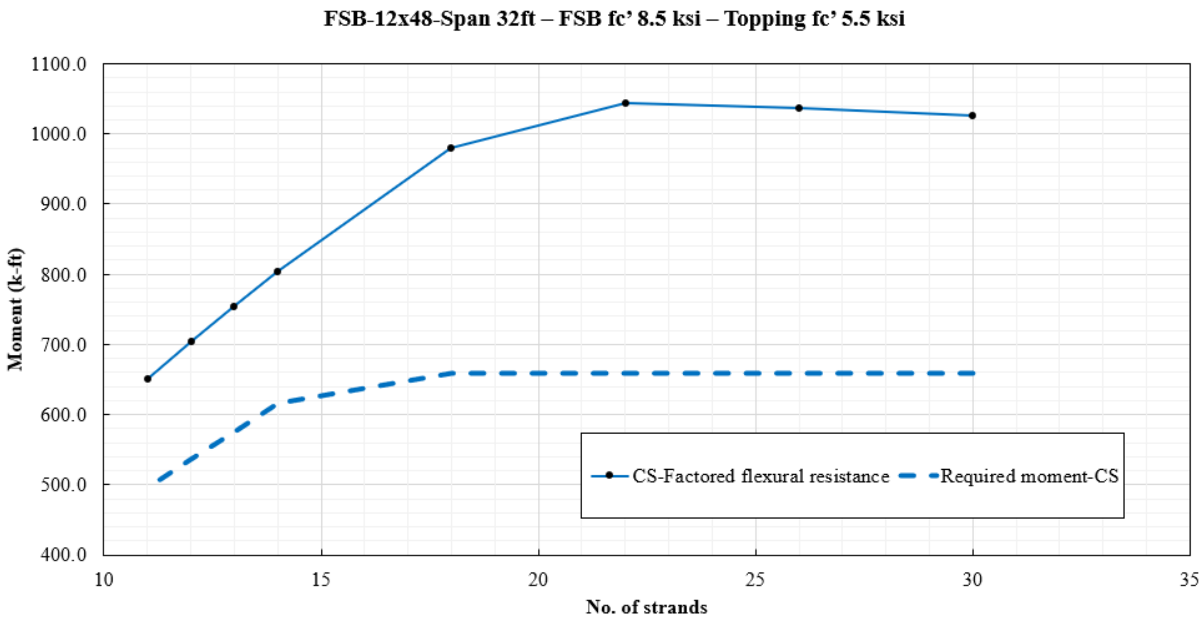


**Figure 9-26. Required flexural resistance and factored flexural resistance vs. number of carbon steel strands**

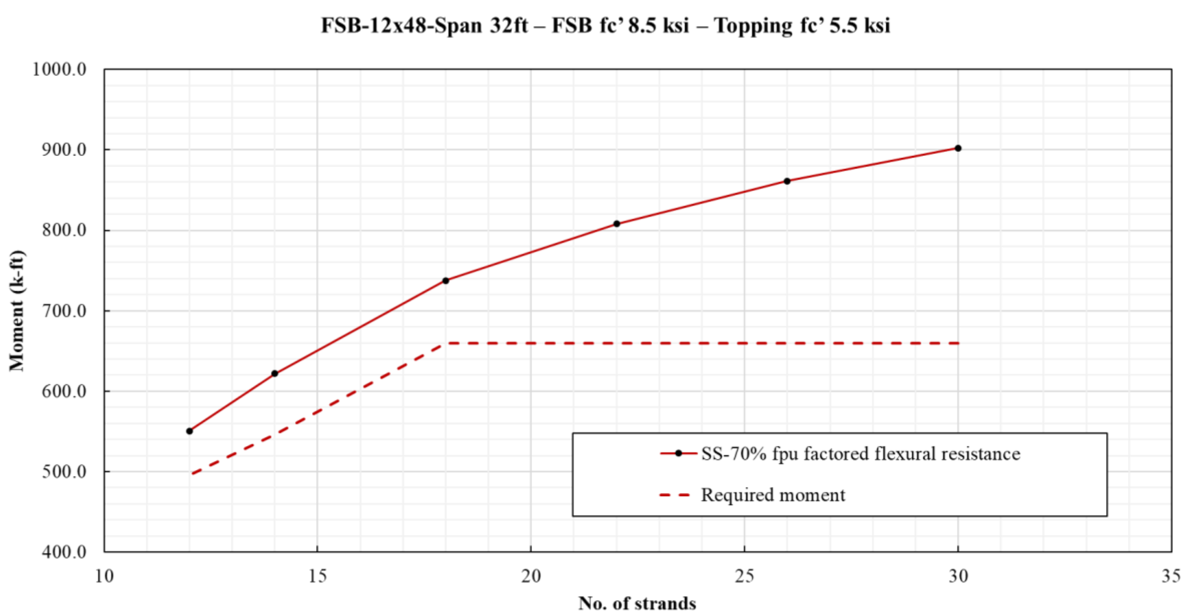


**Figure 9-27. Required flexural resistance and factored flexural resistance vs. number of stainless steel strands (at 70% $f_{pu}$)**

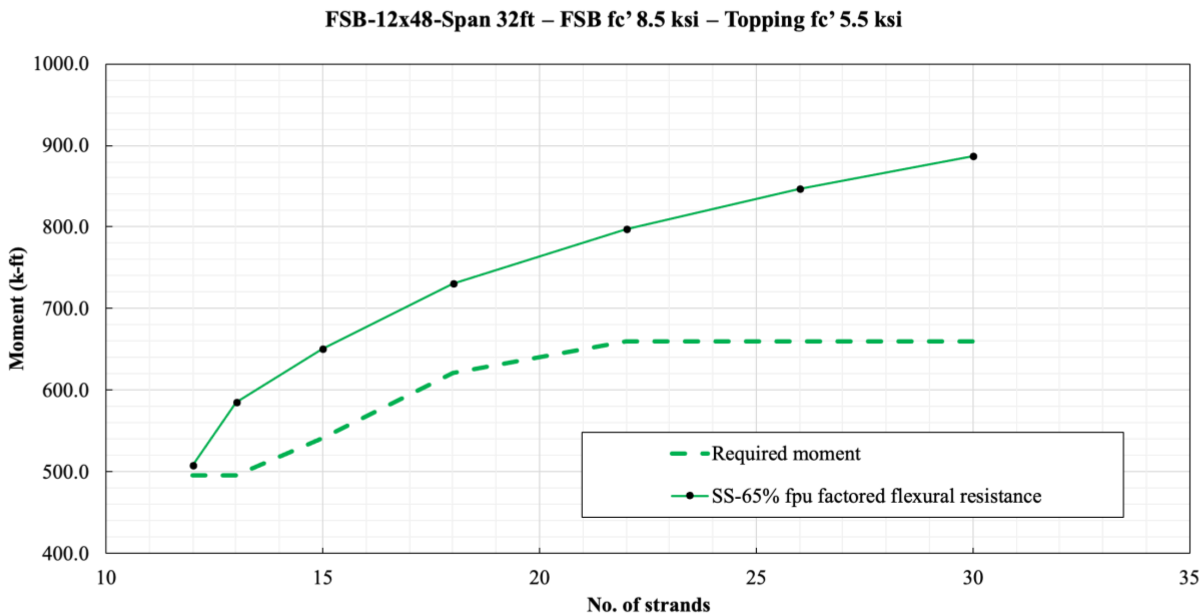


**Figure 9-28. Required flexural resistance and factored flexural resistance vs. number of stainless steel strands (at 65% $f_{pu}$)**

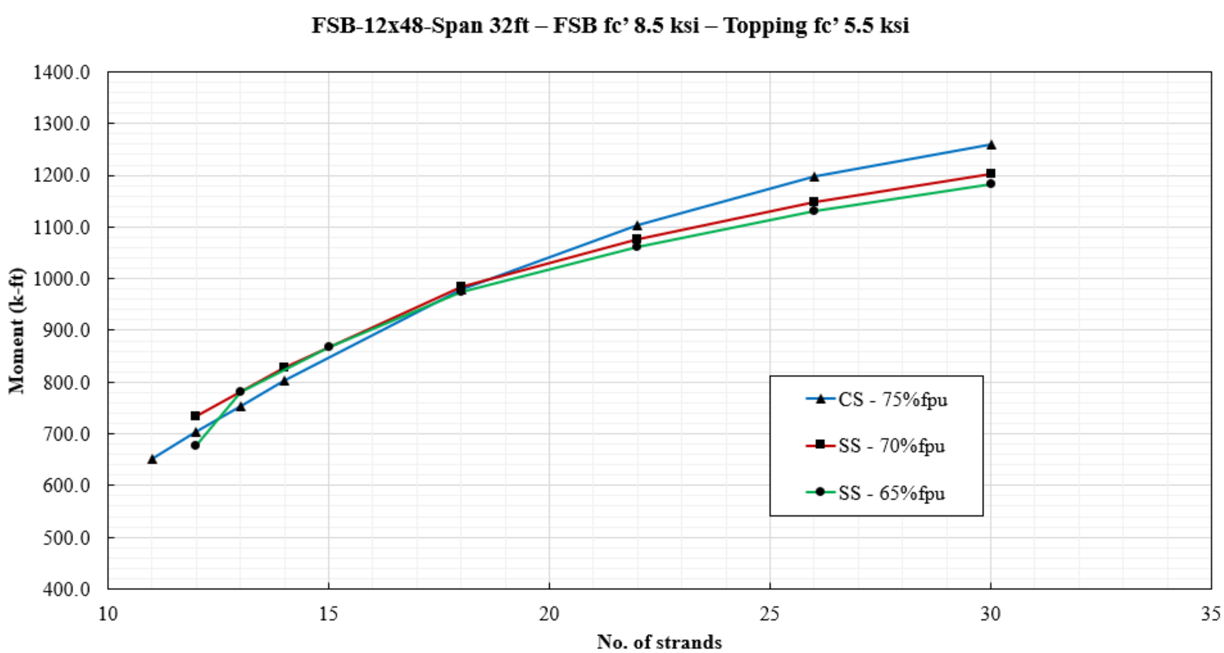


**Figure 9-29. Nominal flexural resistance variation with number of strands for carbon steel strands vs. stainless steel strands**

## 9.6.4 Flexural behavior of FSBs

According to FDOT (2026b), the environmental exposure for a bridge superstructure is defined based on the site location – whether it is located near waterbodies and whether it is exposed to high chlorides.  Environmental exposure will affect the choice of concrete strength, concrete cover and reinforcement type. This also affects the stress limit for Service III. According to AASHTO (2024), the stress limit for prestressed members located in moderate corrosion conditions is $0.19\lambda\sqrt{f_c'}$, while this limit in severe corrosive environments is reduced to $0.0948\lambda\sqrt{f_c'}$. This limit mostly controls the required number of strands for FSBs prestressed with carbon steel strands when located in severe corrosive environments as shown in Table 9-2. In the case of FSBs prestressed with stainless steel strands, camber mostly controls the required number of strands.

**Table 9-2. Carbon steel strands (at 75% $f_{pu}$) vs. stainless steel strands (at 70% $f_{pu}$) design comparison for severe corrosive conditions**

| Section type | Strand type | Span | No. of strands required for camber | No. of strands required for Service III | No. of strands required for flexural resistance | Design controlled by |
|---|---|---|---|---|---|---|
| **12x48** | SS | 32 | 14 | 12 | 11 | Camber |
| **12x48** | CS | 32 | 13 | 12 | <11 | Camber |
| **12x54** | SS | 36 | 19 | 16 | 15 | Camber |
| **12x54** | CS | 36 | 17 | 16 | 11 | Camber |
| **12x60** | SS | 36 | 20 | 17 | 16 | Camber |
| **12x60** | CS | 36 | 18 | 17 | 12 | Camber |
| **15x48** | SS | 44 | 19 | 17 | 17 | Camber |
| **15x48** | CS | 44 | 16 | 17 | 13 | Service III |
| **15x54** | SS | 46 | 22 | 21 | 20 | Camber |
| **15x54** | CS | 46 | 20 | 19 | 15 | Service III |
| **15x60** | SS | 48 | 27 | 25 | 24 | Camber |
| **15x60** | CS | 48 | 22 | 24 | 18 | Service III |
| **18x48** | SS | 50 | 20 | 19 | 19 | Camber |
| **18x48** | CS | 50 | 17 | 18 | 14 | Service III |
| **18x54** | SS | 52 | 24 | 22 | 22 | Camber |
| **18x54** | CS | 52 | 20 | 21 | 16 | Service III |
| **18x60** | SS | 52 | 26 | 24 | 24 | Camber |
| **18x60** | CS | 52 | 22 | 23 | 18 | Service III |

The previously verified analytical model was used to evaluate flexural behavior by plotting the moment-curvature relationship for each design. The required number of strands in the case of FSBs prestressed with stainless steel strands with a jacking stress of 70% $f_{pu}$ is higher than if the FSBs are prestressed with carbon steel strands, as shown in Table 9-2.

The flexural behaviors of the designs were compared by evaluating the net tensile strain, moment-curvature relationship, reserved capacity index, and load-deflection relationship. From

Figure 9-30, the evaluated 12x48 FSB section had similar net tensile strain for a given number of strands for all three strand scenarios.

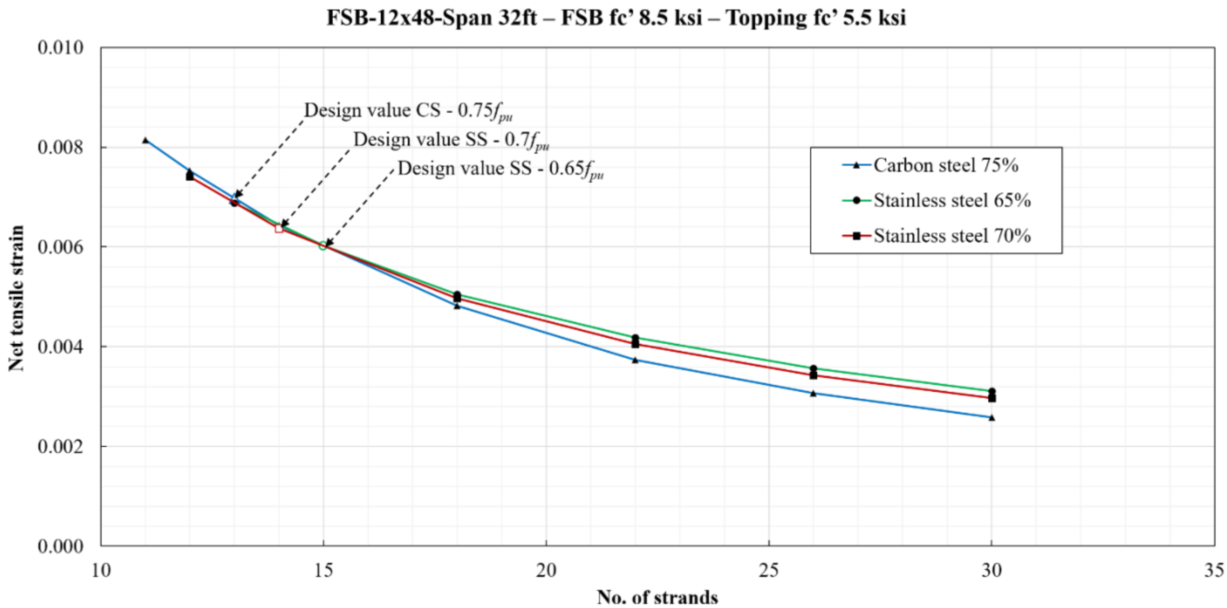


**Figure 9-30. Net tensile strain (N.T.S) comparison between CS designs and SS designs**

Figure 9-31 shows the moment-curvature relationships for the 12x48 FSB designs with the controlling number of strands for each strand scenario (13 carbon steel strands at 75% $f_{pu}$, 14 stainless steel strands at 70% $f_{pu}$, and 15 stainless steel strands at 65% $f_{pu}$; the moment-curvature curves are similar in shape and magnitude. As shown in Figure 9-32, all FSB sections evaluated show similar moment-curvature relationships for the strand scenarios.

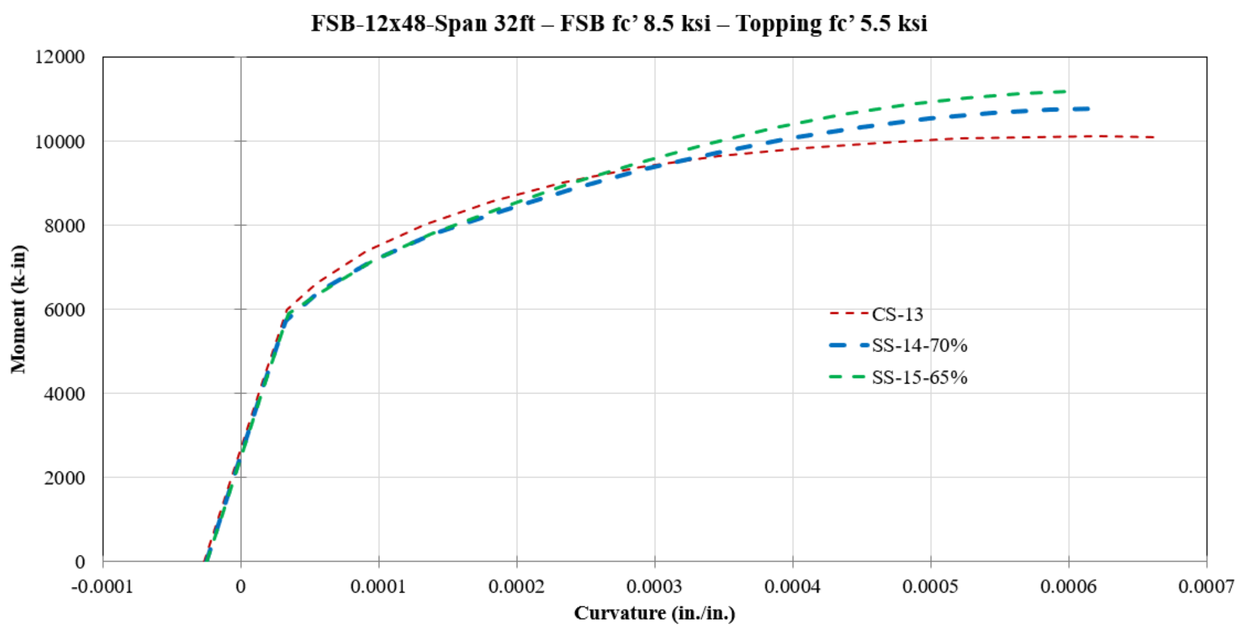


**Figure 9-31. Moment-curvature relationship comparison between CS designs and SS designs**

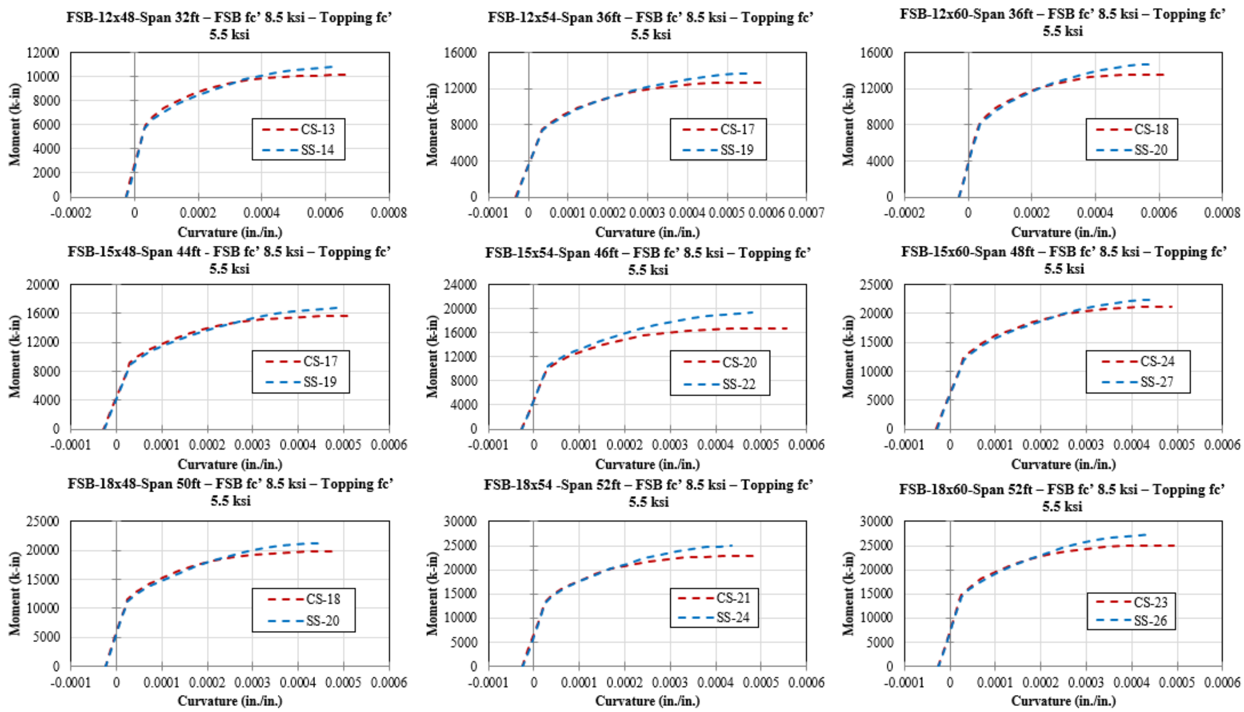


**Figure 9-32. Moment-curvature relationship for all 9 design cases (CS at 75% $f_{pu}$ and SS at 70% $f_{pu}$)**

Table 9-3 provides, for the controlling design cases presented in Table 9-2, values taken from the flexural model for the moment capacity, cracking moment, curvatures at ultimate and cracking, reserved capacity index, and net tensile strain. These values were obtained using an Excel-based flexural model that was validated against the experimental data.

The designs with stainless steel strands achieve slightly higher moment capacities and lower curvatures at ultimate. Whereas, the cracking moment and curvature are somewhat lower when each section is designed with stainless steel strands.

Based on the reserved capacity index values in Table 9-3, the ductility of members designed with stainless steel strands is on average 91.5% of those designed with carbon steel strands. Also, the net tensile strain of members with stainless steel strands is on average within 87.5% of that for members with carbon steel strands.

Furthermore, the analytical model was used to generate the load-deflection curves (Figure 9-33) for the designed 12x48 FSB loaded similarly to experimental tests in four-point bending. Comparing the load-deflection relationships, the FSBs prestressed with stainless steel strands reach higher deflection compared to the FSB prestressed with carbon steel strands. In addition, the higher required number of strands for the stainless steel strand designs results in higher load capacity.

**Table 9-3. Ductility comparison**

| Section type | Strand type | Span (ft) | Ultimate moment (k-ft) | Cracking moment (k-ft) | Ultimate curvature (in./in.) | Cracking curvature (in./in.) | Reserved capacity index | Net tensile strain |
|---|---|---|---|---|---|---|---|---|
| **12x48** | SS | 32 | 897.3 | 476.8 | 0.000625 | 0.000032 | 19.3 | 0.00637 |
| **12x48** | CS | 32 | 841.6 | 498.3 | 0.000665 | 0.000033 | 20.0 | 0.00698 |
| **12x54** | SS | 36 | 1138.6 | 608 | 0.000556 | 0.000035 | 16.0 | 0.00533 |
| **12x54** | CS | 36 | 1054.3 | 621.8 | 0.000601 | 0.000035 | 17.0 | 0.00601 |
| **12x60** | SS | 36 | 1222.7 | 662.4 | 0.000579 | 0.000035 | 16.6 | 0.00568 |
| **12x60** | CS | 36 | 1128.5 | 669.9 | 0.000628 | 0.000035 | 18.2 | 0.00642 |
| **15x48** | SS | 44 | 1392.5 | 733 | 0.000485 | 0.000029 | 16.7 | 0.00573 |
| **15x48** | CS | 44 | 1303.4 | 760 | 0.000525 | 0.000030 | 17.8 | 0.00644 |
| **15x54** | SS | 46 | 1605.8 | 875.2 | 0.000479 | 0.000031 | 15.3 | 0.00562 |
| **15x54** | CS | 46 | 1397.8 | 822.5 | 0.000556 | 0.000029 | 19.4 | 0.00701 |
| **15x60** | SS | 48 | 1866.0 | 995.8 | 0.000452 | 0.000031 | 14.7 | 0.00513 |
| **15x60** | CS | 48 | 1759.0 | 1030.4 | 0.000487 | 0.000031 | 15.7 | 0.00577 |
| **18x48** | SS | 50 | 1777.3 | 925.2 | 0.000451 | 0.000024 | 18.5 | 0.00647 |
| **18x48** | CS | 50 | 1654.5 | 959.2 | 0.000489 | 0.000025 | 19.7 | 0.00726 |
| **18x54** | SS | 52 | 2081.1 | 1091.9 | 0.000434 | 0.000025 | 17.4 | 0.00612 |
| **18x54** | CS | 52 | 1909.2 | 1115.5 | 0.000482 | 0.000025 | 19.2 | 0.00713 |
| **18x60** | SS | 52 | 2275.1 | 1196.7 | 0.000445 | 0.000025 | 18.0 | 0.00634 |
| **18x60** | CS | 52 | 2090.7 | 1230.1 | 0.000493 | 0.000025 | 19.8 | 0.00735 |

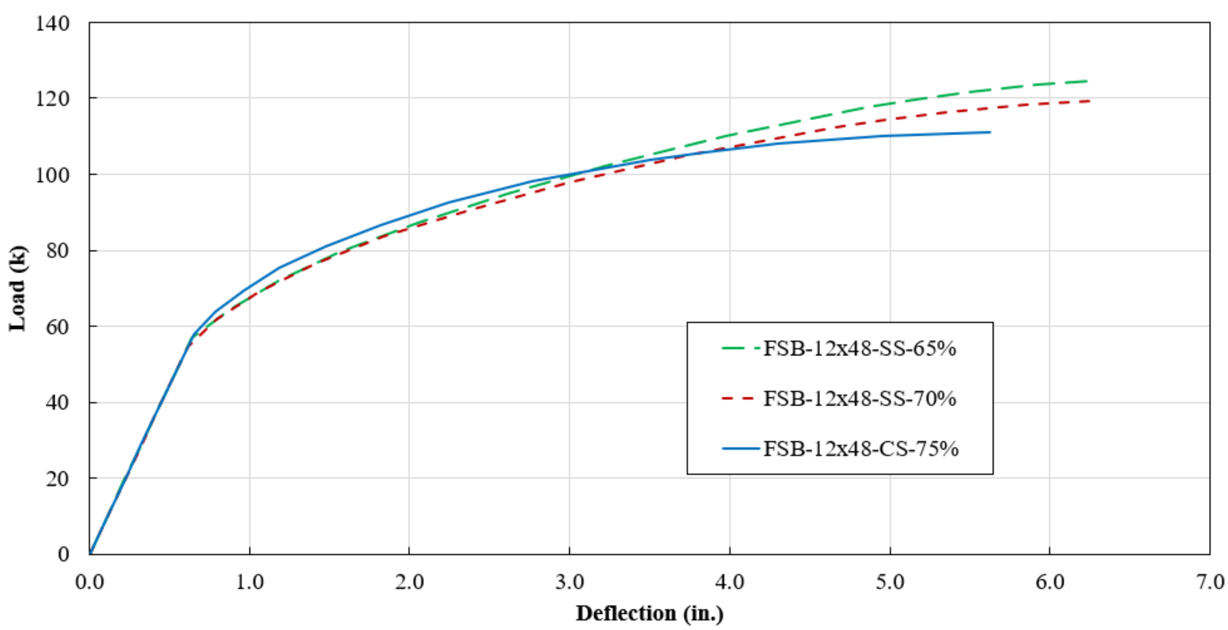


**Figure 9-33. Load-deflection relationship for 12x48-32ft FSB design**

## 9.6.5 Dormant strands

Dormant prestressing strands are sometimes placed in the top region of a prestressed concrete beam to reduce stresses at prestress release. They are also used to stabilize the lateral reinforcement during construction. Typically, four dormant strands are provided in an FSB, as per FDOT standard plans (FDOT, 2026a), and are stressed to 10 kips. For an FSB prestressed with stainless steel strands, if these dormant strands are removed, the section will still satisfy the design requirements. The effects of removing the dormant strands are an increase in camber and a reduction in the required number of strands (when Service III controls the design), which results in a more economical design. This will also slightly increase the maximum span length for all FSB section sizes.

## 9.6.6 c/d ratio

Previous literature aimed to ensure ductility by limiting the net tensile strain (N.T.S.) and $c/d$ ratio. Figure 9-34 shows the variation of $c/d$ ratio with the number of strands for FSBs with stainless steel strands and with carbon steel strands. For smaller numbers of strands, the $c/d$ values are almost equal for both stainless steel strands and carbon steel strands. However, because the designs with stainless steel require a higher number of strands, the $c/d$ ratio for carbon steel designs is lower. Further extension for more sections of this comparison is shown in Figure 9-35.

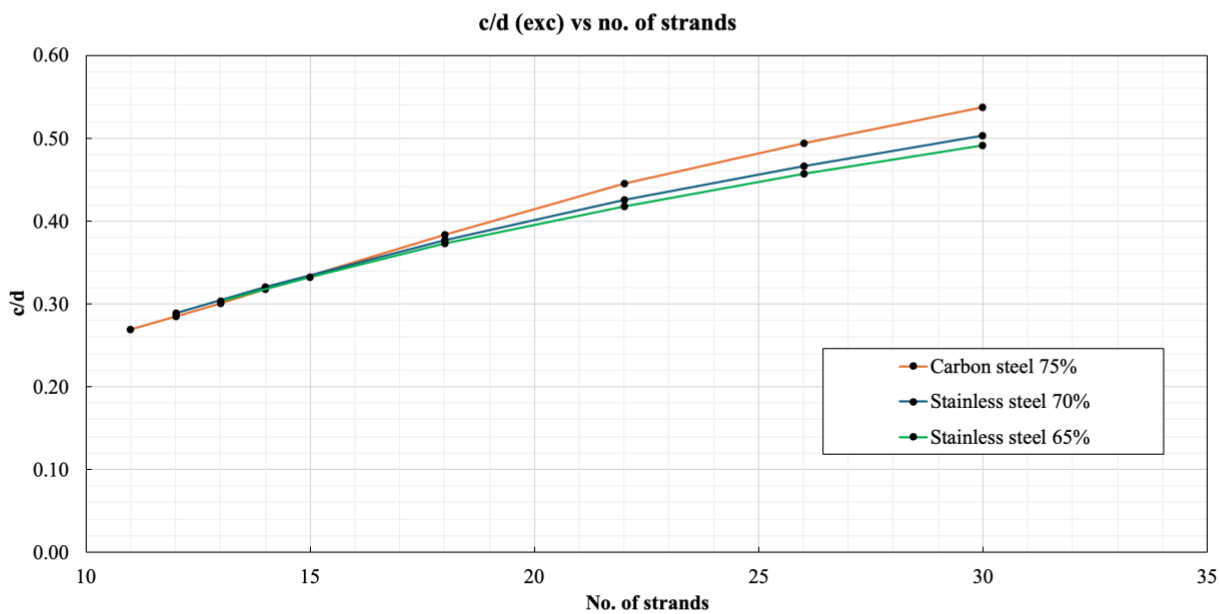


**Figure 9-34. Comparison of *c/d* values for FSB-12x48 with span of 32 ft for CS and SS designs**

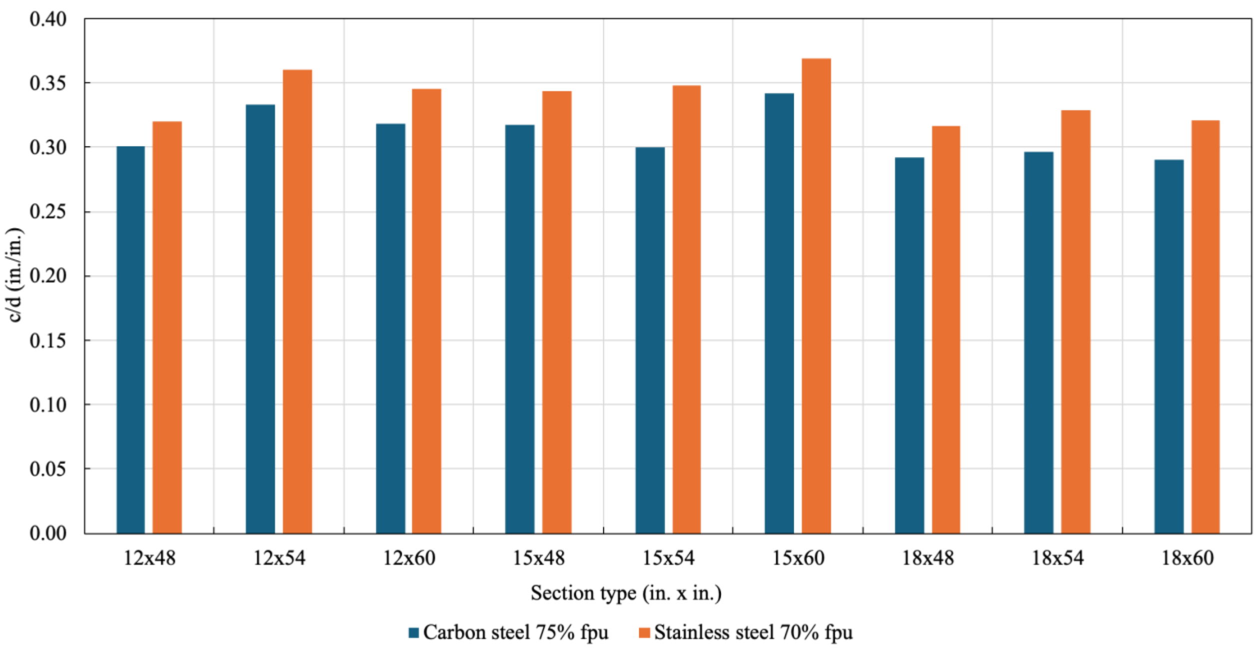


**Figure 9-35. $c/d$ values for designs with different FSB sections and prestressing materials (carbon steel at 75% $f_{pu}$ and stainless steel at 70% $f_{pu}$)**

## 9.7 Summary and conclusions

The analytical model for this project was created to include tension stiffening, which accounts for the tensile stresses in the concrete between cracks. Previous research on deep members with narrow webs, where the depth-to-web width ratio is significantly greater than one, concluded that tension stiffening has negligible effect on the flexural behavior of prestressed concrete members. However, no studies have investigated the contribution of tension stiffening in shallow members such as slab beams, where the depth-to-width is significantly less than one. For wide flexural members, flexural cracks might be largely spaced in the transverse direction of the member, leaving uncracked concrete between those flexural cracks. The uncracked concrete most likely contributes to the flexural behavior of the concrete. Therefore, the analytical model was modified to account for tension stiffening in the concrete; the model developed by Bentz (2000) was employed, and the equation proposed by Collins and Mitchell (1991) was used to calculate the effective area of the cracked concrete under tension.

The modified analytical model better predicts the experimental flexural behavior of the tested FSBs. Then, the modified analytical model was used to conduct parametric studies to investigate the flexural behavior of FSBs prestressed with carbon steel or stainless steel strands.

One method to evaluate the flexural behavior of a flexural member is by measuring its ductility, which can be determined from the moment-curvature relationship and/or load-deflection relationship. Several ductility equations from the literature were examined. It was concluded that the ratio of ultimate curvature to cracking curvature might be a suitable measure for the ductility of prestressed concrete FSBs. This ductility measure is referred to as Reserved Capacity Index in this report.

A wide range of Florida slab beam bridges with different span lengths and different FSB sections were designed. Those designs were performed to determine the minimum required number of carbon steel or stainless steel strands to satisfy the AASHTO LRFD (AASHTO, 2024) and FDOT SDG (FDOT, 2026b) requirements. Regardless of the strand material, it was found that no design was controlled by the strength limit state. Most designs were controlled by camber (FDOT requires positive camber under service loads), while some designs were controlled by the Service III Limit State for bridges prestressed with carbon steel strands. Therefore, for the same bridge design, a larger number of stainless steel strands are required compared to the required number of carbon steel strands because the initial prestressing stress – which is a significant parameter for designs controlled by camber and Service III Limit State – is lower for stainless steel. Because of the controlling limit state, an FSB bridge prestressed with stainless steel strands produces a moment-curvature curve that is relatively similar to an FSB bridge prestressed with carbon steel strands. This indicates that both beams might result in a comparable ductility index. The failure mode is concrete crushing regardless of the strand material. This means that the limited ultimate strain in the stainless steel strands does not influence the design of FSBs for the sections studied. The load-deflection relationship was generated using a load setup similar to the one used in the experiments, four-point bending. Comparing the relationship between the same bridge design with different types of prestressing strands showed similar behavior. The FSB design with stainless steel prestressing strands showed higher values of deflection that are mainly due to the larger number of strands, yielding higher moment resistance.

Currently, FDOT SDG limits the initial prestressing stress of stainless steel strands to 65% of its ultimate stress ($f_{pu}$ = 240 ksi), compared to 75% of the ultimate stress ($f_{pu}$ = 270 ksi) for carbon steel strands. An initial prestressing stress limit of 70% of 240 ksi, which is the limit used in the experimental specimens in this project, was investigated for bridge designs. An initial prestressing limit of 70% of $f_{pu}$ significantly reduces the required number of strands.

The effect of dormant strands on the required number of strands was investigated. Dormant strands are placed near the top of the section to aid in the placement of transverse reinforcement and to reduce tensile stresses at release. Analytical studies revealed that removing the dormant strands might slightly reduce the required number of stainless steel strands or increase the maximum span length of an FSB section.

The following conclusions are made:

1. Incorporating tension stiffening in the FSB flexural model results in better predictions of the capacity and tensile strain in strands. FSBs have higher width-to-depth ratios compared to prestressed concrete girders, which results in more significant contribution in stiffness from cracked concrete in the tensile strain region, causing higher stiffness beyond the cracking moment. Combining models by Bentz (2000) and Collins and Mitchell (1991) are recommended for tension stiffening modeling. However, in this research, including tension stiffening slightly overpredicted the cracking load in some cases. Therefore, for design purposes, it may not be prudent to use the tension stiffening.
2. Increasing the allowable stress immediately prior to transfer ("initial prestressing") for stainless steel strands from 65% to 70% of ultimate tensile strength ($f_{pu}$ = 240 ksi) results

in a lower number of strands with relatively the same ductility for FSBs. However, there is concern about premature rupture of strands during the detensioning process, and using a higher initial prestressing stress would contribute to that issue. The last strands that are detensioned are the most likely to be affected. Also, the shorter the free length of the strands (the distance between the anchors and the end of the concrete member), the more likely the strands would rupture prematurely, theoretically.

3. Dormant strands are typically provided in a prestressed concrete member to reduce tensile stresses during detensioning and help secure reinforcement. Not using dormant strands, however, will increase camber and decrease the required number of strands without exceeding the serviceability limit states during strand release. However, constructability of placing mild transverse reinforcement would need to be considered.
4. FSB designs with prestressed stainless steel strands exhibit similar ductile behavior to FSB designs with carbon steel strands. FSB designs with stainless steel strands typically require a larger number of strands, causing higher flexural capacity and deformation as compared to a design with carbon steel strands. However, the differences are not significant.

# CHAPTER 10 – FSBs WITH GFRP: TESTS AND DATA

## 10.1 Introduction

The durability and performance of prestressed concrete structures are vitally important, especially in aggressive corrosive environments. Typical carbon steel reinforcement, even though widely used for its familiar mechanical properties, is vulnerable to corrosion, leading to deterioration, increased maintenance costs, and reduced service life. Population and traffic demand increase the need for more resilient reinforcement solutions. In response, non-metallic alternatives such as GFRP bars have emerged as an option due to their non-corrosive nature and cost effectiveness.

Shallow precast prestressed concrete members with C-I-P toppings are widely used for short-span bridges. The performance of these structures depends on the lateral reinforcement resisting shear forces. The lateral reinforcement reduces cracking in the anchorage zone, ensures composite action at the interface between the precast member and cast-in-place topping, and resists shear forces.

Existing design specifications, including AASHTO LRFD Bridge Design Specifications (AASHTO, 2024) and ACI 318 (ACI Committee 318, 2025), include design models that are based on research performed on carbon steel reinforcement. Those models may not be directly applicable to a prestressed concrete member with GFRP as lateral reinforcement due to its unique mechanical properties such as the absence of yielding, lower elastic modulus, and weaker tensile strength at bent locations.

This chapter investigates using GFRP bars as lateral reinforcement in a shallow prestressed concrete member, the FSB, by testing two full-scale specimens with instrumented lateral reinforcement under a four-point bending test setup. First, available literature is reviewed, and limitations are identified. Then, experimental data is presented and compared to the existing codes. Finally, conclusions are made about the use of GFRP reinforcement as lateral reinforcement in FSBs.

## 10.2 Literature review

### 10.2.1 Vertical shear

The shear design approach in the AASHTO LRFD Bridge Design Specifications (AASHTO, 2024) is a mechanistic model based on the Sectional Design Model, originally derived from the Modified Compression Field Theory (MCFT) (Hawkins and Kuchma, 2008). A method proposed by Vecchio and Collins (1986) was adopted in the 1994 AASHTO LRFD Bridge Design Specifications (Hawkins and Kuchma, 2008). The Sectional Design Model in AASHTO LRFD is comprehensive, versatile, and applicable to both reinforced and prestressed concrete, but it posed challenges to engineers due to the iterative process (Holt et al., 2022). A simplification of MCFT by Bentz et al. (2006) led to a non-iterative approach, which was adopted into AASHTO LRFD. All these models were developed for designing carbon steel rebar as transverse reinforcement; however, the applicability of these models to different types of materials is still being investigated.

Corrosion is a common problem in reinforced concrete with carbon steel rebars (Ahmed et al., 2010a). Corrosion-resistant or corrosion-free material as reinforcement in concrete structures in severe environments is becoming widely accepted as a replacement for steel and to avoid deterioration caused by corrosion. FRP as reinforcement in concrete has shown to be a promising solution (Plecnik and Ahmad, 1989), and extensive research has been conducted on its use. FRPs are classified based on the type of fiber used, such as carbon (CFRP), aramid (AFRP), basalt (BFRP), and glass (GFRP). Among these, GFRP rebars have gained greater attention due to their non-corrosive nature and cost-effectiveness, making them a practical alternative to carbon steel in many structural applications (Al-Kaimakchi and Rambo-Roddenberry, 2022).

GFRP rebars have been investigated as transverse reinforcement in reinforced concrete. Compared to steel, GFRP rebars generally have relatively lower elastic modulus, higher tensile strength but without a distinct yield point, and approximately 40% reduced strength in bent portions (Nanni et al., 2014). Research has shown that, similar to steel stirrups, GFRP stirrups enhance shear capacity after the formation of the first crack, and that stirrup spacing affects the shear resistance (Ahmed et al., 2010b). Design codes calculate shear resistance using the same basic expression:

$$V_n = V_c + V_s \qquad \text{(Eq. 10.1)}$$

where
$V_c$ = the concrete contribution (kips), and
$V_s$ = the transverse reinforcement contribution (kips)

However, each code evaluates theses terms differently including only the part of the section in compression. For example, ACI CODE-440.1R-15 (ACI, 2015) and ACI CODE-440.11 (ACI Committee 440, 2022) for non-prestressed applications estimate the concrete contribution as:

$$V_c = 5\sqrt{f_c'}b_w(kd) \qquad \text{(Eq. 10.2)}$$

where
$f_c'$= the concrete compressive strength (ksi),
$b_w$ = the web width (in.),
$d$ = the effective depth (in.), and
$k$ = a factor related to the depth of the neutral axis.

In AASHTO LRFD, the concrete contribution is calculated as follows:

$$V_c = 0.0316\beta\lambda\sqrt{f_c'}b_v d_v \qquad \text{(Eq. 10.3)}$$

where
β = a factor for cracked concrete ability to transfer tension and shear,

$\lambda$ = the concrete density modification factor (taken as 1.0 for normal concrete),
$b_v$ = the effective web width, and
$d_v$ = the effective shear depth, calculated as the distance perpendicular to the neutral axis between the tensile and compressive forces.

The shear contribution of GFRP stirrup reinforcement, assuming a nominal 45° critical shear crack angle, is given as:

$$V_f = \frac{A_{fv} f_{fv} d}{s} \quad \text{(Eq. 10.4)}$$

where
$A_{fv}$ = the area of FRP transverse reinforcement ($in^2$) within spacing s (in.),
$s$ = stirrup spacing (in.), and
$f_{fv}$ = the FRP tensile strength used in shear design (ksi).

In AASHTO (2018), concrete shear strength contribution for GFRP-reinforced members is calculated using an expression similar to that used for steel, which is dependent on the contribution of steel flexural reinforcement. However, a specific equation that reflects the behavior of stainless steel strands is not currently available. Recently, NCHRP project 12-120 investigated this issue and proposed guidance for consideration to the AASHTO technical committee for concrete design. Therefore, the shear contribution in this study is based on the AASHTO LRFD expression for carbon steel. AASHTO LRFD expressions for GFRP are similar to those used for steel, except using the mechanical properties of GFRP reinforcement.

### 10.2.2 Anchorage zone

An essential aspect of prestressed concrete design is controlling crack formation in the anchorage zone. The anchorage zone refers to the region where the prestressing force is transferred from the prestressing strands to the concrete. This transfer is gradual by bonding between the strands and concrete until the force is fully transferred to the member at a distance called the transfer length. This force causes tensile stress in the normal direction to the prestressing force, which causes cracks. Cracks may occur during the strands' release at the end zone of the members, and standards require closely spaced transverse reinforcement in this zone. The reinforcement does not completely prevent cracking but plays a key role in limiting it (Crispino et al., 2009). These cracks are more likely to form in deeper members having an I or T section than rectangular shallow members, because of the small width of the cross-section that resists tensile forces in the anchorage zone (Marshall and Mattock, 1962).

The anchorage zone has been investigated since the 1960s, and no significant change has occurred in the anchorage zone provisions. Marshall and Mattock (1962) proposed simple expressions for the required area to resist splitting at the anchorage zone. They also suggested uniformly spacing end zone reinforcement within a distance of a fifth of the girder depth. Currently, AASHTO LRFD (AASHTO, 2024) limits the allowable stress in end zone transverse reinforcement to 20 ksi and requires reinforcement to resist 4 percent of the total prestress force at transfer. The reinforcement needs to be at an equal spacing within a distance of $h/4$, where $h$ is either the depth or the width, depending on the section type. However, in AASHTO LRFD for

GFRP reinforcement, there are no requirements established for the use of GFRP as transverse reinforcement in the anchorage zone. To fill this knowledge gap, NCHRP project 12-121 is currently working on recommendations.

### 10.2.3 Interface shear

Concrete beams consisting of girders with a cast-in-place topping are described as composite beams. Typically, such types of beams have girders that are fabricated at a precast facility and then moved to their final location in the structure, where the concrete topping is applied. This type of construction reduces the time for project delivery, and it has the advantage of producing lighter and shallower beams for transportation to the construction site. However, having concrete cast at two different times forms a cold joint at the interface between them. An effective mechanism is required at the interface to transfer stresses and ensure these two components work together monolithically. Such a mechanism is called interface shear (Figure 10-1).

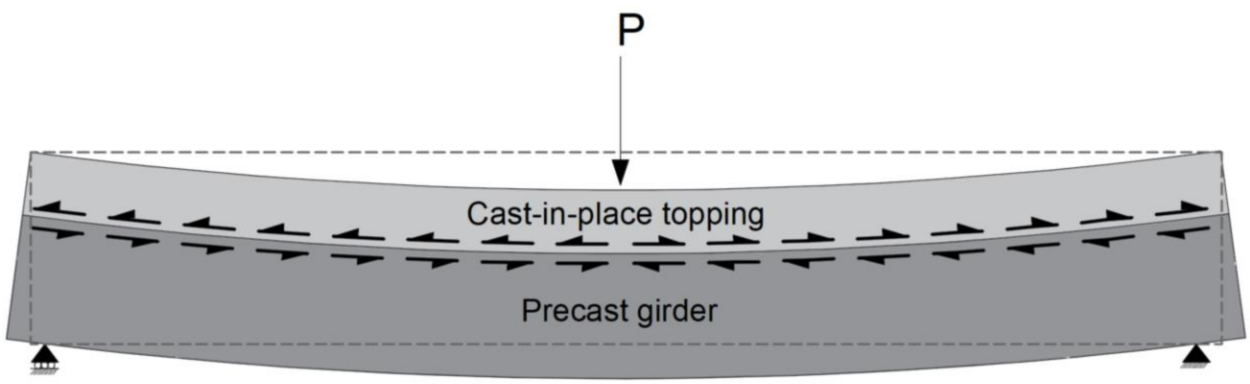


**Figure 10-1. Interface shear in composite members**

This mechanism relies on three primary parameters: cohesion from concrete bond and aggregate interlock; friction between the surfaces; and dowel action from the reinforcement crossing the interface. At low load levels, cohesion dominates, while shear resistance transitions to a combination of friction and dowel action at higher loads. Friction mechanisms are often explained by the interface-shear model, which highlights the role of reinforcement-induced tensile stresses in increasing regular forces at the interface and enhancing friction. These principles are the basis for interface shear provisions in principal design codes, including ACI Committee 318 (2025), AASHTO (2024), and CSA Group (2025).

Longitudinal interface shear stresses can be determined using equilibrium conditions at critical sections under the ultimate load. This approach is used in ACI CODE-318-22, ACI CODE-440.11-22, and CSA S6:25 and S806:26. The horizontal shear is defined as the difference in the compressive (C) and tensile (T) forces between two sections, as shown in Figure 10-2, and the following expression is used to find shear stress at the interface:

$$v_h = \frac{C}{bl} \qquad \text{(Eq. 10.5)}$$

where
$v_h$ = horizontal shear stress at the interface (ksi),
$l$ = the length is the distance between two sections (in.), and
$b$ = width of the section at the interface (in.).

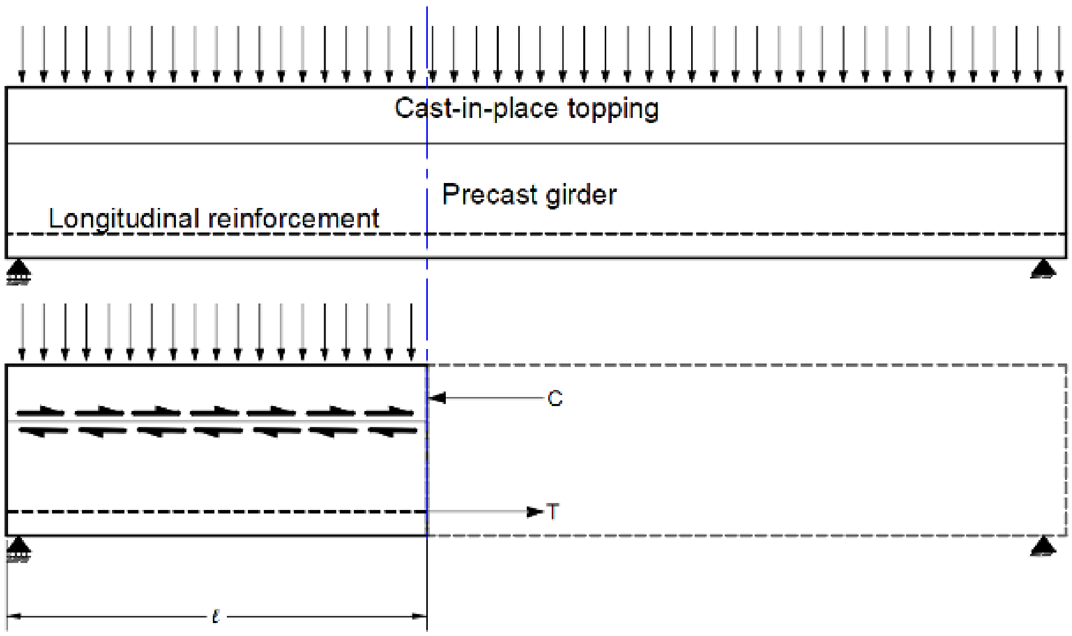


**Figure 10-2. Evaluation of the longitudinal shear interface by the equilibrium condition**

Another way to evaluate interface shear force at the critical section at the ultimate state is using the factored vertical shear force in the following expression:

$$v_h = \frac{V}{bd} \quad \text{(Eq. 10.6)}$$

where $d$ is the depth of the section (in.).

The concept of interface shear was first discussed by Birkeland and Birkeland (1966). They suggested a model that considered only friction in the interface. The model indicated that when the concrete-to-concrete rough interfaces slide against each other, a separation crack occurs due to the roughness. The separation will cause tensile stress in the reinforcement across the interface. The reinforcement embedded in the concrete will cause normal compressive forces at the interface and consequently increase friction. Their study suggested the following model:

$$V_n = A_s\, f_y\, tan\phi \quad \text{(Eq. 10.7)}$$

where
$A_s$ = the area of reinforcement across the interface (in$^2$),
$f_y$ = the yield strength of reinforcement (ksi), and
$\phi$ = the angle of internal friction (for a roughened artificial interface, the value is $tan\phi = 1.4$).

Based on push-off tests, the model proved a good lower bound for experimental results (Birkeland and Birkeland, 1966). It also suggested limiting the shear stress at the gross area to 800 psi for an interface reinforcement ratio higher than 0.015. Mast (1968) suggested the same model and proposed an approach to calculate the interface horizontal shear. The approach calculates horizontal shear at the interface by equilibrium of the normal forces at the ultimate limit state in the critical section (Figure 10-3).

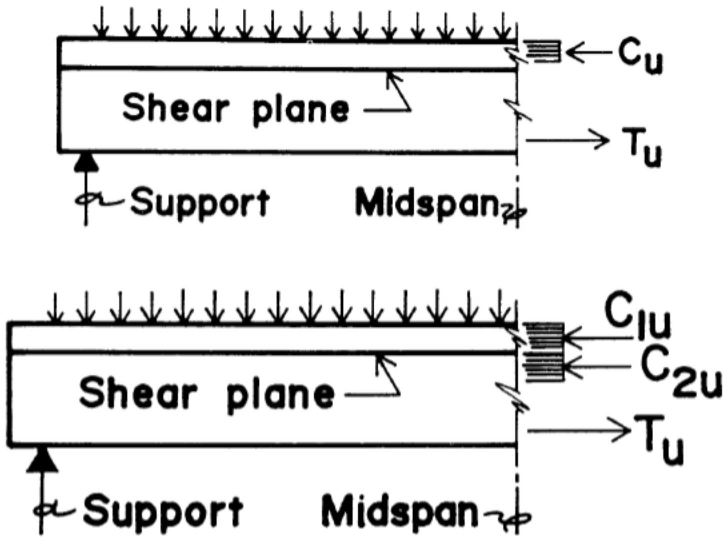


**Figure 10-3. Horizontal shear at ultimate capacity**

Hofbeck et al. (1969) performed a more extensive study on the interface shear. This study further limited the interface stress to 600 psi at a 0.015 reinforcement ratio or higher. It also successfully related push-off tests to the interface shear. These tests were first used by Anderson and the Portland Cement Association (PCA) (Mast, 1968). The tests use L-shaped specimens to simulate direct shear stresses, including horizontal or vertical setups. However, alternative methods such as slant shear tests, splitting tests, pull-off tests, corbel tests, and beam tests have also been used, each with a distinct advantage (Soltani and Ross, 2017). For example, Loov and Patnaik (1994) used beams under a 3-point test setup to evaluate shear strength at the interface. That is relevant for cast-in-place concrete bridge decks and girders. Besides that, push-off tests on the pre-cracked interface are more relevant to the cold joints at the interface between girders and bridge decks. Several researchers performed push-off tests on specimens with a cold joint (Harries et al., 2012; Shaw and Sneed, 2014; and Kahn and Mitchell, 2002).

Until now, steel reinforcement has proved reliable in interface shear. However, cast-in-place slabs are continuously exposed to corrosive, harsh environments. As a result, reinforcement may become deficient due to corrosion, requiring inspection, maintenance, and replacement. Therefore, interest in corrosion-resistant materials is rising. GFRP is a well-known nonmetallic material used in structures. It is desirable due to its economy compared to other alternatives (Deshmukh et al., 2023). Many codes have issued design guidelines for GFRP, such as shear reinforcement CSA S806:26 and S6:25, ACI Code 440.11-22, and AASHTO (2018).

Despite extensive research on interface shear in steel-reinforced concrete, limited studies exist on the role of GFRP reinforcement in interface shear transfer, particularly in prestressed concrete.

Alkatan (2016) highlighted the need for a minimum reinforcement ratio to activate GFRP's contribution to interface shear. Al-Kaimakchi and Rambo-Roddenberry (2022) demonstrated that replacing stainless steel with GFRP reduces shear capacity and may alter the failure mode, emphasizing the anisotropic and non-ductile nature of GFRP. While AASHTO LRFD applies the same shear-friction equations for GFRP and steel, experimental studies have shown discrepancies depending on design parameter assumptions. For instance, push-off test results for GFRP-reinforced specimens revealed that AASHTO overestimates GFRP interface shear strength compared to experimental data (Vega et al., 2024). Moreover, ACI 440.11 lacks provisions for GFRP in interface shear design, and Canadian codes have also begun to address these challenges in S806:26 and S6:25.

Recently, the contribution of GFRP was investigated using 27 push-off specimen tests (Vega et al., 2024). The study included cold-joint interfaces with different reinforcement ratios. It showed that GFRP enhances the interface shear strength. Furthermore, the GFRP reinforcement improves strength through clamping force and dowel action. It was also found that interface capacity might be affected by the crack opening. Therefore, it suggests the inclusion of the elastic modulus of reinforcement in calculating the capacity. This study found that the AASHTO LRFD interface capacity is unconservative when using the full tensile strength of GFRP straight bars in push-off tests, which contradicts the results of Al-Kaimakchi and Rambo-Roddenberry (2022) full-scale beam studies.

A similar study investigates GFRP stirrups' role as shear friction reinforcement in concrete joints under various interface conditions, including roughened and non-roughened cold joints and monolithic interfaces (Aljada et al., 2024). A total of 18 large-scale push-off specimens were tested under monotonic loading to failure. The study examines the effects of reinforcement type (GFRP or steel), reinforcement ratio (ranging from 0.24% to 0.47%), and interface conditions on the load-carrying capacity, slip, and reinforcement strain. It was observed that GFRP stirrups performed similarly to steel stirrups until failure, with monolithic specimens demonstrating superior load-carrying capacity compared to cold joints. The results suggest that roughening the interface marginally affects GFRP specimens, attributed to the lower modulus of elasticity of GFRP, which diminishes surface roughness effects. Additionally, the CSA S6:25 design code predictions for shear friction strength of the GFRP-RC elements were found to be conservative, while the ACI 318-25 equation using the tensile design strength of GFRP overestimated the strength in specific scenarios. This research highlights the need for revised design provisions to account for the unique mechanical properties of GFRP in shear friction reinforcement.

The growing interest in replacing steel with corrosion-resistant materials like GFRP underscores the need for further research. Although GFRP is cost-effective and durable, its unique mechanical properties—linear-elastic behavior and lower shear strength—demand a reevaluation of current design methodologies. Existing studies focus predominantly on conventional reinforced concrete, leaving a significant gap in understanding GFRP's role in prestressed concrete interface shear transfer. Investigating GFRP's performance in prestressed applications is essential to developing design guidelines that can be integrated into modern codes and standards.

## 10.3 Experimental setup and material properties

### 10.3.1 Specimens overview

Two (2) FSB specimens were constructed to investigate the GFRP contribution to shear resistance. Both specimens had a standard FDOT FSB cross-section measuring 12 in. by 48 in. and a length of 34 ft. The specimens' designs were identical in every aspect, except for the transverse reinforcement: one specimen had GFRP rebars, while the other (control specimen) had conventional carbon steel rebars. Both specimens were prestressed with 30 high-strength stainless steel (HSSS) strands as flexural reinforcement. The two specimens were named FSB-1 and FSB-4.

The FSB section includes four types of transverse reinforcement: 4K, 5E, 4D, and 3C, as shown in Figure 10-4, and 6Y. Among these, types 4K and 4D were instrumented with strain gauges, as shown in Figure 10-5. Type 4D reinforcement was instrumented in the anchorage zone to monitor strain induced during strand release at the casting yard, while type 4K reinforcement was instrumented at different locations along the length to monitor shear and interface stresses during the flexural test. Instrumentation details were presented in Chapter 3.

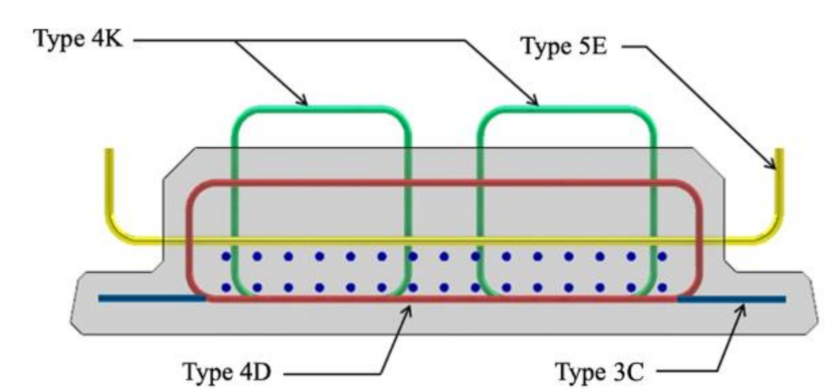


**Figure 10-4. FSB cross section with reinforcement**

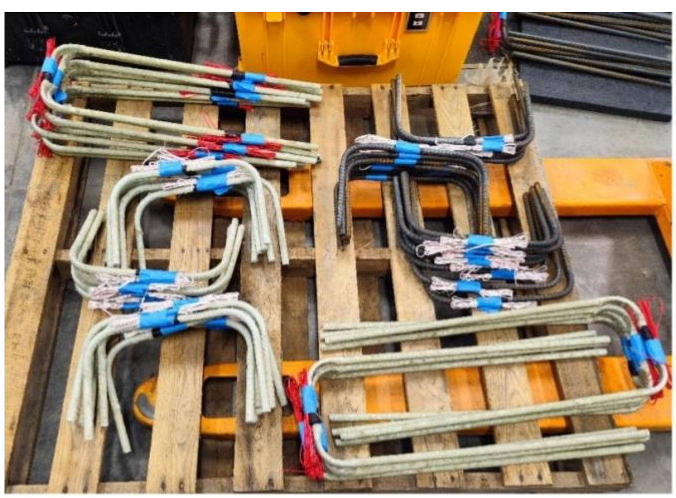

**Figure 10-5. Strain gauges installed on type 4D and 4K reinforcement**

## 10.3.2 Material properties

### 10.3.2.1 GFRP rebars

Four rebar sizes were used in specimen FSB-4: No. 3, No. 4, No. 5 and No. 6. Table 10-1 presents the manufacturer-reported mechanical properties of the GFRP rebars and their comparison with ASTM D7957/D7957M-22 (ASTM, 2022c).

**Table 10-1. GFRP manufacturer test properties**

| Property | Source | No. 3 rebar | No. 4 rebar | No. 5 rebar | No. 6 rebar |
|---|---|---|---|---|---|
| Fiber mass content (%) | Reported | 84 | 76 | 74 | 78 |
| Fiber mass content (%) | Required | 70 | 70 | 70 | 70 |
| Glass transition temperature (°F) | Reported | 221 | 232 | 236 | 231 |
| Glass transition temperature (°F) | Required | 212 | 212 | 212 | 212 |
| Degree of cure (%) | Reported | 100 | 100 | 100 | 99 |
| Degree of cure (%) | Required | 95 | 95 | 95 | 95 |
| Cross-sectional area ($in^2$) | Reported | 0.135 | 0.247 | 0.384 | 0.535 |
| Cross-sectional area ($in^2$) | Required | 0.104 – 0.161 | 0.185 – 0.263 | 0.288 – 0.388 | 0.415 – 0.539 |
| Ultimate tensile force (kips) | Measured | 21.9 | 33.4 | 50.8 | 77.0 |
| Ultimate tensile force (kips) | Required | 13.2 | 21.6 | 29.1 | 40.9 |
| Tensile modulus of elasticity (ksi) | Measured | 9,190 | 7,667 | 7,887 | 7,681 |
| Tensile modulus of elasticity (ksi) | Required | 6,500 | 6,500 | 6,500 | 6,500 |
| Ult. tensile force bent portion (ksi) | Measured | - | 21.6 | 34.5 | 46.3 |
| Ult. tensile force bent portion (ksi) | Required | - | 13.0 | 17.5 | 24.5 |
| Moisture absorption 24h (%) | Measured | 0.07 | 0.09 | 0.09 | 0.07 |
| Moisture absorption 24h (%) | Required | ≤0.25 | ≤0.25 | ≤0.25 | ≤0.25 |

### 10.3.2.2 Carbon steel rebars

Similar GFRP rebar sizes were used in FSB-1. Table 10-2 lists mill test results for carbon steel rebars, all conforming to ASTM A615/A615M-22, Grade 60 (ASTM, 2022b).

**Table 10-2. Carbon steel rebars mill test results**

| Property | Source | No. 3 rebar | No. 4 rebar | No. 5 rebar | No. 6 rebar |
|---|---|---|---|---|---|
| Yield strength (ksi) | Measured | 71 | 62.5 | 64.6 | 69.8 |
| Yield strength (ksi) | Required | 60.0 | 60.0 | 60.0 | 60.0 |
| Tensile strength (ksi) | Measured | 109.7 | 100.8 | 106 | 110.4 |
| Tensile strength (ksi) | Required | 80.0 | 80.0 | 80.0 | 80.0 |
| Ratio of actual tensile strength to actual yield | Measured | 1.54 | 1.62 | 1.65 | 1.58 |
| Ratio of actual tensile strength to actual yield | Required | 1.10 | 1.10 | 1.10 | 1.10 |
| Elongation in 8 in. (%) | Measured | 13.3 | 13.5 | 11.5 | 16 |
| Elongation in 8 in. (%) | Required | 9 | 9 | 9 | 9 |

### 10.3.3 Anchorage zone instrumentation

To monitor strain during the strand detensioning, strain gauges were installed on four sets of type 4D reinforcement pairs at both ends of each specimen, as shown in Figure 10-6, Figure 10-7, and Figure 10-8. Only four gauges were actively monitored due to cable limitations: CSD-106, CSD-107 (in FSB-1 with steel stirrups), and GFD-126, GFD-127 (in FSB-4 with GFRP stirrups).

In Figure 10-9, the strain measurements are plotted against time for the gauges in FSB-1. These strains were converted to stress by multiplying them by the elastic modulus for steel (29,000 ksi), and results are shown in Figure 10-10. The strain and stress measurements for the GFRP reinforcement in FSB-4 are shown in Figure 10-11 and Figure 10-12. The stress was calculated using the GFRP elastic modulus from Table 10-1.

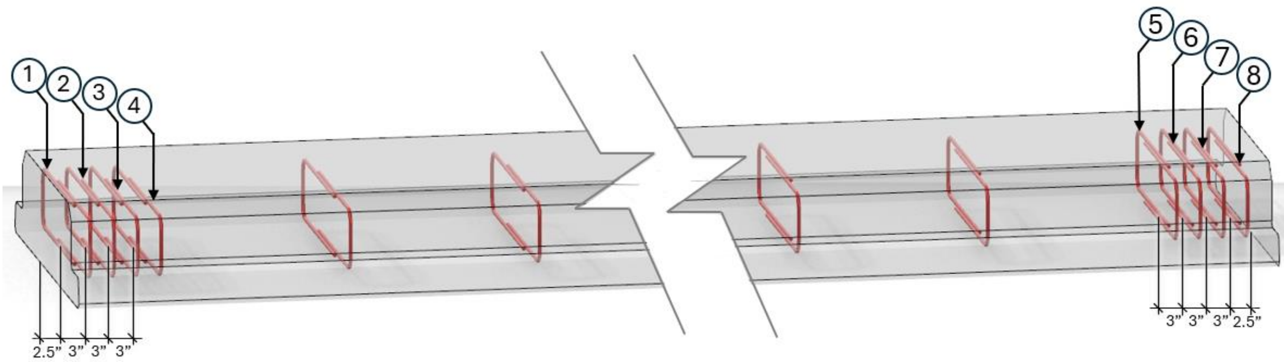


**Figure 10-6. Instrumented type-4D reinforcement pairs at each specimen**

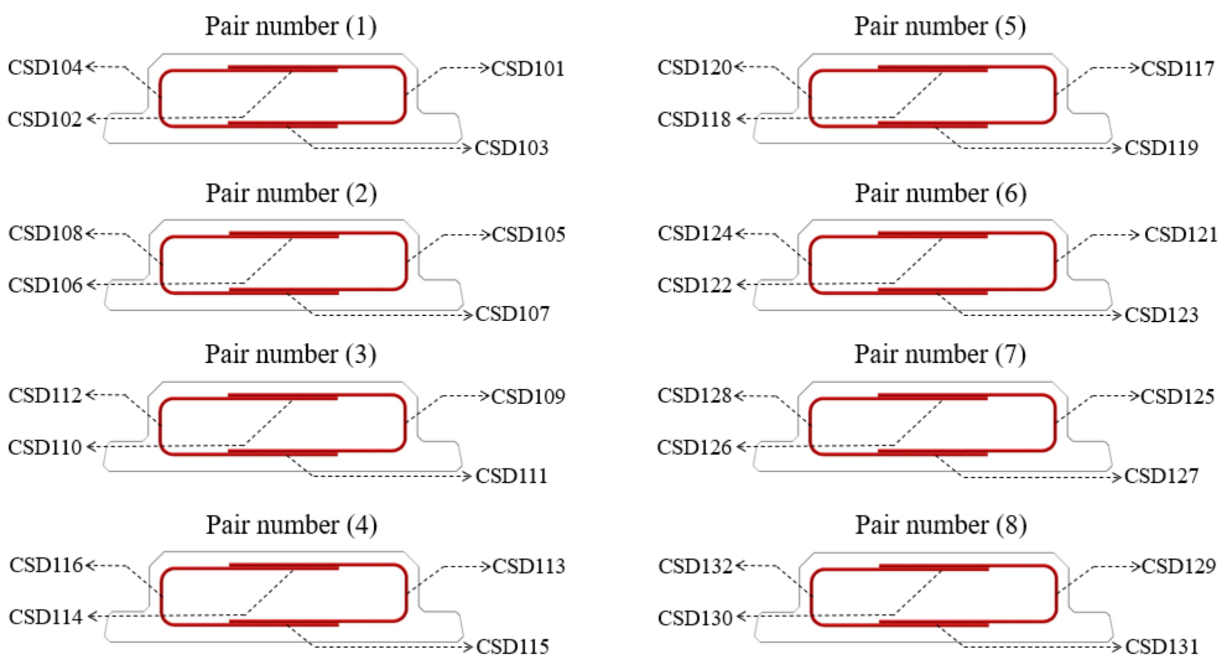


**Figure 10-7. Strain gauge names at specimen FSB-1 (with carbon steel stirrups)**

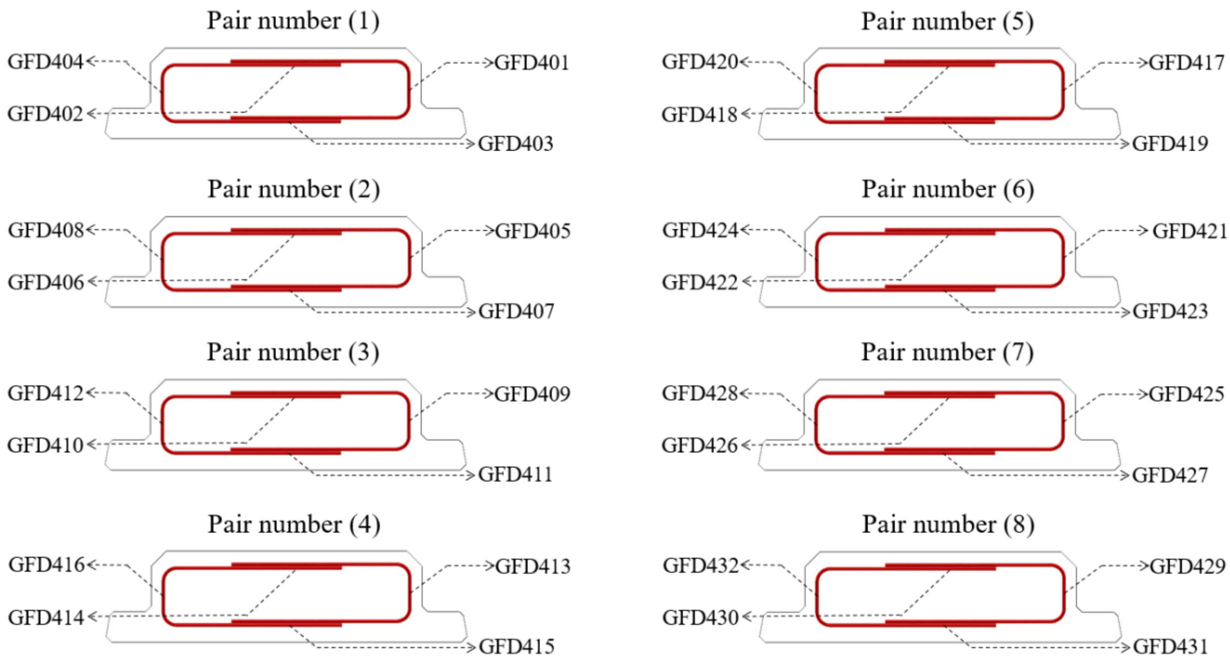


**Figure 10-8. Strain gauge names at specimen FSB-4 (with GFRP stirrups)**

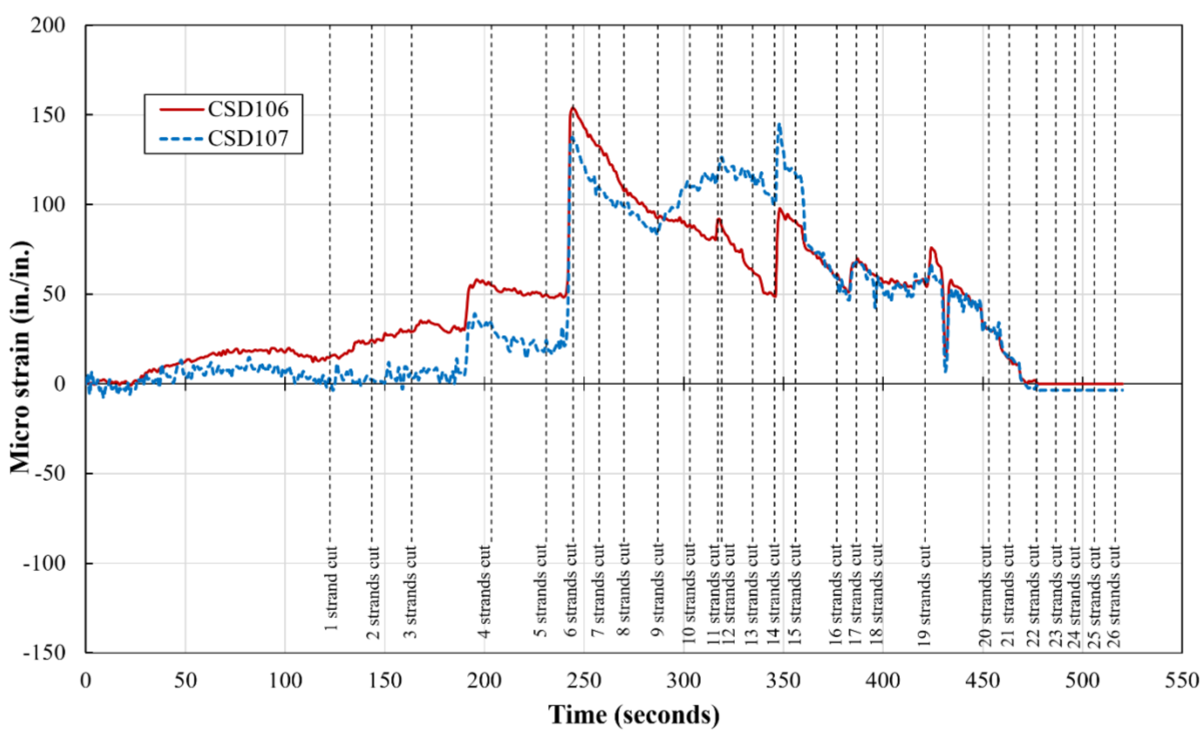


**Figure 10-9. Strain measurements in FSB-1 near live end and during detensioning**

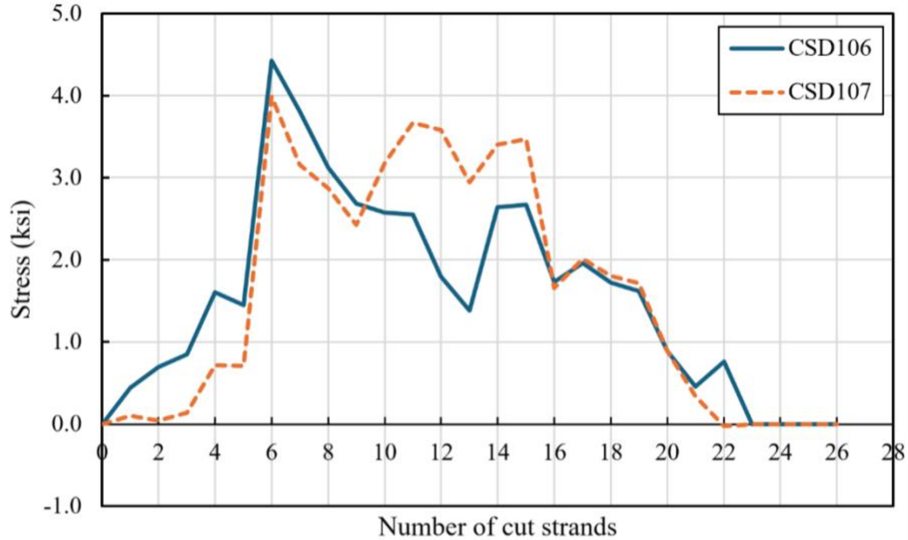


**Figure 10-10. Stress measurements in FSB-1 near live end against number of cut strands**

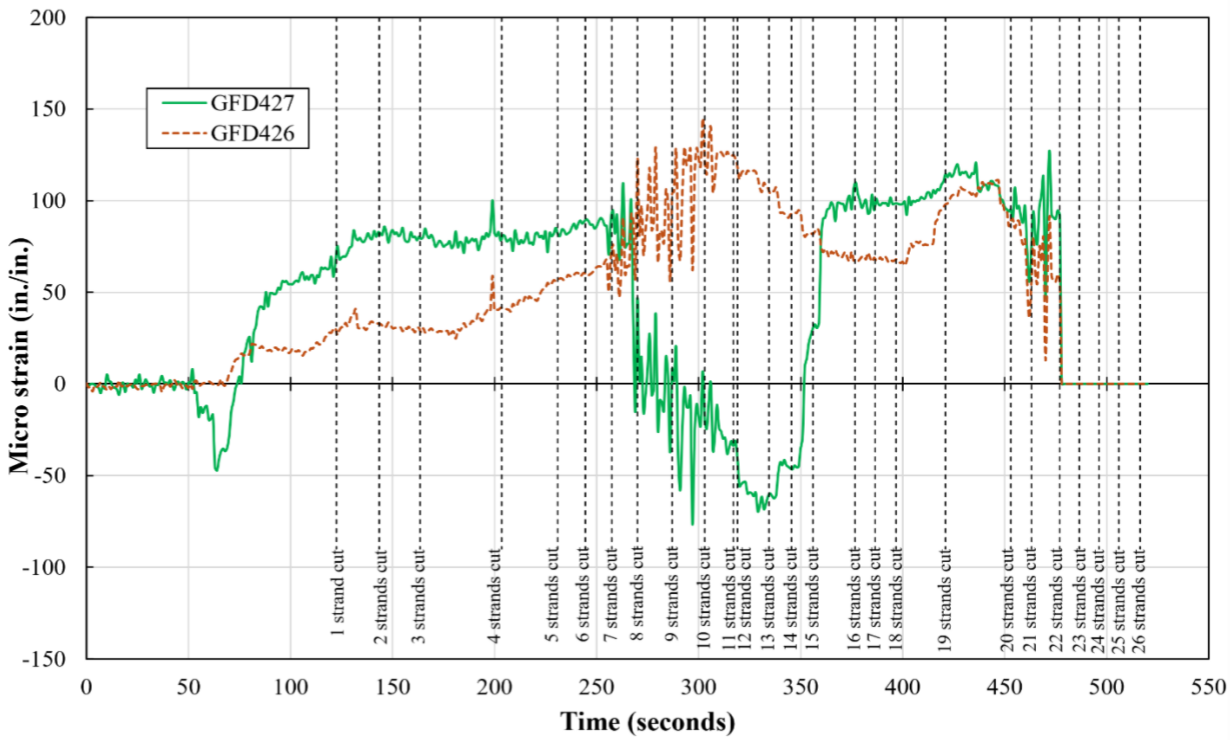


**Figure 10-11. Strain measurements in FSB-4 near dead end during detensioning**

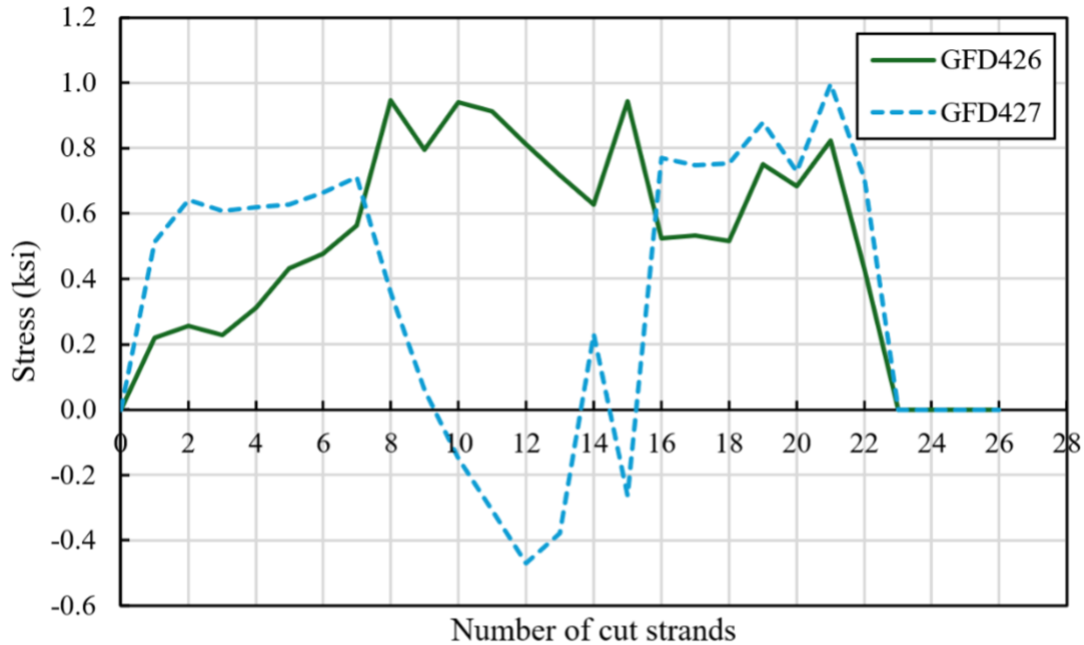


**Figure 10-12. Stress measurements in FSB-4 near dead end against the number of cut strands**

### 10.3.4 Interface and shear reinforcement instrumentation

The combined shear and shear interface resistance in the FSB is provided by the type 4K reinforcement, extending through the full depth of the FSB and connecting the C-I-P topping to the precast member. Each pair consisted of four U-shaped rebars forming two closed stirrups. As shown in Figure 10-13, 40 pairs were uniformly spaced along the beam length, starting at 6.5 in. from the ends, with 8.5-in. spacing to the second pair, and 10-in. spacing for the remaining pairs up to the mid-span. Strain gauges were used to monitor the level of strain in the rebars. Three (3) sets of pairs were instrumented with four (4) strain gauges. Figure 10-13 shows the type 4K reinforcement with the location of the instrumented set along the length of the member. The location of the strain gauges on each set is further illustrated in Figure 10-14 for FSB-1 and Figure 10-15 for FSB-4.

The provided reinforcement ratio in FSB-1 (with carbon steel) was 0.0042 $in^2/ft$ and in FSB-4 (with GFRP reinforcement) was 0.0051 $in^2/ft$. The same longitudinal distribution was provided. However, the reinforcement ratio is higher because the GFRP rebars have larger cross-sectional areas (see Table 10-1). The interface between the C-I-P topping and FSB was roughened to an amplitude of ¼ in., as shown in Figure 10-16, to improve the bond strength.

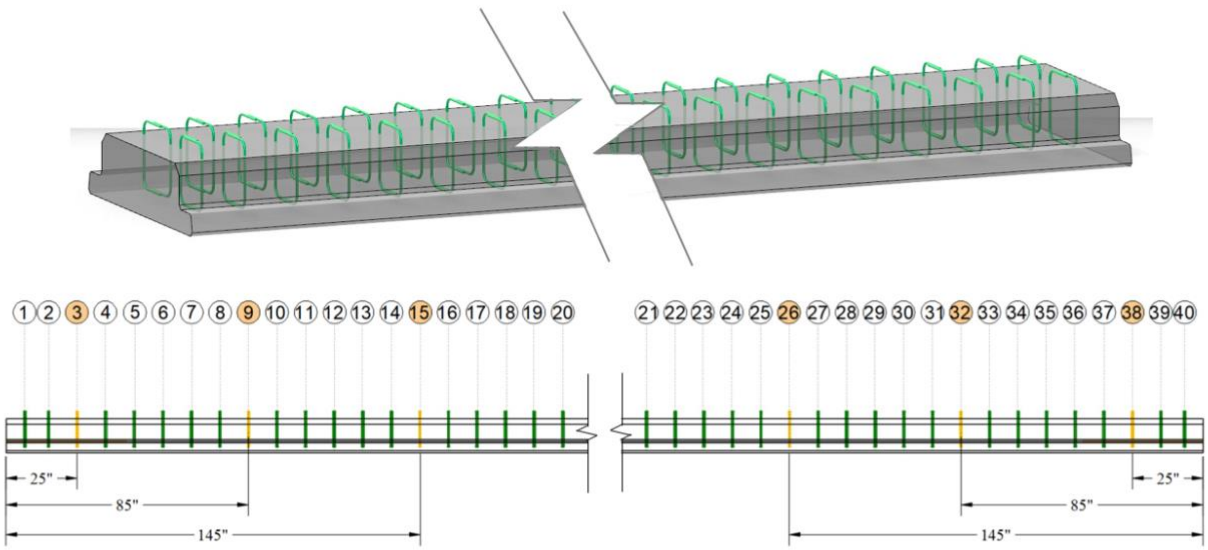


**Figure 10-13. Instrumented type-4K rebar location**

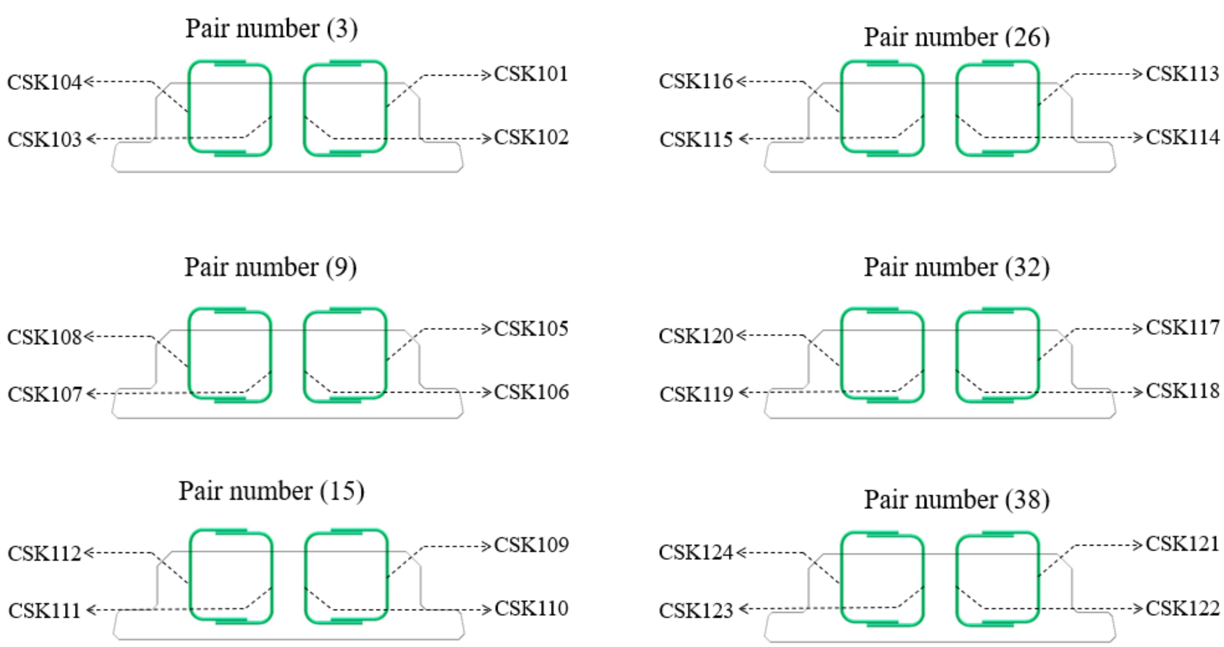


**Figure 10-14. Strain gauge locations in FSB-1**

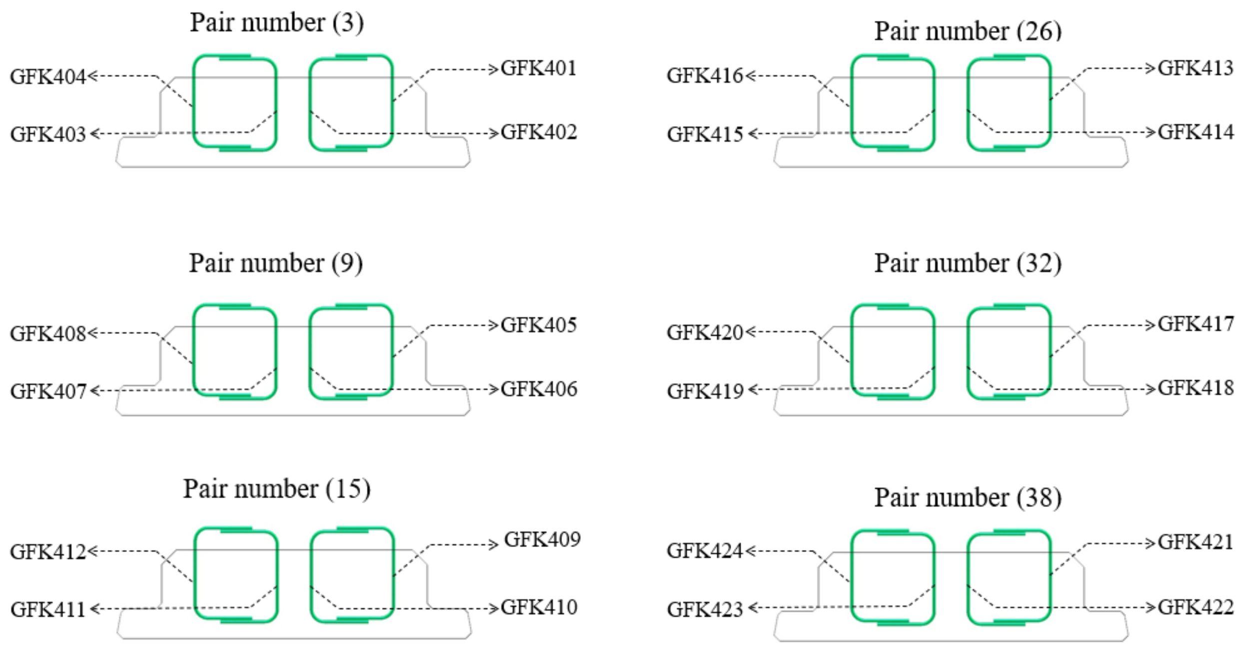


**Figure 10-15. Strain gauge locations in FSB-4**

**Figure 10-16. Roughened interface surface after concrete casting**

## 10.4 Experimental results

A four-point bending test setup was used for all specimens, as illustrated in Chapter 6. The load was incrementally applied at two locations spaced 3 ft away from mid-span. Upon the appearance of the first cracks at the bottom of the specimens, the test was temporarily halted and unloaded. Cracks were marked, and then the specimens were reloaded. As the loading increased, additional cracks formed and extended until they reached the interface joint (Figure 10-17). The cracks eventually merged with the joint and propagated deeper into the C-I-P topping until failure occurred. Both specimens had flexural failure by concrete crushing in the top flange (Figure 10-18).

**Figure 10-17. Flexural cracks at bottom flanges**

(a) FSB-1 (Carbon steel stirrups) (b) FSB-4 (GFRP stirrups)

**Figure 10-18. Failure mode of the two specimens**

Both specimens exhibited similar flexural behavior with minor differences in the load-deflection relationship as shown in Figure 10-19. This difference in behavior is mainly due to the different concrete strengths of the C-I-P topping and FSB for the specimens. Although all specimens were designed to have the same concrete strength, FSB-1 had a compressive strength of 6.22 ksi for the C-I-P topping and 10.81 ksi for the FSB, while FSB-4 had compressive strengths of 7.11 ksi and 11.91 ksi, respectively.

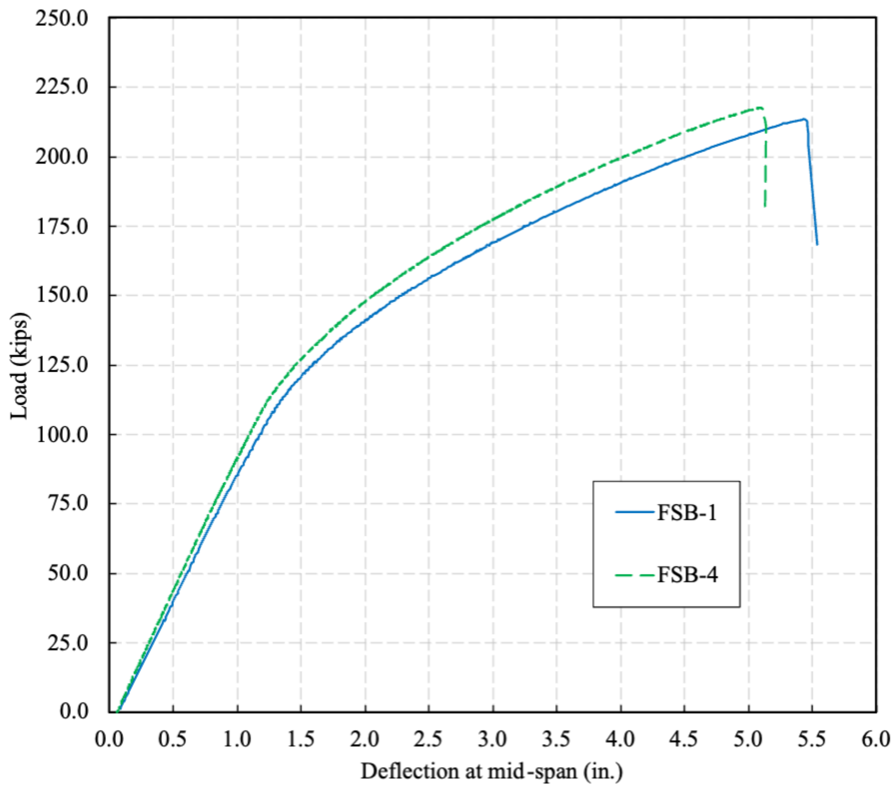


**Figure 10-19. Load-deflection curve**

The ultimate load was 213.6 kips and 217.7 kips for FSB-1 and FSB-4, respectively. To determine the horizontal shear force at the interface near the instrumented 4K stirrups, the shear force and moment distribution at ultimate load along the length of the specimens were calculated (Figure 10-20, Figure 10-21, Figure 10-22, and Figure 10-23). In Chapter 9, a flexural behavior prediction model was introduced and verified. The analytical model used strain compatibility and sectional analysis to find the stress distribution at the critical section, which is located at mid-span. This model was adapted to calculate stress distribution and corresponding normal forces at the section containing the instrumented 4K pairs (as shown in Figure 10-13).

The horizontal shear force was calculated from equilibrium of the section as illustrated in Figure 10-24. The neutral axis depth can be determined from the previously verified analytical model as 7.313 in. for FSB-1 and 6.831 in. for FSB-4. If the neutral axis lies below the interface, compressive forces develop in the C-I-P topping and the upper portion of the FSB, while tension is resisted by the prestressing strands. The resultant horizontal shear force $V_h$ balances these internal forces at the interface. Additionally, the vertical shear force also generates horizontal shear force at the interface. According to AASHTO (2024), this horizontal shear can be calculated as the vertical shear divided by the effective depth (Figure 10-25). The total interface horizontal shear force for each section is summarized in Table 10-3.

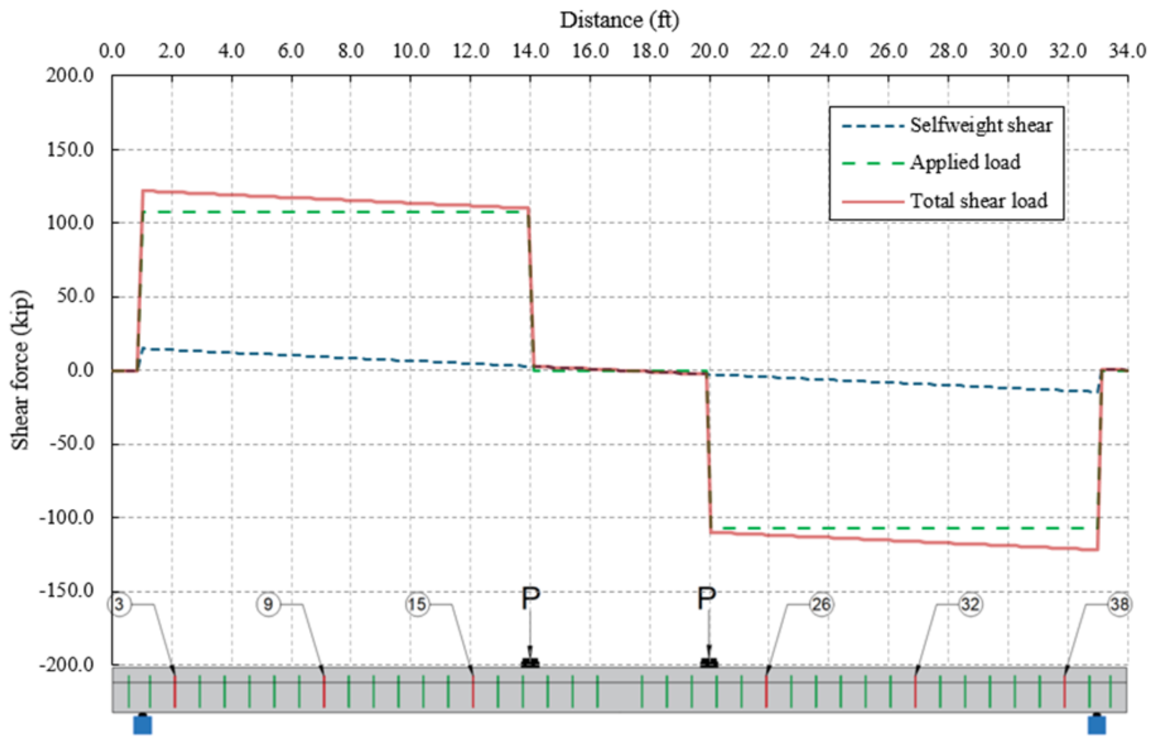


Figure 10-20. Shear distribution diagram FSB-1

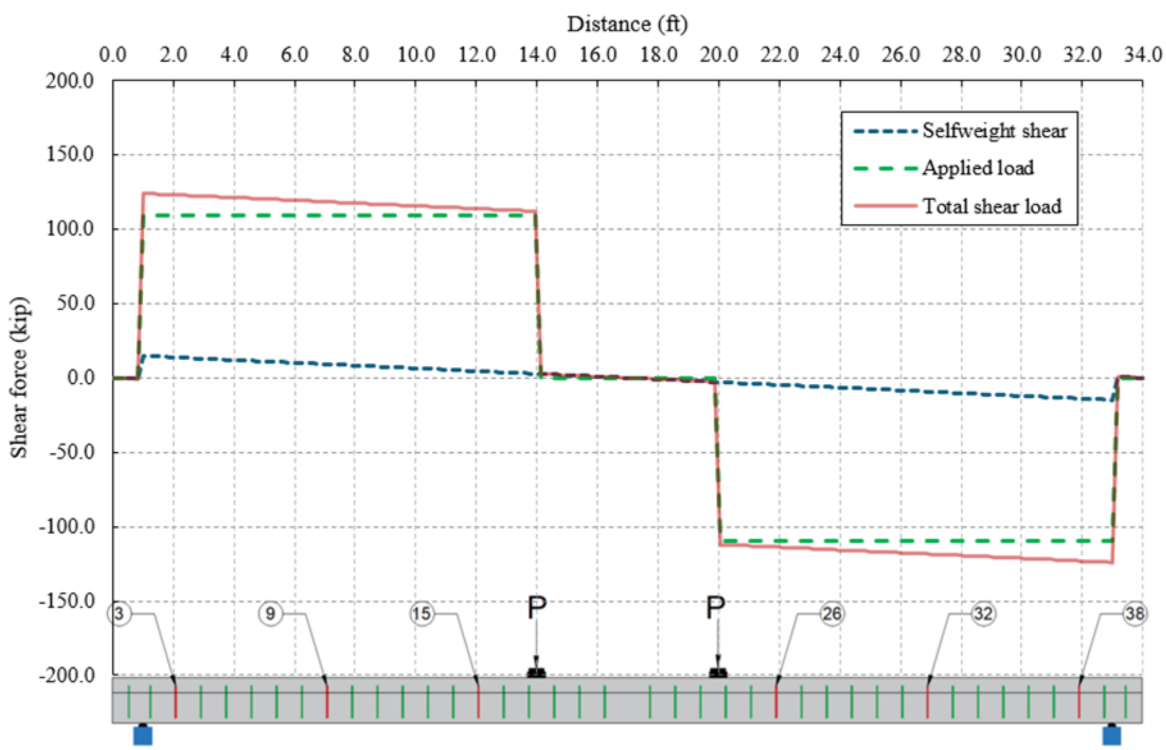


Figure 10-21. Shear distribution diagram FSB-4

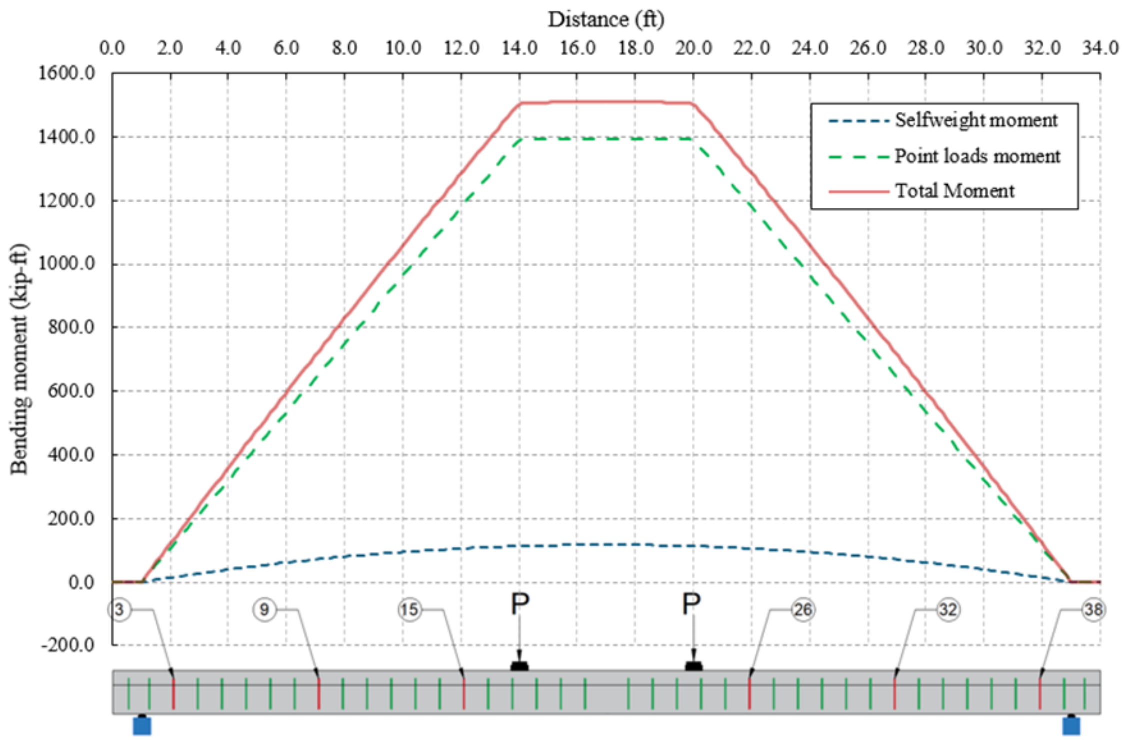


Figure 10-22. FSB-1 bending moment distribution at ultimate

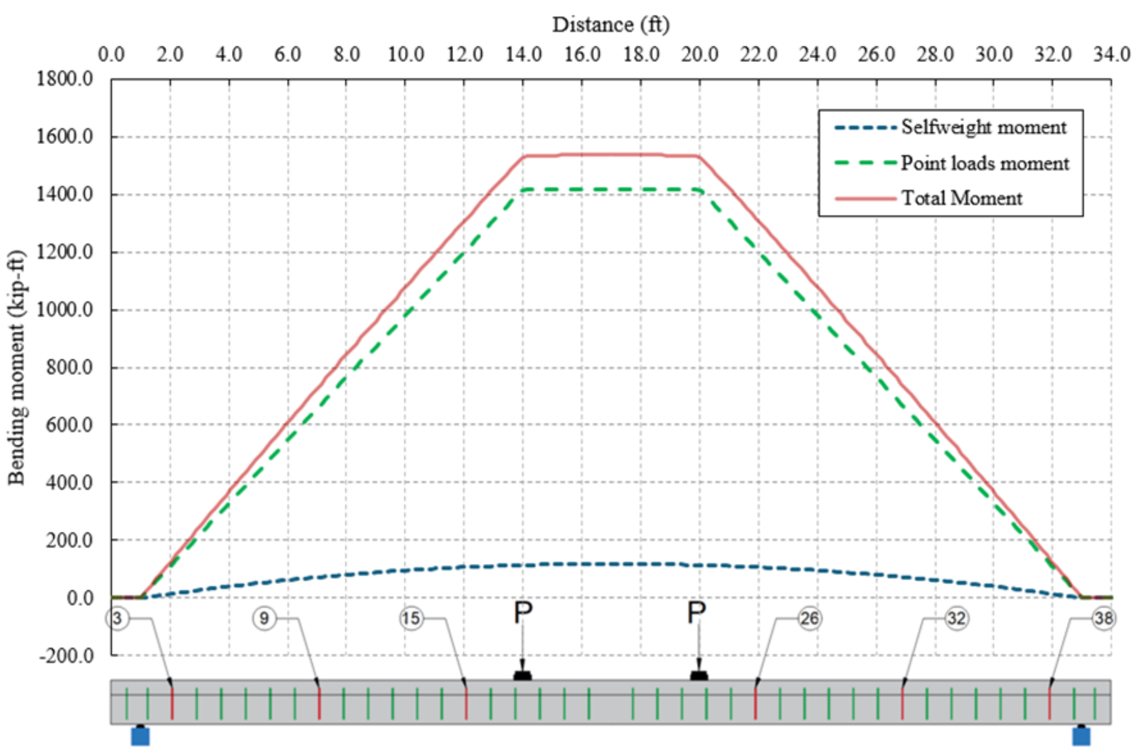


Figure 10-23. FSB-4 bending moment distribution at ultimate

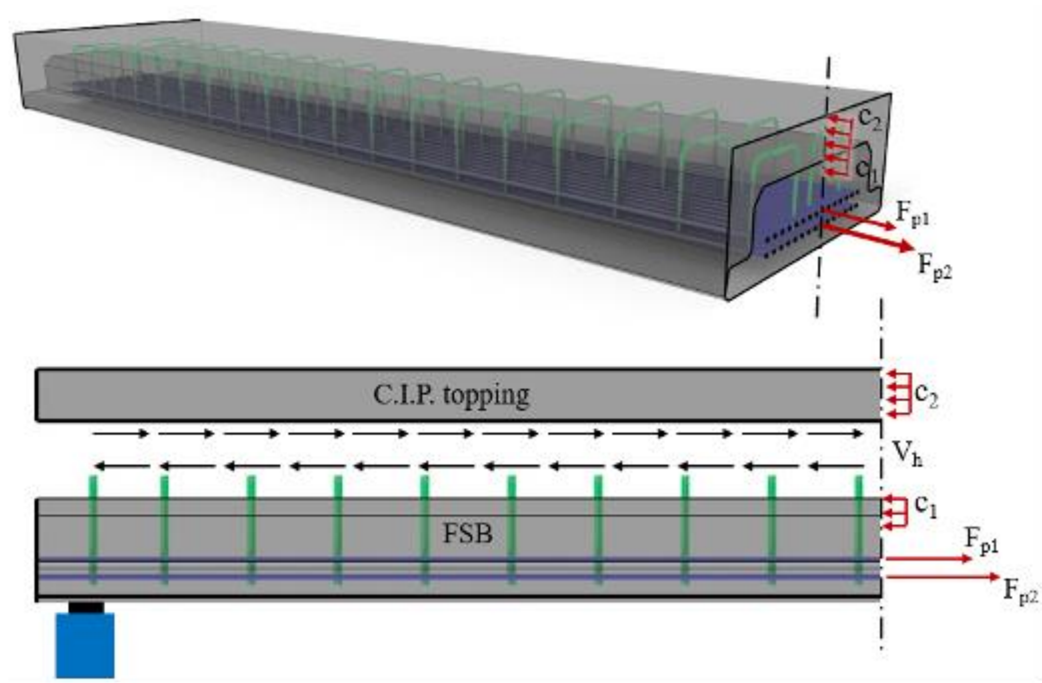


**Figure 10-24. Interface horizontal shear due to bending moment**

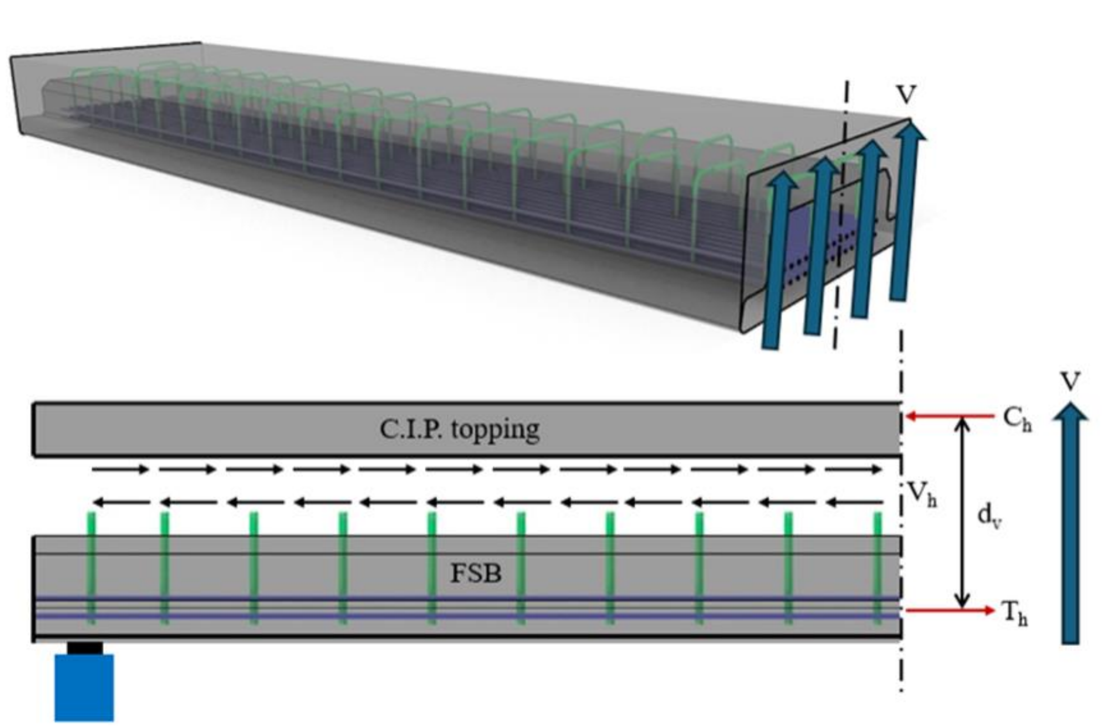


**Figure 10-25. Interface horizontal shear due to vertical shear**

**Table 10-3. Horizontal shear value at instrumented pairs**

| Specimen | Stirrup material | Location | Distance (in.) | $V_h$-shear (kips) | $d_v$ (in.) | Total $V_h$ (kips/in.) |
|---|---|---|---|---|---|---|
| **FSB-1** | Carbon steel | Pair 3 & 38 | 25 | 120.8 | 12.96 | 9.32 |
| **FSB-1** | Carbon steel | Pair 9 & 32 | 85 | 116.3 | 12.96 | 8.97 |
| **FSB-1** | Carbon steel | Pair 15 & 26 | 145 | 111.6 | 12.96 | 8.61 |
| **FSB-4** | GFRP | Pair 3 & 38 | 25 | 122.8 | 12.96 | 9.48 |
| **FSB-4** | GFRP | Pair 9 & 32 | 85 | 118.3 | 12.96 | 9.13 |
| **FSB-4** | GFRP | Pair 15 & 26 | 145 | 113.7 | 12.96 | 8.77 |

Strain measurements near the ends of the specimens (pairs 3 & 38) showed linear-elastic behavior as shown in Figure 10-26. The strain measurements were low, indicating that the reinforcement is not engaged, and these measurements are for concrete bond to the rebars near the gauges.

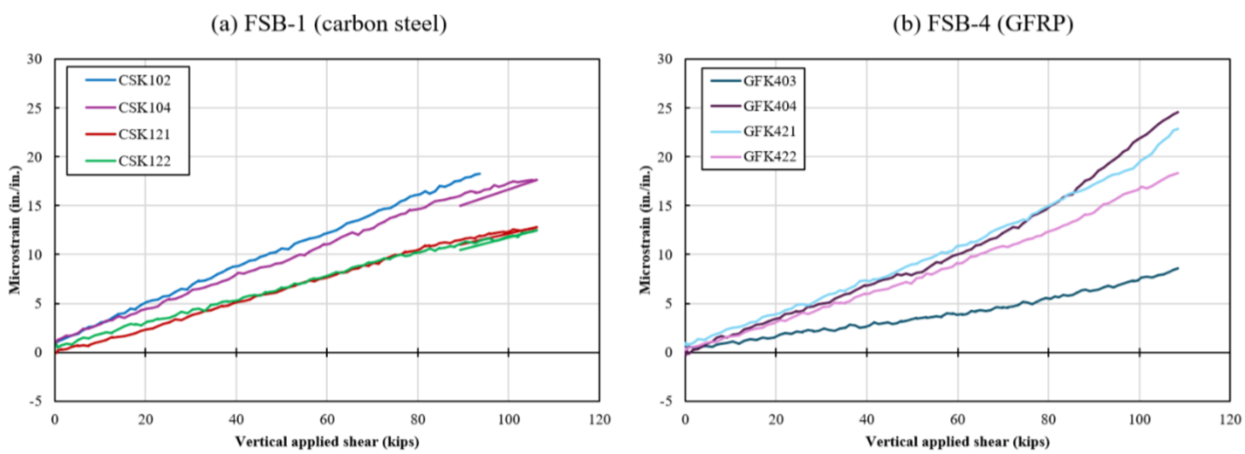


**Figure 10-26. Strain measurements for pairs 3 & 38 in both specimens**

Strain gauges at 85 in. from the ends (pairs 9 & 32) showed higher strain measurements with similar behavior, except for FSB-4 (Figure 10-27). Some of the strain gauges showed a significant change in slope of readings that might refer to cracking at the interface and reinforcement starting to engage.

Near mid-span (pairs 15 & 26), the behavior changed notably. Initial strains were followed by a jump in the strain value then a reversal in slope for both specimens, as shown in Figure 10-28. This change might be due to localized failure in the interface.

To clarify the behavior of the interface reinforcement measurements in pairs 15 & 26, the gauges' measurements before the reinforcement becomes effective are ignored. Figure 10-29 shows the strains in the instrumented pairs beyond the slope change. These strains might to be due to the separation in the interface prior to the flexural failure.

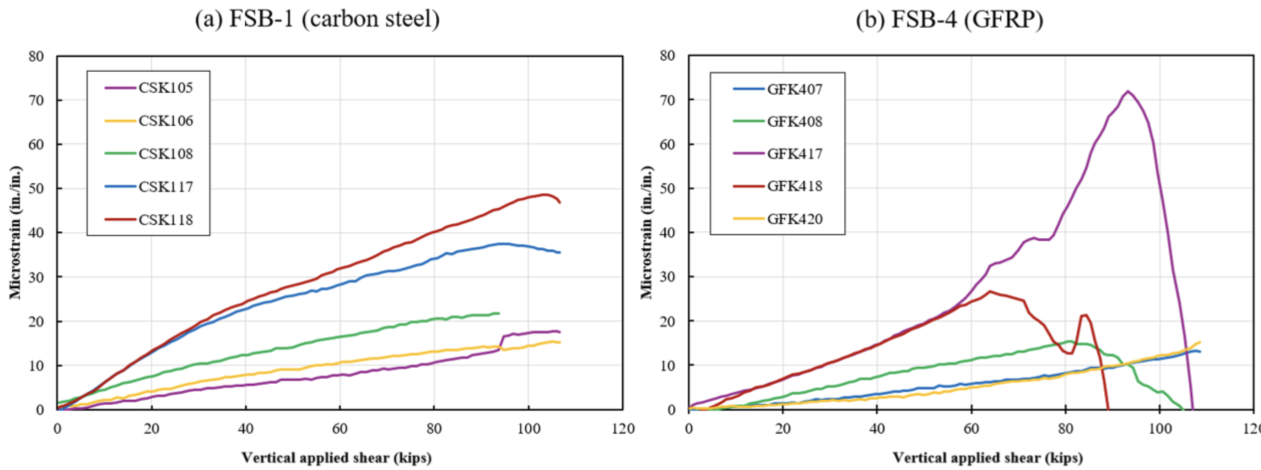


**Figure 10-27. Strain measurements for pairs 9 & 32 in both specimens**

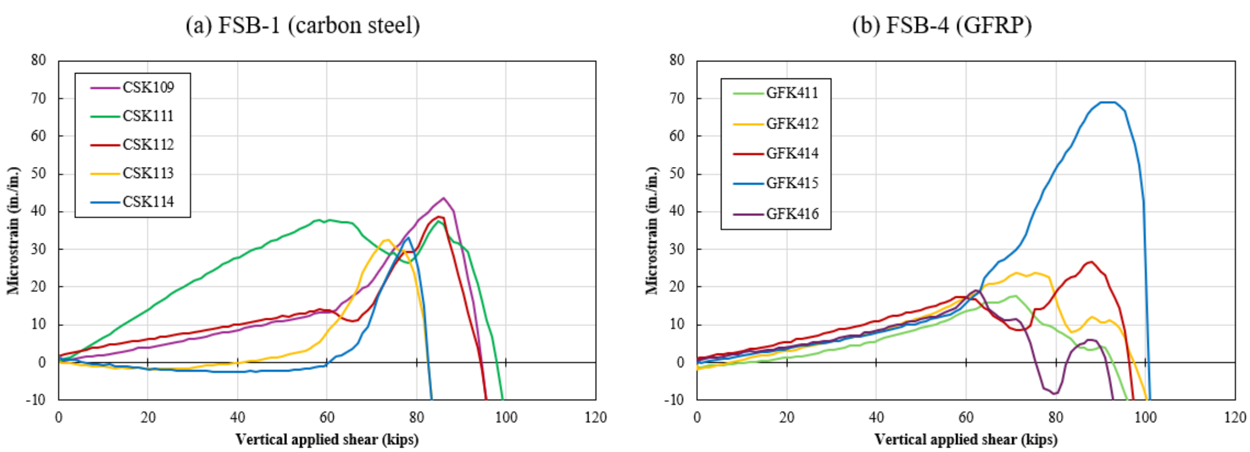


**Figure 10-28. Strain measurements for pairs 15 & 26 in both specimens**

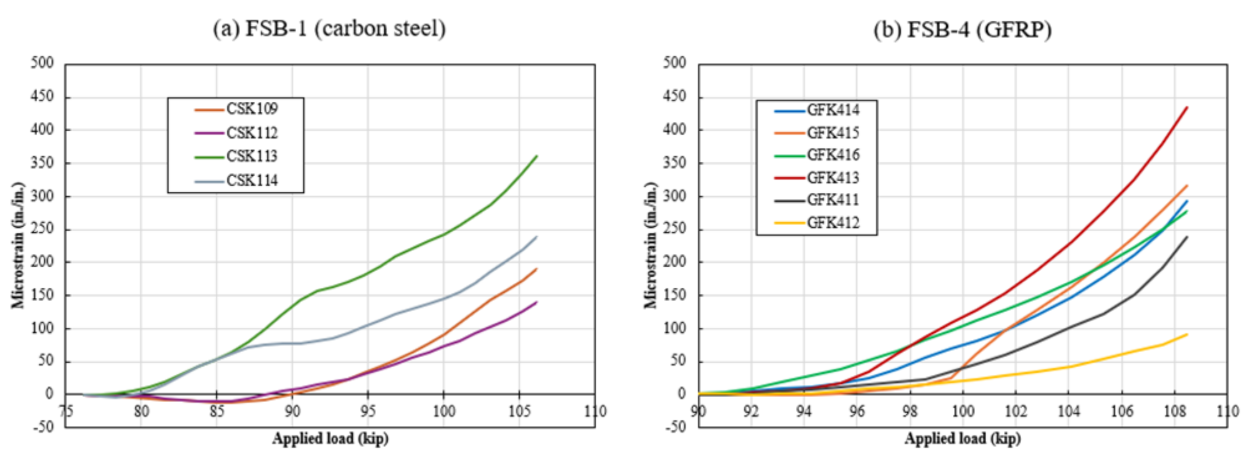


**Figure 10-29. Tensile strain measurements in pairs 15 & 26**

## 10.5 Design of transverse reinforcement

The transverse reinforcement design follows AASHTO LRFD (AASHTO, 2024) using the sectional model to determine shear resistance at the critical sections along the member's span. This critical section is located at a distance equal to the effective depth from the support ends. However, the shear calculation in this section includes only sections where strain gauges on 4K pairs were provided (refer to Figure 10-13). AASHTO LRFD outlines two methods for calculating shear resistance: a general procedure based on Modified Compression Field Theory and the simplified method. Each is described in the sections that follow.

### 10.5.1 Nominal shear resistance – General procedure

Nominal shear resistance per AASHTO (2024) is determined by finding concrete resistance using this expression:

$$V_c = 0.0316\beta\lambda\sqrt{f_c{}'}b_v d_v \quad \text{(Eq. 10.8)}$$

where
$V_c$ = the nominal shear resistance of the concrete (kips),
β = a factor for cracked concrete ability to transfer tension and shear,
λ = the concrete density modification factor (taken as 1.0 for normal-weight concrete),
$b_v$ = the effective web width (taken as 47 in. for the FSB standard 12 in. x 48 in. section used in the experimental program), and
$d_v$ = the effective shear depth, calculated as the distance perpendicular to the neutral axis between the tensile and compressive forces (in.).

The following expression can be used for fully prestressed flexural members:

$$d_v = \frac{M_n}{A_{ps}f_{ps}} \quad \text{(Eq. 10.9)}$$

where
$M_n$ = the nominal flexural resistance,
$A_{ps}$ = the area of the prestressing steel strands (equal to 7.11 in$^2$ for both FSB-1 and FSB-4), and
$f_{ps}$ = the average stress in the prestressing steel strands at nominal flexural resistance.

As an example, the effective depth is calculated for FSB-1 at 4K pairs located at a distance of 25 in. (pairs 3 and 38) as shown in Figure 10-13. From the analytical model based on strain compatibility, the nominal flexural strength is 1365.2 kip-ft, with an average stress in the prestressing strands of 195.34 ksi (the average of the two layers, 187.85 ksi and 202.84 ksi). This results in an effective depth:

$$d_v = \frac{M_n}{A_{ps}f_{ps}} = \frac{1365.2*12}{7.11*195.34} = 11.8\ in. \quad \text{(Eq. 10.10)}$$

The effective depth should not be less than the greater of $0.9d_e$ and $0.72h$:

$$d_e = \frac{A_{ps}f_{ps}d_p + A_s f_s d_s}{A_{ps}f_{ps} + A_s f_y} = \frac{3.555*187.85*13 + 3.555*202.84*15 + 0}{3.555*187.85 + 3.555*202.84 + 0} = 14.04\ in. \quad \text{(Eq. 10.11)}$$

$$\begin{aligned} &\max(0.9d_e\,, 0.72h) = \max(0.9(14.04)\,, 0.72(18)) \\ &\qquad = \max(12.63\ in., 12.96\ in.) = 12.96\ in. \end{aligned} \quad \text{(Eq. 10.12)}$$

Therefore, $d_v$ is equal to $12.96\ in.$

The factor β can be calculated as per AASHTO LRFD as:

$$\beta = \frac{4.8}{(1+750\varepsilon_s)} \quad \text{(Eq. 10.13)}$$

where $\varepsilon_s$ is the net tensile strain at the centroid of the tensile reinforcement, calculated using the expression:

$$\varepsilon_s = \frac{\left(\frac{|Mu|}{d_v} + 0.5N_u + |V_u - V_p| - A_{ps}f_{po}\right)}{E_s A_s + E_p A_{ps}} \quad \text{(Eq. 10.14)}$$

where $M_u$ is the factored moment at the section, taken as the applied moment at 25 in. from the support that is equal to 135.1 kip-ft (refer to Table 10-3), $N_u$ is the factored axial force, taken as 0 kips, and $V_u$ is the factored shear force, taken as 120.8 kips (refer to Table 10-3).

The parameter $f_{po}$ is found as the product of the strands' elastic modulus and the locked-in strain difference between the strands and surrounding concrete; this stress can be taken as the effective stress in the strands prior to the flexural test; however, since the section is located within the transfer length (typically it is 50d, but for design purposes it is taken as 60d, that is 36 in.), the stress is conservatively:

$$f_{po} = \frac{25}{36} * 142.48 = 98.9\ ksi \quad \text{(Eq. 10.15)}$$

$$\varepsilon_s = \frac{\left(\frac{|135.1*12|}{11.8} + 0 + |120.8 - 0| - 7.11*98.9\right)}{0 + 24{,}000*7.11} = -0.0026\ (in./in.) < \ 0 \quad \text{(Eq. 10.16)}$$

Therefore $\varepsilon_s = 0$. Substitution into the expression for $\beta$:

$$\beta = \frac{4.8}{(1+750*0)} = 4.8 \quad \text{(Eq. 10.17)}$$

Now, the nominal shear resistance in the concrete is determined as:

$$V_c = 0.0316\beta\lambda\sqrt{f_c{}'}b_v d_v = 0.0316 * 4.8 * 1 * \sqrt{10.81} * 47 * 12.96 = 303.8\ kips \quad \text{(Eq. 10.18)}$$

The shear resistance, provided by the transverse reinforcement for FSB-1 which had carbon steel as the lateral reinforcement, is:

$$V_s = \frac{A_v f_y d_v \cot \theta}{s} \quad \text{(Eq. 10.19)}$$

where
$V_s$ = shear resistance by transverse reinforcement (kips),
$A_v$ = the area of transverse reinforcement (in$^2$) within distance $s$,
$f_y$ = yield stress for transverse reinforcement (ksi), and
θ = angle of inclination of diagonal compressive stresses.

The area of transverse reinforcement with distance $s = 24\ in.$ is the area of two (2) legs of type 4D reinforcement and eight (8) legs of four (4) pairs of 4K reinforcement, which constitute an area of $0.2 * 10 = 2\ in^2$ for carbon steel.

The angle of inclination θ is calculated using the following expression:

$$\theta = 29 + 3500\varepsilon_s \quad \text{(Eq. 10.20)}$$

Therefore, θ for FSB-1 is:

$$\theta = 29 + 3500\varepsilon_s = 29 + 3500 * 0 = 29 \text{ degrees} \quad \text{(Eq. 10.21)}$$

$$V_s = \frac{2*60*12.96 \cot 29}{24} = 116.9\ kips \quad \text{(Eq. 10.22)}$$

The nominal shear resistance for FSB-1 is the lesser of:

$$V_n = V_c + V_s + V_p = 303.8 + 116.9 + 0 = 420.7\ kips\text{, and} \quad \text{(Eq. 10.23)}$$

$$V_n = 0.25 f_c' b_v d_v + V_p = 0.25(10.81)(47)(12.96) + 0 = 1{,}644.1\ kips > 420.7\ kips \quad \text{(Eq. 10.24)}$$

Therefore, the nominal shear strength for FSB-1 at a distance of 25 in. from the support is equal to 420.7 kips.

The calculations were repeated for FSB-4 and pairs 3 and 38, which were also located 25 in. from the ends. However, since the transverse reinforcement was GFRP, the shear resistance calculation is according to AASHTO (2018).

The effective depth is similar to FSB-1, equal to 12.96 in. The $\beta$ factor is equal to 4.8. The concrete resistance $V_c$ is equal to 318.9 k. To calculate the transverse reinforcement resistance $V_s$, the angle $\theta$ is first found to be 29 degrees. The yield strength is replaced by the design tensile strength for GFRP transverse reinforcement. As per AASHTO (2018), this value can be found using the following expressions:

$$f_{fv} = 0.004E_f \leq f_{fb} \quad \text{(Eq. 10.25)}$$

$$f_{fb} = \left(0.05\frac{r_b}{d_b} + 0.3\right) f_{fd} \leq f_{fd} \quad \text{(Eq. 10.26)}$$

$$f_{fd} = C_E f_{fu} \quad \text{(Eq. 10.27)}$$

NCHRP project 12-121 recommends a value of $0.006E_f$ for $f_{fv}$, while CSA S806:26 uses $0.005E_f$.

where
$E_f$ = the elastic tensile modulus for GFRP transverse reinforcement, reported by the manufacturer as 7,667 ksi for No. 4 GFRP rebars,
$f_{fb}$ = the design tensile strength of the bent portion of GFRP stirrups,
$r_b$ = the internal radius of GFRP rebars, equal to three times the rebar diameter, while it was 3 in. as per design drawings,
$d_b$ = GFRP rebar diameter, equal to 0.5 in. for No. 4 rebar,
$C_E$ = the environmental factor taken as 1.0, as it is not applicable for testing, and
$f_{fu}$ = the reported GFRP strength from the manufacturer, equal to 135.2 ksi found by dividing the ultimate force by the cross-sectional area of rebar reported by the manufacturer (refer to Table 10-1).

Substituting these values in the design tensile strength equations results in:

$$f_{fd} = 1.0 * 135.2 = 135.2\ ksi \quad \text{(Eq. 10.28)}$$

$$f_{fb} = \left(0.05\frac{3}{0.5} + 0.3\right)135.2 = 81.1\ ksi \leq f_{fd} \ \ (\text{or } 81.1\ ksi) \quad \text{(Eq. 10.29)}$$

$$f_{fv} = 0.004 * 7{,}667 = 30.7 \text{ ksi} \leq f_{fb} \quad \text{(Eq. 10.30)}$$

NCHRP project 12-121 recommends this expression as:

$$f_{fv} = 0.006E_f = 0.006 * 7{,}667 = 46.0 \text{ ksi} \leq f_{fb} \quad \text{(Eq. 10.31)}$$

Substitution in the reinforcement shear resistance expression results in:

$$V_f = \frac{A_{fv} f_{fv} d_v \cot\theta}{s} = \frac{2.47*30.7*12.96*\cot 29}{24} = 73.9\ kips \quad \text{(Eq. 10.32)}$$

Per NCHRP project 12-121 recommendation, the value is:

$$V_f = \frac{A_{fv} f_{fv} d_v \cot\theta}{s} = \frac{2.47*46.0*12.96*\cot 29}{24} = 110.9\ kips \quad \text{(Eq. 10.33)}$$

The nominal shear resistance is therefore the lesser of:

$V_n = V_c + V_f + V_p = 318.9 + 73.9 + 0 = 392.7\ kips$, and (Eq. 10.34)

$$V_n = 0.25 f_c' b_v d_v + V_p = 0.25(11.912)(47)(12.96) + 0$$
$$= 1{,}814\ kips > 392.7\ kips \quad \text{(Eq. 10.35)}$$

The nominal shear strength for FSB-4 at a distance of 25 in. from the support is equal to 392.7 kips.

Per NCHRP project 12-121, the nominal shear resistance is the lesser of:

$V_n = V_c + V_f + V_p = 318.9 + 110.9 + 0 = 429.8\ kips$, and (Eq. 10.36)

$$V_n = 0.25 f_c' b_v d_v + V_p = 0.25(11.912)(47)(12.96) + 0$$
$$= 1{,}814\ kips > 429.8\ kips \quad \text{(Eq. 10.37)}$$

Per NCHRP project 12-121, the nominal shear strength for FSB-4 at a distance of 25 in. from the support is equal to 429.8 kips.

Table 10-4 compares the nominal shear resistance calculated using the general method to the applied shear at different locations along FSB-1 and FSB-4.

**Table 10-4. Nominal shear resistance using the general method compared to applied shear at different locations along FSB-1 and FSB-4**

| Specimen | Distance from support (in.) | Location of 4K rebar pairs | Applied shear (kips) | Applied moment (kip-ft) | Predicted nominal shear resistance {NCHRP 12-121} (kips) | Ratio of applied shear to nominal shear resistance {NCHRP 12-121} |
|---|---|---|---|---|---|---|
| **FSB-1** | 25 | 3 and 38 | 120.8 | 135.1 | 420.7 | 0.29 |
| **FSB-1** | 85 | 9 and 32 | 116.3 | 723.2 | 420.7 | 0.28 |
| **FSB-1** | 145 | 15 and 26 | 111.6 | 1306.0 | 420.7 | 0.27 |
| **FSB-4** | 25 | 3 and 38 | 122.8 | 137.2 | 392.7 {429.8} | 0.31 {0.29} |
| **FSB-4** | 85 | 9 and 32 | 118.3 | 735.4 | 392.7 {429.8} | 0.30 {0.28} |
| **FSB-4** | 145 | 15 and 26 | 113.7 | 1328.7 | 392.7 {429.8} | 0.29 {0.26} |

Note: Values in brackets {} are calculated per NCHRP project 12-121 recommendation.

### 10.5.2 Nominal shear resistance – Simplified method

The simplified method is similar to the general method except that the value of $\beta = 2$ and $\theta = 45$ degrees. Substituting these values, the shear resistance of concrete for FSB-1 is:

$V_c = 0.0316\beta\lambda\sqrt{f_c'} b_v d_v = 0.0316 * 2 * \sqrt{10.81} * 47 * 12.96 = 126.6\ kips$ (Eq. 10.38) and for FSB-4 is:

$$V_c = 0.0316\beta\lambda\sqrt{f_c{}'}b_v d_v = 0.0316 * 2 * \sqrt{11.912} * 47 * 12.96 = 132.9\ kips \qquad \text{(Eq. 10.39)}$$

Substituting the θ value in the reinforcement shear resistance expression results in:

$$V_s = \frac{A_v f_y d_v \cot\theta}{s} = \frac{2*60*12.96 \cot 45}{24} = 64.8\ kips \qquad \text{(Eq. 10.40)}$$

$$V_f = \frac{A_{fv} f_{fv} d_v \cot\theta}{s} = \frac{2.47*30.7*12.96*\cot 45}{24} = 40.9\ kips \qquad \text{(Eq. 10.41)}$$

The nominal resistance for FSB-1 is:

$$V_n = V_c + V_s + V_p = 126.6 + 64.8 + 0 = 191.4\ kips \qquad \text{(Eq. 10.42)}$$

and for FSB-4 is:

$$V_n = V_c + V_f + V_p = 132.9 + 40.9 + 0 = 173.8\ kips \qquad \text{(Eq. 10.43)}$$

Or per NCHRP project 12-121, $V_n = 194.2\ kips$. (Eq. 10.44)

Table 10-5 compares the nominal shear resistance calculated using the simplified method to the applied shear at different locations along FSB-1 and FSB-4.

**Table 10-5. Nominal shear resistance using the simplified method compared to the applied shear at different locations along FSB-1 and FSB-4**

| Specimen | Distance from support (in.) | Location of 4K rebar pairs | Applied shear (kips) | Applied moment (kip-ft) | Predicted nominal shear resistance {NCHRP 12-121} (kips) | Ratio of applied shear to nominal shear resistance {NCHRP 12-121} |
|---|---|---|---|---|---|---|
| **FSB-1** | 25 | 3 and 38 | 120.8 | 135.1 | 191.4 | 0.63 |
| **FSB-1** | 85 | 9 and 32 | 116.3 | 723.2 | 191.4 | 0.61 |
| **FSB-1** | 145 | 15 and 26 | 111.6 | 1306.0 | 191.4 | 0.58 |
| **FSB-4** | 25 | 3 and 38 | 122.8 | 137.2 | 173.8 {194.2} | 0.71 {0.63} |
| **FSB-4** | 85 | 9 and 32 | 118.3 | 735.4 | 173.8 {194.2} | 0.68 {0.61} |
| **FSB-4** | 145 | 15 and 26 | 113.7 | 1328.7 | 173.8 {194.2} | 0.65 {0.59} |

Note: Values in brackets {} are calculated per NCHRP project 12-121 recommendation.

## 10.6 Required transverse reinforcement

AASHTO (2024) requires transverse reinforcement in regions where the following expression is satisfied:

$$V_u > 0.5\ \phi\ (V_c + V_p) \qquad \text{(Eq. 10.45)}$$

where
$V_u$ = factored shear force, and
ϕ = resistance factor equal to 0.9 for a prestressed concrete section.

The value of $V_u$ will be replaced by the maximum shear measured during experimental tests. The maximum shear for FSB-1 was 121.7 kips, while FSB-4 was 123.7 kips. The maximum shear is compared using the above expression, for FSB-1:

$$V_u = 121.7 > 0.5\,(0.9)(126.6 + 0) = 56.97\ kips \quad \text{(Eq. 10.46)}$$

and for FSB-4:

$$V_u = 123.7 > 0.5\,(0.9)(132.9 + 0) = 59.8\ kips \quad \text{(Eq. 10.47)}$$

The expression is satisfied; therefore, the section has regions that require transverse reinforcement. In case the region does not require any transverse reinforcement, minimum reinforcement can be provided. The minimum reinforcement area must satisfy the following:

$$A_v \geq 0.0316\,\lambda\,\sqrt{f_c{}'}\,\frac{b_v\,s}{f_y} \quad \text{(Eq. 10.48)}$$

For FSB-1:

$$A_v \geq 0.0316\,(1)\sqrt{10.81} * \frac{47*24}{60} = 1.95\ in^2 < 2\ in^2\ (provided\ reinforcement) \quad \text{(Eq. 10.49)}$$

For GFRP reinforcement, the AASHTO (2018) requirements are to satisfy the following expression:

$$A_v \geq 0.05\,\frac{b_v\,s}{f_{fv}} = 0.05 * \frac{47*24}{30.7} = 1.84\ in^2 < 2\ in^2\ (provided\ reinforcement) \quad \text{(Eq. 10.50)}$$

Per NCHRP project 12-121, the value is:

$$A_v \geq 0.05\,\frac{b_v\,s}{f_{fv}} = 0.05 * \frac{47*24}{46.0} = 1.23\ in^2 < 2\ in^2\ (provided\ reinforcement) \quad \text{(Eq. 10.51)}$$

## 10.7 Pretensioned anchorage zone

This section presents the calculations used to determine the splitting resistance of the anchorage zone in accordance with AASHTO LRFD Bridge Design Specifications (AASHTO, 2024) and FDOT Structures Design Guidelines (FDOT, 2026b). The experimental program utilized the design provisions developed for carbon steel reinforcement because no established design guidelines were available for GFRP reinforcement in pretensioned anchorage zones.

AASHTO requires the anchorage reinforcement located within a distance of *d*/4 from the end of the member to be designed using a reinforcement stress not exceeding 20 ksi. The parameter *d* is defined as the overall dimension of the precast member in the direction in which splitting resistance is being evaluated. For the FSB, the member width is greater than its depth, and splitting cracks are expected to develop in the horizontal direction, on the top or bottom surfaces of the member. Therefore, $d$ is taken as the width of the member.

For the FSB specimens used in this study, the member width is 48 in.; therefore, the anchorage reinforcement considered in the splitting resistance calculation is located within a distance of 12 in. The reinforcement located within this region consists of four pairs of Type D reinforcement, with each pair providing two legs, and three No. 5 U-shaped bars placed at the end zone according to the FDOT standard plans. Each U-shaped bar contributes one leg to the splitting resistance. The total reinforcement area contributing to splitting resistance is:

$$A_s = 3(0.31) + 8(0.20) = 2.53\ in.^2 \qquad \text{(Eq. 10.52)}$$

The splitting resistance provided by this reinforcement is:

$$P_r = f_s * A_s = 20 * 2.53 = 50.6\ kips \qquad \text{(Eq. 10.53)}$$

According to AASHTO, the anchorage reinforcement is required to resist 4% of the initial bonded prestressing force. Each strand was stressed to 38.8 kips, and a total of 30 bonded strands were provided. Therefore, the required splitting resistance is:

$$P_{splitting} = 0.04(38.8)(30) = 46.6\ kips \qquad \text{(Eq. 10.54)}$$

Because the available splitting resistance exceeds the required resistance, the provided anchorage reinforcement satisfies the AASHTO splitting resistance requirement.

## 10.8 Horizontal shear

Mattock (1974) suggested that a minimum reinforcement ratio should provide at least 0.2 ksi clamping stress for carbon steel rebar. This ensures that the stirrups provide extra shear strength beyond the cracking load at the interface region. With 60 ksi bar stress, this ratio is around 0.30%, much higher than the current AASHTO minimum.

GFRP rebar differs from carbon steel rebar because of their mechanical properties and lower (≥ 22 ksi) transverse shear capacity, which means the usual amount of reinforcement needed for steel bars does not apply. According to a study by Alkatan (2016), a minimum interface reinforcement ratio of 0.405% is necessary to activate GFRP rebars beyond the point where they start cracking. Since GFRP does not have a yield point, the authors suggested using the reinforcement stiffness ($E\rho$), calculated by multiplying the elastic modulus ($E$) and the reinforcement ratio ($\rho$), to establish requirements. A stiffness of at least 29.44 ksi was recommended based on a modulus of 7,252 ksi. If the modulus is lower, the reinforcement ratio must be higher. Alkatan (2016) also determined a minimum clamping stress of 0.148 ksi to utilize GFRP shear stirrups and improve shear strength after cracking, with a maximum strain of about 5,000 micro-strains at the point of failure. The provided reinforcement ratio is 0.51%, as previously stated, while the elastic modulus for rebar, 7,667 ksi, refers to Table 10-1. Therefore, the GFRP reinforcement provided is higher than the minimum reinforcement that Alkatan recommended.

The current NCHRP 12-121 project proposes an expression to determine the horizontal shear resistance provided by GFRP transverse reinforcement. The expression is similar to AASHTO (2024), except it limits the strain in GFRP to 0.002. This limit is provided based on push-off tests performed in the project's experimental program.

AASHTO (2018), section 5.7.4, was used to calculate the shear capacity for carbon steel and GFRP reinforcements. The nominal interface strength ($V_{ni}$) was calculated using equation 5.7.4.3-3. The cohesion factor $c$ is 0.24 ksi for roughened concrete to concrete with a 1/4" amplitude interface. The friction factor $\mu$ of 1.0 was used. The area of interface $A_{cv}$ per unit ft was calculated using interface width $b_{vi}$ of 34 in. and length of 12 in. Across each ft, typically, the reinforcement area provided for carbon steel is 1.6 in$^2$/ft. In contrast, GFRP was 1.976 in$^2$/ft. The permanent force $P_c$ was calculated from the self-weight of the C-I-P topping as 0.314 kip/ft. The reinforcement yield stress $f_y$ of 60 ksi was used for the carbon steel rebar. However, GFRP reinforcement does not yield, so the design tensile strength was used instead (AASHTO, 2018). The design tensile strength per section 2.4.2 in the AASHTO (2018) for GFRP-reinforced concrete is calculated as the product of the environmental reduction factor of $C_E$ equal to 0.7 for long term and the reported tensile strength from the manufacturer, as provided in Table 10-1. The design tensile strength used for interface calculations was 94.66 ksi. The interface capacity is also calculated per ACI Committee 318 (2025) by multiplying the yield strength of carbon steel (60 ksi) by the area of provided interface reinforcement, by a coefficient of friction factor taken as 1.0 for the roughened concrete interface. Because ACI-440.11-2 is based on ACI 318 (ACI Committee 318, 2025) design approach, it does not include a cohesion factor or any expression for the shear interface strength of GFRP due to insufficient research data.

### 10.8.1 AASHTO LRFD provision

AASHTO LRFD Bridge Design Specification (AASHTO, 2024) uses a shear-friction model. The model involves three parameters: interface roughness; normal clamping force in the reinforcement; and dowel action from reinforcement across the interface. The interface shear capacity is calculated from equation 5.7.4.3-3 in AASHTO LRFD Article 5.7.4:

$$V_{ni} = cA_{cv} + \mu(A_{fv}f_y + P_c) \quad \text{(Eq. 10.55)}$$

where
$V_{ni}$ = the nominal interface shear capacity (kips),
$c$ = a cohesion factor,
$A_{cv}$ = the area of concrete that contributes to interface shear (in$^2$),
$\mu$ = the factor account for friction,
$A_{fv}$ = the interface shear reinforcement area (in$^2$),
$f_y$ = reinforcement yield stress (ksi), and
$P_c$ = the permanent normal force to the interface plane (kips).

For GFRP reinforcement, AASHTO (2018) for GFRP-reinforced concrete was used to calculate the capacity for specimens with GFRP reinforcement. This specification used expressions similar to those of carbon steel; however, the tensile design strength of GFRP instead of yield strength was used. Recently, NCHRP project 12-121 proposed the following equation to calculate the interface shear strength:

$$V_{ni} = cA_{cv} + 0.002\mu A_{fv}E_f \quad \text{(Eq. 10.56)}$$

### 10.8.2 Canadian CSA provision

The Canadian code also uses a shear-friction model similar to AASHTO. The model assumes a crack occurs in the plane of the interface. Along the rough interface, the crack separation force will cause cracks to widen, causing tensile stresses in the reinforcement across the plane, as shown in Figure 10-30. These stresses are resisted by compressive stress in the concrete across the crack.

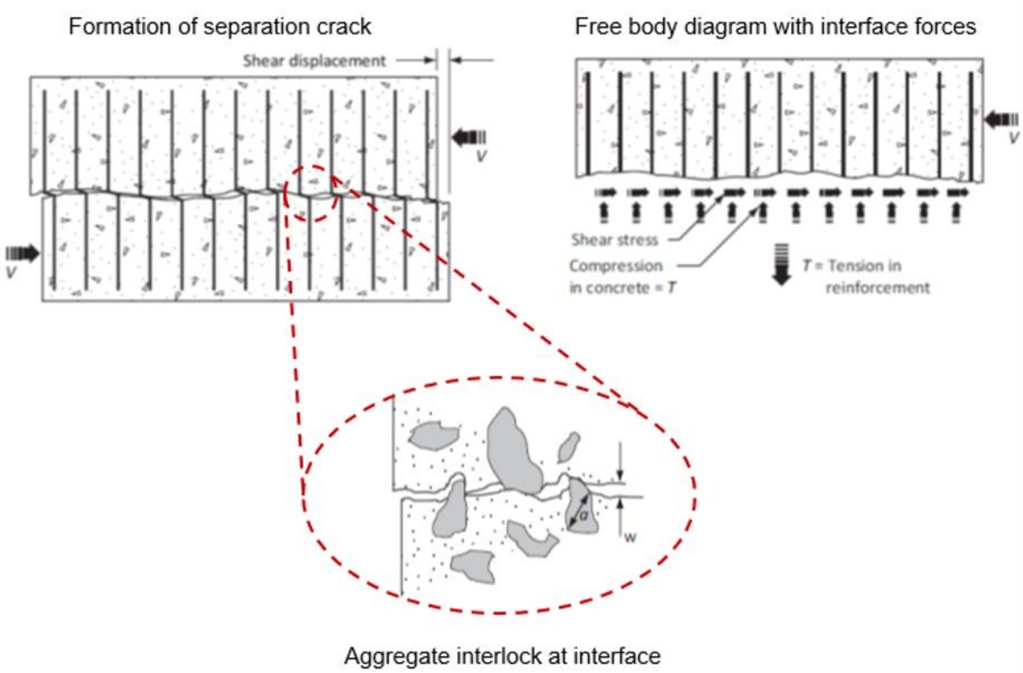


**Figure 10-30. Interface friction model used by CSA S6:25**

The capacity of interface shear can be calculated per 8.9.5 in the Canadian code CSA S6:25:

$$V_{ni} = \phi_c(c + \mu\,\sigma) \quad \text{(Eq. 10.57)}$$

$$\sigma = \frac{A_{vf}}{A_{cv}}f_y + \frac{N}{A_{cv}} \quad \text{(Eq. 10.58)}$$

where

$\phi_c$ = resistance factor for concrete taken as 0.75,

$c$ = the cohesion factor taken as 72.5 psi for roughened concrete,

$\mu$ = friction coefficient taken as 1.0, and
$\sigma$ = the compressive stress across the interface.

The Canadian code uses a similar expression for GFRP; however, the only difference is the yield strength $f_y$. GFRP is calculated as 0.004 strain multiplied by the elastic modulus.

### 10.8.3 ACI 318-25 code provision

The ACI 318 code (ACI Committee 318, 2025) uses the shear friction method to predict the shear interface capacity. The nominal interface capacity in ACI 318 can be calculated using equation 22.9.4.2:

$$V_{ni} = \mu A_{vf} f_y \quad \text{(Eq. 10.59)}$$

where $\mu$ is the coefficient of friction that is taken as 1.0 for the roughened interface.

## 10.9 Results comparison against code

### 10.9.1 Vertical shear

The applied vertical shear for FSB-1 and FSB-4 reached about 28% and 30% of the nominal shear capacity, respectively. The measured strains in the transverse reinforcement were lower than 1 ksi for pairs located at 25 in. from the member end, 1.6 ksi at 85 in. from the member end, and 1.4 ksi at 145 in. from the member end. The reason is that the concrete alone resists the applied shear. However, as shown in Figure 10-31, Figure 10-32, and Figure 10-33, the stress in the GFRP is significantly lower than that in the carbon steel likely due to lower stiffness. Even though the measured strains are comparable, refer to Figure 10-26, Figure 10-27, and Figure 10-28. This is due to the lower elastic modulus for GFRP, 7667 ksi, compared to carbon steel's elastic modulus, about 29,000 ksi. This lower stress means a lower contribution in shear force, with about 26% in the elastic limit range.

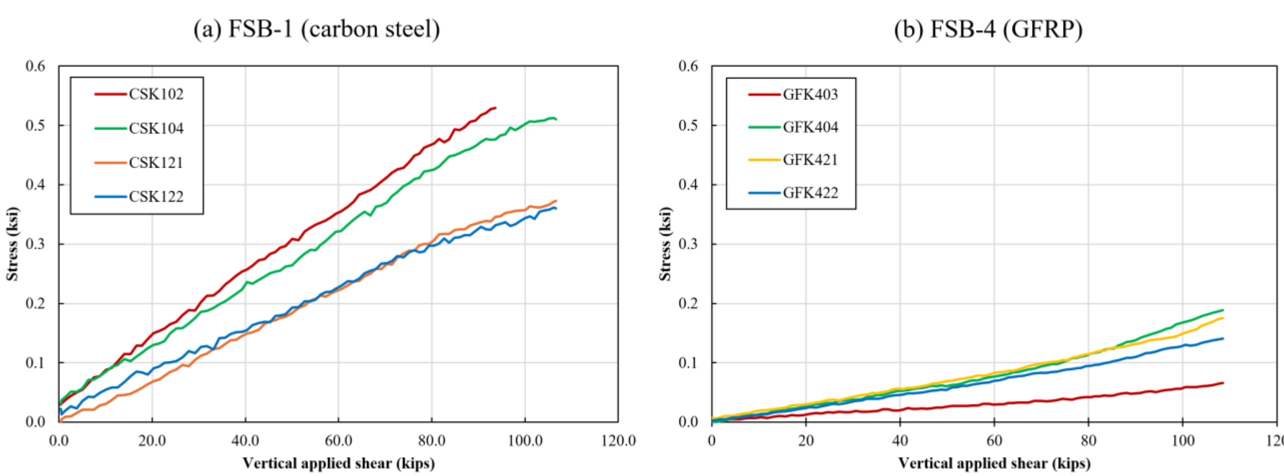


**Figure 10-31. Shear stress in 4K reinforcement located 25 in. from the end for (1) Carbon steel and (2) GFRP**

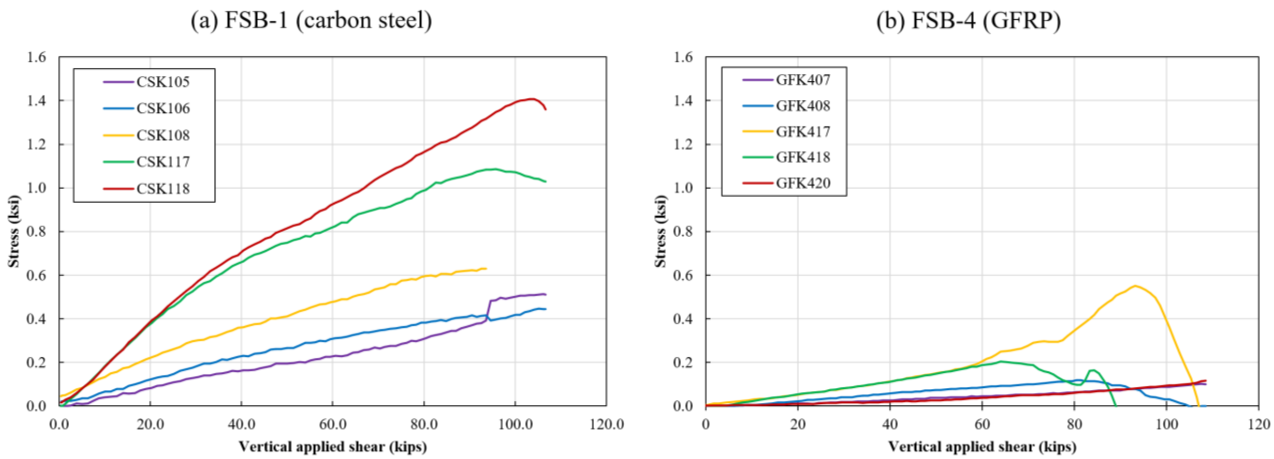


**Figure 10-32. Shear stress in 4K reinforcement located 85 in. from the end for (1) Carbon steel and (2) GFRP**

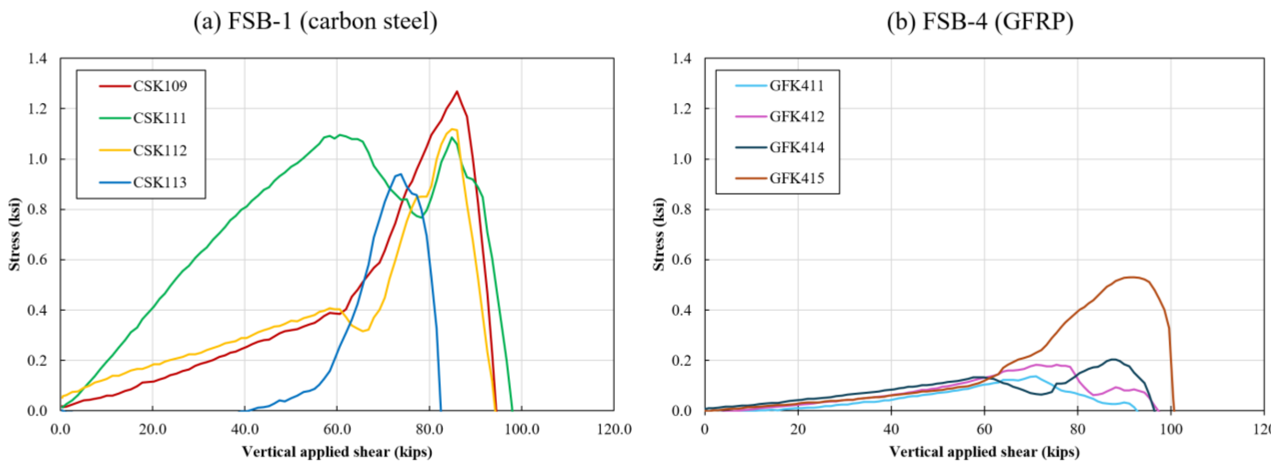


**Figure 10-33. Shear stress in 4K reinforcement located 145 in. from the end for (1) Carbon steel and (2) GFRP**

## 10.9.2 Interface shear

Table 10-6 reports the shear strength capacity for the specimens based on AASHTO, ACI 318-25, and CSA S6:25 and the test value measured.

**Table 10-6. Calculated shear interface capacities and test value**

| Stirrup material | Test value (kips/ft) | AASHTO Nominal (kips/ft) | AASHTO Strength (kips/ft) | ACI Nominal (kips/ft) | ACI Strength (kips/ft) | CSA Nominal (kips/ft) | CSA Strength (kips/ft) |
|---|---|---|---|---|---|---|---|
| **Carbon steel** | 111.84 | 239.9 | 203.9 | 132.4 | 99.3 | 160.2 | 120.2 |
| **GFRP** | 113.76 | 405.0 (144.3) | 303.7 (108.2) | - | - | 95.7 | 71.8 |

Note: Values in parentheses () are calculated as per NCHRP project 12-121 recommendation.

According to AASHTO, the carbon steel reinforcement at the interface will fail when the rebar reaches its yield stress. The yield stress for ASTM A615 Grade 60 rebar is 60 ksi. The measured stress at ultimate load capacity was less than 20% of its yield capacity, as shown in Figure 10-34. However, for GFRP, according to AASHTO (2018), the reinforcement will fail when the rebar reaches its design tensile strength. The design tensile strength is obtained by multiplying the reported tensile strength (135.22 ksi) from the manufacturer by the environmental factor of 0.7 for concrete exposed to weather. However, for testing comparison, this value is assumed equal to 1.0. The measured stress during the tests was less than 4% of the design strength (Figure 10-34).

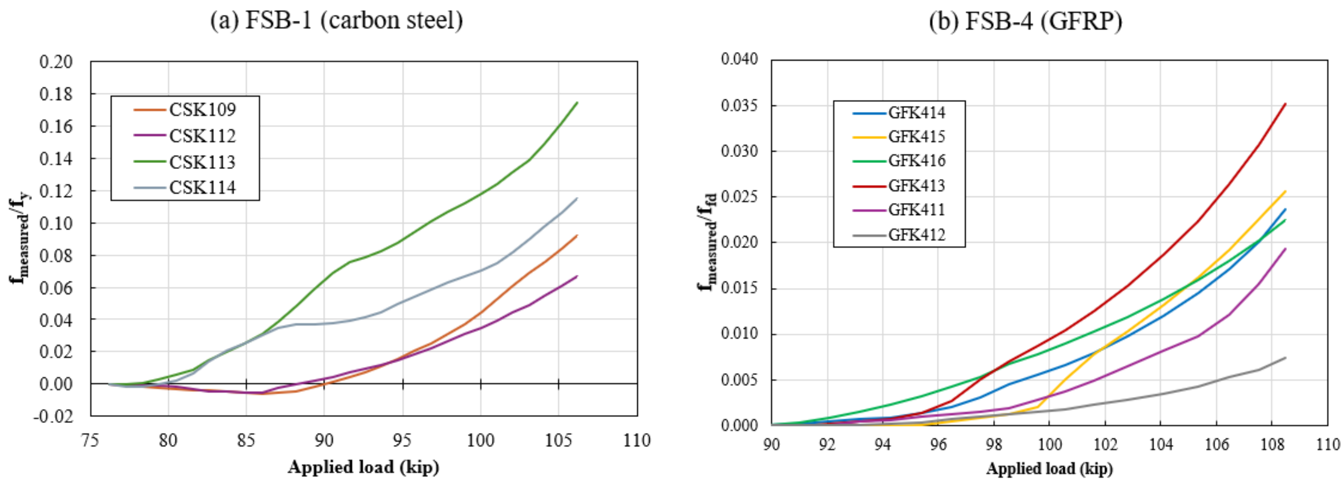


**Figure 10-34. Comparison of measured stress level with capacity of rebars plotted against the applied shear load**

### 10.9.3 Anchorage zone

This section compares the measured strains in the anchorage-zone reinforcement to the requirements of AASHTO (2024). In addition, the recommendations of NCHRP project 12-121 for GFRP reinforcement in pretensioned anchorage zones are evaluated and compared with the experimental results for GFRP reinforcement.

The measured strains in the anchorage-zone reinforcement of FSB-1 (carbon steel reinforcement) and FSB-4 (GFRP reinforcement) are shown in Figure 10-35. The measured strains were relatively similar for both specimens and remained below 150 microstrain (in./in.) throughout prestress transfer.

AASHTO limits the stress in transverse reinforcement located within a distance of $d/4$ from the member end to 20 ksi. However, NCHRP project 12-121 recommends using the same stress limit of 20 ksi while increasing the required splitting resistance from 4% to 12% of the initial bonded prestressing force. Furthermore, the reinforcement considered in resisting splitting forces is extended from a distance of $d/4$ to $3d/4$ from the member end. For the FSB section used in this study, the member width is 48 in.; therefore, the reinforcement considered according to the NCHRP recommendation is located within a distance of 36 in. Within this distance, the reinforcement contributing to splitting resistance consists of five pairs of Type D reinforcement (10 legs) and three No. 5 U-shaped bars located at the end zone.

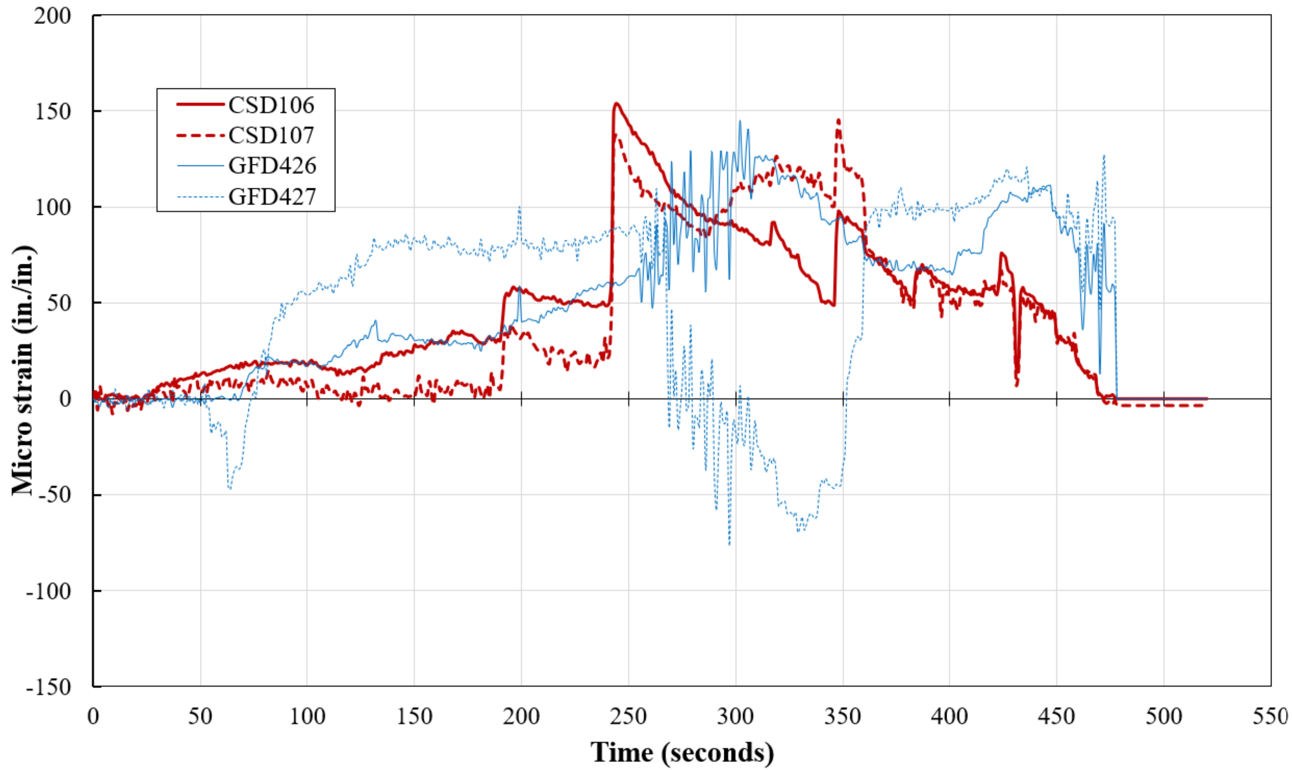


**Figure 10-35. Strain measurement comparison for GFRP and carbon steel reinforcements in the anchorage zone**

The total reinforcement area is:

$$A_f = 10(0.20) + 3(0.31) = 2.93\ in.^2 \quad \text{(Eq. 10.60)}$$

Using the NCHRP recommended stress limit of 20 ksi, the available splitting resistance is:

$$P_r = f_f * A_f = 20 * 2.93 = 58.6\ kips \quad \text{(Eq. 10.61)}$$

The NCHRP 12-121 recommendation requires the anchorage reinforcement to resist 12% of the initial bonded prestressing force. Each strand was stressed to 38.8 kips, and a total of 30 bonded strands were provided. Therefore, the required splitting resistance is:

$$P_{NCHRP} = 0.12(38.8)(30) = 139.7\ kips \quad \text{(Eq. 10.62)}$$

Therefore, the provided reinforcement does not satisfy the splitting-resistance requirement proposed by NCHRP project 12-121. To satisfy this requirement for the FSB section investigated in this study, a total of 16 pairs of Type D reinforcement, instead of 4 for carbon steel, would be required within the first 36 in. from the member end, corresponding to an average spacing of approximately 2.25 in.

Despite not meeting the recommended NCHRP 12-121 resistance requirement, the measured stresses in both specimens remained significantly below the allowable stress limit of 20 ksi. The maximum measured stress in the carbon steel reinforcement of FSB-1 was less than 5 ksi, while the maximum measured stress in the GFRP reinforcement of FSB-4 was less than 1.2 ksi. These values correspond to approximately 25% and 6% of the allowable stress limit, respectively. Furthermore, both FSB-1 and FSB-4 exhibited no visible cracking or damage in the anchorage zone during prestress transfer, despite sudden rupture of the strands at the free strands near End 8 and End 1, as shown in Figure 10-36 and Figure 10-37. These observations suggest that the NCHRP recommendations may be conservative for the FSB section investigated in this study.

**Figure 10-36. End 1 in FSB-1 immediately after strands release**


**Figure 10-37. End 8 in FSB-4 immediately after strands release**

## 10.10 Summary and conclusions

The FSB transverse reinforcement is required to resist three types of shear forces: vertical shear; horizontal shear; and splitting force at the anchorage zone. AASHTO LRFD provides two methods to calculate vertical shear resistance for carbon steel transverse reinforcement and uses similar expressions for GFRP rebars. For horizontal shear, AASHTO LRFD has a similar expression for interface shear resistance for carbon steel and GFRP. The AASHTO anchorage zone requirements are limited to a tensile stress level in reinforcement applicable for carbon steel reinforcement, which might not be appropriate for GFRP rebars.

The experimental program used two specimens, one of which served as a control specimen, FSB-1, that had carbon steel rebar as transverse reinforcement, and the other specimen, FSB-4, which had GFRP rebars as transverse reinforcement. The specimens failed in flexure by crushing of concrete at the top. Because both specimens failed in flexure, this should not be interpreted as GFRP and carbon steel reinforcement having equivalent shear or interface shear capacity.

The applied vertical shear was less than 28% of the concrete shear resistance for FSB-1 and 30% for FSB-4. The measured strains in the GFRP and carbon steel reinforcement showed insignificant values, except in the instrumented K-pairs located close to the constant moment region, suggesting that these strain measurements are due to horizontal shear at the interface between the FSB and C-I-P topping approaching flexural resistance limits.

The anchorage-zone reinforcement strains were monitored during strand release in the casting yard. The provided end-zone reinforcement for both specimens satisfied the AASHTO LRFD Bridge Design Specifications (AASHTO, 2024) for carbon steel reinforcement, as no specific GFRP provisions were available at the time of the experimental program. The measured strains in both specimens were comparable and remained below the 20 ksi stress limit; however, the GFRP reinforcement developed lower stresses due to its lower elastic modulus compared to steel. When evaluated using the more recent NCHRP project 12-121 recommendations, the designed GFRP reinforcement is not fully satisfactory in terms of the required splitting resistance. Despite this, the measured stresses in the GFRP reinforcement remained low, and no cracks or damage were observed in FSB-4, even after the impact associated with sudden strand rupture during detensioning. These observations suggest that the NCHRP project 12-121 recommendations may be conservative for the FSB section considered in this study.

Limited standards currently address the use of GFRP as shear-interface reinforcement; however, additional guidance is expected upon publication of the final NCHRP Project 12-121 report. Currently, AASHTO LRFD Bridge Design Specifications are recommended to deal with GFRP similarly to carbon steel. Based on that, the GFRP interface capacity was higher than the carbon steel interface capacity at 68.6%; the reinforcement ratio of carbon steel was lower than that of GFRP at 17.6%. Per the current AASHTO Bridge Design Specifications for GFRP-reinforced concrete (AASHTO, 2018), interface strength is unconservative compared to the equation proposed by NCHRP Project 12-121. The Canadian standard CSA S6:25 GFRP interface capacity prediction was lower than the interface horizontal shear measured during the tests. Besides that, the measured strain in the GFRP rebars is still lower than 4% of the design tensile strain. This means that the CSA S6:25 expression is conservative for the studied case.

The GFRP strain levels under the relatively same horizontal shear force are similar to the carbon steel rebars (Figure 10-29).  This suggests that GFRP reinforcement works similarly to carbon steel rebar under service loads.

# REFERENCES


AASHTO (American Association of State Highway and Transportation Officials). 2023. T119M/T119, Standard method of test for slump of hydraulic cement concrete. Washington, DC: AASHTO.

AASHTO (American Association of State Highway and Transportation Officials). 2024. AASHTO LRFD bridge design specifications, 10th ed. Washington, DC: AASHTO.

AASHTO (American Association of State Highway and Transportation Officials). 2018. AASHTO LRFD bridge design guide specifications for GFRP-reinforced concrete, 2nd ed. Washington, DC: AASHTO.

Abdelrahman, A. A., G. Tadros, and S. H. Rizkalla. 1995. "Test model for the first Canadian smart highway bridge." *ACI Struct. J.* 92 (4): 451–458. https://doi.org/10.14359/994

ACI (American Concrete Institute) Committee 318. 2025. *Building code for structural concrete: Code requirements and commentary*. ACI CODE-318-25. Farmington Hills, MI: ACI.

ACI (American Concrete Institute) Committee 440. 2015. *Guide for the design and construction of structural concrete reinforced with fiber-reinforced polymer (FRP) bars*. ACI CODE-440.1R-15. Farmington Hills, MI: ACI.

ACI (American Concrete Institute) Committee 440. 2022. *Building code requirements for structural concrete reinforced with glass fiber-reinforced polymer (GFRP) bars: Code and commentary*. ACI CODE-440.11-22. Farmington Hills, MI: ACI.

Ahmed, E. A., E. F. El-Salakawy, and B. Benmokrane. 2010a. "Shear performance of RC bridge girders reinforced with carbon FRP stirrups." *J. Bridge Eng.* 15 (1): 44–54. https://doi.org/10.1061/(ASCE)BE.1943-5592.0000035

Ahmed, E. A., E. F. El-Salakawy, and B. Benmokrane. 2010b. "Performance evaluation of glass fiber-reinforced polymer shear reinforcement for concrete beams." *ACI Struct. J.* 107 (1): 53–62.

Al-Kaimakchi, A., and M. Rambo-Roddenberry. 2021a. "Mechanical and bond properties of Grade 2205 duplex high-strength stainless steel strand." *PCI J.* 66 (4): 66–81. https://doi.org/10.15554/pcij66.4-01

Al-Kaimakchi, A., and M. Rambo-Roddenberry. 2021b. "Measured transfer length of 15.2-mm (0.6-in.) duplex high-strength stainless steel strands in pretensioned girders." *Eng. Struct.* 237: 112178. https://doi.org/10.1016/j.engstruct.2021.112178

Al-Kaimakchi, A., and M. Rambo-Roddenberry. 2021c. "Full-scale AASHTO Type II girders prestressed with stainless steel strands." *J. Bridge Eng.* 26 (9): 04021065. https://doi.org/10.1061/(ASCE)BE.1943-5592.0001765

Al-Kaimakchi, A., & Rambo-Roddenberry, M. 2021d. "Flexural behavior of concrete bridge girders prestressed with stainless steel strands." *ACI Structural J.* 118 (4): 137–152. https://doi.org/10.14359/51730541

Al-Kaimakchi, A., and M. Rambo-Roddenberry. 2022. "Structural assessment of AASHTO Type II prestressed concrete girder with GFRP or stainless-steel shear reinforcement." *J. Bridge Eng.* 27 (7): 04022056. https://doi.org/10.1061/(ASCE)BE.1943-5592.0001899

Aljada, B. H., A. El-Ragaby, and E. F. El-Salakawy. 2024. "GFRP stirrups as shear friction reinforcement for different concrete interfaces." *J. Compos. Constr.* 28 (6): 04024036. https://doi.org/10.1061/JCCOF2.CCENG-4516

Alkatan, J. 2016. "FRP shear transfer reinforcement for composite concrete construction." M.S. thesis, Dept. of Civil and Environmental Engineering, Univ. of Windsor, Windsor, ON, Canada.

ASTM International. 2017. A276/A276M-17, Standard specification for stainless steel bars and shapes. West Conshohocken, PA: ASTM International.

ASTM International. 2020a. C143/C143M, Standard test method for slump of hydraulic-cement concrete. West Conshohocken, PA: ASTM International.

ASTM International. 2020b. A1114/A1114M-20, Standard specification for low-relaxation, seven-wire, Grade 240 [1655], stainless steel strand for prestressed concrete. West Conshohocken, PA: ASTM International.

ASTM International. 2020c. A1061/A1061M-20, Standard test methods for testing multi-wire steel prestressing strand. West Conshohocken, PA: ASTM International.

ASTM International. 2022a. C231/C231M-22, Standard test method for air content of freshly mixed concrete by the pressure method. West Conshohocken, PA: ASTM International.

ASTM International. 2022b. ASTM A615/A615M-22, Standard specification for deformed and plain carbon-steel bars for concrete reinforcement. West Conshohocken, PA: ASTM International.

ASTM International. 2022c. ASTM D7957/D7957M-22, Standard specification for solid round glass fiber reinforced polymer bars for concrete reinforcement. West Conshohocken, PA: ASTM International.

Bentz, E. C. 2000. "Sectional analysis of reinforced concrete members." Ph.D. thesis, Dept. of Civil Engineering, Univ. of Toronto, Toronto.

Bentz, E. C., F. J. Vecchio, and M. P. Collins. 2006. "Simplified modified compression field theory for calculating shear strength of reinforced concrete elements." *ACI Struct. J.* 103 (4): 614–624. https://doi.org/10.14359/16438

Birkeland, P. W., and H. W. Birkeland. 1966. "Connections in precast concrete construction." *ACI J. Proc.* 63 (3): 345–368. https://doi.org/10.14359/7627

CEN. 2006. Eurocode 3: Design of steel structures—Supplementary rules for stainless steels (EN 1993-1-4:2006). Brussels: CEN.

Cohn, M. Z., and P. Riva. 1991. “Flexural ductility of structural concrete sections.” *PCI J.* 36 (2): 50–87.

Collins, M. P., and D. Mitchell. 1991. *Prestressed concrete structures*. Englewood Cliffs, NJ: Prentice Hall.

Crispino, E. D., T. E. Cousins, C. L. Roberts-Wollmann, and M. C. Brown. 2009. *Anchorage zone design for pretensioned precast bulb-T bridge girders in Virginia*. Report No. FHWA/VTRC 09-CR15. Charlottesville, VA: Virginia Transportation Research Council.

CSA (Canadian Standards Association) Group. 2025. *Canadian highway bridge design code*. CSA S6:25. Toronto: CSA Group.

CSA (Canadian Standards Association) Group. 2026. *Design and construction of building structures with fibre-reinforced polymers*. CSA S806:26. Toronto: CSA Group.

Deshmukh, A., W. J. Gold, G. H. AlAithan, and A. Nanni. 2023. “Non-metallic reinforcement for concrete.” *STRUCTURE Mag.*, November, 36–39.

FDOT (Florida Department of Transportation). 2022. Stainless steel strands and lightweight concrete for pretensioned concrete girders, BDV30-977-22. Tallahassee, FL: FDOT.

FDOT (Florida Department of Transportation). 2025. Standard specifications for road and bridge construction. Tallahassee, FL: FDOT.

FDOT (Florida Department of Transportation). 2026a. *Standard Plans Instructions*, Index 20450 Series. Tallahassee, FL: FDOT Structures Design Office.

FDOT (Florida Department of Transportation). 2026b. *Structures manual: Volume 1: Structures design guidelines*. Topic No. 625-020-018. Tallahassee, FL: FDOT Structures Design Office. https://www.fdot.gov/structures/structuresmanual/currentrelease/structuresmanual.shtm.

Gar, S. P., M. Head, and S. Hurlebaus. 2012. “Tension stiffening in prestressed concrete beams using moment-curvature relationship.” *J. Struct. Eng.* 138 (8): 1075–1078. https://doi.org/10.1061/(ASCE)ST.1943-541X.0000534

Gardner, L. 2005. “The use of stainless steel in structures.” *Prog. Struct. Eng. Mater.* 7 (2): 45–55. https://doi.org/10.1002/pse.190.

Grace, N. F., and G. A. Sayed. 1998. “Ductility of prestressed concrete bridges using CFRP strands.” *Concrete Int.* 20 (6): 25–30.

Harries, K. A., G. Zeno, and B. Shahrooz. 2012. “Toward an improved understanding of shear-friction behavior.” *ACI Struct. J.* 109 (6): 835–844.

Hawkins, N. and D. Kuchma. 2008. “Recent changes to concrete shear strength provisions of AASHTO LRFD Bridge Design Specifications,” Structures Congress, 1–8.

Hill, H. N. 1944. “Determination of stress–strain relations from ‘offset’ yield strength values.” NACA Tech. Note 927, National Advisory Committee for Aeronautics, Washington, DC.

Hofbeck, J. A., I. O. Ibrahim, and A. H. Mattock. 1969. “Shear transfer in reinforced concrete.” *ACI J. Proc.* 66 (2): 119–128. https://doi.org/10.14359/7349

Holt, J., O. Bayrak, P. Okumus, A. Stavridis, T. Murphy, D. Panchal, A. Dutta, and A. Randiwe. 2022. Concrete bridge shear load rating guide and examples: Using the modified compression field theory. Report No. FHWA-HIF-22-025. Washington, DC: Federal Highway Administration.

Kahn, L. F., and A. D. Mitchell. 2002. “Shear friction tests with high-strength concrete.” *ACI Struct. J.* 99 (1): 98–103. https://doi.org/10.14359/11040

Kannel, J., C. French, and H. Stolarski. 1997. “Release methodology of strands to reduce end cracking in pretensioned concrete girders.” *PCI J.* 42 (1): 42–54.

Lee, J. D. 2022. “The effect of tension stiffening in moment-curvature responses of prestressed concrete members.” *Eng. Struct.* 256: 114013. https://doi.org/10.1016/j.engstruct.2022.114013.

Lequesne, R. D., W. N. Collins, E. Lucon, D. Darwin, and A. Poudel. 2020. “Interlaboratory study of standard methods for testing multiwire steel prestressing strand.” *PCI J.* 65 (4): 71–86. https://doi.org/10.15554/pcij65.4-03

Loov, R. E., and A. K. Patnaik. 1994. “Horizontal shear strength of composite concrete beams with a rough interface.” *PCI J.* 39 (1): 48–69. https://doi.org/10.15554/pcij.01011994.48.69

Marshall, W. T., and A. H. Mattock. 1962. “Control of horizontal cracking in the ends of pretensioned prestressed concrete girders.” *PCI J.* 7 (5): 56–74. https://doi.org/10.15554/pcij.10011962.56.74

Mast, R. F. 1968. “Auxiliary reinforcement in concrete connections.” *J. Struct. Div.* 94 (6): 1485–1504.

Mast, R. F. 1992. “Unified design provisions for reinforced and prestressed concrete flexural and compression members.” *ACI Struct. J.* 89 (2): 185–199. https://doi.org/10.14359/3209

Mast, R. F., M. Dawood, S. H. Rizkalla, and P. Zia. 2008. “Flexural strength design of concrete beams reinforced with high-strength steel bars.” *ACI Struct. J.* 105 (5): 570–577. https://doi.org/10.14359/19940

Mattock, A. H. 1974. “Shear transfer in concrete having reinforcement at an angle to the shear plane.” In *Shear in reinforced concrete*, 17–42. Special Publication SP-42. Farmington Hills, MI: American Concrete Institute.

Mattock, A. H. 1979. "Flexural strength of prestressed concrete sections by programmable calculator." *PCI J.* 24 (1): 32–54. https://doi.org/10.15554/pcij.01011979.32.54.

Mirza, J. F., and M. E. Tawfik. 1978. "End cracking in prestressed members during detensioning." *PCI J.* 23 (2): 66–78.

Moon, D. Y., G. Zi, J.-H. Kim, S.-J. Lee, and G. Kim. 2010. "On strain change of prestressing strand during detensioning procedures." *Eng. Struct.* 32 (9): 2570–2578. https://doi.org/10.1016/j.engstruct.2010.04.025.

Moser, R. D., L. F. Kahn, P. M. Singh, and K. E. Kurtis. 2013. "Preliminary studies of high-strength stainless prestressing steels." ACI Spec. Publ. 291: 1–10. https://doi.org/10.14359/51685617.

Moser, R. D. 2011. "High-strength stainless steels for corrosion mitigation in prestressed concrete." Ph.D. thesis, School of Civil and Environmental Engineering, Georgia Institute of Technology, Atlanta.

Mufti, A. A., J. P. Newhook, and G. Tadros. 1996. "Deformability versus ductility in concrete beams with FRP reinforcement." In *Proc., 2nd Int. Conf. on Advanced Composite Materials in Bridges and Structures (ACMBS-II)*, 189–199. Montreal: Canadian Society for Civil Engineering.

Naaman, A. E., and S. M. Jeong. 1995. "Structural ductility of concrete beams prestressed with FRP tendons." In *Non-metallic (FRP) reinforcement for concrete structures*, edited by L. Taerwe, 379–386. London: E & FN Spon.

Naaman, A. E., M. H. Harajli, and J. K. Wight. 1986. "Analysis of ductility in partially prestressed concrete flexural members." *PCI J.* 31 (3): 64–87. https://doi.org/10.15554/pcij.05011986.64.87

Nanni, A., A. De Luca, and H. J. Zadeh. 2014. *Reinforced concrete with FRP bars: Mechanics and design*. Boca Raton, FL: CRC Press.

Park, R., and T. J. Falconer. 1983. "Ductility of prestressed concrete piles subjected to simulated seismic loading." *PCI J.* 28 (5): 112–144. https://doi.org/10.15554/pcij.09011983.112.144

Paul, A., L. B. Gleich, and L. F. Kahn. 2017a. "Transfer and development length of high-strength duplex stainless steel strand in prestressed concrete piles." *PCI J.* 62 (3): 59–73. https://doi.org/10.15554/pcij62.3-01

Pessiki, S., M. Kaczinski, and H. H. Wescott. 1996. "Evaluation of effective prestress force in 28-year-old prestressed concrete bridge beams." *PCI J.* 41 (6): 78–89. https://doi.org/10.15554/pcij.11011996.78.89

Plecnik, J. M., and S. H. Ahmad. 1989. *Transfer of composite technology to design and construction of bridges*. Report No. FHWA-RD-89-142. Washington, DC: Federal Highway Administration.

Podolny, W., Jr. 1992. “Corrosion of prestressing steels and its mitigation.” *PCI J.* 37 (5): 34–55. https://doi.org/10.15554/pcij.09011992.34.55.

Polak, M. A., and K. G. Blackwell. 1998. “Modelling tension in reinforced concrete members subjected to bending and axial load.” *J. Struct. Eng.* 124 (9): 1017–1024.

Ramberg, W., and W. R. Osgood. 1943. “Description of stress–strain curves by three parameters.” NACA Tech. Note 902. National Advisory Committee for Aeronautics.

Russell, B. W., and N. H. Burns. 1996. “Measured transfer lengths of 0.5 and 0.6 in. strands in pretensioned concrete.” *PCI J.* 41 (5): 44–65. https://doi.org/10.15554/pcij.09011996.44.65

Shaw, D. M., and L. H. Sneed. 2014. “Interface shear transfer of lightweight-aggregate concretes cast at different times.” *PCI J.* 59 (3): 130–144. https://doi.org/10.15554/pcij.06012014.130.144

Skogman, B. C., M. K. Tadros, and R. Grasmick. 1988. “Ductility of reinforced and prestressed concrete flexural members.” *PCI J.* 33 (6): 94–107. https://doi.org/10.15554/pcij.11011888.94.107

Soltani, M., and B. E. Ross. 2017. “Evaluation of a four-point bending-test method for interface shear transfer in concrete members.” *Pract. Period. Struct. Des. Constr.* 22 (4): 04017013. https://doi.org/10.1061/(ASCE)SC.1943-5576.0000325

Thompson, K. J., and R. Park. 1980. “Ductility of prestressed and partially prestressed concrete beam sections.” *PCI J.* 25 (2): 46–70. https://doi.org/10.15554/pcij.03011980.46.70

Transportation Research Board. In press. *Guidelines for the design of prestressed concrete bridge girders using FRP auxiliary reinforcement*. NCHRP Project 12-121. Washington, DC: National Academies of Sciences, Engineering, and Medicine.

Transportation Research Board. 2025. *Stainless steel strands for prestressed concrete bridge elements*. NCHRP Project 12-120 Research Report 1161. Washington, DC: National Academies of Sciences, Engineering, and Medicine.

Vecchio, F. J., and M. P. Collins. 1986. “The modified compression-field theory for reinforced concrete elements subjected to shear.” *ACI J.* 83 (2): 219–231.

Vega, C., A. Belarbi, and A. Nanni. 2024. “Experimental assessment of shear transfer capacity of GFRP reinforcement using the push-off test.” *J. Compos. Constr.* 28 (6): 04024053. https://doi.org/10.1061/jccof2.cceng-4680

Zou, P. X. W. 2003. “Flexural behavior and deformability of fiber reinforced polymer prestressed concrete beams.” *J. Compos. Constr.* 7 (4): 275–284. https://doi.org/10.1061/(ASCE)1090-0268(2003)7:4(275)

# APPENDIX 1 – DESIGN CALCULATIONS

# Materials:

## Concrete:

Assumptions:

1- $K_1$ for calculation of modulus of elasticity is equal $(K_1 = 1.0)$.

2- Unit weight of normal weight of concrete for the beam and deck (LRFD Table 3.5.1-1):

$$w_{c,beam} = 0.14 + 0.001 f_c' = 0.14 + 0.001 * 8.5 = 0.1485\ kcf$$

$$w_{c,slab} = 0.145\ kcf \qquad since\ f_c' = 4.5\ ksi\ \leq 5.0\ ksi$$

3- Unit weight of reinforced concrete for applied loads calculation:

$$\gamma_{beam} = w_{c,beam} + 0.005 = 0.1535\ kcf$$

$$\gamma_{slab} = w_{c,slab} + 0.005 = 0.150\ kcf$$

4- Table 1.4.2.1 specify concrete cover a 3” cover will be used.

5- For prestressed concrete Class VI is chosen (SDG table 1.4.3.1) $f_c' = 8.5\ ksi$.

6- For concrete bridge deck Class II is chosen (SDG table 1.4.3.1) $f_c' = 4.5\ ksi$ .

7- The design value of $f_{ci}' = 0.8 f_c' = 6.8\ ksi$.

8- Modulus of elasticity:

At final:

$$E_{c,beam} = 120{,}000\ K_1 w_c^{2.0} f_c'^{0.33} = 120{,}000 *\ 1 * 0.1485^2 * 8.5^{0.33} = 5362.2\ ksi$$

At transfer:

$$E_{ci,beam} = 120{,}000\ K_1 w_c^{2.0} f_c'^{0.33} = 120{,}000 *\ 1 * 0.1485^2 * 6.8^{0.33} = 4981.5\ ksi$$

For deck:

$$E_{c,slab} = 120{,}000\ K_1 w_c^{2.0} f_c'^{0.33} = 120{,}000 *\ 1 * 0.145^2 * 4.5^{0.33} = 4144.5\ ksi$$

## Carbon steel reinforcement rebar:

ASTM A615, Grade 60 deformed carbon-steel bar

## Stainless steel strands:

Stainless steel strands are the choice for bridges located in splash zone, and harsh environments, (SDG 4.3.1.A.2).

1- Stainless steel type $ASTM\ A1114\ grade\ 240\ low\ relaxation$ with straight configuration is used.

2- Modulus of elasticity of $(Eps = 24{,}000\ ksi)$.

3- Rupture strand failure is $\varepsilon_{pu} = 0.014$ for extreme strand layer.

4- Area of strand = 0.231 $in^2$

## Glass Fiber Reinforced Polymer (GFRP) Reinforcing Bars:

the rebars shall meet ASTM D7957.

**Table A1-1. Section properties for Florida slab beam specimen**

# Section properties:

## Gross:

| | Value | Unit |
|---|---|---|
| Beam width | 4 | ft |
| Area | 473.76 | $in^2$ |
| Perimeter | 114.33 | in |
| Ixx | 5,772 | $in^4$ |
| yt | 6.43 | in |
| yb | 5.57 | in |
| Strands eccentricity e | 1.57 | in |

## Transformed section at release (30 strands:

| | Value | Unit |
|---|---|---|
| Area | 500 | $in^2$ |
| Modular ratio npi | 4.82 | |
| Ixx | 5,829 | $in^4$ |
| yt | 6.41 | in |
| yb | 5.59 | in |
| Strands eccentricity e | 1.59 | in |

## Transformed section after losses (30 strands):

| | Value | Unit |
|---|---|---|
| Area | 497.9 | $in^2$ |
| Modular ratio np | 4.48 | |
| Ixx | 5,829 | $in^4$ |
| yt | 6.51 | in |
| yb | 5.49 | in |
| Strands eccentricity e | 1.49 | in |

## Composite transformed section (30 strands):

| | Value | Unit |
|---|---|---|
| Area | 797 | $in^2$ |
| Modular ratio n1 | 4.48 | |
| Modular ratio n2 | 0.78 | |
| Ixx | 20902 | $in^4$ |
| yt | 9.59 | in |
| yb | 8.41 | in |

# Applied loads and moments:

## Self-weight dead load:

Beam self-weight:

$$w_D = \gamma_{beam} * A_g = 0.1535 * \frac{474}{144} = 0.51\ \frac{k}{ft}$$

## Superimposed (deck) dead load:

Topping self-weight:

$$A_{topping} = 6 * 48 + 8 * 6 * 2 = 384\ in^2$$

$$w_D = \gamma_{slab} * A_{topping} = 0.150 * \frac{384}{144} = 0.4\ \frac{k}{ft}$$

# Prestressing force and losses:

## Jacking:

The SDG is specifying maximum steel stress immediately prior to transfer $f_{pbt} = 0.65 f_{pu}$ for this project $f_{pbt} = 0.7 f_{pu}$ as modifications to monitor the behavior of HSSS strands during fabrication and load testing.

$$f_{pj} = 0.7 * 240 = 168\ ksi$$

## Initial prestressing (prestressing at transfer):

Estimating elastic shortening (LRFD 5.9.3.2.3a):

Using trial and error to find elastic shortening (last loop is illustrated below):

$$\Delta f_{pES} = -11.33\ ksi$$

$$f_{pi} = f_{pj} + \Delta f_{pES} = 168 - 11.33 = 156.67\ ksi$$

$$P_i = f_{pj} A_{ps} = 156.67 * 6.93 = 1085.7\ kips < 1240\ kips \quad O.K.$$

$$f_{cgp} = -\frac{P_i}{A_{trans}} - \frac{P_i * e^2}{I_{trans}} + \frac{M_d * e}{I_{trans}} = -\frac{1085.7}{500} - \frac{1085.7 * 1.59}{5829} + \frac{73 * 12}{5829} = 2.352\ ksi$$

$$\Delta f_{pES} = \frac{E_p}{E_{ci}} f_{cgp} = \frac{24000}{4982} * 2.352 = -11.33\ ksi$$

$$f_{pi} = f_{pj} + \Delta f_{pES} = 168 - 11.33 = 156.67\ ksi \quad the\ assumption\ is\ valid.$$

## Losses:

Approximate estimate time dependent losses (LRDF 5.9.3.3):

$Assuming\ the\ relative\ humdity\ H = 75\%$

$$\gamma_h = 1.7 - 0.01H = 1.7 - 0.01 * 75 = 0.95$$

$$\gamma_{st} = \frac{5}{1 + f'_{ci}} = \frac{5}{1 + 6.8} = 0.64$$

$$\Delta f_{pR} = 2.4\ ksi$$

$$\Delta f_{pLT} = 10.0 \frac{f_{pj} A_{ps}}{A_g} \gamma_h \gamma_{st} + 12.0 \gamma_h \gamma_{st} + \Delta f_{pR}$$

$$= 10 * \frac{168 * 6.92}{473.7} * 0.95 * 0.64 + 12 * 0.95 * 0.64 + 2.4 = -24.6\ ksi$$

## Final prestressing:

$$f_{pe} = f_{pj} + \Delta f_{pES} += 168 - 11.33 - 24.6 = 143.4\ ksi$$

## Transfer length:

$$L_t = 60 * d_p = 60 * 0.62 = 37.2\ in = 3.1\ ft$$

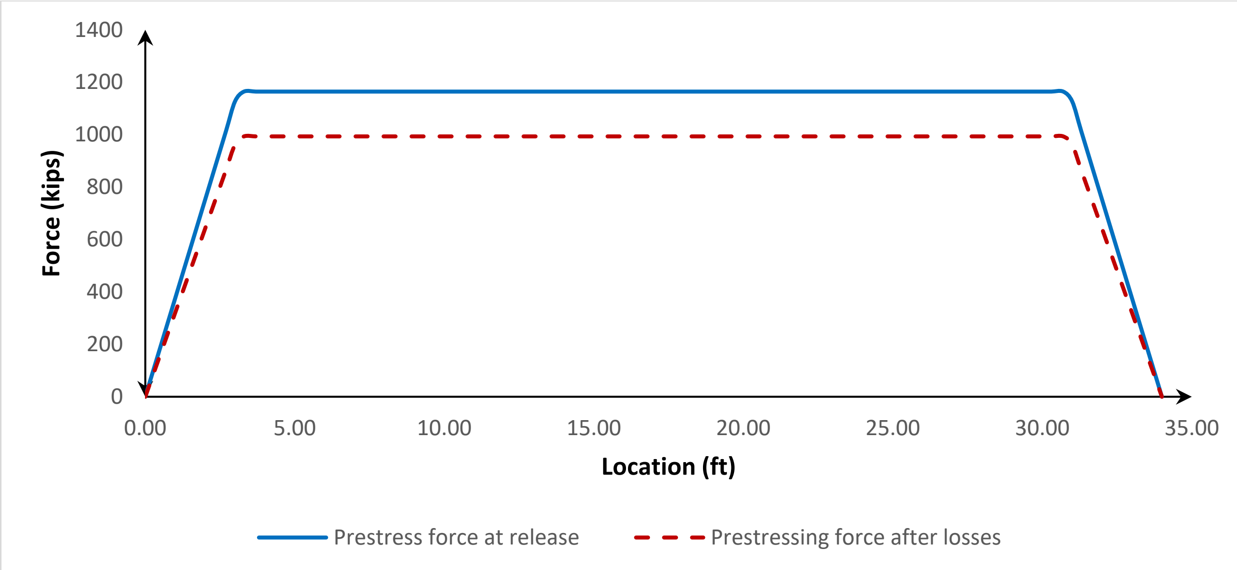


**Figure A1-1. Prestressing force distribution**

# Stress check:

## At release:

**For gross section:**

$$P_i = f_{pi} * A_{ps} = 156.67 * 6.93 = 1085.7\ k$$

Moments' calculations

Moment due to self-weight at mid span:

$$L = 34\ ft \quad the\ beam\ length\ is\ taken\ as\ length\ of\ span.$$

$$M_D = \frac{w_D . L^2}{8} = \frac{0.51 * 34^2}{8} = 73.01\ k - ft = 876.14\ k - in$$

Moment due to prestressing at mid span:

$$M_{Pi} = P_i * e_g = 1085.7 * 1.57 = 1704.6\ k - in$$

Stress check at Mid-span:

- At transfer:

Top: $f_t = -\frac{P_i}{A_g} + \frac{M_{Pi} - M_D}{S_t} = -\frac{1085.7}{474} + \frac{1704.6 - 876.14}{897.7} = -1.37\ ksi\ (compression)$

Bottom: $f_b = -\frac{P_i}{A_g} + \frac{M_D - M_{pi}}{S_b} = -\frac{1085.7}{474} + \frac{876.14 - 1704.6}{1036.3} = -3.09\ ksi\ (compression)$

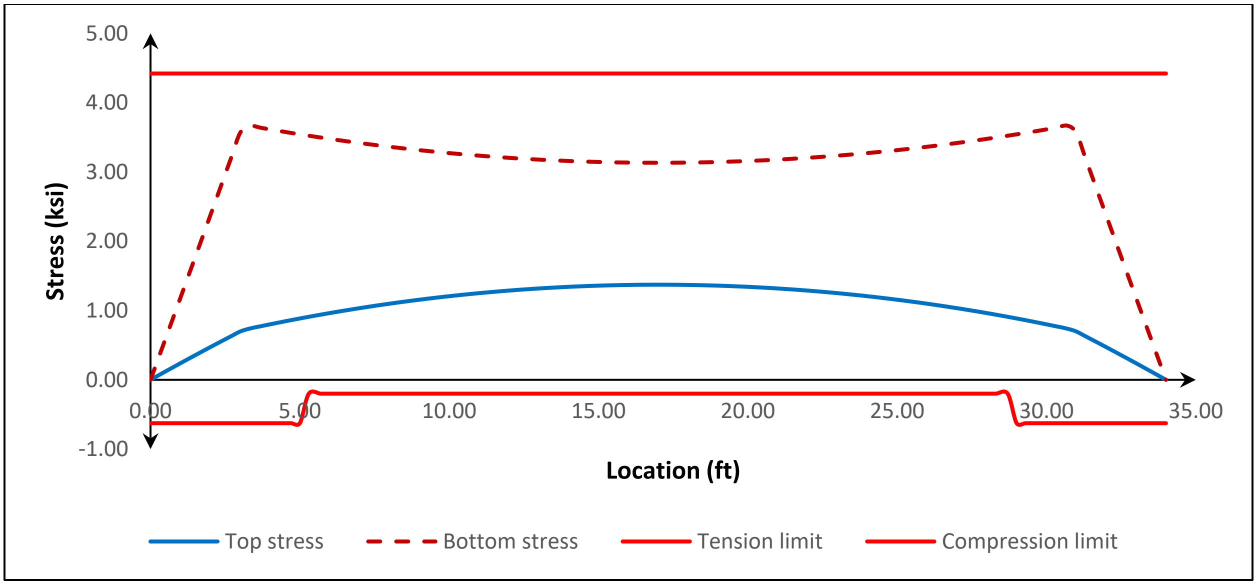


**Figure A1-2. Stress distribution at release**

**For transformed section:**

The elastic shortening can be assumed = 0 when using transformed section properties (LRDF 5.9.3.2.3a):

$$P_j = f_{pi} * A_{ps} = 168 * 6.93 = 1164.24\ k$$

Moments' calculations

Moment due to prestressing at mid span:

$$M_{Pi} = P_i * e_{trans} = 1164.24 * 1.47 = 1711.4\ k - in$$

Stress check at Mid-span:

- At transfer:

Top: $f_t = -\frac{P_i}{A_g} + \frac{M_{Pi} - M_D}{S_t} = -\frac{1164.24}{500.2} + \frac{1711.4 - 876.14}{892} = -1.39\ ksi\ (compression)$

Bottom: $f_b = -\frac{P_i}{A_g} + \frac{M_D - M_{pi}}{S_b} = -\frac{1164.24}{500.2} + \frac{876.14 - 1711.4}{1066} = -3.11\ ksi\ (compression)$

## After losses:

**For transformed section:**

$$P_e = f_{pe} * A_{ps} = 143.4 * 6.93 = 993.76\ k$$

Moments' calculations

Moment due to prestressing at mid span:

$$M_{Pe} = P_e * e_{trans} = 993.76 * 1.47 = 1460.8\ k - in$$

Stress check at Mid-span:

- At transfer:

Top: $f_t = -\frac{P_e}{A_g} + \frac{M_{Pe}-M_D}{S_t} = -\frac{993.76}{500.2} + \frac{1460.8-876.14}{892} = -1.33\ ksi\ (compression)$

Bottom: $f_b = -\frac{P_e}{A_g} + \frac{M_D-M_{pe}}{S_b} = -\frac{993.76}{500.2} + \frac{876.14-1460.8}{1066} = -2.54\ ksi\ (compression)$

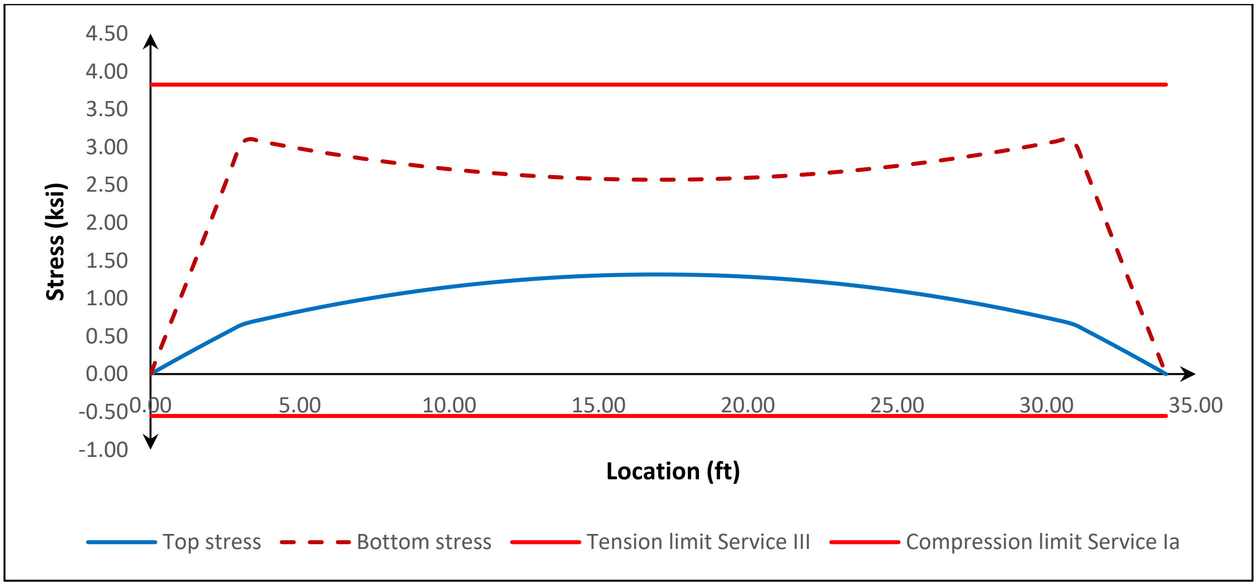


**Figure A1-3. Stress distribution after losses**

## Changing support condition:

Moments' calculations

Moment due to self-weight at mid span after the support and the distance is (1ft) from the edge for both side:

$$l = 32\ ft\ clear\ span\ between\ supports$$

At mid-section:

$$M_D = \frac{w_D}{2}\left(c^2 - \frac{l^2}{4}\right) = \frac{0.505}{2}\left(1^2 - \frac{32^2}{4}\right) = 64.39\ k-ft = 772.65\ k-in$$

## After applying topping:

Moment due to topping self-weight at mid span:

$$l = 32\ ft$$

$$M_{D,topping} = \frac{w_{D,topping}}{2l}\left(c^2 - \frac{l^2}{4}\right) = \frac{0.4}{2}\left(1^2 - \frac{32^2}{4}\right) = 51\ k-ft = 612\ k-in$$

Stress check at Mid-span:

- At transfer:

Top: $f_t = -\frac{P_e}{A_g} + \frac{M_{Pe}-M_D}{S_t} = -\frac{993.76}{500.2} + \frac{1460.8-612-772.65}{892} = -1.90\ ksi\ (compression)$

Bottom: $f_b = -\frac{P_e}{A_g} + \frac{M_D-M_{pe}}{S_b} = -\frac{993.76}{500.2} + \frac{612+772.65-1460.8}{1066} = -2.06\ ksi\ (compression)$

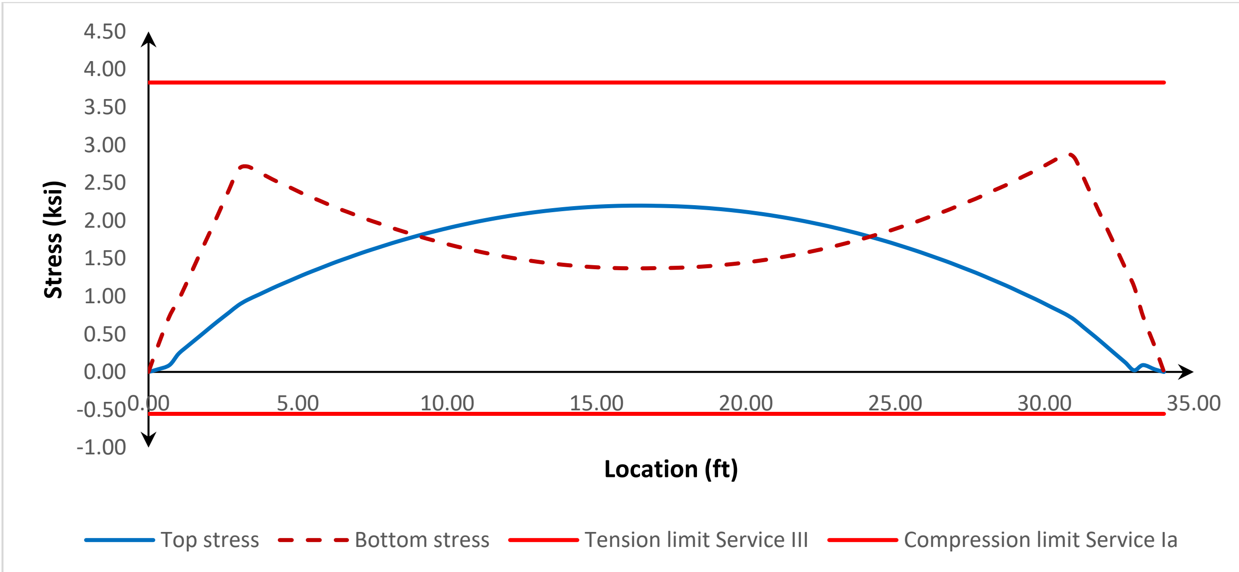


**Figure A1-4. Stress distribution at service III**

## At service:

Moments' calculations

Moment due to self-weight at mid span:

$$M_{LL} = 183.33\ k - ft = 2{,}199.96\ k - in$$

$$M_{SIII} = 2{,}199.96 * 0.8 = 1{,}760\ k - in$$

Stress check at Mid-span:

- At transfer:

Top: $f_t = -1.90 - \frac{M_{SIII}}{S_t} = -1.90 - \frac{1760}{2184} = -2.71\ ksi\ (compression)$

Bottom: $f_b = -2.06 + \frac{M_{SIII}}{S_b} = -2.06 + \frac{1760}{2481} = -1.35\ ksi\ (compression)$

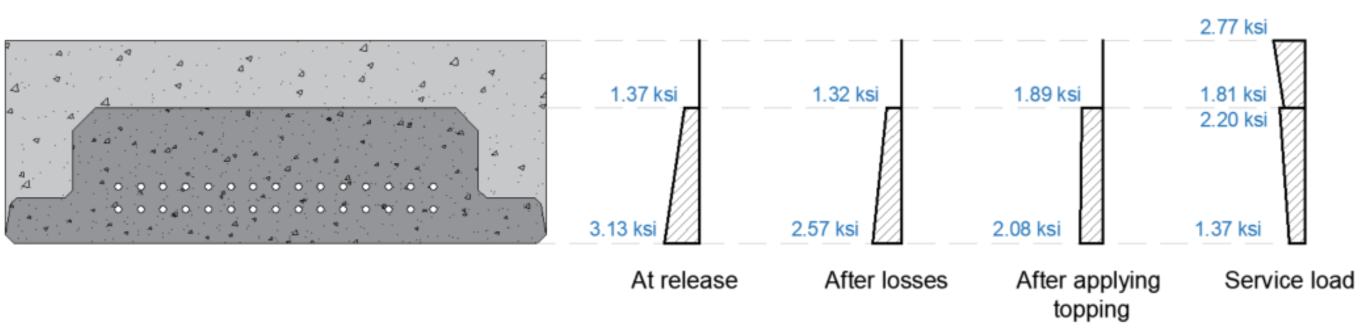


**Figure A1-5. Stress distribution at mid span**

# Section capacity:

## Flexural capacity:

### FSB-1 and FSB-4 (30 strands):

Strain due to effective prestress $f_{pe}$:

$$\varepsilon_1 = \varepsilon_{pe} = \frac{f_{pe}}{E_{ps}} = \frac{143.4}{24{,}000} = 0.005975$$

Strain at decompression:

$$r^2 = \frac{I_c}{A_c} = \frac{5{,}829}{473.76} = 12.18$$

For first bottom layer (distance=3" from member bottom):

$$\varepsilon_2 = \varepsilon_{decomp} = \frac{P_e}{AE_c} + \frac{P_e e}{IE_c} = \frac{993.76}{497.9*5362.2} + \frac{993.76*0.49^2}{5829*5362.2} = -0.00038$$

Stress increment due to overload beyond the decompression:

$$\varepsilon_3 = \varepsilon_{cu}\left(\frac{d-c}{c}\right) = 0.003 * \frac{13-8.09}{8.09} = 0.00182$$

$$\varepsilon_{p1} = \varepsilon_1 + \varepsilon_2 + \varepsilon_3 = 0.00742$$

$$f_{ps1} = E_{ps}\varepsilon_p\left[0.06 + \frac{1-0.06}{\left[1+(101\varepsilon_p)^{6.45}\right]^{\frac{1}{6.45}}}\right] =$$

$$24000 * 0.00742\left[0.06 + \frac{0.94}{\left[1 + (101 * 0.00742)^{6.45}\right]^{\frac{1}{6.45}}}\right] = 174.4\ kips$$

For 2nd bottom layer (distance=5" from member bottom):

$$\varepsilon_2 = \varepsilon_{decomp} = \frac{P_e}{AE_c} + \frac{P_e e}{IE_c} = \frac{993.76}{497.9*5362.2} + \frac{993.76*2.49^2}{5829*5362.2} = -0.00057$$

Stress increment due to overload beyond the decompression:

$$\varepsilon_3 = \varepsilon_{cu}\left(\frac{d-c}{c}\right) = 0.003 * \frac{15-8.09}{8.09} = 0.00256$$

$$\varepsilon_p = \varepsilon_1 + \varepsilon_2 + \varepsilon_3 = 0.00796$$

$$f_{ps} = E_{ps}\varepsilon_p\left[0.06 + \frac{1-0.06}{\left[1+(101\varepsilon_p)^{6.45}\right]^{\frac{1}{6.45}}}\right] =$$

$$24000 * 0.00796\left[0.06 + \frac{0.94}{\left[1 + (101 * 0.00796)^{6.45}\right]^{\frac{1}{6.45}}}\right] = 185.2\ kips$$

$$T = A_{ps}\, f_{ps} = 15 * 0.231 * (174.4 + 185.2) = 1{,}245.9\ kips$$

$$M_n = 1096.32\ kip - ft$$

**Table A1-2. Calculated design stresses in Florida slab beams**

| | | FSB-1 | FSB-2 | FSB-3 | FSB-4 |
|---|---|---|---|---|---|
| **Number of strands** | | 30 | 22 | 14 | 30 |
| **Stress check** | | | | | |
| **At release** | **Top (ksi)** | 1.39 | 0.94 | 0.75 | 1.39 |
| | **Bottom (ksi)** | 3.11 | 2.40 | 1.43 | 3.11 |
| **After losses** | **Top (ksi)** | 1.32 | 0.95 | 0.78 | 1.32 |
| | **Bottom (ksi)** | 2.57 | 1.94 | 1.11 | 2.57 |
| **At service** | **Top (ksi)** | 2.20 | 1.82 | 1.65 | 2.20 |
| | **Bottom (ksi)** | 1.37 | 0.74 | -0.1 | 1.37 |
| **Capacity of the section (kips-ft)** | | 1096.3 | 990.0 | 788.2 | 1096.3 |

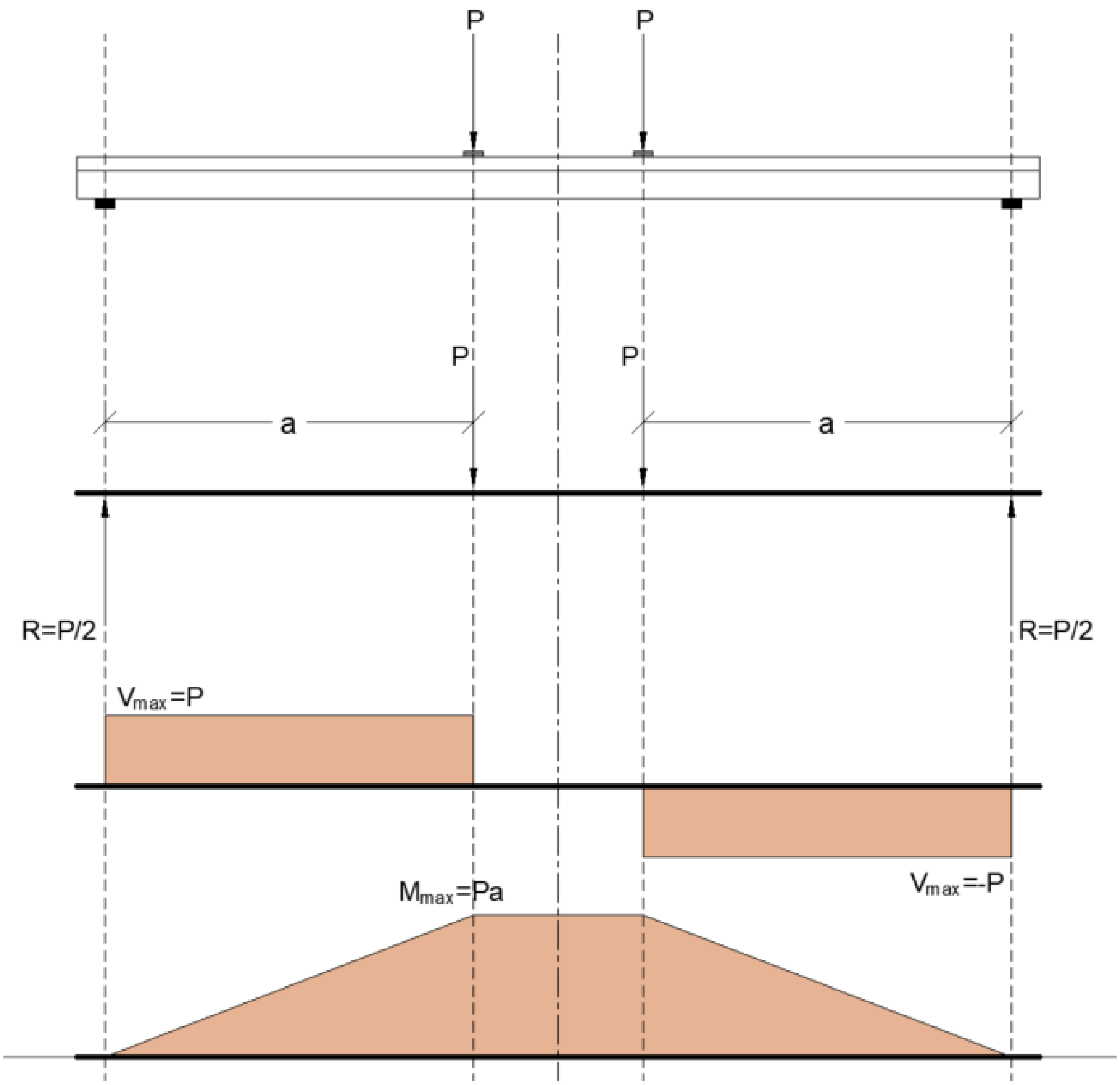


**Figure A1-6. Shear and bending moment diagrams for concentrated force in test setup**

$$a = \frac{32}{2} - \frac{6}{2} = 13\ ft$$

$$M_n = Pa \rightarrow P = \frac{M_n}{a} = \frac{1096.32}{13} = 84.3\ kip$$

$$V_1 = 84.3\ kip$$

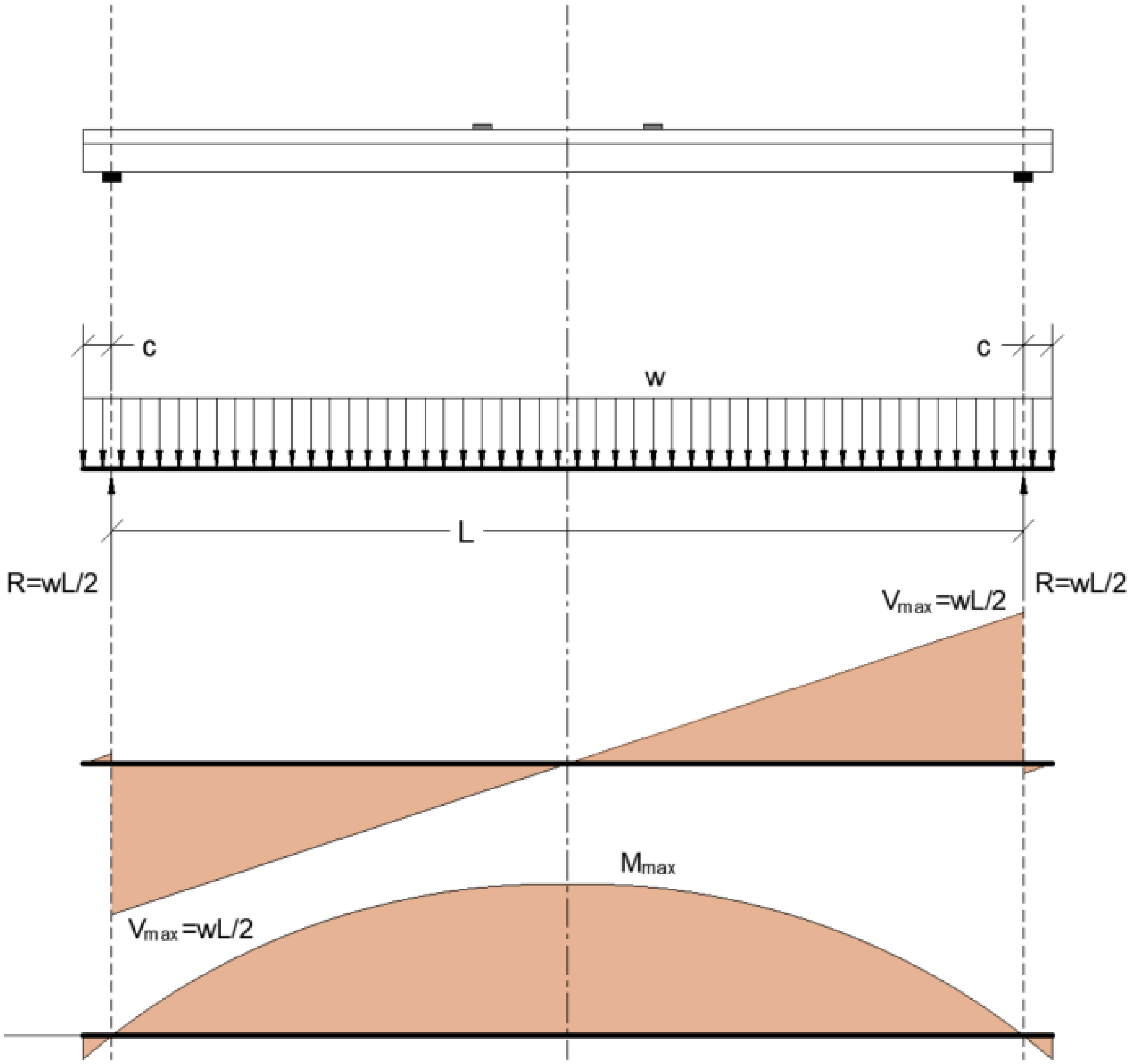


**Figure A1-7. Shear and bending moment diagrams for self-weight of the member**

$$w_{beam} = 0.51 \ \ kip/ft$$

$$w_{Deck} = 0.41 \ \ kip/ft$$

$$w = w_{beam} + w_{Deck} = 0.41 + 0.51 = 0.92 \ \frac{kip}{ft}$$

$$M_d = \frac{w}{2}\left(c^2 - \frac{d^2}{4}\right) = \frac{0.95}{2}\left(1^2 - \frac{32^2}{4}\right) = -121.125 \ \ kip - ft$$

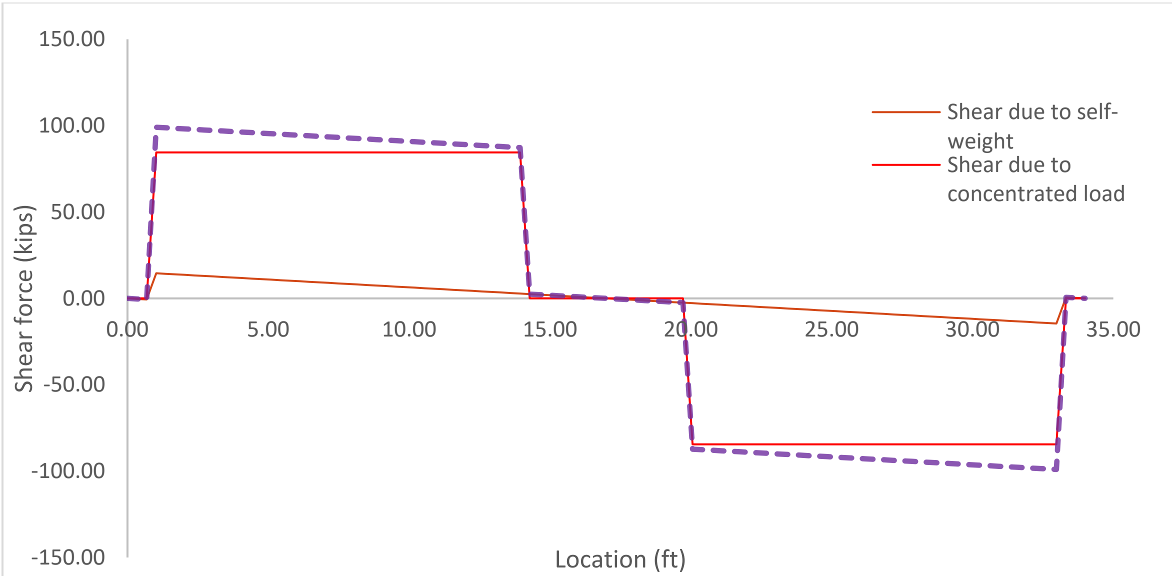


**Figure A1-8. Shear diagram for self-weight, concentrated load and combination**

$V_u = 98.1\ kip$

## Shear capacity (*LRFD 5.7.3.3*):

The effective depth as per (*LRFD 5.7.2.8*):

$$d_v = \frac{M_n}{A_{ps}f_{ps}} = \frac{1097.95}{1252.1} = 0.877\ ft = 10.52\ in$$

$$d_e = d_p = 18 - 4 = 14\ in$$

$$min\ (d_v) = Greater\ of \begin{cases} 0.9d_e = 0.9 * 14 = 12.6\ in \\ 0.72h = 0.72 * 18 = 12.96\ in \end{cases}$$

Then:

$$d_v = 12.6\ in$$

The effective web width (LRFD 5.7.2.8):

$$b_v = 48\ in$$

Minimum transverse reinforcement assuming spacing is 10in (*LRFD 5.7.2.5*):

$$A_v \geq 0.0316\lambda\sqrt{f_c'}\frac{b_v s}{f_y} = 0.0316 * (1) * \sqrt{8.5} * \frac{48*10}{60} = 0.737\ in^2$$

Providing #4 carbon steel rebars stirrups with 4 legs:

$$A_v = 4 * 0.2 = 0.8\ in^2 > A_{v,min} = 0.737\ in^2$$

The shear stress on concrete (*LRFD 5.7.2.8*):

$$\emptyset = 0.9\ (LRFD\ Article\ 5.5.4.2)$$

$$v_u = \left|\frac{V_u - \emptyset V_p}{\emptyset b_v d_v}\right|$$

$$v_u = \left|\frac{98.1 - 0}{0.9 * 48 * 12.6}\right| = 0.18\ ksi$$

Since $v_u < 0.125 f_c' = 1.0625$ maximum spacing (*LRFD 5.7.2.6*):

$$s_{max} = lesser\ of \begin{cases} 0.8d_v = 10.08 \\ 24in \end{cases} = 10.08\ in$$

The nominal Shear resistance (*LRFD equation. 5.7.3.3-1*):

$$V_n = V_c + V_s + V_p$$

$$V_c = 0.0316\lambda\,\beta\sqrt{f_c'}\ b_v\ d_v$$

$$\beta = 2.0\ (LRDF\ 5.7.3.4.1)$$

$$V_c = 0.0316 * 1 * 2 * \sqrt{8.5} * 48 *\ 12.6 = 111.44\ kip$$

$$\theta = 45°\ (LRDF\ 5.7.3.4.1)$$

$$V_s = \frac{A_v f_y d_v cot\theta}{s} = \frac{0.8*60*12.6*\cot(45)}{10} = 60.48\ kip$$

$$V_p = 0 \quad straight\ strands\ layout$$

$$V_n = 111.44 + 60.48 = 171.92\ kip$$

The maximum permitted nominal Shear resistance (*LRFD equation. 5.7.3.3-2*):

$V_n = 0.25 f_c' b_v\, d_v + V_p = 1285.2\ kip$

Then the nominal shear capacity for the section is:

$V_n = 171.92\ kip$

The demand per capacity:

$$DC = \frac{V_u}{V_n} = \frac{98.1}{171.92} = 0.57$$

## Interface shear capacity (*LRFD 5.7.4*):

Minimum area of interface shear reinforcement (*LRDF-5.7.4.2*):

$$A_{cv} = 48 * 12 = 576\ in^2/ft$$

$$A_{vf} \geq \frac{0.05 A_{cv}}{f_y} = \frac{0.05*576}{60} = 0.48\ in^2/ft$$

Horizontal shear force developed at the interface (*LRFD – C5.7.4.5*):

$$V_h = \frac{V_u \Delta\ell}{d_v} = \frac{98*12}{12.6} = 93.33\ in^2/ft$$

$$V_{h,req} = \frac{V_h}{\emptyset} = \frac{93.33}{0.9} = 103.7\ kip/ft$$

The shear interface stress is:

$$v_{ui} = \frac{V_h}{b_v d_v} = \frac{103.7}{48*12.6} = 0.171\ ksi < 0.210$$

$$minimum\ reinforcement\ can\ be\ waived\ for\ this\ section\ based\ on\ \ (LRFD - 5.7.4.2)$$

The nominal shear interface capacity:

$$V_{ni} = K_1 f'_{c,deck} A_{cv}$$

$$K_1 = 0.3 \quad (Roughned\ with\ amplitude = 0.25"\ and\ CIP\ concrete\ top\ LRFD\ 5.7.4.4)$$

$$V_{ni} = 0.3 * 4.5 * 576 = 777.6\ kip$$

$$K_2 = 1.8\ ksi \quad for\ normal\ weight\ concrete.$$

$$V_{ni} = K_2 A_{cv} = 1.8 * 576 = 1036.8\ kip$$

$$V_{ni} = 777.6\ kip > 103.7\ kip/ft$$

## GFRP shear capacity (*LRFD 5.7.4*):

Regions require transverse reinforcement (*LRDF GFRP 2.7.2.2*):

$$V_u > 0.5 \emptyset V_c$$

$$V_c = 111.44\ kips$$

$$V_u = 98.1\ kips$$

$$V_u > 0.5 * 0.9 * 111.44 = 50.15\ kips$$

Environmental reduction factor (*LRFD GFRP Table 2.4.2.1-1*):

$$C_E = 0.7\ for\ concrete\ exposed\ to\ weather$$

The tensile load in GFRP rebar (*FDOT spec Table 932-6*):

$$P = 21.6\ for\ \#4\ GFRP\ rebars$$

The tensile strength of the rebar:

$$f_{pu,GFRP} = \frac{Tensile\ load}{Nominal\ area} = \frac{21.6}{0.2} = 108\ ksi$$

The design tensile strength (*LRFD GFRP 2.4.2*):

$$f_{d,GFRP} = C_E . f_{pu,GFRP} = 0.7 * 108 = 75.6\ ksi$$

Design strength of the bent portion (*LRFD GFRP 2.7.3.5*):

$$r_b = 0.5 * D = 0.5 * 4.5 = 2.25\ in \qquad for \#4\ rebar\ (FDOT\ Development\ Standard\ D21310)$$

$$f_b = \left(0.05\frac{r_b}{d_b} + 0.3\right) f_{fd} = \left(0.05\frac{2.25}{0.5} + 0.3\right) 75.6 = 39.69\ ksi \leq f_{fd} = 75.6\ ksi$$

$$E_f = 6500\ ksi\ for\ GFRP\ (FDOT\ spec\ Table\ 932-9)$$

$$f_{fv} = 0.004 E_f = 0.004(6500) = 26\ ksi\ \leq f_b = 39.69 ksi \quad \rightarrow f_v = 26\ ksi$$

Minimum transverse reinforcement (*LRFD GFRP 2.7.2*):

$$A_{vf,min} \geq 0.05 \frac{b_v s}{f_v} = 0.05 * \frac{48*10}{26} = 0.923\ in^2$$

The maximum permitted transverse reinforcement (*LRFD GFRP 2.7.2.5*):

$$V_c + V_f \leq 0.25\sqrt{f_c'} b_v d_v = 0.25 * \sqrt{8.5} * 48 * 12.6 = 440.8\ kip$$

Maximum spacing (*LRFD GFRP 2.7.2.6*):

$$s_{max} = \min(0.5d = 0.5 * 12.6 = 6.3in\ , 24) = 6.3\ in$$

Shear resistance provided by the transverse GFRP reinforcement (*LRFD GFRP 2.7.3.5*)

$$V_f = \frac{A_{fv} f_v d_v cot\theta}{s} = \frac{0.8 * 26 * 12.6 * cot28}{10} = 49.29\ kips$$

Nominal shear resistance provided by the transverse GFRP reinforcement (*LRFD 2.7.3.3*):

$$V_n = V_c + V_f = 111.44 + 49.29 = 160.73\ kips > V_u = 98.1\ kips$$

Demand per capacity: $DC = \frac{V_u}{V_n} = \frac{98.1}{160.73} = 0.61$

# APPENDIX 2 – DESIGN DRAWINGS

| FLORIDA SLAB BEAM - TABLE OF VARIABLES | | | | | | | | | | | Table Date 01-01-16 |
|---|---|---|---|---|---|---|---|---|---|---|---|
| LOCATION | | BEAM TYPE | CONCRETE PROPERTIES | | | STND. PTRN. | PLAN VIEW CASE | | ANGLE Ø | | REINFORCEMENT TYPE* |
| SPAN NO. | BEAM NO. | | CLASS | STRENGTHS (psi) | | | | | | | MATERIAL |
| | | | | 28 Day | Release | TYPE | END 1 | END 2 | END 1 | END 2 | |
| | 1 | FSB 12x48 | VI | 8500 | 6800 | 1 | 1 | 1 | 90 | 90 | Carbon Steel (See Note 7) |
| | 2 | FSB 12x48 | VI | 8500 | 6800 | 2 | 1 | 1 | 90 | 90 | Carbon Steel (See Note 7) |
| | 3 | FSB 12x48 | VI | 8500 | 6800 | 3 | 1 | 1 | 90 | 90 | Carbon Steel (See Note 7) |
| | 4 | FSB 12x48 | VI | 8500 | 6800 | 1 | 1 | 1 | 90 | 90 | GFRP (See Note 8) |

* For Bars 3C, 4D, 5E, 4K, 6Y and 5Z; see bill of Reinforcing Bars on Sheet 3.

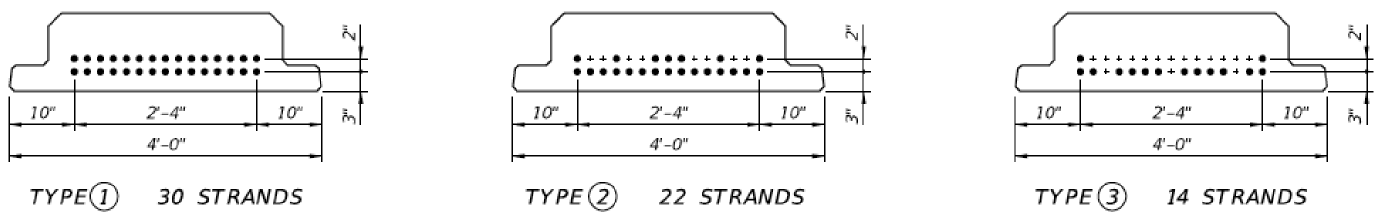


STRAND DESCRIPTION: Use 0.62" Diameter, Low Relaxation Stainless Steel Strands stressed at 38.8 kips each. Area per strand equals 0.231 sq. in.

## STRAND PATTERNS

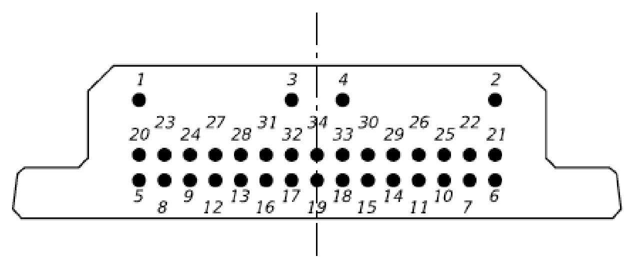


DETENSIONING SEQUENCE

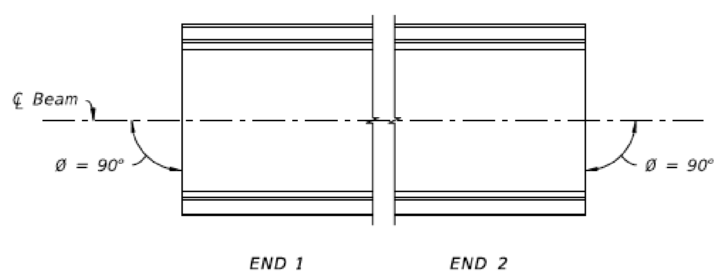


PLAN VIEW - CASE 1

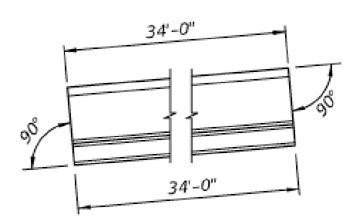


SCHEMATIC SIDE ELEVATION OF BEAM

### STRAND DEBONDING LEGEND

● - Fully bonded strands

Note: Beams 2, and 3 may be cast with one set of 30 strands. This will require sheathing 8 strands for Beam 2, and sheathing 16 strands for Beam 3. Shielded strands may be bonded for 1 ft. length, located approximately 5 ft. from each end of beam.

### FABRICATION NOTES

1. The abbreviated FSB designation for depth and width is FSB "depth"x "width", e.g. FSB 12 x 48.
2. All bar dimensions are out-to-out.
3. Contractor options for strands N:
   A. ASTM A416 Carbon Steel Strands, Grade 250 or 270, 3/8" ø or larger strands, stressed to 10,000lbs each.
   B. ASTM A1114 Stainless Steel Strands, 0.6" ø, stressed to 10,000lbs each.
4. Unless otherwise noted, the minimum concrete cover for reinforcing shall be 2".
5. Bars 4D1 & 6Y1 correspond to END 1, and 4D2 & 6Y2 correspond to END 2.
6. Rake the top surface of the Slab Beams transversely to provide a roughened surface with ¼" amplitude.
7. Carbon Steel reinforcing bars shall be Grade 60 per Specification Section 931.
8. Glass fiber reinforced polymer (GFRP) reinforcing bars shall be in accordance with Specification Section 932.
9. Provide material certifications to FDOT Structures Research Center.
10. FDOT personnel shall be allowed to instrument the beams and monitor them during tensioning and detensioning. Coordinate with the FDOT Structures Research Center prior to fabrication and as stated in the Strand Notes below.
    Contact information is provided below.

### STRAND NOTES

1. Use Stainless Steel Strands. FDOT will supply an adequate length of Stainless Steel Strand to extend length of casting bed and additional length as needed for stressing.
2. Return unused Stainless Steel Strand to FDOT Structures Research Center.
3. FDOT shall be allowed to cut Stainless Steel Strand samples from spool as needed for testing purposes.
4. Internal instrumentation will be mounted to prestressing strands and rebar prior to concrete casting. Instrumentation of the prestressing strands shall be installed after tensioning of the bottom layer and prior to tensioning of the top layers. Instrumentation on rebar will be installed prior to placement of the bar in the girder.

   Structures Research Center Contact Information:
   Contact Person: Yukai Yang
   Email Address: yukai.yang@dot.state.fl.us
   Phone: 850-921-7100

| REVISIONS | | | | | |
|---|---|---|---|---|---|
| DATE | BY | DESCRIPTION | DATE | BY | DESCRIPTION |
| | | | | | |

| | | |
|---|---|---|
| DRAWN BY: JKF<br>CHECKED BY: GD<br>DESIGNED BY: GD<br>CHECKED BY: VAY | STATE OF FLORIDA<br>DEPARTMENT OF TRANSPORTATION<br>ROAD NO. / COUNTY / FINANCIAL PROJECT ID | SHEET TITLE: FLORIDA SLAB BEAM TYPICAL DETAILS AND NOTES<br>PROJECT NAME: BED 30-977-09:FSB's with Stainless steel strands and GFRP shear reinforcement |
| REF. DWG. NO. | SHEET NO. | 1 |

ST986FJ 7/10/2023 7:08:14 AM C:\Users\st986fj\Desktop\Glenda\FSB_Sheet1.dgn

Figure A2-1. Sheet 1: Florida slab beam typical details and notes

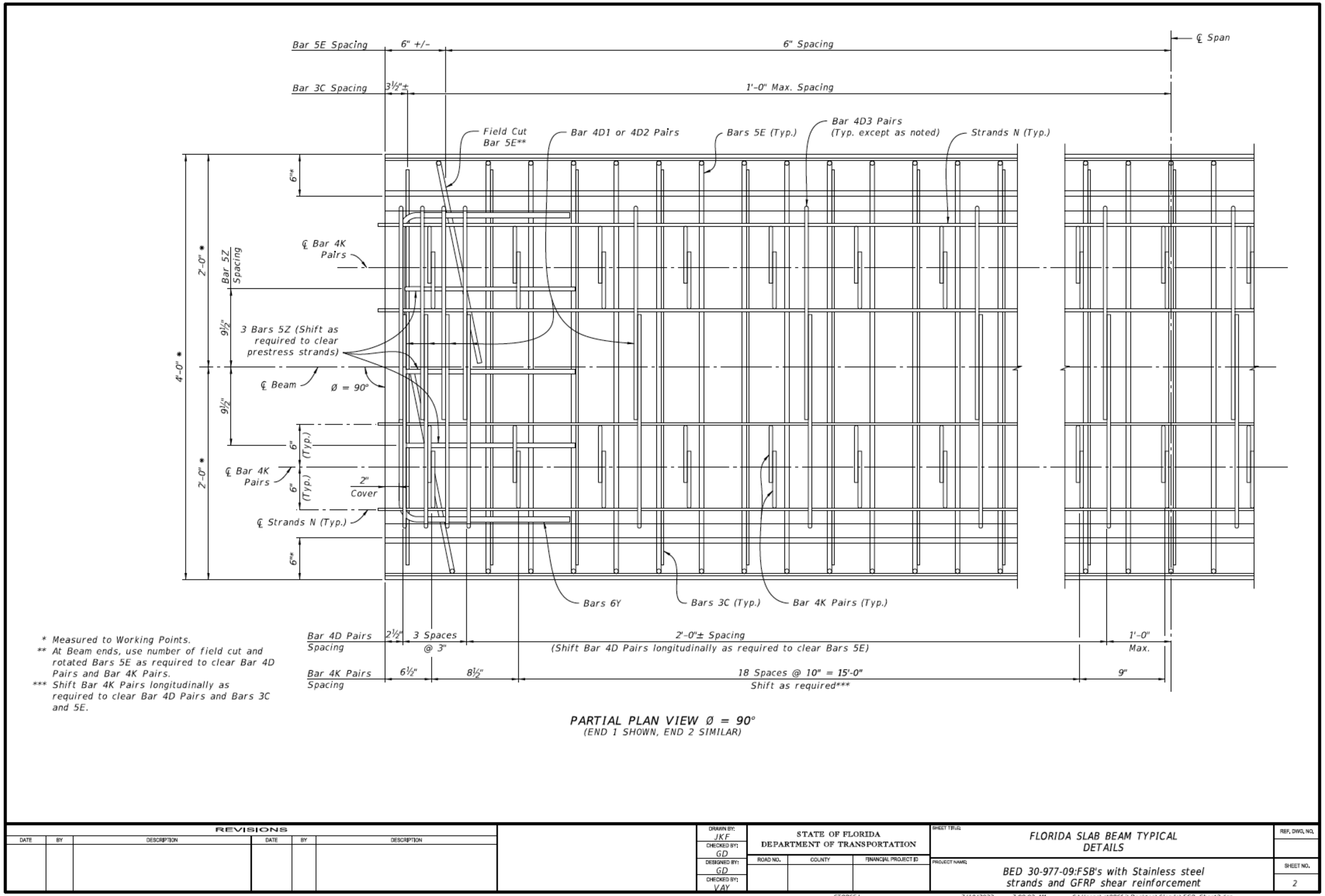


Figure A2-2. Sheet 2: Florida slab beam typical details

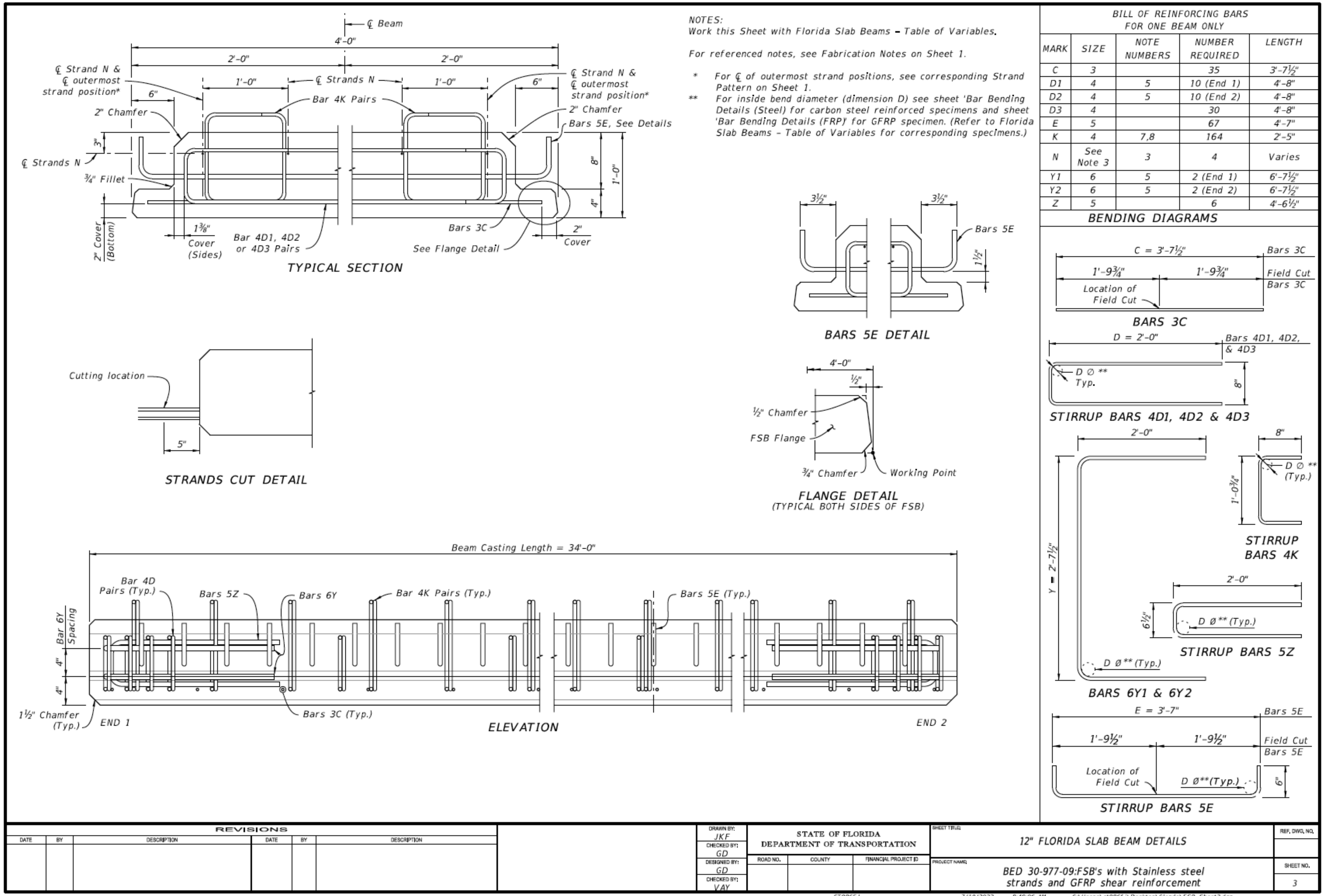


**Figure A2-3. Sheet 3: 12” Florida slab beam details**

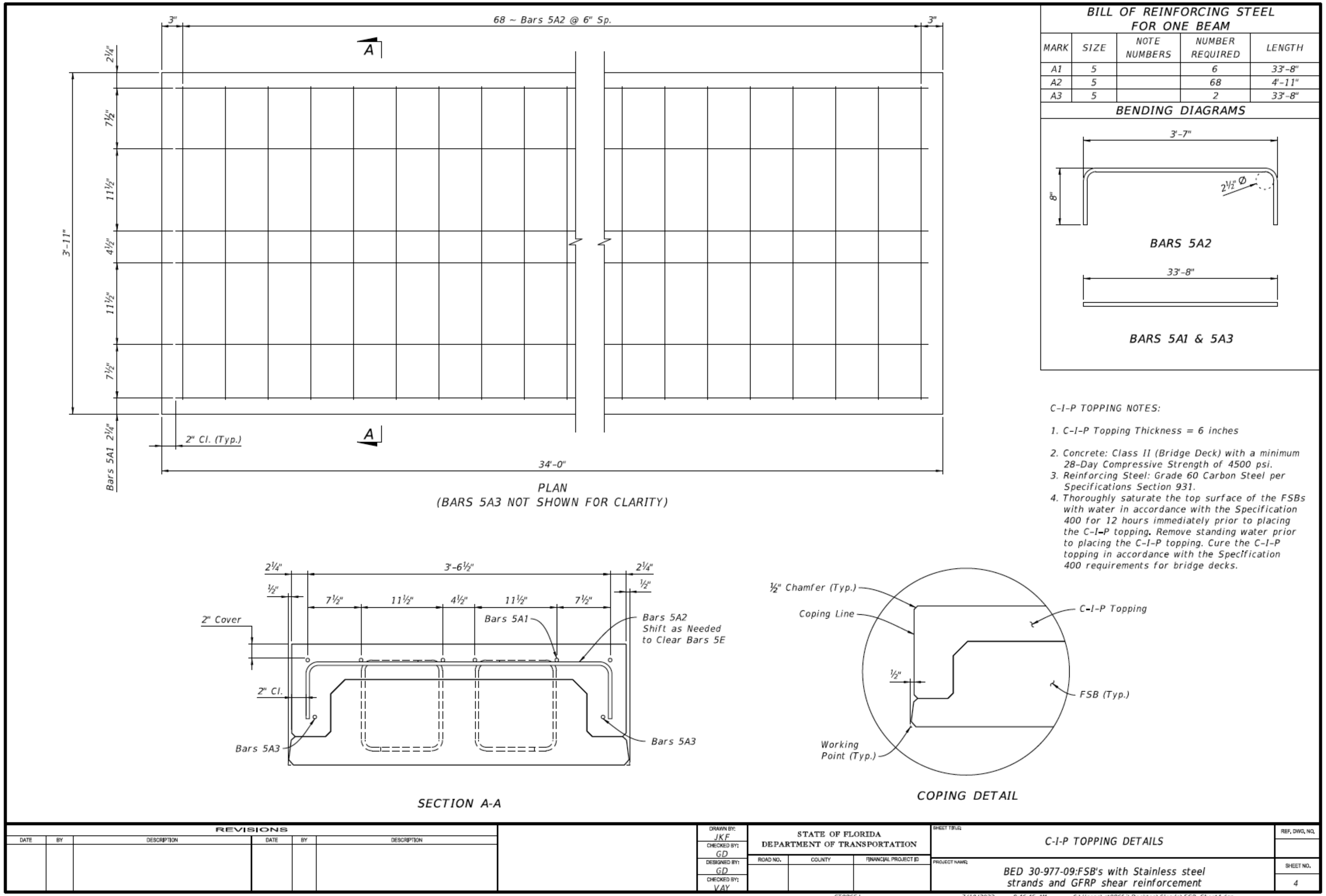


Figure A2-4. Sheet 4: C-I-P topping details

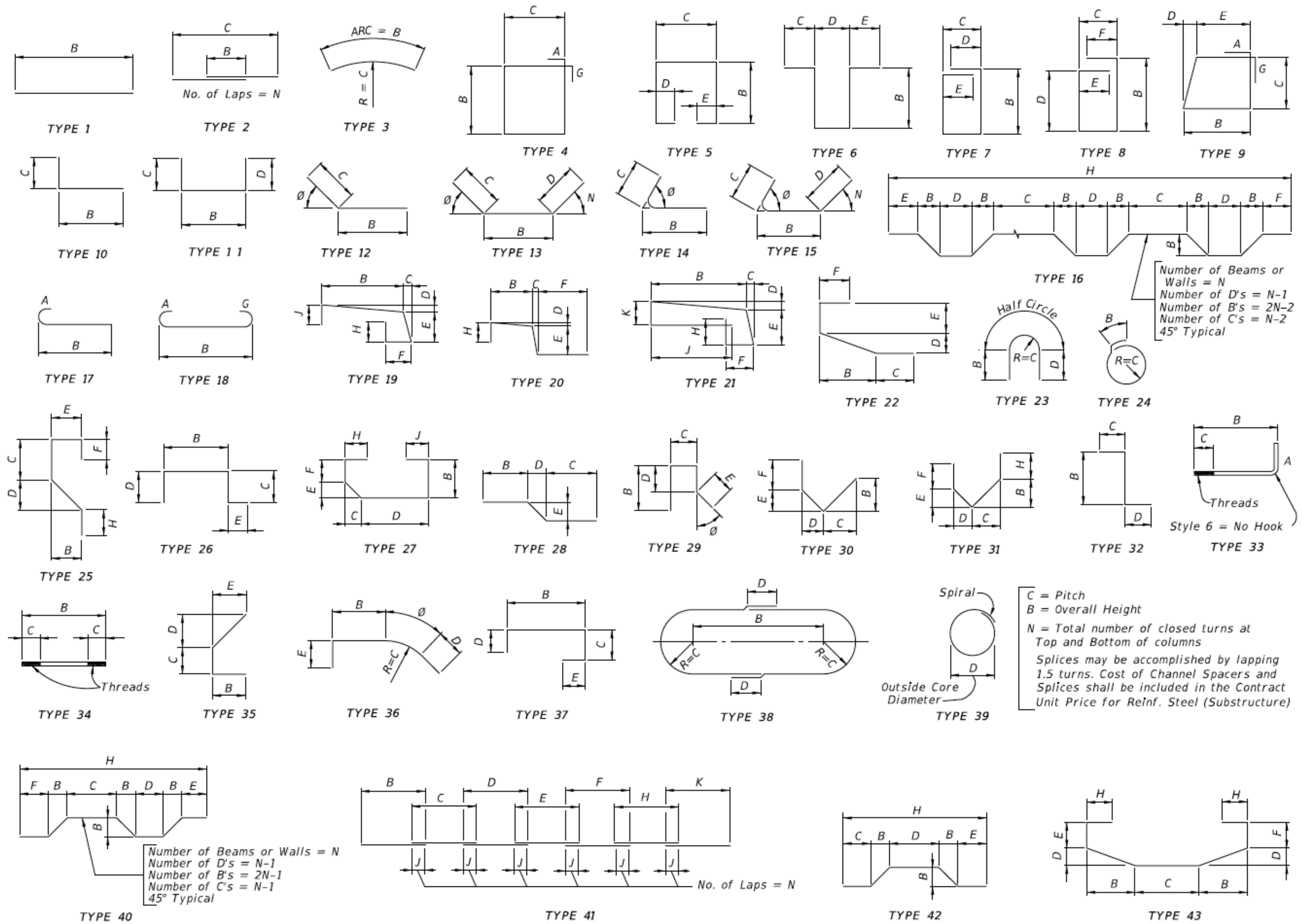


NOTE: For Bar Dimensions See REINFORCING BAR LIST Sheet(s) in Structures Plans.

## HOOK DETAILS

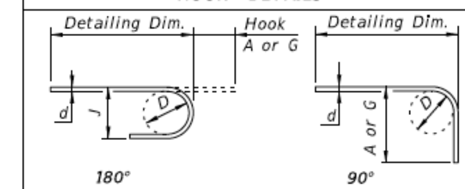


| BAR SIZE | D | 180° HOOKS | | 90° HOOKS |
|---|---|---|---|---|
| | | A OR G | J | A OR G |
| #3 | 2¼" | 5" | 3" | 6" |
| #4 | 3" | 6" | 4" | 8" |
| #5 | 3¾" | 7" | 5" | 10" |
| #6 | 4½" | 8" | 6" | 1'-0" |
| #7 | 5¼" | 10" | 7" | 1'-2" |
| #8 | 6" | 11" | 8" | 1'-4" |
| #9 | 9½" | 1'-3" | 11¾" | 1'-7" |
| #10 | 10¾" | 1'-5" | 1'-1¼" | 1'-10" |
| #11 | 12" | 1'-7" | 1'-2¾" | 2'-0" |
| #14 | 18¼" | 2'-3" | 1'-9¾" | 2'-7" |
| #18 | 24" | 3'-0" | 2'-4½" | 3'-5" |
| STYLE | | 1 | | 3 |

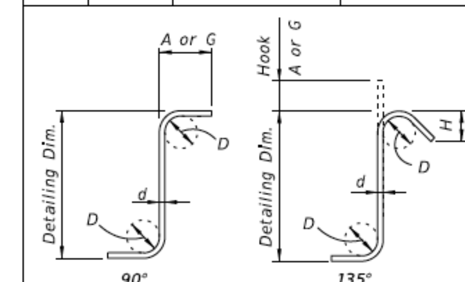


STIRRUPS (TIES SIMILAR)

### STIRRUP & TIE HOOK DIMENSIONS

| BAR SIZE | D | 90° HOOKS | 135° HOOKS | |
|---|---|---|---|---|
| | | A or G | A or G | H * |
| #3 | 1½" | 4" | 4" | 2½" |
| #4 | 2" | 4½" | 4½" | 3" |
| #5 | 2½" | 6" | 5½" | 3¾" |
| #6 | 4½" | 1'-0" | 8" | 4½" |
| #7 | 5¼" | 1'-2" | 9" | 5¼" |
| #8 | 6" | 1'-4" | 10½" | 6" |
| STYLE | | 4 | 5 | |

STYLE 6 = NO HOOK

* Dimension is approximate.

Hook Styles Detailed on this sheet are for Illustration Only.

Actual Hook Style for any particular bar will be shown under A or G Heading on REINFORCING BAR LIST sheet(s) in Structures Plans.

All Dimensions are out-to-out.

| LAST REVISION | REVISION | DESCRIPTION: | FDOT | FY 2024-25 STANDARD PLANS | BAR BENDING DETAILS (STEEL) | INDEX | SHEET |
|---|---|---|---|---|---|---|---|
| 11/01/20 | | | | | | 415-001 | 1 of 1 |

**Figure A2-5. Index 415-001: Bar bending details (steel)**

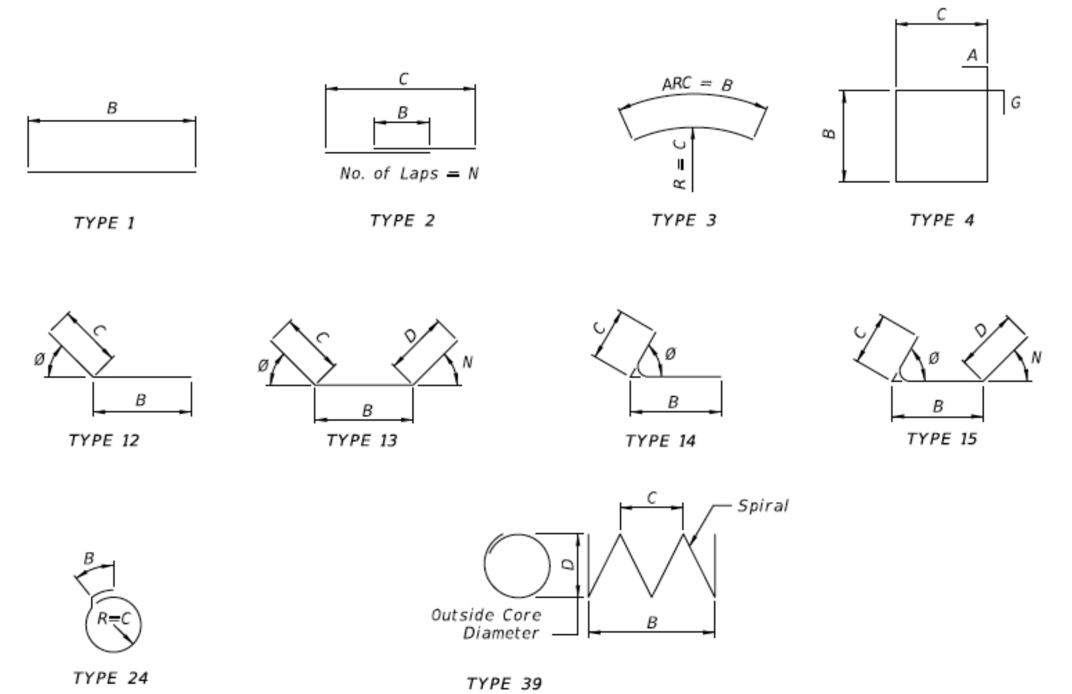


SINGLE BAR BENDING DETAILS

HOOK DETAILS

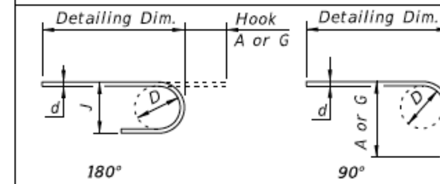


| BAR SIZE | D | 180° HOOKS | | 90° HOOKS |
|---|---|---|---|---|
| | | A OR G | J | A OR G |
| #3 | 2¼" | 5" | 3" | 6" |
| #4 | 3" | 6" | 4" | 8" |
| #5 | 3¾" | 7" | 5" | 10" |
| #6 | 4½" | 8" | 6" | 1'-0" |
| #7 | 5¼" | 10" | 7" | 1'-2" |
| #8 | 6" | 11" | 8" | 1'-4" |
| STYLE | | 1 | | 3 |

NOTES

GENERAL
All dimensions are out-to-out.
For Bar dimensions See REINFORCING BAR LIST Sheet(s) in Structures Plans.

SPIRALS (TYPE 39 BARS)

C = Pitch
B = Overall Height
N = Total number of closed turns at Top and Bottom of columns
Spirals = 1.5 turns

Include spiral splice in Contract Unit Price for FRP Reinforcing.

HOOKS
All Dimensions are approximate.
Hook Styles Detailed on this sheet are for Illustration Only.
Actual Hook Style for any particular bar will be shown under A or G Heading on REINFORCING BAR LIST sheet(s) in Structures Plans.

| LAST REVISION | REVISION | DESCRIPTION: | FDOT | FY 2024-25 STANDARD PLANS | BAR BENDING DETAILS (FRP) | INDEX | SHEET |
|---|---|---|---|---|---|---|---|
| 11/01/23 | | | | | | 415-010 | 1 of 1 |

**Figure A2-6. Index 415-010: Bar bending details (FRP)**

# APPENDIX 3 – DRAWINGS AND DETAILS OF TESTING AND INSTRUMENTATION PLANS

# Casting bed

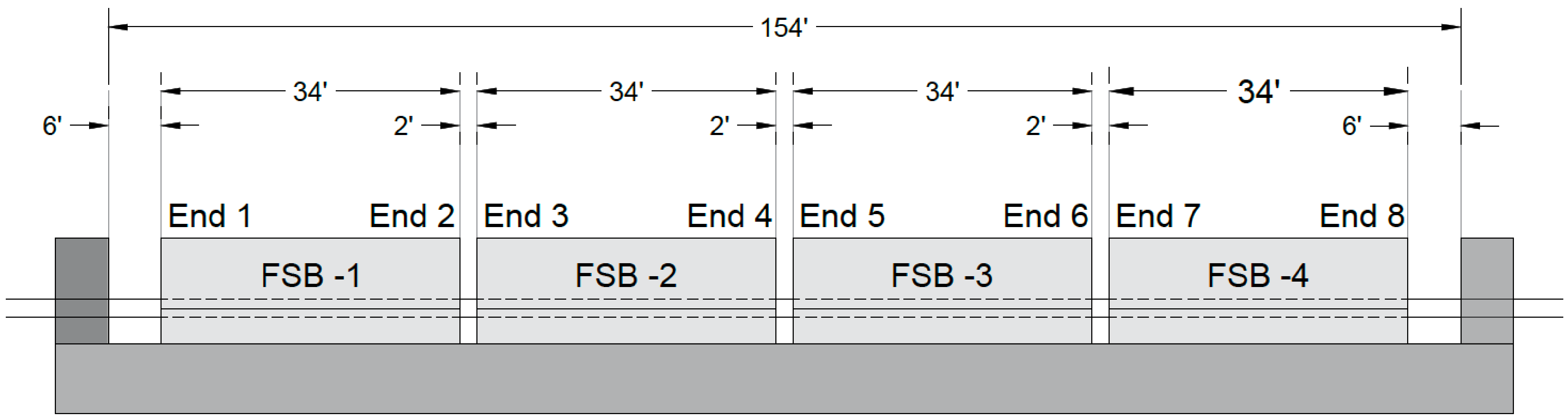


| Table 1 | | | | | | | | |
|---|---|---|---|---|---|---|---|---|
| Girder No. | External strain gauges | Shear Internal strain gauges | | Deflection gauges | Slip gauges | Vibrating Wires | Fiber optic | ERSG |
| | | 4D- pairs | 4K- pairs | | | | | |
| FSB -1 | S101 - S113 | CSD101 - CSD-132 | CSK101 - CSK124 | D101 - D112 | Slip101 - Slip112 | VW101 - VW102 | FO101 - FO102 | W1-W12 |
| FSB -2 | S201 - S213 | - | - | D201 - D212 | Slip201 - Slip212 | VW201 - VW202 | - | |
| FSB -3 | S301 - S413 | - | - | D301 - D312 | Slip301 - Slip312 | VW301 - VW302 | - | |
| FSB -4 | S401 - S413 | GFD401 - GFD432 | GFK401 - GFK424 | D401 - D412 | Slip401 - Slip412 | VW401 - VW402 | FO401 - FO402 | E1-E12 |

FAMU-FSU College of Engineering

FDOT

Project: Florida Slab Beam with Stainless Steel Strands and GFRP reinforcement

TITLE: Sheet No.1 Casting bed

SCALE AT A3: | DATE: 08/02/23 | DRAWN: OA | CHECKED:

PROJECT NO: | DRAWING NO: | REVISION:

**Figure A3-1. Sheet 1: Casting bed**

## Deflection gauges and Slip distribution

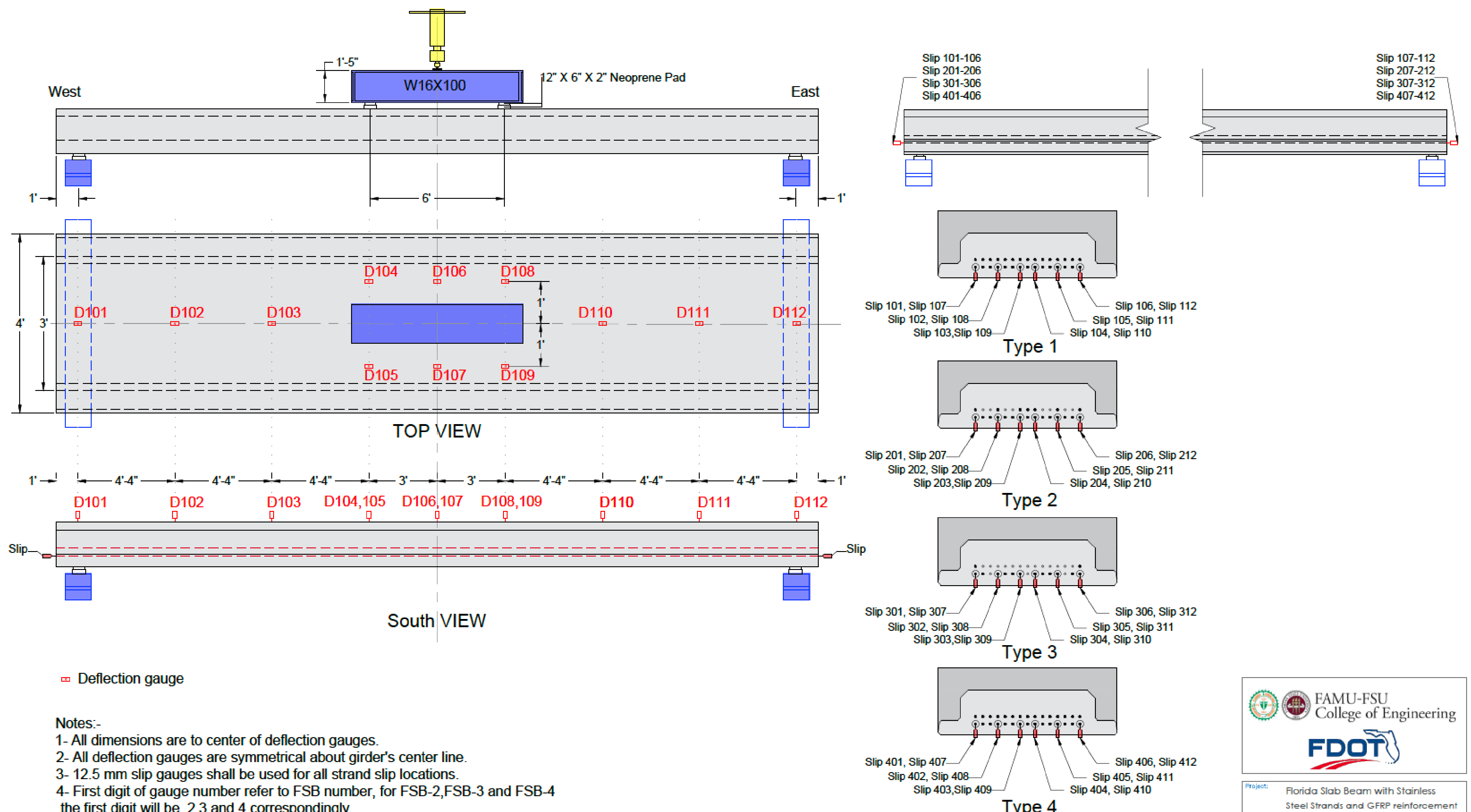


Deflection gauge

Notes:-
1- All dimensions are to center of deflection gauges.
2- All deflection gauges are symmetrical about girder's center line.
3- 12.5 mm slip gauges shall be used for all strand slip locations.
4- First digit of gauge number refer to FSB number, for FSB-2,FSB-3 and FSB-4 the first digit will be, 2,3 and 4 correspondingly.
5- Deflection gauges have same configuration for all girders.

FAMU-FSU College of Engineering
FDOT

| | | | |
|---|---|---|---|
| Project: | Florida Slab Beam with Stainless Steel Strands and GFRP reinforcement | | |
| TITLE: | Sheet No.2 Deflection gauges | | |
| SCALE AT A3: | DATE: 08/02/23 | DRAWN: OA | CHECKED: |
| PROJECT NO: | DRAWING NO: | | REVISION: |

**Figure A3-2. Sheet 2: Deflection gauges**

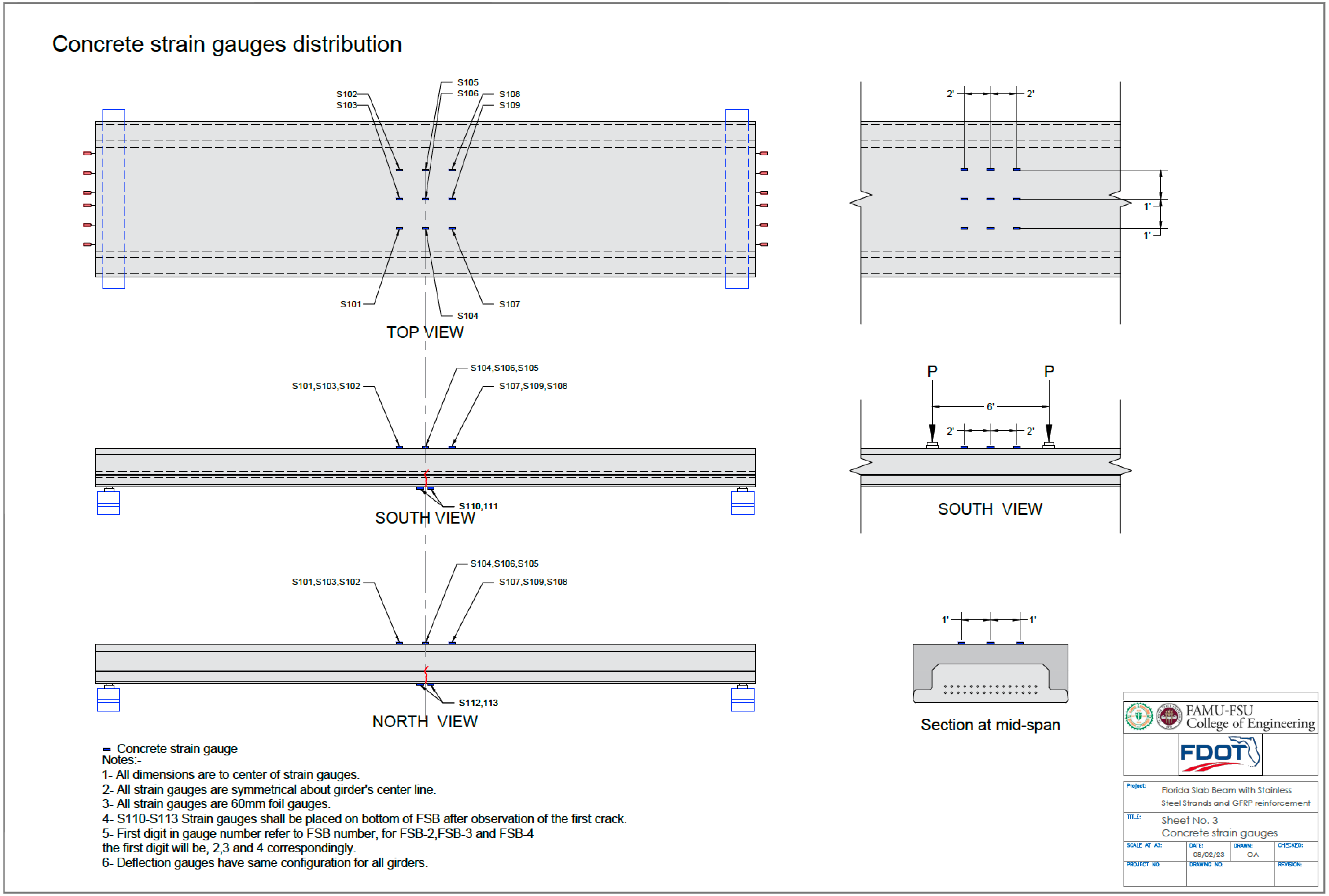


**Figure A3-3. Sheet 3: Concrete strain gauges**

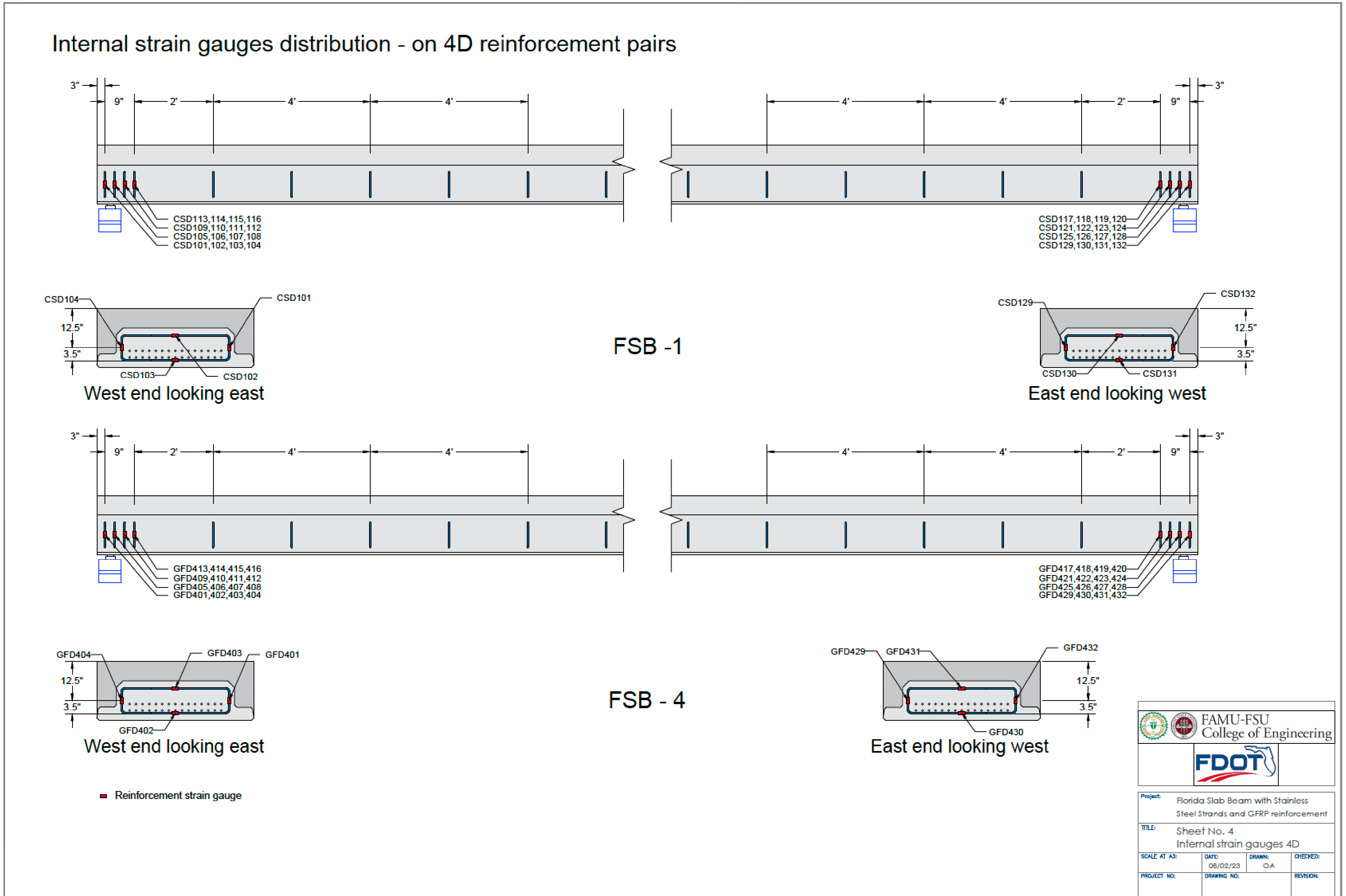


Figure A3-4. Sheet 4: Internal strain gauges 4D

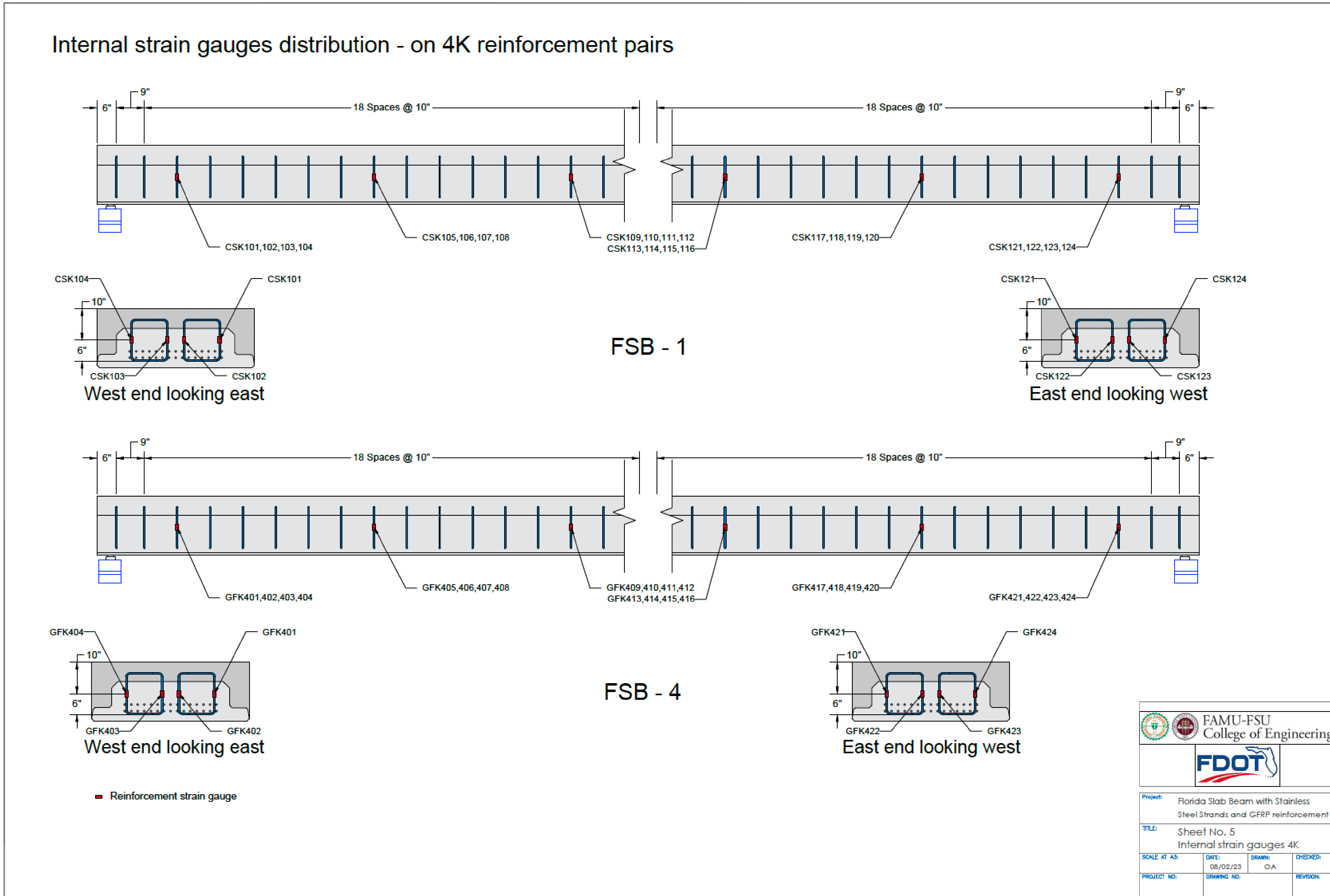

Figure A3-5. Sheet 5: Internal strain gauges 4K

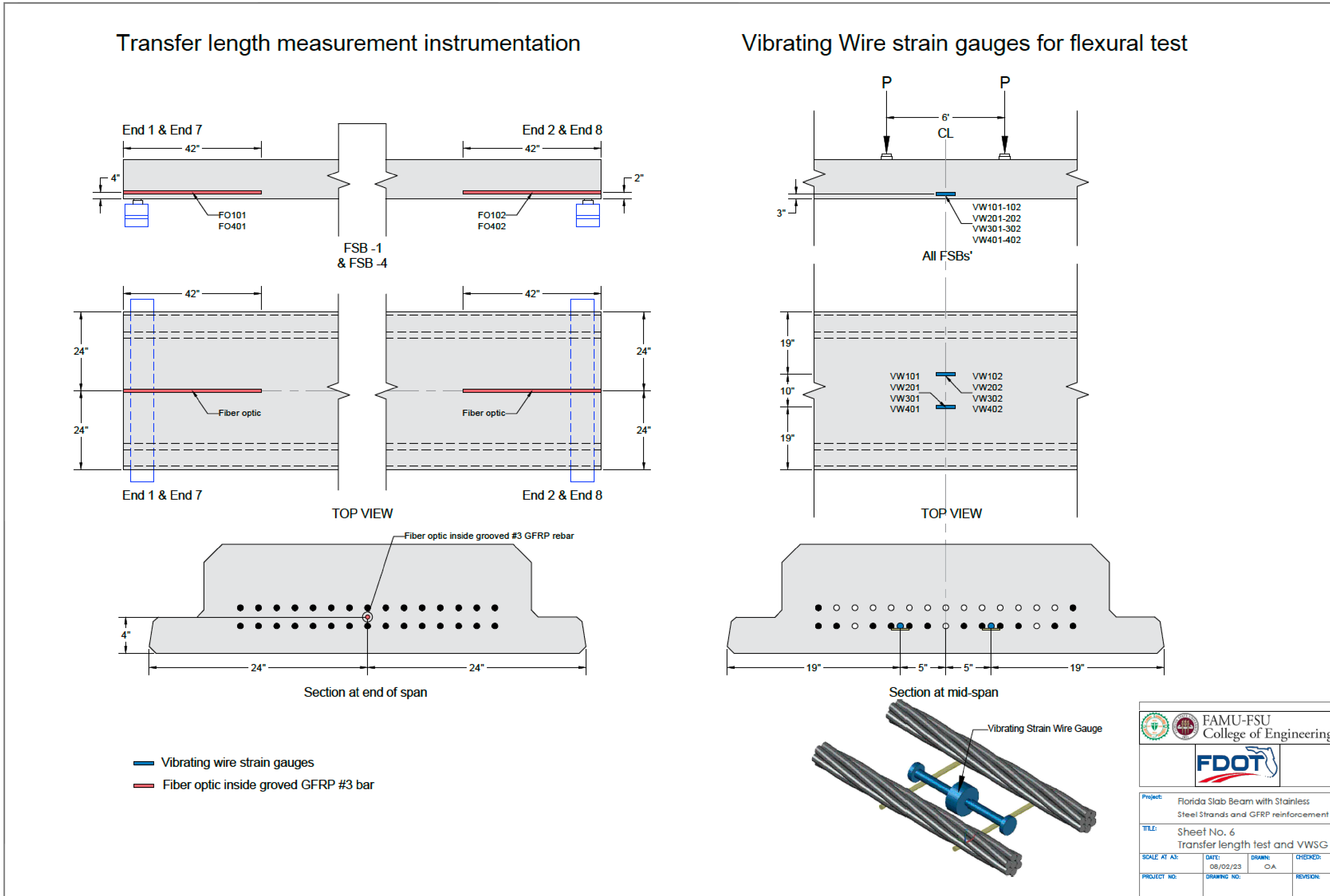


**Figure A3-6. Sheet 6: Transfer length test and VWSG**

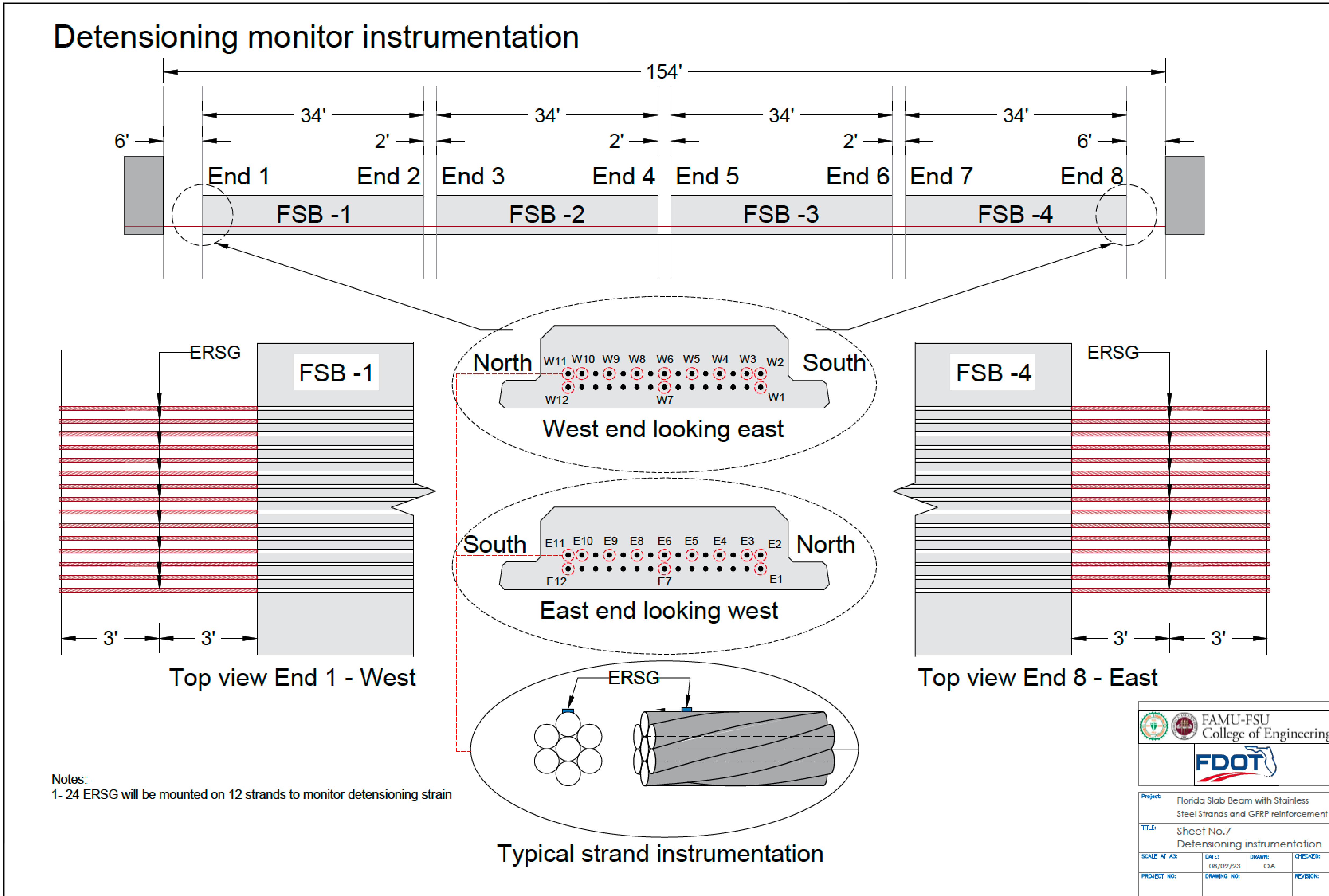


**Figure A3-7. Sheet 7: Detensioning instrumentation**

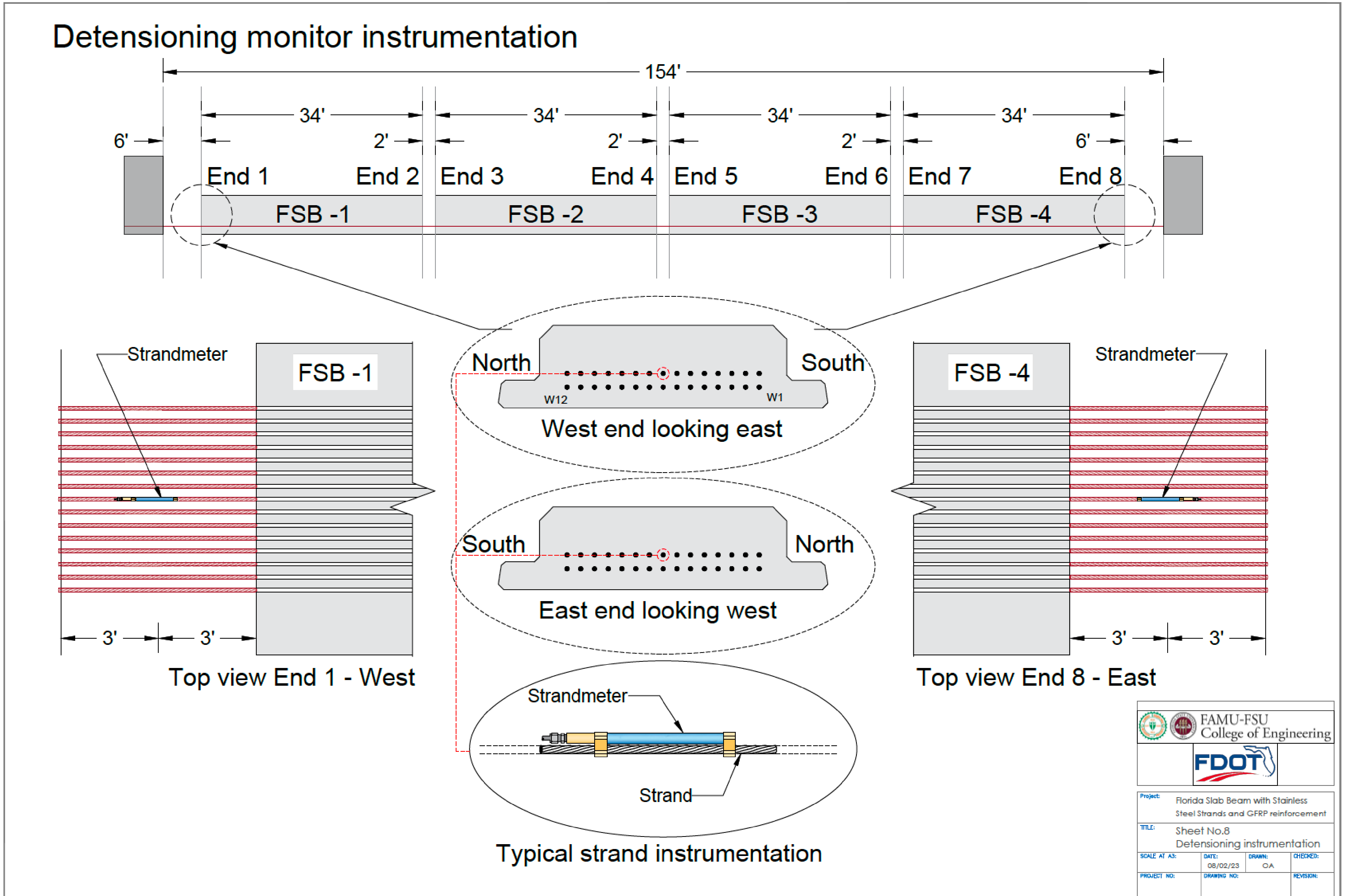


**Figure A3-8. Sheet 8: Detensioning instrumentation**

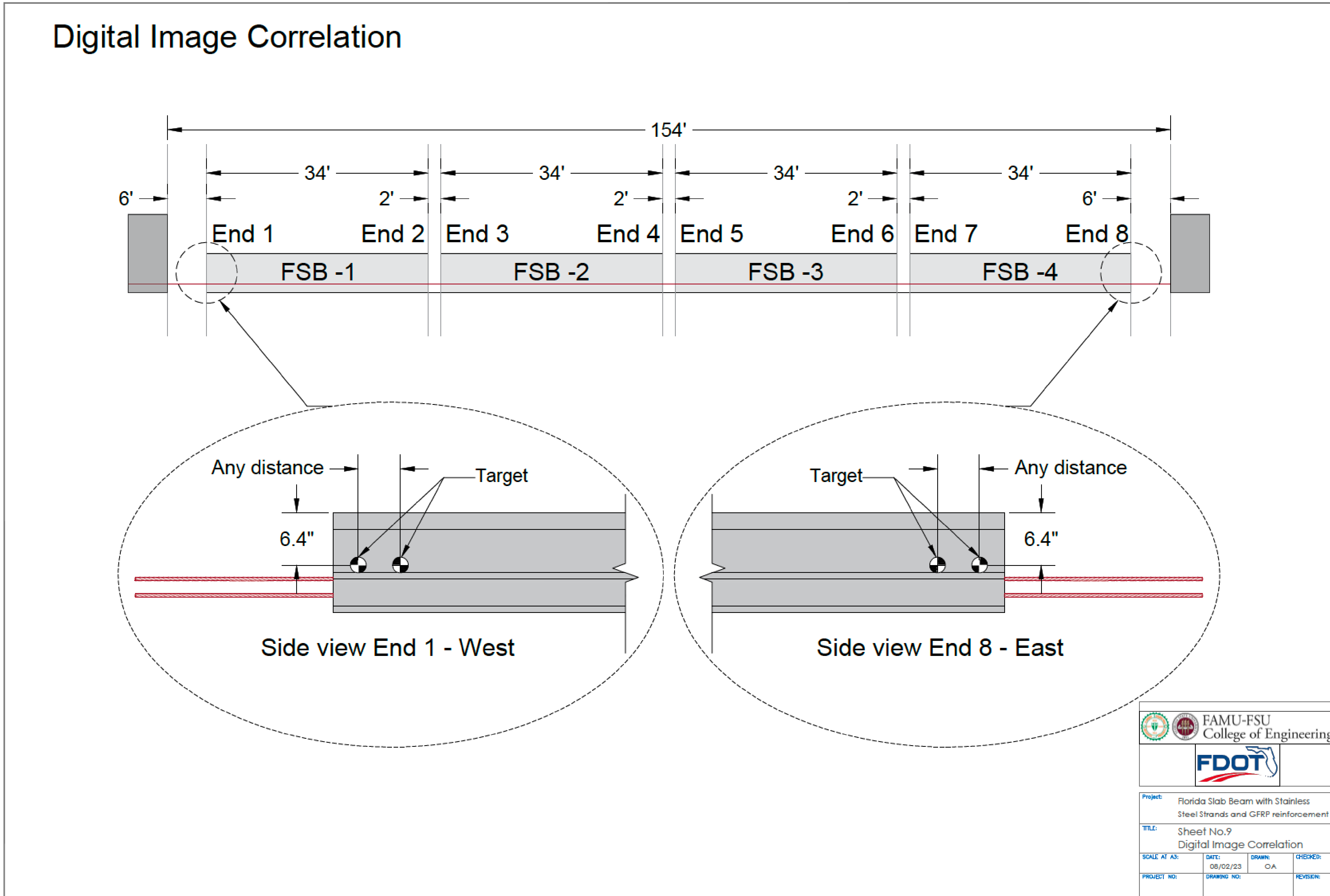


**Figure A3-9. Sheet 9: Digital image correlation**

## Test Setup

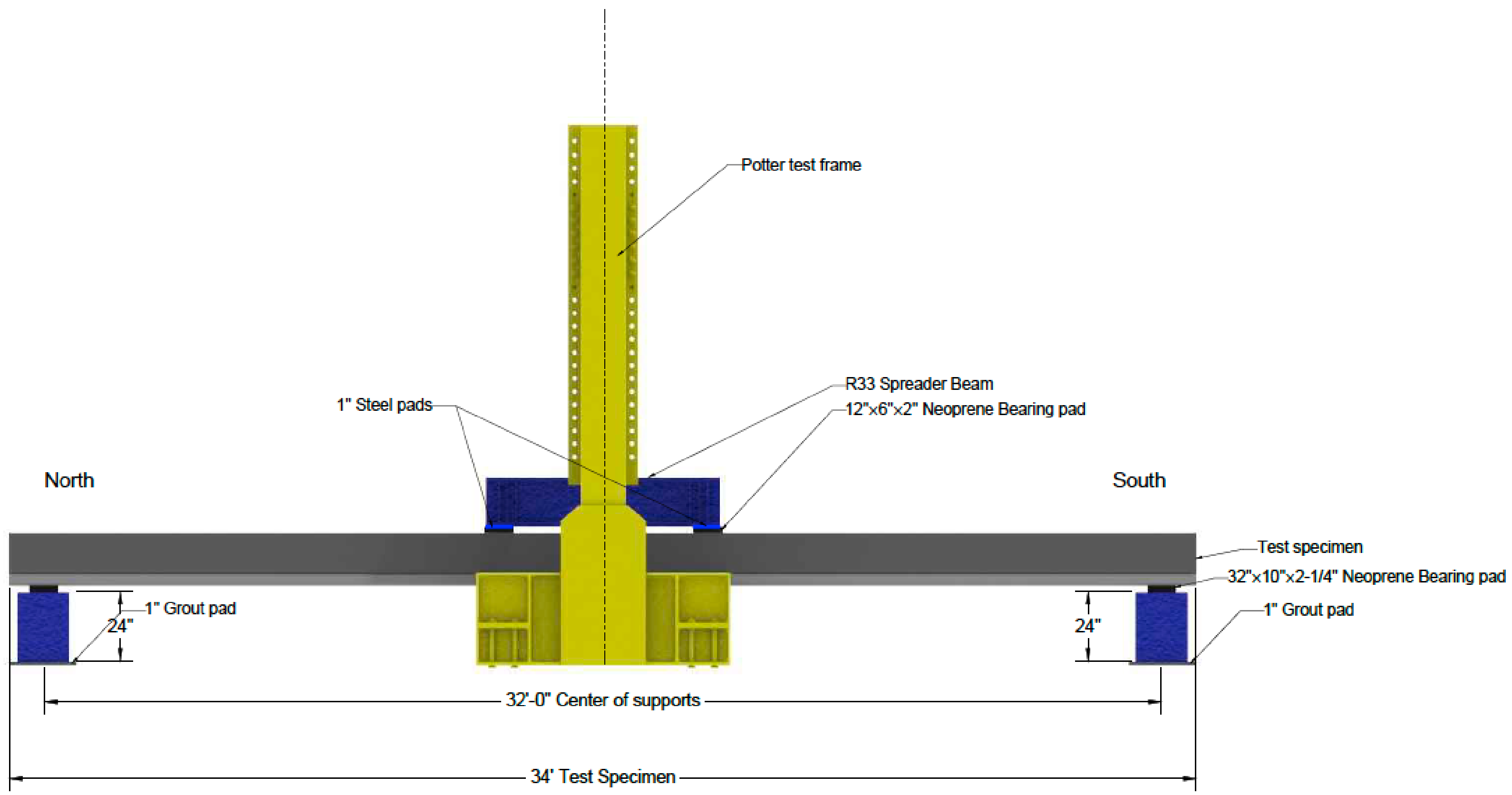


Front View

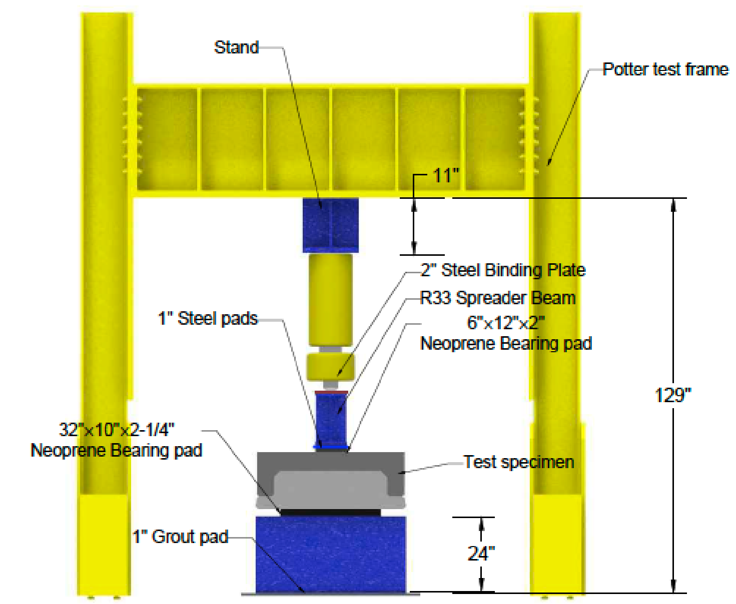


| Table 2 | | | | |
|---|---|---|---|---|
| FSB | Cracking | | Ultimate | |
| | Load (kips) | Deflection (in) | Load (kips) | Deflection (in) |
| FSB-1 | 92.0 | 0.904 | 153.1 | 3.804 |
| FSB-2 | 71.8 | 0.705 | 134.2 | 4.565 |
| FSB-3 | 55.4 | 0.863 | 102.4 | 6.165 |
| FSB-4 | 92.0 | 0.904 | 153.1 | 3.804 |

FAMU-FSU College of Engineering

FDOT

| | |
|---|---|
| Project: | Florida Slab Beam with Stainless Steel Strands and GFRP reinforcement |
| TITLE: | Sheet No.10 Test setup |
| SCALE AT A3: | DATE: 08/03/23 |
| DRAWN: OA | CHECKED: |
| PROJECT NO: | DRAWING NO: |
| REVISION: | |

**Figure A3-10. Sheet 10: Test setup**

## Load rate for test setup

| 1st Loading* | | |
|---|---|---|
| Load (kips) | | |
| FSB-1&4 | FSB-2 | FSB-3 |
| 0 | 0 | 0 |
| 70 | 50 | 30 |
| 80 | 60 | 40 |
| 90 | 70 | 50 |
| 100 | 80 | 60 |
| 110 | 90 | 70 |

| 2nd Loading** | | |
|---|---|---|
| Load (kips) | | |
| FSB-1&4 | FSB-2 | FSB-3 |
| 0 | 0 | 0 |
| 160 | 140 | 120 |

Testing plan notes:-

1- Hydraulic jacking load rate is (0.25 kips/sec).

* 1st loading is applied from zero to the values specified in the table then it is applied gradually until cracks are visible then the specimen will be unloaded to allow strain gauges installation.

** 2nd loading is applied until failure (strand rupture or concrete top crushing).

FAMU-FSU College of Engineering

FDOT

| | |
|---|---|
| Project: | Florida Slab Beam with Stainless Steel Strands and GFRP reinforcement |
| TITLE: | Sheet No.11<br>Load rate for test |

| SCALE AT A3: | DATE: 08/03/23 | DRAWN: OA | CHECKED: |
|---|---|---|---|
| PROJECT NO: | DRAWING NO: | | REVISION: |

Figure A3-11. Sheet 11: Load rate for test

# APPENDIX 4 – DATA COLLECTED DURING FABRICATION

The strand strains were measured using two methods. First, foil type strain gages were glued to the top of 12 strands. Second, strandmeter gauges were mounted to the middle strand in the top layer at the two free lengths at the ends of the casting bed. Figures A4-1 and A4-2 show foil type strain gauge readings at both ends. Figures A4-3 and A4-4 show strandmeter gauge readings. Both measurements have a similar trend. However, the foil type gauges provided high resolution measurements; they measured strain every 0.1 seconds compared to 30 seconds for the strandmeter. Furthermore, the curve obtained from the strain gauge measurements includes abrupt jumps, indicating sudden increases in strain each time a strand was cut.

During the detensioning process, the ends' movements and rotations at Ends 1 and 8 were monitored via a camera and two Imetrum targets located at each end. Figures A4-5 and A4-6 show End 1, located at FSB-1, horizontal movement and rotation with respect to the horizontal axis. Figures A4-7 and A4-8 show the values for End 8, located at FSB-4. Overall, the end movement curves show sudden changes in movement due to impact and elastic shortening of the member. In the case of end rotation, sudden changes due to impact are less noticeable. The end rotation is due to eccentric forces that occur when the strands are cut.

Vibrating wire readings were collected at mid span during detensioning. Figures A4-9 to A4-12 show the VWSG raw readings with respect to time. The values of the measurements were constant until the strands were released, then they started to decrease.

The fiber optic sensors measured strain every 0.1 seconds at approximately 169 locations along the length of each end. Readings from the fiber optic sensors, after all the strands were released, that were located in FSB-1 and FSB-4 are shown in Figures A4-13 to A4-16.

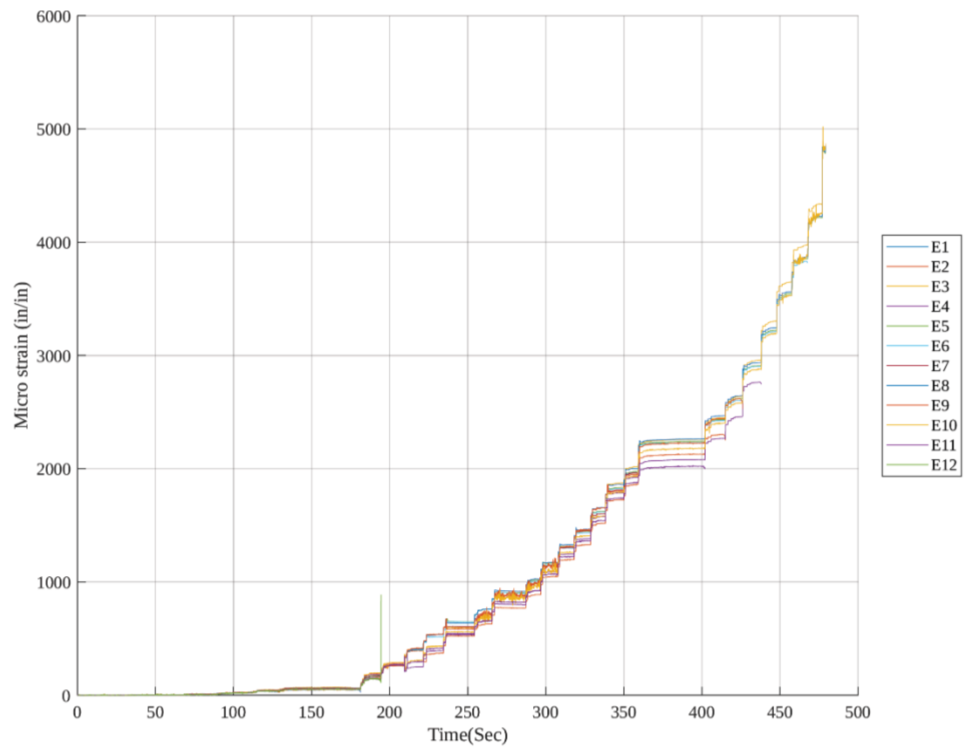


**Figure A4-1. Strain gauges reading during detensioning in the strands at free length near End 1**

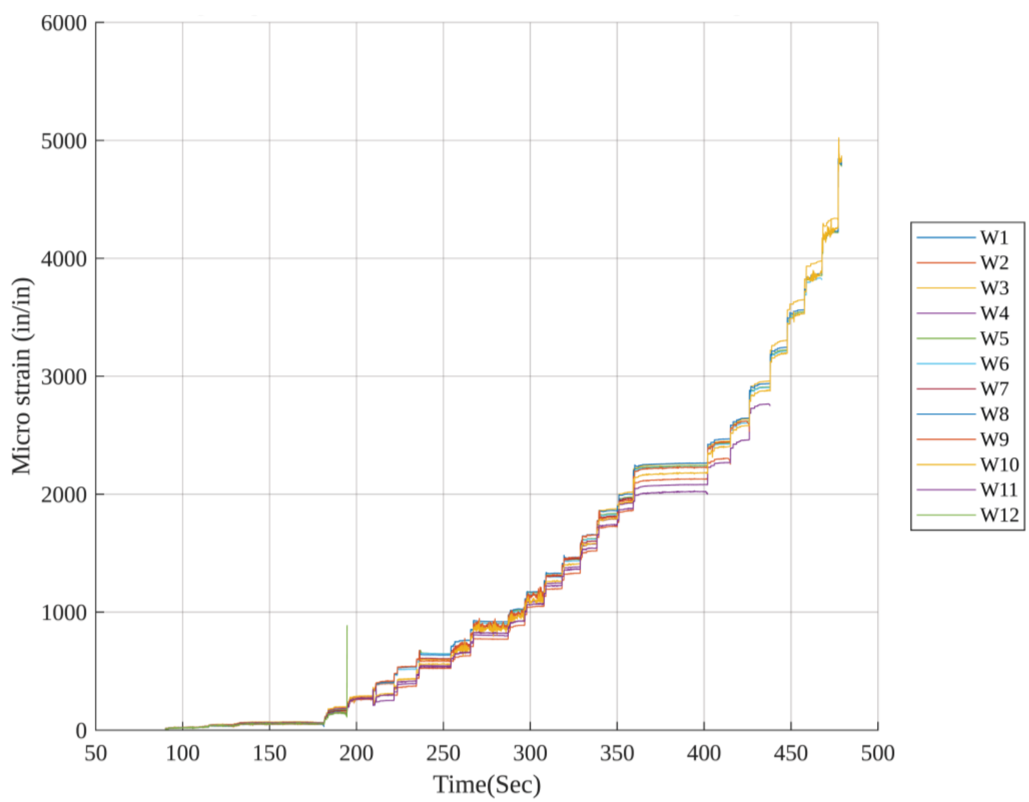


**Figure A4-2. Strain gauges reading during detensioning in the strands at free length near End 8**

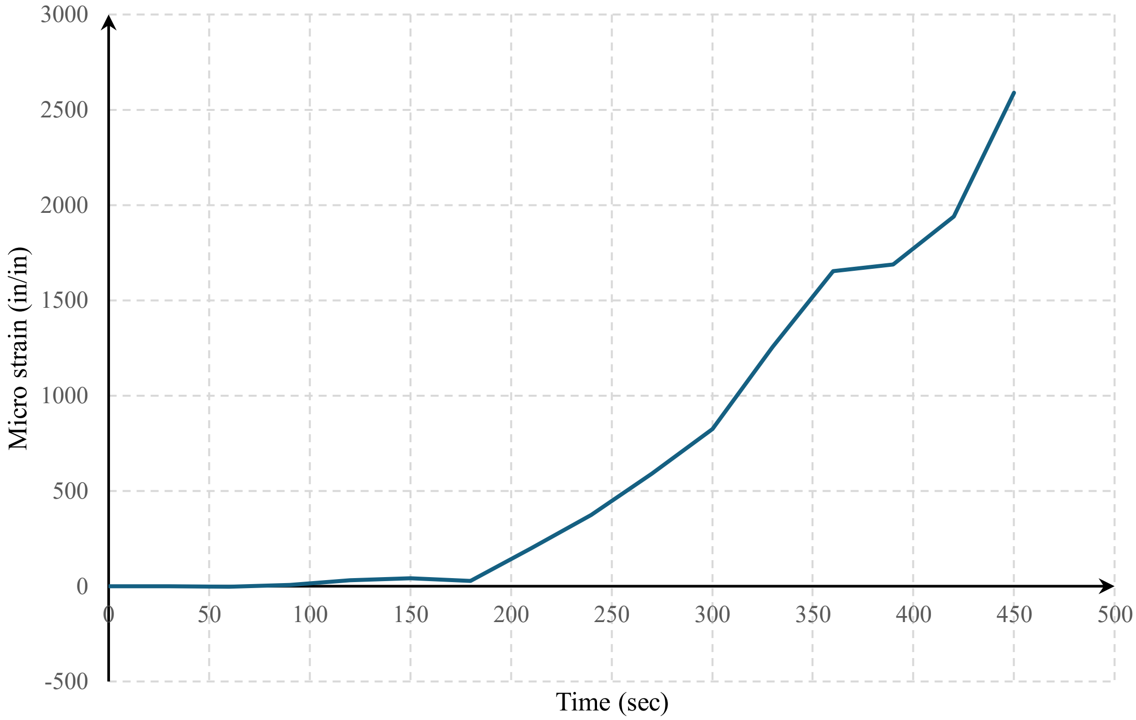


**Figure A4-3. Strandmeter measurements at free length near End 1**

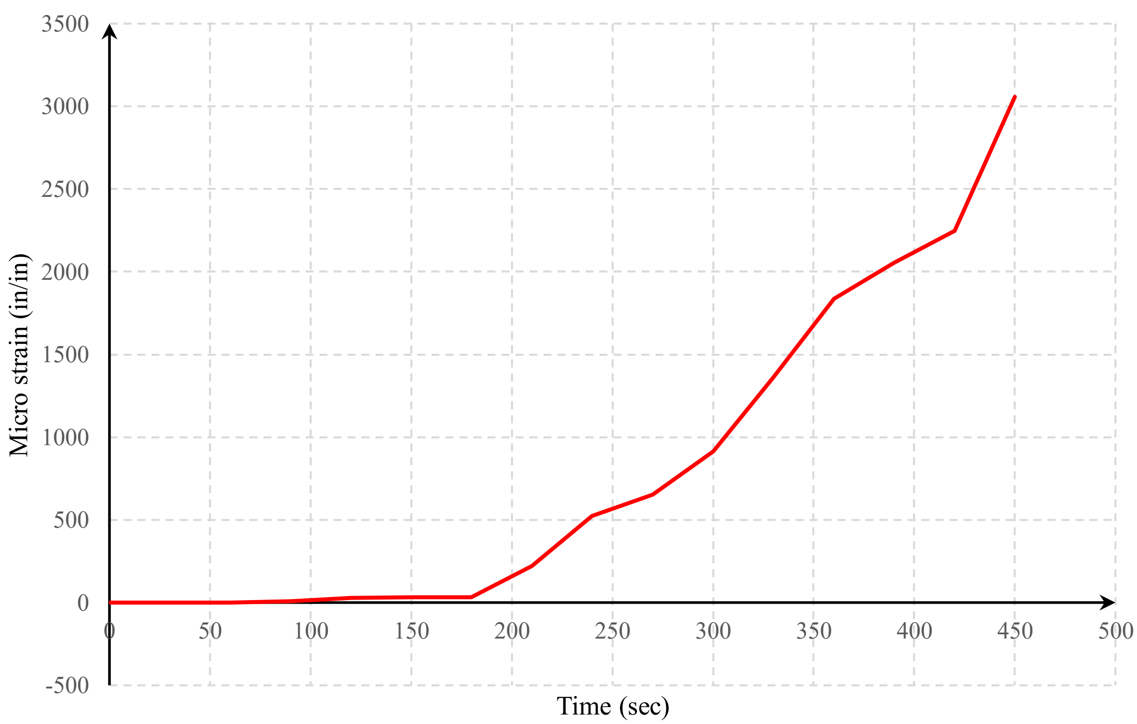


**Figure A4-4. Strandmeter measurements at free length near End 8**

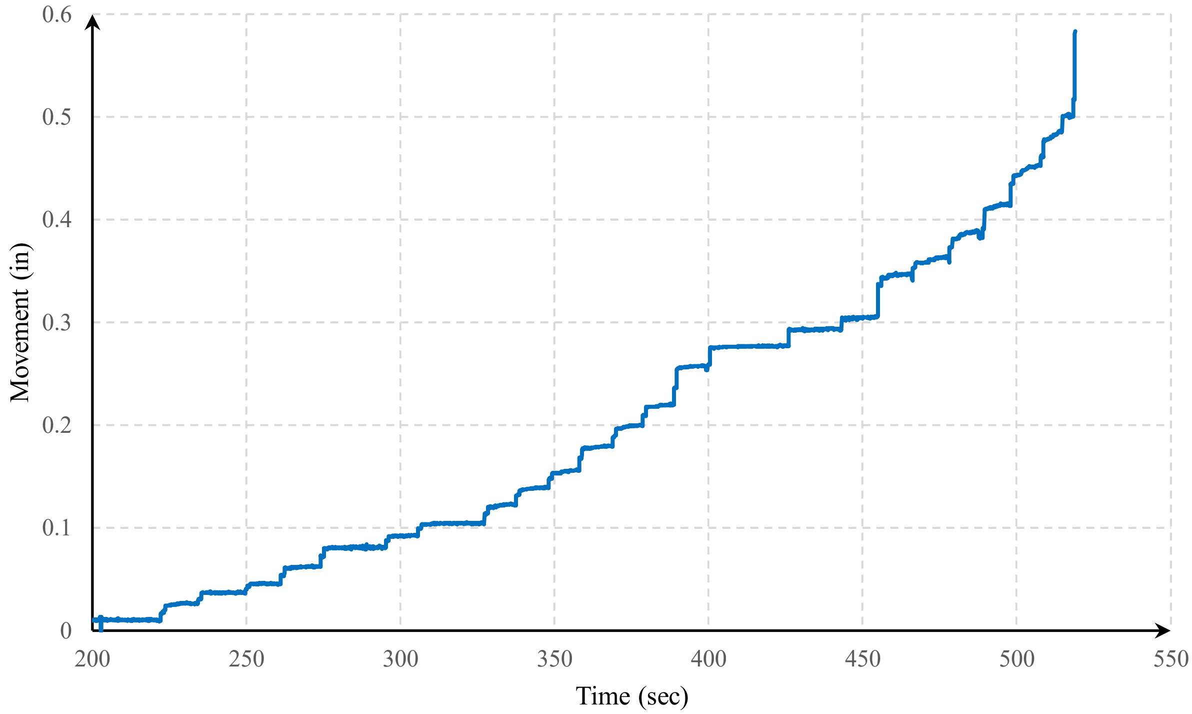


**Figure A4-5. Camera and Imetrum target measurements for End 1 FSB 1 horizontal movement**

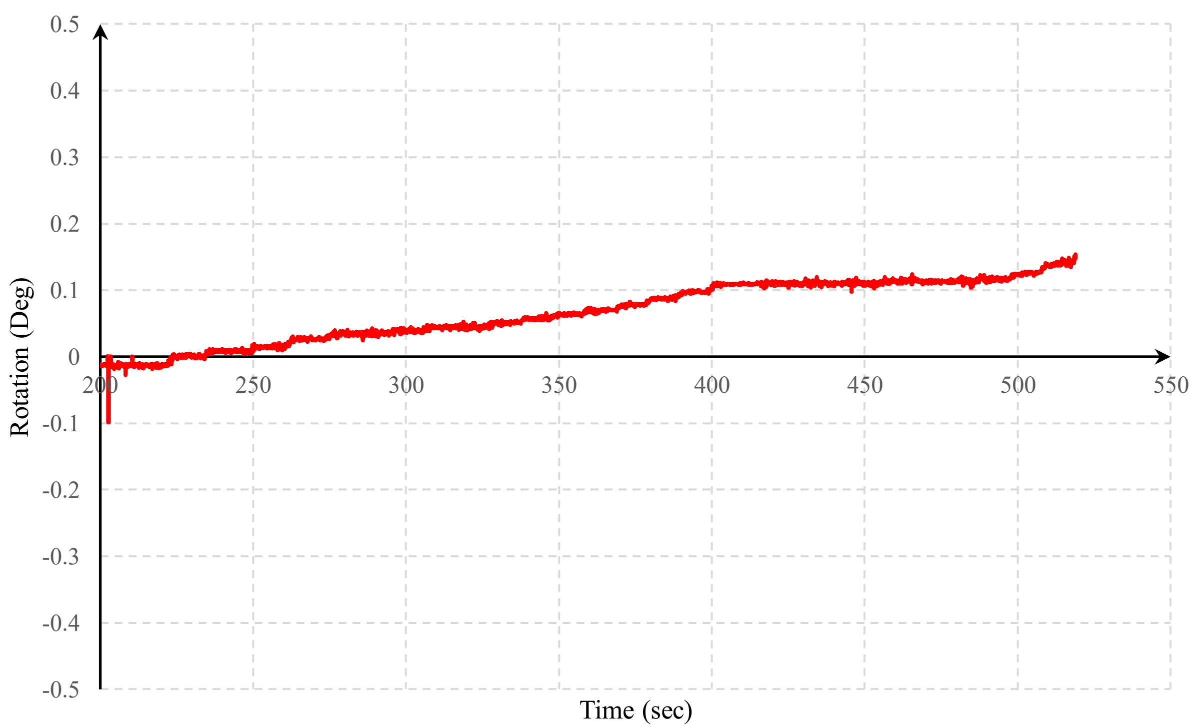


**Figure A4-6. Camera and Imetrum target measurements for End 1 FSB 1 rotation with respect to horizontal axis**

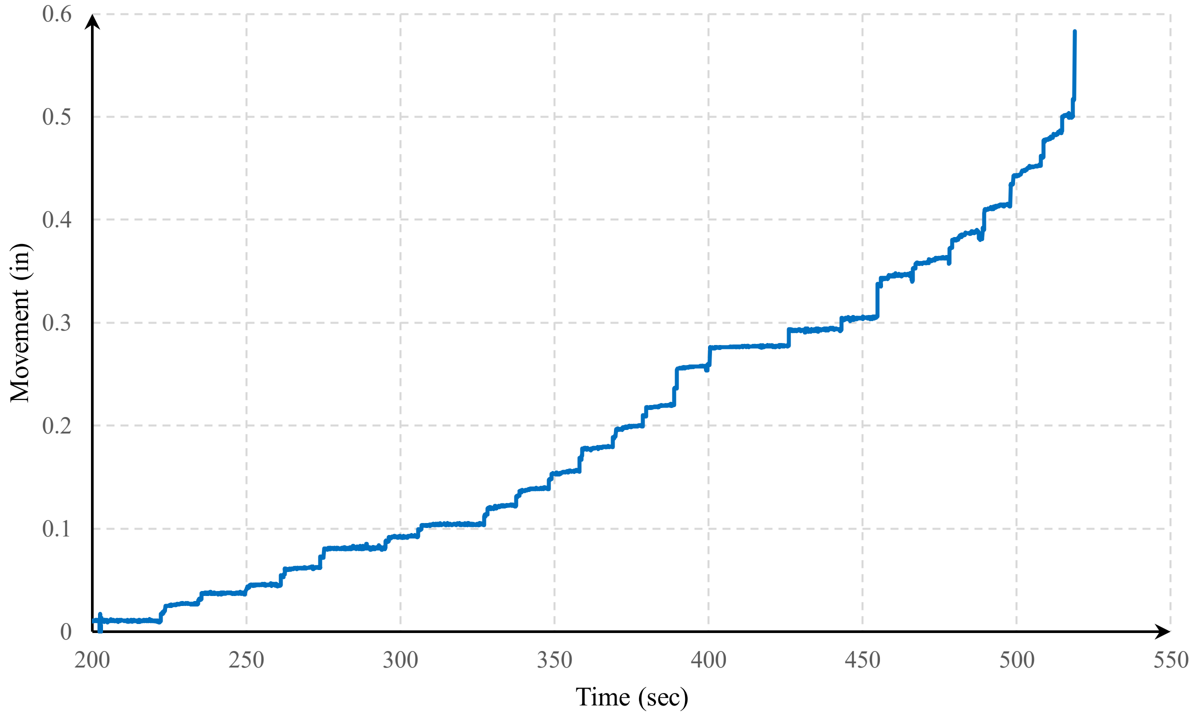


**Figure A4-7. Camera and Imetrum target measurements for End 8 FSB 4 horizontal movement**

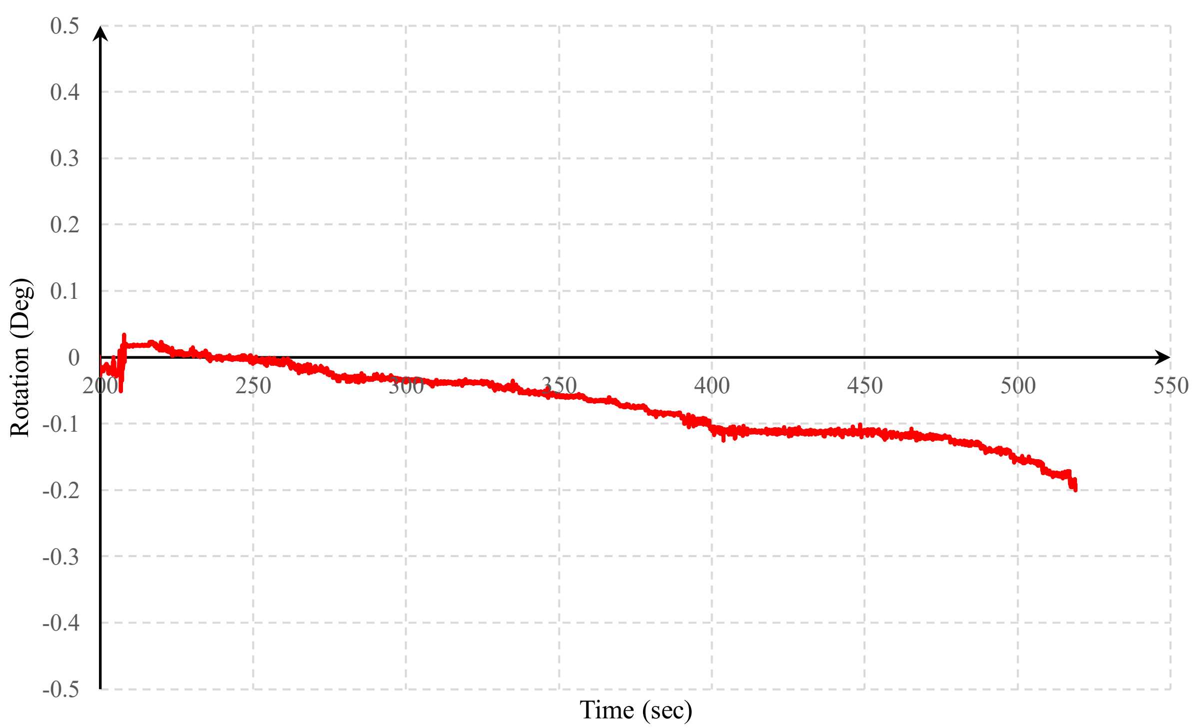


**Figure A4-8. Camera and Imetrum target measurements for End 8 FSB 4 rotation with respect to horizontal axis**

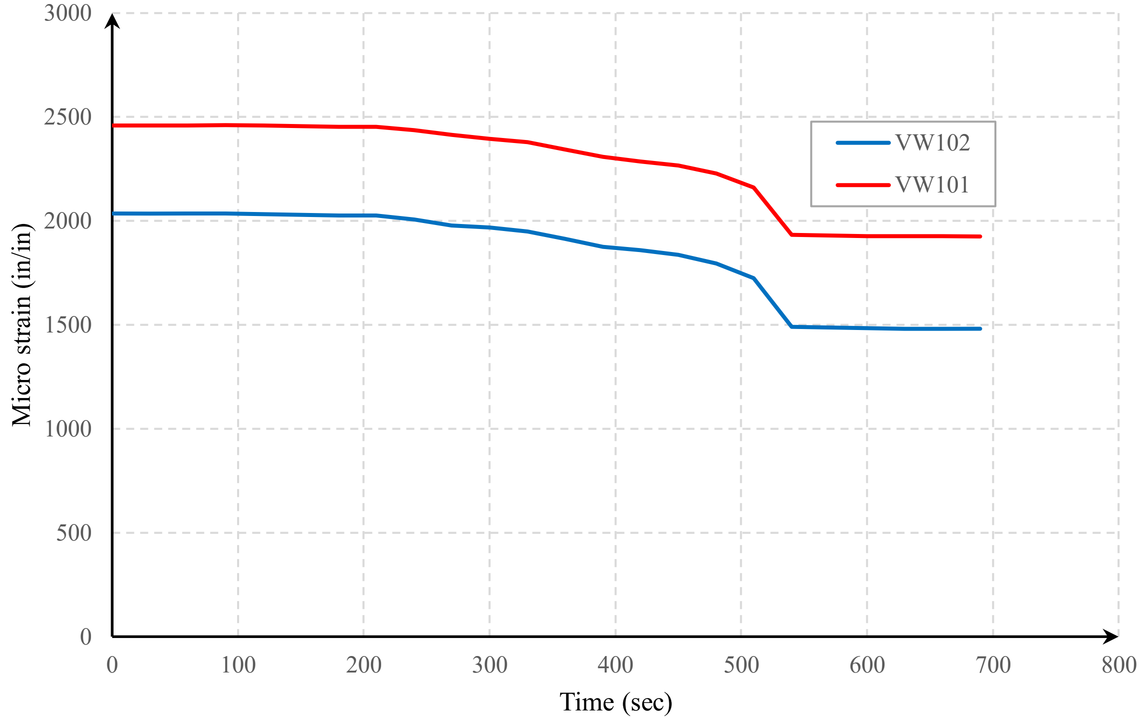


**Figure A4-9. VWSG measurements during detensioning at FSB-1**

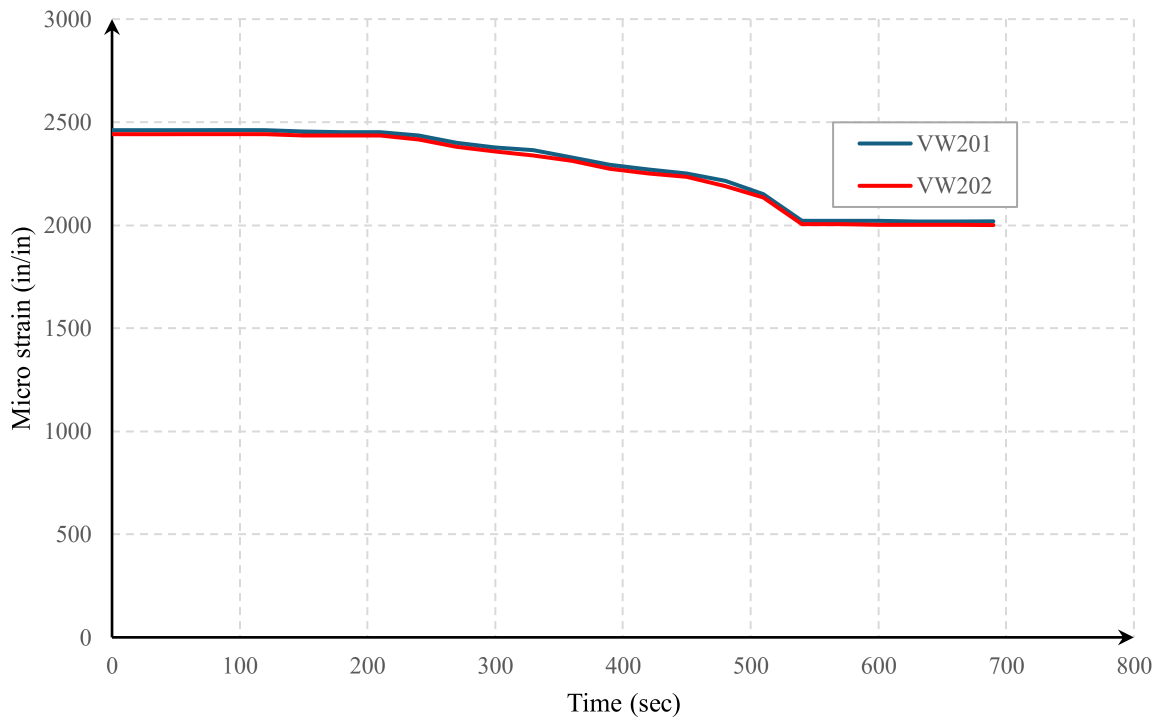


**Figure A4-10. VWSG measurements during detensioning at FSB-2**

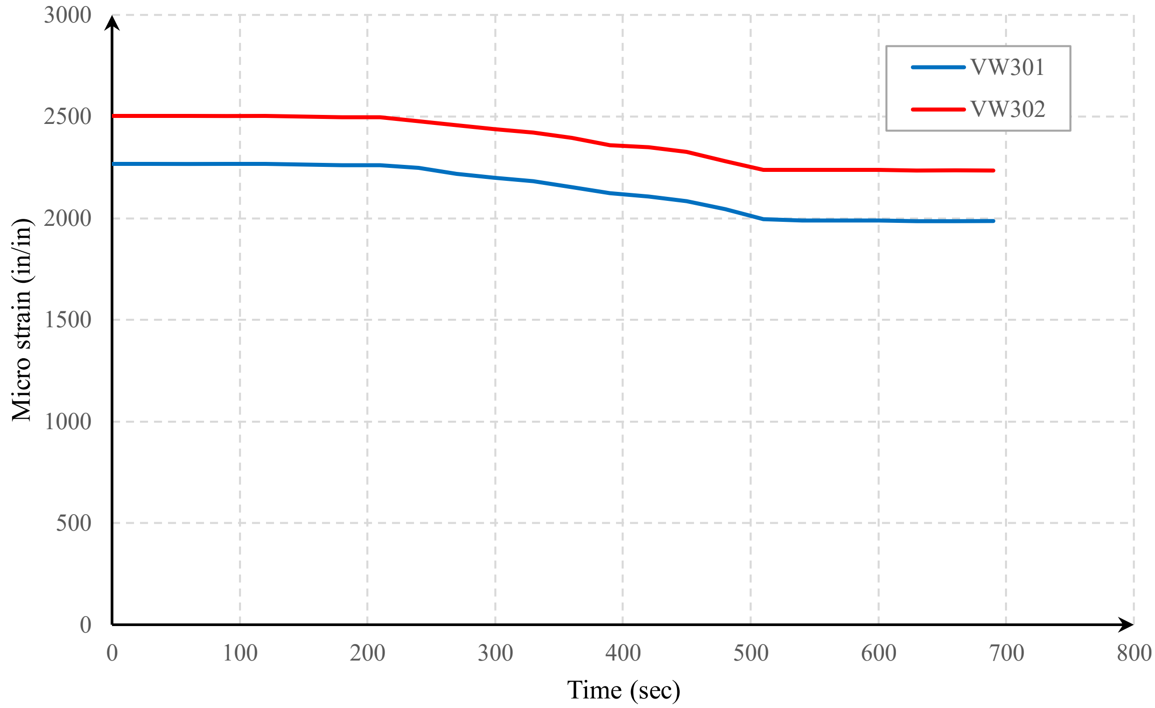


**Figure A4-11. VWSG measurements during detensioning at FSB-3**

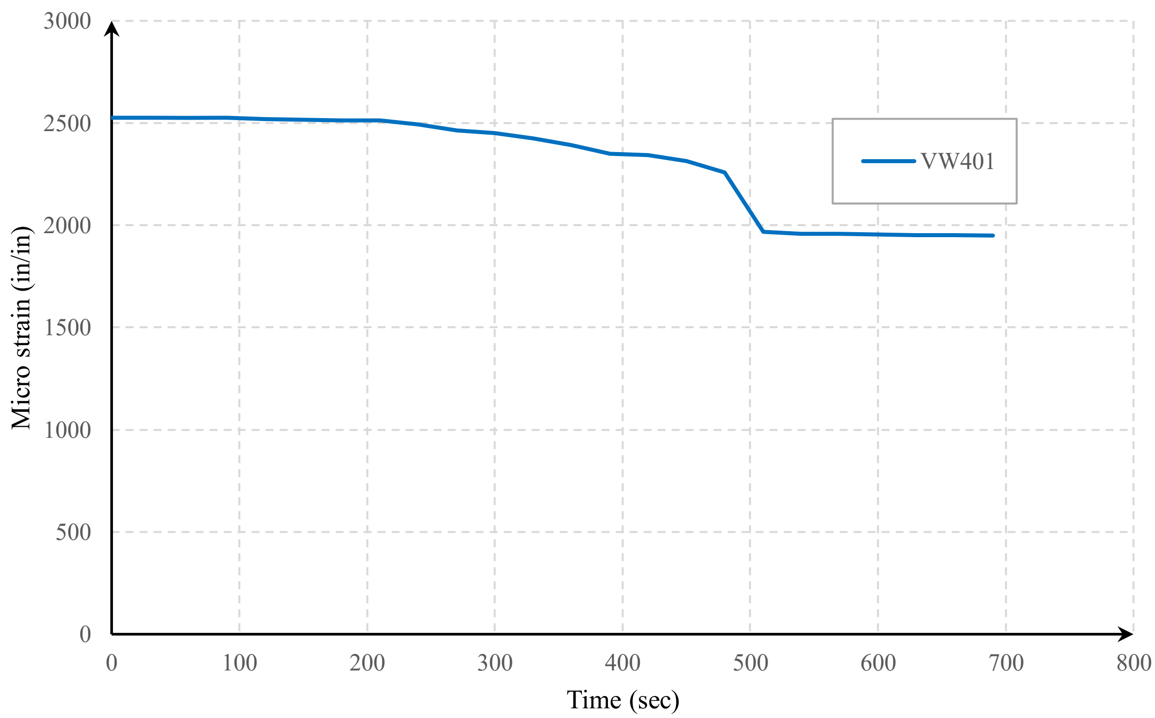


**Figure A4-12. VWSG measurements during detensioning at FSB-4**

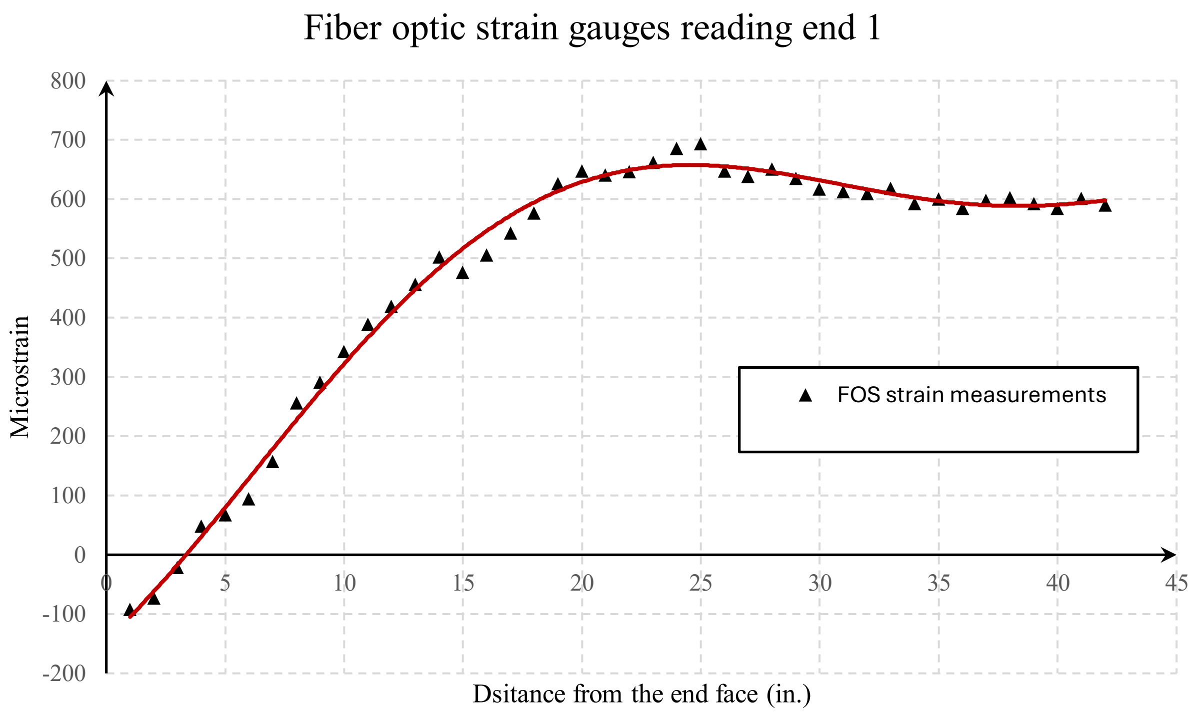


**Figure A4-13. FOS-1 measurements during detensioning at End 1 FSB-1**

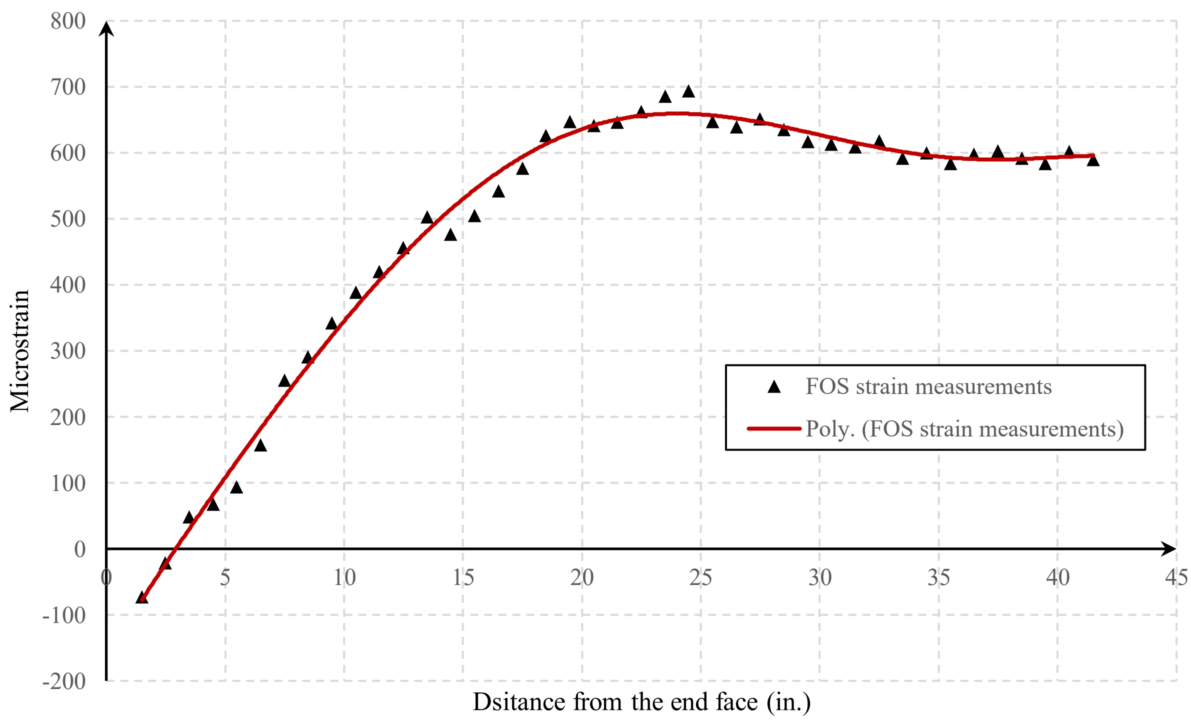


**Figure A4-14. FOS-2 measurements during detensioning at End 2 FSB-1**

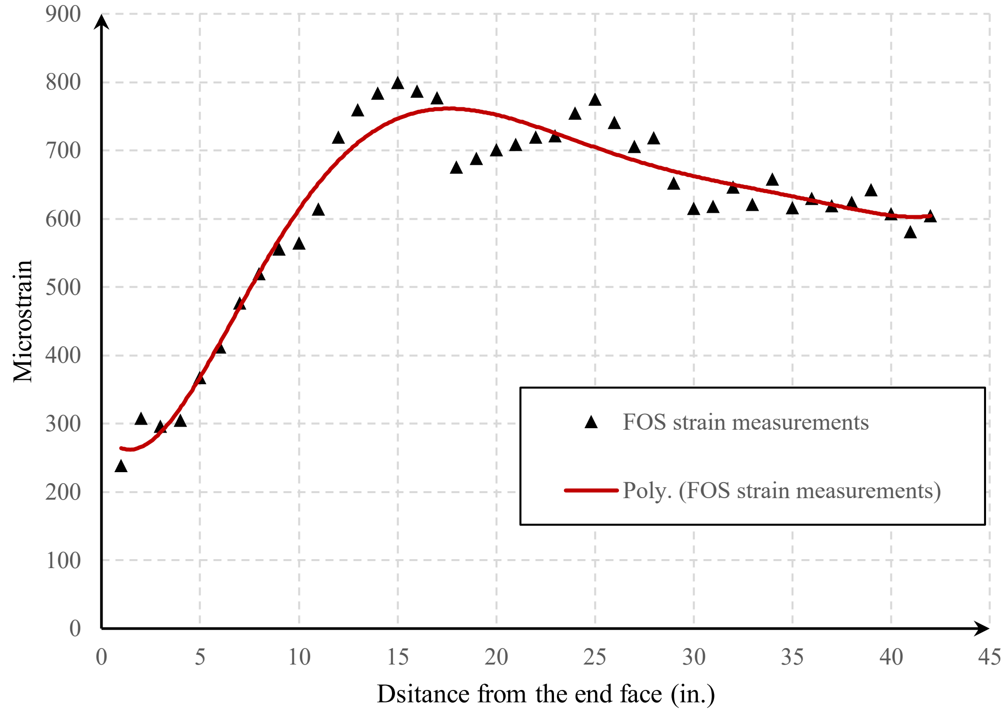


**Figure A4-15. FOS-3 measurements during detensioning at End 7 FSB-4**

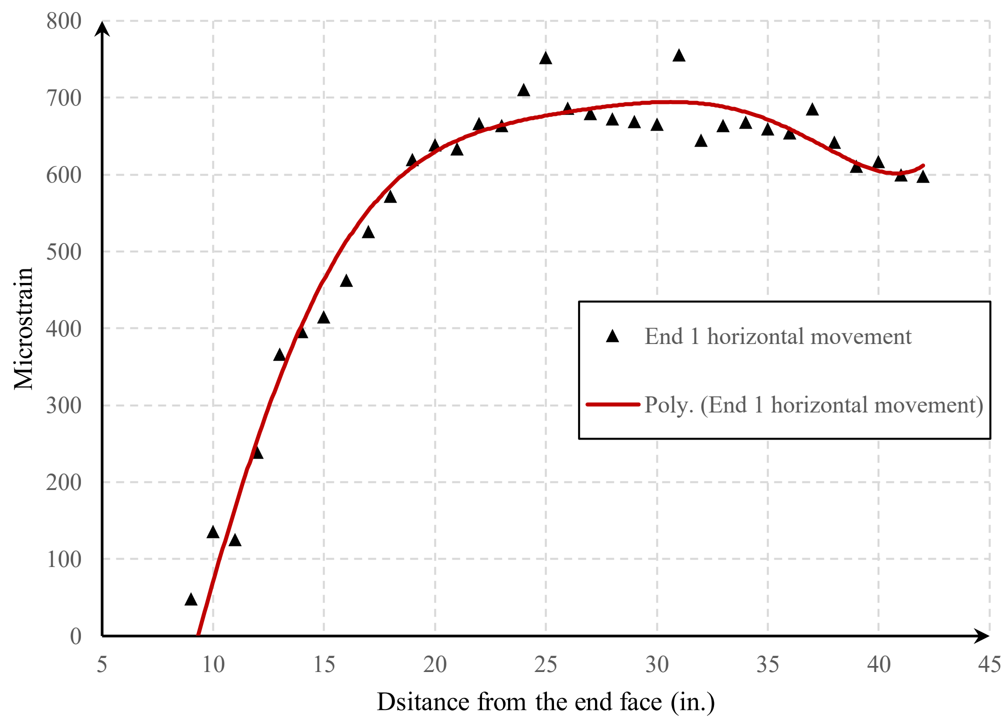


**Figure A4-16. FOS-4 measurements during detensioning at End 8 FSB-4**

# APPENDIX 5 – DELIVERY OF FABRICATED GIRDERS

Four (4) FSBs with 4-in.-thick CIP toppings were fabricated at CDS Manufacturing Inc. The FSBs were delivered to FDOT Structures Research Center (SRC). FSB-1 and FSB-4 were delivered on September 13, 2023, and FSB-2 and FSB-3 were delivered on October 24, 2023. Figures A5-1 through A5-3 show the FSBs being delivered. Figures A5-4 through A5-7 show the delivery tickets for each FSB.

The fabrication activities timeline is as follows:

- FSBs Fabrication: 8/09/2023 – 8/21/2023
- FSB-1 & FSB-4 Delivery: 9/13/2023
- FSB-2 & FSB-3 Delivery: 10/24/2023
- FSB Testing:

| | | |
|---|---|---|
| FSB Testing: | FSB-4 | 10/10/2023 |
| | FSB-1 | 10/12/2023 |
| | FSB-2 | 10/27/2023 |
| | FSB-3 | 11/09/2023 |


Figure A5-1. FSB 1&4 arriving at FDOT Structures Research Center


Figure A5-2. Lifting FSB 4 from the truck

**Figure A5-3. Two FSBs at FDOT Structures Research Center**

Johnny

BOL/DOT-

№ 43144

# CDS MANUFACTURING, INC.

106 Charles Hayes Sr. Drive • Gretna, FL 32332
(850) 627-3902 phone • (850) 627-3904 fax

SOLD TO:

PHONE:

FAX:

SHIP TO:
FSU structures Laboratory
2007 E. Paul Dirac Dr.
Tallahassee, Fl 32310

PHONE:

FAX:

| DATE | DELIVERY | PICKUP | SHIP VIA | F.O.B. | TERMS | ORDER NO. |
|---|---|---|---|---|---|---|
| | X | | CDS | | | |

| QTY | DESCRIPTION | PRICE | AMOUNT |
|---|---|---|---|
| 1 | FSB | | |
| | Bm.Mark Lot Cast Date | Length | |
| | 1-1 FSU1 8/10/2023 | 34' | |
| | | CASEY MATHERS | |
| | | 9-12-23 | |

**Compliance statement with Buy America Provision**
**The dollar amount of Non-domestic steel or iron incorporated in the precast prestressed products listed above is \$0.00. Therefore, we hereby certified that the product(s) described above was (were) manufactured in accordance with the Buy America provisions of 23 CFR 635.410, as amended.**

*All products described herein are in compliance with all Florida Department of Transportation standard specifications.*

*Q.C. Manager* ____ *DATE:* 9-12-23

Customer Signature: ____ DATE: ____

CDS Representative: ____ DATE: 9/13/23

WHITE - FILE COPY CANARY - STATEMENT COPY PINK - CUSTOMER'S COPY GOLDENROD - QUALITY CONTROL COPY

**Figure A5-4. FSB-1 delivery ticket**

Armand

**BOL/DOT-**

№ 43145

# CDS MANUFACTURING, INC.

**106 Charles Hayes Sr. Drive • Gretna, FL 32332**
**(850) 627-3902 phone • (850) 627-3904 fax**

SOLD TO:

PHONE:

FAX:

SHIP TO: FSU Structures Laboratory
2007 E. Paul Dirac Dr.
Tallahassee Fl. 32310

PHONE:

FAX:

| DATE | DELIVERY | PICKUP | SHIP VIA | F.O.B. | TERMS | ORDER NO. |
|---|---|---|---|---|---|---|
| | X | | CDS | | | |

| QTY | DESCRIPTION | PRICE | AMOUNT |
|---|---|---|---|
| 1 | FSB | | |
| | Bm.Mark Lot Cast Date | Length | |
| | 1-4 FSU1 3/10/2023 | 34' | |
| | | | |
| | | | |
| | | | |
| | | | |
| | | | |
| | | | |
| | | | |
| | | | |
| | | | |

**Compliance statement with Buy America Provision**
**The dollar amount of Non-domestic steel or iron incorporated in the precast prestressed products listed above is $0.00. Therefore, we hereby certified that the product(s) described above was (were) manufactured in accordance with the Buy America provisions of 23 CFR 635.410, as amended.**

*All products described herein are in compliance with all Florida Department of Transportation standard specifications.*

*Q.C. Manager* ________ *DATE:* 9-12-23

Customer Signature: ________ DATE: ________

CDS Representative: ________ DATE: ________

**WHITE - FILE COPY  CANARY - STATEMENT COPY  PINK - CUSTOMER'S COPY  GOLDENROD - QUALITY CONTROL COPY**

**Figure A5-5. FSB-4 delivery ticket**

BOL/DOT-

№ 43541

# CDS MANUFACTURING, INC.

106 Charles Hayes Sr. Drive • Gretna, FL 32332
(850) 627-3902 phone • (850) 627-3904 fax

SOLD TO: FSU Rosenberry

PHONE:

FAX:

SHIP TO: Laboratory
2007 E. Paul Dirac Dr.
Tallahassee

PHONE:

FAX:

| DATE | DELIVERY | PICKUP | SHIP VIA | F.O.B. | TERMS | ORDER NO. |
|---|---|---|---|---|---|---|
| | X | | CDS | | | |

| QTY | DESCRIPTION | PRICE | AMOUNT |
|---|---|---|---|
| 1 | Slab beam | | |
| | | | |
| | SPAN # 1 | | |
| | PC. Mark # 1-2 | | |
| | Lot # FSU1 | | |
| | Cast # 8-10-2023 | | |
| | length # 34' | | |
| | | | |
| | | | |
| | | | |
| | | | |
| | | | |

**Compliance statement with Buy America Provision**
**The dollar amount of Non-domestic steel or iron incorporated in the precast prestressed products listed above is $0.00. Therefore, we hereby certified that the product(s) described above was (were) manufactured in accordance with the Buy America provisions of 23 CFR 635.410, as amended.**

*All products described herein are in compliance with all Florida Department of Transportation standard specifications.*

*Q.C. Manager* [illegible] *DATE:* 10-23-23

Customer Signature: [illegible] DATE:

CDS Representative: Lonnie Jones DATE: 10-24-23

**WHITE - FILE COPY CANARY - STATEMENT COPY PINK - CUSTOMER'S COPY GOLDENROD - QUALITY CONTROL COPY**

**Figure A5-6. FSB-2 delivery ticket**

BOL/DOT-

№ 43542

# CDS MANUFACTURING, INC.

106 Charles Hayes Sr. Drive • Gretna, FL 32332
(850) 627-3902 phone • (850) 627-3904 fax

SOLD TO: FSU Rosenberry

SHIP TO: Laboratory
2007 E. Paul Dirac Dr.
Tallahassee

PHONE:

FAX:

PHONE:

FAX:

| DATE | DELIVERY | PICKUP | SHIP VIA | F.O.B. | TERMS | ORDER NO. |
|---|---|---|---|---|---|---|
| | X | | CDS | | | |

| QTY | DESCRIPTION | PRICE | AMOUNT |
|---|---|---|---|
| 1 | Slab beam | | |
| | | | |
| | SPAN # 1 | | |
| | Pc Mark # 1-3 | | |
| | lot # FSU 1 | | |
| | Cast # 8-10-2023 | | |
| | length # 34' | | |
| | | | |
| | | | |
| | | | |
| | | | |
| | | | |

**Compliance statement with Buy America Provision**
**The dollar amount of Non-domestic steel or iron incorporated in the precast prestressed products listed above is $0.00. Therefore, we hereby certified that the product(s) described above was (were) manufactured in accordance with the Buy America provisions of 23 CFR 635.410, as amended.**

*All products described herein are in compliance with all Florida Department of Transportation standard specifications.*

*Q.C. Manager* [signature] *DATE:* 10-23-23

Customer Signature: [signature] DATE: 10/24/23

CDS Representative: [signature] DATE: 10/24/23

**WHITE - FILE COPY CANARY - STATEMENT COPY PINK - CUSTOMER'S COPY GOLDENROD - QUALITY CONTROL COPY**

Figure A5-7. FSB-3 delivery ticket